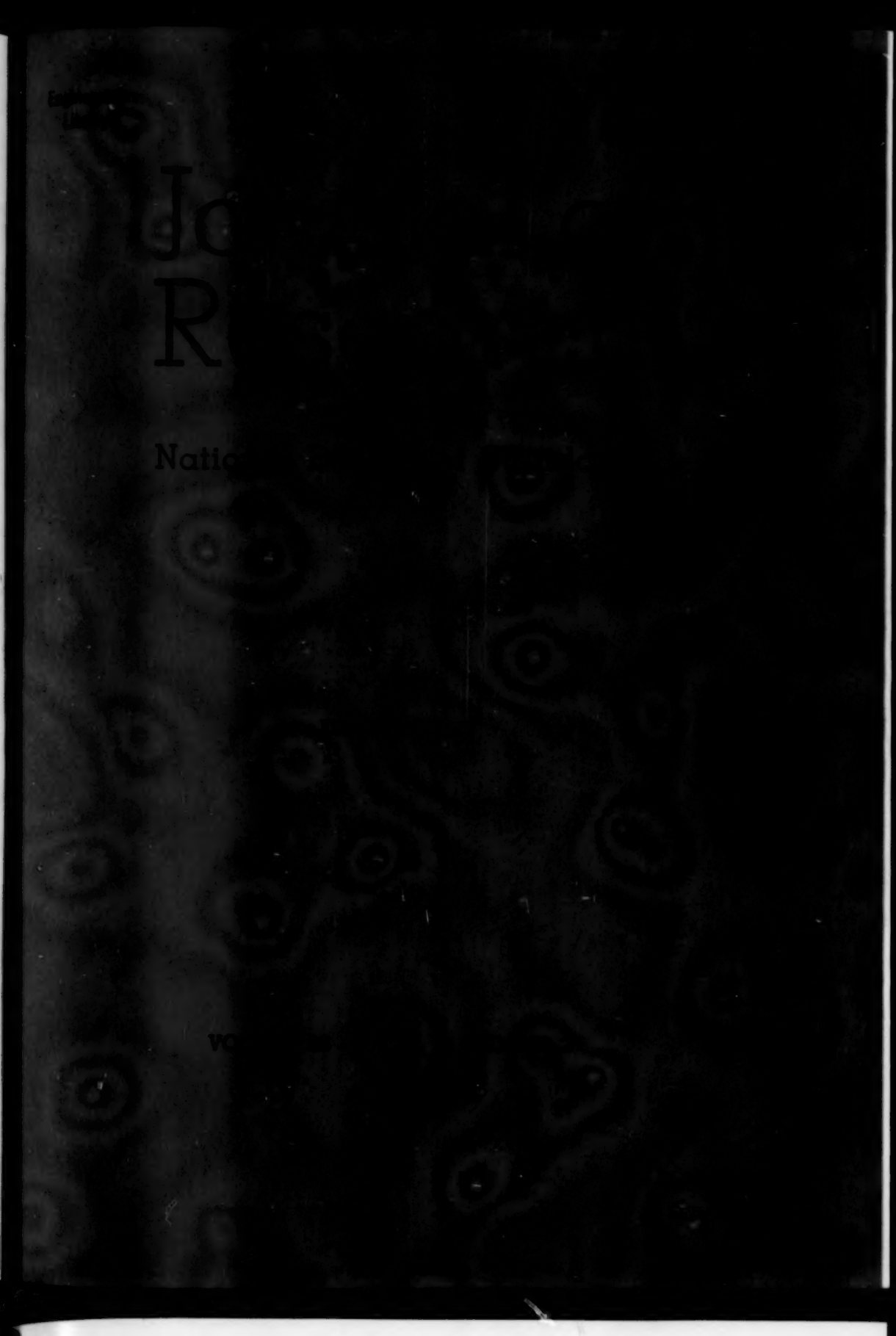

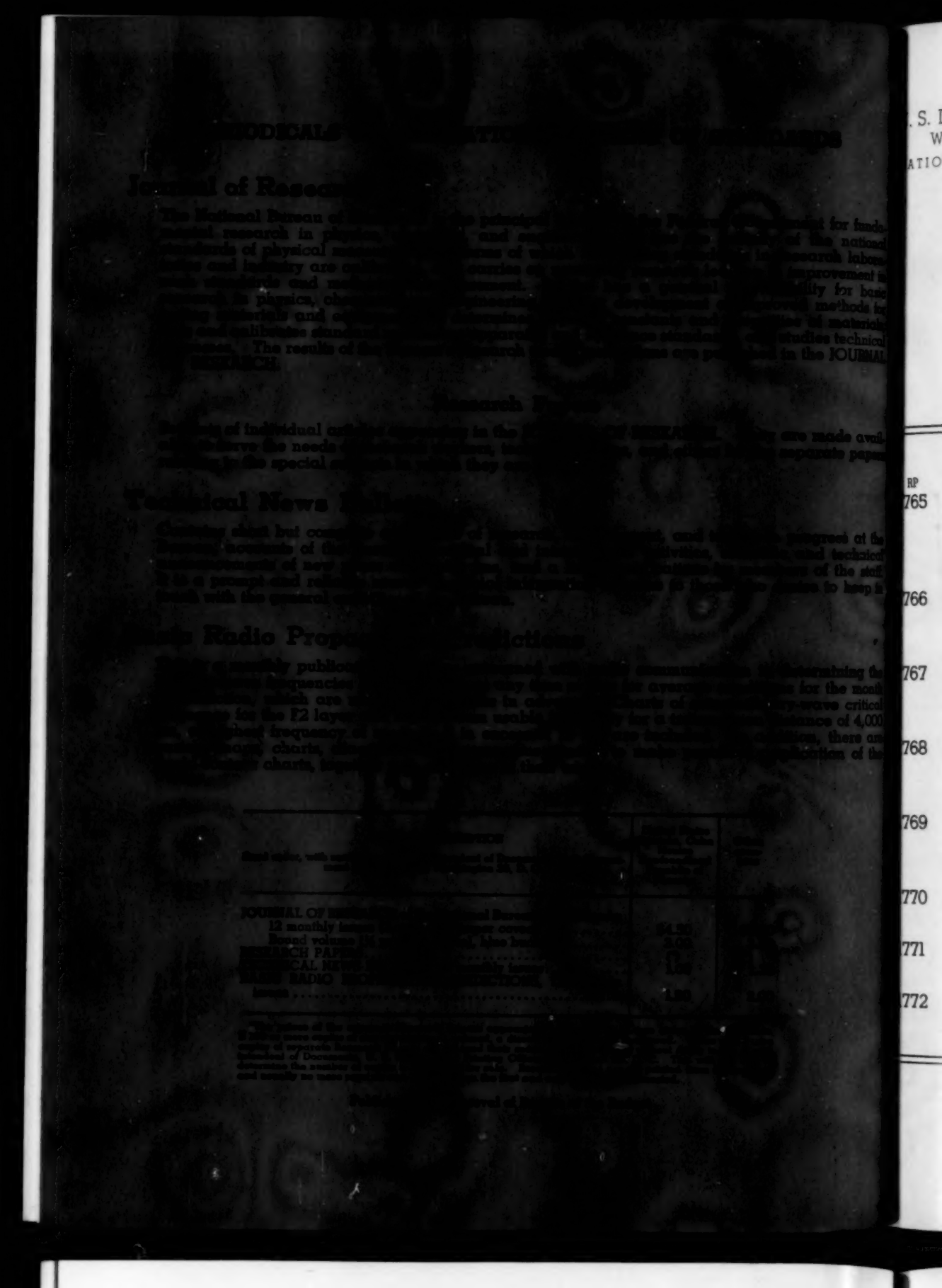

. S. DEPARTMENT OF COMMERCE
W. Averell Harriman, Secretary
ATIONAL BUREAU OF STANDARDS
E. U. Condon, Director

FEBRUARY 1947
VOLUME 38
NUMBER 2

JOURNAL OF RESEARCH

of the

NATIONAL BUREAU OF STANDARDS

Contents

RP		Page
765	Concentration of isotopes of potassium by the countercurrent electro migration method. A. Keith Brewer, Samuel L. Madorsky, John Keenan Taylor, Vernon H. Dibeler, Paul Bradt, O. Lee Parham, Roy J. Britten, and J. Gilman Reid, Jr. (Price 15 cents)	137
766	Concentration of potassium[39] by countercurrent electromigration: Some theoretical aspects of the operation. James W. Westhaver. (Price 10 cents)	169
767	Concentration of isotopes of chlorine by the countercurrent electromigration method. Samuel L. Madorsky and Sidney Straus. (Price 10 cents)	185
768	Normal coordinate analysis of the vibrational frequencies of ethylene, propylene, *cis*-2-butene, *trans*-2-butene, and isobutene. John E. Kilpatrick and Kenneth S. Pitzer. (Price 15 cents)	191
769	Infrared absorption spectra of seven cyclopentanes and five cyclohexanes. Earle K. Plyler, Ralph Stair, and Curtis J. Humphreys. (Price 15 cents)	211
770	Elastic behavior and creep of refractory bricks under tensile and compressive loads. Lewis E. Mong. (Price 10 cents)	229
771	Surface tensions of some optical glasses. Leo Shartsis and Alden W. Smock. (Price 10 cents)	241
772	Laminar boundary-layer oscillations and transition on a flat plate. Galen B. Schubauer and Harold K. Skramstad. (Price 20 cents)	251

UNITED STATES GOVERNMENT PRINTING OFFICE, WASHINGTON : 1947

S. Department of Commerce
ational Bureau of Standards

Research Paper RP1765
Volume 38, February 1947

Part of the Journal of Research of the National Bureau of Standards

Concentration of Isotopes of Potassium by the Countercurrent Electromigration Method [1]

By A. Keith Brewer,[2] Samuel L. Madorsky, John Keenan Taylor, Vernon H. Dibeler, Paul Bradt, O. Lee Parham, Roy J. Britten, and J. Gilman Reid, Jr.

A new electromigration method for the separation of isotopes is described. This method is based on the principle of setting up a flow of electrolyte through a packed column in a direction countercurrent to the flow of the isotopic ions being separated and at a rate intermediate between the velocities of these ions. Under these conditions, the faster moving ions will make headway against the electrolyte stream, while the slower moving ions will be carried back. The separation coefficient $\epsilon - 1$ in the case, for example, of cations, is given as equal to $FV_eC \ln S/1000\, I^+t$, where F is the Faraday constant, V_e is cathode volume in cubic centimeters, C is normality of the electrolyte, S is separation factor, I^+ is positive ion current, and t is time in seconds. Free space and temperature distribution in the packing, balance between ion transport and stream counter flow, and other factors which determine column efficiency are described. In a series of experiments for the concentration of ^{39}K in the cathode compartment of the electromigration cell, the abundance ratio $N = {}^{39}K/{}^{41}K$ was increased from its normal value of 14.2 to a maximum of 24 in about 500 hours of operation and a maximum separation coefficient of 0.385×10^{-3} was obtained. Attempts to concentrate ^{41}K in the anode compartment resulted in a lowering of the isotope abundance ratio to a minimum of 9.1. A study of the distribution of ^{39}K in the packing in experiments carried out for the concentration of ^{39}K in the cathode compartment, showed that the abundance ratio decreases rapidly from the cathode to anode direction. A description is given of the mass spectrometer used in measuring the abundance ratio $^{39}K/^{41}K$, also, of the automatic control used in regulating the counter flow in some of the electromigration cells.

Discussion of Method for Concentration of Potassium Isotopes

By A. Keith Brewer and Samuel L. Madorsky

1. Introduction

The separation of isotopes by ion transport in olution was first suggested in 1921 by Lindemann].* A mechanism was proposed based on an trinsic difference in the velocities of the isotopic ns. It was postulated that an ion of mass m tains a fraction $m/(M+m)$ of its momentum after collision with a solvent molecule of mass M. Lindemann suggested that the electrolysis should be carried out in a medium such as agar-agar to cut down diffusion. Mulliken and Harkins [2], in commenting on Lindemann's proposal, expressed the opinion that the slight differences in ionic mobility to be expected would be masked by diffusion and convection.

The first experimental test of the method was made by Kendall and Crittenden [3] on chlorine and lithium isotopes. Later Kendall [4] transported chlorine ions through 100 feet of agar-agar filled tubes, using the moving boundary method; an atomic-weight determination failed to show any

*Figures in brackets indicate the literature references at the end of this per.

[1] This paper will be included in volume 6, division III, of the Manhattan Project Technical Series.
[2] At present with the U. S. Navy Department.

isotope shift. Pilley [5], using the same technic, failed to detect an isotope shift for chlorine and magnesium. A further attempt by the same method led Jette [6] to conclude that "any difference in the mobilities of isotopic ions is exceedingly improbable."

A countercurrent reflux mechanism has recently been developed at the Bureau [7] which unquestionably establishes a difference in the forward transport velocities of isotopic ions of potassium. The basic principle of this method rests on an imposed flow of electrolyte through a packed column or capillary in the cathode to anode direction at a rate just sufficient to reduce the net forward transport of K^+ ions to zero. Under these conditions, the faster moving $^{39}K^+$ ions will make headway against the electrolyte stream, whereas the slower moving $^{41}K^+$ ions are carried back. This results in a concentration of ^{39}K being built up in the cathode compartment.

The concentrations that can be built up by this method are limited only by the number of theoretical plates that can be realized in the packing. The conditions that must be observed in order to obtain a short height of theoretical unit are essentially the same as in any conventional reflux column. A mathematical analysis of the mechanism is presented in RP1766 [10].

The experimental setup used in the separation of ^{39}K and ^{41}K is indicated by the following elementary arrangement. Consider a tube bent upward at the ends and filled with sand in the horizontal section. Let one arm serve as the cathode compartment and the other as the anode. The anode compartment is provided with a spillway to maintain a constant level in the system. When the tube is filled with a potassium sulfate solution and the current turned on, K^+ ions move toward the cathode and SO_4^{--} ions toward the anode. Conditions for total reflux are established by adding sulfuric acid to the cathode compartment at such a rate and concentration that the pH and concentration of the cathode solution remain unchanged. At the same time a solution of potassium hydroxide is added to the anode compartment at an equivalent rate. The result is a flow of electrolyte from the cathode to the anode, and from an overflow at a rate just sufficient to prevent a net forward transport of K^+ ions. The velocity of the electrolyte stream, in consequence, is equal to that of the average K^+ ion, and the current carried by the K^+ ions is reduced to zero. As $^{39}K^+$ has a slightly greater mobility than $^{41}K^+$, it will make headway against the electrolyte stream, whereas $^{41}K^+$ is washed back.

As the anode compartment is constantly being supplied with KOH, the ^{39}K concentration will remain at its normal value. As a result, this compartment serves as a constant-supply reservoir.

The point balance between ion migration and stream flow is confined to the uniform porous packing separating the cathode and anode compartments.

2. Separation Coefficient

The countercurrent reflux mechanism just outlined is dependent only on a difference in mobility for the isotopic ions. The basis for this difference in mobility is not pertinent. Nevertheless, it is interesting to speculate on the phenomena involved, which can give rise to a difference in forward transport. Several possibilities exist.

The forward motion of an ion in an electric field can best be considered as an unidirectional drift superimposed upon the random motion due to kinetic agitation; the ion receives a forward acceleration during the interval between collisions. The mean time between collisons is given by l/v_{th}, where l is the mean free patb and v_{th} is the average thermal velocity. The velocity due to the electric field is equal to the force times the time between collisions divided by the mass, m, i. e., $v=Eel/(v_{th}m)$. Thus the average forward drift velocity is $v_a=Eel/2mv_{th}$. The mobility of the ior, $\mu=v_a/E$, is then

$$\mu=\frac{el}{2mv_{th}}=\frac{el}{2(3mkT)^{1/2}}, \quad (1)$$

since $v_{th}=\sqrt{3kT/m}$.

On the basis of the above analysis, the electric field can be considered as imposing a drift velocity on the velocity of the thermal agitation, which is inversely proportional to the square root of the ion masses.

A further possible cause for a difference in isotopic ion mobility is a probable difference in the hydration of the ions. As ^{41}K has been shown to be held more tenaciously in a zeolite structure than is ^{39}K [8, 9], a difference in attachment to water molecules is to be expected.

A difference in forward transport of the isotopes

may also exist if there is an isotope effect between ions and undissociated molecules. The isotope shift between carbonate ion and carbon dioxide is an example. This mechanism, however, may not apply to potassium salts, which are highly ionized.

The countercurrent ion-transport mechanism, although having much in common with conventional reflux columns used in adiabatic distillation, is different in that no single-stage or single-plate process exists. In consequence, it is impossible to define the height elemental theoretical plate for the column in an exact sense; for this reason it is preferable to use the term "height theoretical unit" to define the segment length of column required to produce a change in concentration, ϵ, where ϵ is the separation coefficient, defined as the ratio of the mobilities of the two isotopic ions. Assuming eq 1 to be correct, ϵ can be expressed according to eq 2 as the inverse ratio of the square root of the isotope-ion masses. The hydration of K^+ ions is not known with certainty, but $K^+.7H_2O$ is a reasonable value. The theoretical separation coefficient, therefore, has been given the arbitrary value of

$$\epsilon=\sqrt{\frac{^{41}\text{K}7\text{H}_2\text{O}}{^{39}\text{K}.7\text{H}_2\text{O}}}=1.006. \tag{2}$$

3. The Transport

The rate of transport of $^{39}K^+$ and $^{41}K^+$ ions across the tube is

$$AC_l\left(\mu_l\frac{P}{l}-v\right) \tag{3}$$

$$AC_h\left(\mu_h\frac{P}{l}-v\right), \tag{4}$$

Where A is the free cross-sectional area of the packing, C_l and C_h are the concentrations on the light and heavy ions in moles per cubic centimeter, μ_l and μ_h are the mobilities of the ions in centimeters second^{-1} volt^{-1}, P is the potential difference across the packing in volts; l is the length of the packing; v is the velocity of the liquid in centimeters per second.

As the velocity of the liquid, v, is adjusted so that the net transport of K^+ ions is zero, the sum of the transports of ^{39}K and ^{41}K are zero, hence

$$v=\frac{P}{l}\times\frac{C_l\mu_l+C_h\mu_h}{C_l+C_h}. \tag{5}$$

The transports of light and heavy ions obtained by substituting eq 5 in eq 3 and 4 are

$$\pm A\frac{P}{l}C_lC_h\frac{\mu_l-\mu_h}{C_l+C_h}.$$

The initial change in concentration of the light and heavy isotopes at the cathode is given by

$$\frac{dC_l}{dt}\left[\frac{P}{l}\frac{dC_h}{dt}\right]=\frac{AP}{V_cl}C_lC_h\frac{\mu_l-\mu_h}{C_l+C_h},$$

so that

$$\frac{d}{dt}\ln\frac{C_l}{C_h}=\frac{AP}{V_cl}(\mu_l-\mu_h), \tag{6}$$

where V_c is the cathode volume, and t is time in seconds.

Equation 6 can be rewritten

$$\ln S=\frac{AP}{V_cl}(\epsilon-1)\mu t, \tag{7}$$

where μ is the mobility of the average K ion, ϵ is the separation coefficient, and S is the separation factor.

The separation factor, S, is defined as the ratio of the concentration of light to heavy isotopes at the cathode at time t divided by the normal ratio at time zero. Thus

$$S_{t=\infty}=\frac{R_c}{R_a}=\epsilon^n, \tag{8}$$

where $R=C_l/C_h$, c and a refer to the cathode and anode, and n is the number of theoretical plates.

It is often more convenient to calcaluate ϵ in terms of the current rather than the voltage. In this case, the molar isotope transport can be considered as equal to the gain in concentration of the faster isotope in the cathode compartment. This can be expressed initially in terms of moles ^{39}K by the simple equation

$$\frac{I^+t(\epsilon-1)}{F}=\frac{V_cC\ln S}{1{,}000}, \tag{9}$$

or more exactly by the equation

$$\frac{I^+t(\epsilon-1)N_1N_2}{F}=\frac{V_cC}{1{,}000}\times\frac{R_l-R_0}{(R_l+1)(R_0+1)}, \tag{10}$$

where I^+ is the positive ion current in amperes before superimposing the counterflow: t is the

time in seconds; N_1N_2 are the mole fractions of ^{39}K and ^{41}K, V_c is the cathode volume in cubic centimeters, C is the normality of the electrolyte, and F is the Faraday constant (96,500 coulomb/mole), R_t and R_0 are N_1/N_2 at times t and 0, respectively.

Neither the voltage nor the current equation can be considered to hold precisely except at initial stages of the experiment as both neglect the concentration built up in the packing. Likewise, both equations neglect back diffusion and remixing processes, which set in as soon as a concentration gradient is established. Both expressions anticipate that the process will continue until the gradient reaches the point where the forward transport is balanced by back diffusion.

4. Free Space and Packing Temperature

The reduction of remixing and back diffusion to a point below the forward transport necessitates that the ion-electrolyte reflux balance be established in a porous packing capillary, or thin sheet. In order to apply eq 7 to a packed column, it is necessary to know the free cross-sectional area, A, of the packing. In addition, a knowledge of the temperature distribution in the packing is required in order to evaluate μ.

(a) Free Space in Packing Materials

The free space in various packings was measured by the displacement of water. The values observed for several packings are

Material	Free space (percent)
Glass wool	75
Glass beads	38
Sand	34 to 36
Silicon Carbide	35

By comparison, the free space for perfect spheres of uniform size is 26 percent for close packing, where each bead is in contact with 12 others; and 48 percent for loose packing, where each sphere is in contact with 6 others. The glass beads used were No. 28, 48, 70, and 107 mesh. The free space was essentially the same for all sizes.

The electrical free space, which is not the same as the volume free space, was measured by comparing the conductivities of packed and unpacked columns. KCl, 1:60, was used as the electrolyte. The packings were carefully tamped in a glass U-tube, the electrodes being placed immediately above the packing surface. Care was taken to insure that the electrodes were replaced in exactly the same position in successive experiments. Measurements were made with 60-c a-c current over the range from 0.06 to 0.25 amp. The conductivity was independent of the current. The electrical free space obtained for various packings was

Material	Free space (percent)
Glass beads	28. 9
Sand	28. 1
Silicon carbide	27. 5

These values are appreciably lower than for the volume free space as the pores are not straight but have a tortuous path that is longer than the packing itself.

(b) Temperature in Packed Tubes

The temperature in the center of a diaphragm packing can be estimated by assuming that the heat leaving an element of volume within the tube is equal to the heat generated within that element.

The temperature was measured under operating conditions by inserting a thermocouple incased in a thin-walled glass envelope at various points within the packing. The diameter of the tubes used was 1.4 cm and the wall thickness 0.8 mm. The solution was 1:60 KCl. The cells were operated at the indicated current for 30 minutes prior to reading the temperature. The temperature reached its maximum at a point about 4 cm from the end of the packing. The maximum temperature for various packings immersed in a 25° C water bath is as follows:

Current	Temperature		
	Glass beads	Silicon carbide	Sand
amp	*°C*	*°C*	*°C*
0. 30	46	34	
. 40	59	40	44
. 50	73	45	50
. 60	86	51	61
. 70	Boiling	60	70

Two sizes of glass beads were tested, 60 and 107 mesh; no appreciable difference was observed; the sand and silicon carbide were 100 and 150 mesh, respectively.

5. Factors Determining Column Efficiency

The efficiency of the separation mechanism is determined by the power required to change the isotope ratio by one theoretical unit. As the conductivity of the column is independent of the isotope ratio the problem resolves itself into the number of theoretical units that can be realized in one centimeter of packing, i. e., the concentration gradient. It is obvious that a concentration gradient can be built up only to the point where the forward transport is balanced by back diffusion.

Back mixing in a reflux column can enter in a number of ways. Some of these can be eliminated by proper design of cell, but others are inherent in the mechanism.

The factors giving rise to back-mixing will be discussed in a qualitative manner in this report. A quantitative discussion of the problem is given in RP1766 [10].

(a) Diffusion

Back-mixing cannot be reduced below the limit set by diffusion in a stagnant liquid. The relation between the mobility, μ, and diffusion, D, is given by kinetic theory to be

$$\mu = \frac{e}{kT} D, \tag{11}$$

where μ in a normal solution of K_2SO_4 for K^+ is 4.98×10^{-4} cm sec $^{-1}$ volt $^{-1}$, e is the charge on the positive ion, k is Boltzman's constant, and D is in square centimeters per second. An evaluation of the constants gives $D=0.026\mu$ for singly charged ions in a gradient of 1 v/cm. As the gradient in most of the experiments to be described in this series ranged from 5 to 10 v/cm, the forward transport, μ, will exceed the back-diffusion coefficient by 200 to 400. From this it may be inferred that an upper limit for n in eq 8 could approach 200 theoretical units per centimeter, under ideal conditions.

(b) Balance Between Ion Transport and Stream Flow

Separation, as has been pointed out, is dependent on the establishment of an exact balance between stream flow and ion transport. For potassium the fractional difference in mobility of the two ions, as derived from eq 1 is taken to be $\epsilon - 1 = 0.006$. The abundance ratio of the isotopes is $^{39}K/^{41}K = 14.20$. In consequence, for zero current to be carried by the K^+ ions the stream velocity will be very close to the ^{39}K mobility. If the stream velocity falls below that of ^{41}K, then both isotopes will be carried into the cathode compartment. The tolerances are well defined, a decrease in rate of more than 14.2/15.2 of 0.6 percent from balance will admit ^{41}K to the cathode. An increase in rate of 1/15.2 of 0.6 percent will cause ^{39}K to be flooded out of the cathode compartment. The system will operate at moderate efficiency, however, if fluctuations in the stream flow do not exceed more than 1 percent of the balance velocity.

(c) Pore Size and Convection

The pore size is of importance, first, because it determines the length of the theoretical unit, and second, because it limits disturbances due to convection. The first is discussed in detail in RP1766 [10].

The effective pore size was determined by measuring the flow of water through vertical tubes packed with glass beads of various mesh sizes. The rates were determined over a range of pressure heads. The corrected results (cm/sec) gave the empirical relation

$$Q_s = 0.28 d^2 h / l\eta, \tag{12}$$

where Q_s is the flow in milliliters per second divided by the total cross section in square centimeters; d is the bead diameter in centimeters, h is the pressure head in centimeters of water, l is the length of packing, η is the viscosity in poises.

As the free space in the beads is 38 percent, the average lattice is more cubic than tetrahedral. In consequence, the number of beads per square centimeter of cross section is close to $(l/d)^2$. This is also the number of pores in 1 cm^2 of cross section. The volume rate of flow (ml/sec) through the average individual pore is

$$Q_p = 0.28 d^4 h / l\eta. \tag{12a}$$

If the bead packing is replaced by a bundle of straight capillary tubes equal in number to the number of pores and of the same length and operated under the same head, the two structures are

hydraulic equivalents when the radius of each capillary is such that the flow is the same as the average pore.

The flow (ml/sec) through a capillary tube is determined in accordance with Poiseuille's law

$$Q=980\pi r^4 H/8l\eta.$$

On equating the rate of flow it is found that, for 38 percent voids,

$$r=0.165d,$$

where r is the equivalent radius of the straight capillary. This radius, however, is smaller than the mean radius of the pore since the path is longer in the packing by a factor of about $\sqrt{2}$. The mean pore radius normal to the tube axis is in reality close to $38/29\times0.165=0.216d$.

Convection within the packing cannot be evaluated accurately, but can be approximated by considering the flow upward through the heated and downward through the cooled region to be comparable to that through hot and cold capillaries connected to a common reservoir at the top and bottom. The velocity flow through an individual capillary is given by Poiseuille's law to be $v_a=Pr^2/8\eta l$, where v_a is the average velocity in centimeters per second, P is the pressure in dynes per square centimeter, r is the radius in centimeters, η is the viscosity in poises, l is the length of capillary in centimeters.

The flow due to convection when the hot and cold capillaries are at 50° and 30° C, respectively, is

Diameter (mm)	v_a (cm/sec)
0. 02	1.5×10^{-4}
. 04	6.2×10^{-4}
. 08	2.5×10^{-3}

These values show that convection velocities are of the same order of magnitude as the ion mobility. Remixing due to convection is dependent on the direction of the convection stream with respect to the electrolyte stream. In the conventional horizontal tube, where the stream flow is in the axial direction, the convection flow in the radial direction will not be as disastrous as in vertical tubes, where both convection and ion migration are in the axial direction.

(d) Nonuniformity of Porosity

Nonuniformity of porosity and channeling are the principle sources of poor efficiency in operation. Their effect on the ion-stream balance follows from the fact that ion velocity is independent of the pore radius, whereas stream velocity varies with the square of the radius. In consequence, an excessively large pore need represent but a small fraction of the total cross-sectional area to throw the system out of point balance by more than 1 percent.

(e) Temperature Variation in Viscosity-Conductance ratio

An exact balance between ion transport and stream velocity at all points in the packing can be realized only if the effect of temperature on each is the same, i. e., the product of specific conductance, Λ, times viscosity, η, for KCl (1:60) must be constant. The values for several temperatures are

T	Λ	η	$\Lambda\times\eta$
°C			
0	0. 03345	0. 01713	0. 000574
25	. 05800	. 00890	. 000522
45	. 0810	. 00618	. 000500

A 5-percent difference is observed for a 20 degree difference in temperature. As the limits of tolerance are the same here as for difference in pore size, the effect of a temperature gradient across the tube on the value of h cannot be neglected.

(f) Potential Distribution Across Packing

Nonuniformity of potential across the packing is identical in its effect to nonuniformity in pore size. Probe measurements made on various cell designs showed that voltage deviations as large as 5 percent often existed between the top and bottom of horizontal packings. These irregularities can be eliminated by proper design of electrodes and by having the packing set back about the distance of one radius from the cathode compartment.

6. Cell Design

It is now possible to specify the prerequisites for successful cell operation. Maximum separation will be attained when the electrolyte stream velocity balances the average K-ion velocity. To approach this condition the following requirements must be satisfied: (1) The packing must be fine, 100 mesh or finer, if a height theoretical unit of 0.01 cm is to be realized. (2) The porosity of the packing must be uniform. As the difference in mobility of ^{39}K and ^{41}K is estimated at only 0.6 percent, the ideal limits of variation should be within this quantity. (3) Temperature distribution across the packing should be uniform. Variations in excess of a few degrees will seriously impair the efficiency since a temperature gradient not only gives rise to convective disturbances but disrupts the balance between ion and stream flow. (4) The potential distribution across the packing must be uniform to within a fraction of 1 percent.

On the basis of the above considerations, the highest efficiency should be expected in capillary tubes. A sheet capillary between closely spaced parallel plates placed horizontally should be as efficient, provided the spacing is accurate and the potential distribution and temperature uniform. Columns packed with uniformly grained material constructed so that the cooling is primarily at the ends should also possess a low value for h.

Part of the material presented in this report has been taken from a report by S. L. Madorsky, A. Keith Brewer, and Gregory Breit on file at the Bureau. The authors also express their appreciation for the cooperation of J. W. Westhaver throughout the course of this work. Above all, the authors express their thanks to Lyman J. Briggs for his continued interest and practical suggestions, which have been an inspiration throughout the progress of this research.

II. Experimental Development of Method for Concentration of ^{39}K

By Samuel L. Madorsky and A. Keith Brewer

1. Introduction

The successful operation of an electromigration cell depends primarily on (1) suitable cell design and packing, (2) suitable electrolyte, and (3) proper means for maintaining a balance between the ion transport and the electrolyte stream flow. Section I develops the general theory of electromigration, and this section describes a series of initial experiments designed to study the principal conditions for concentration of ^{39}K in an electromigration cell.

2. Cell Design and Construction

Two of the original designs of the electromigration cell are shown in figures 1 and 2. In figure 1 the packing consisted of well-rounded Ottawa sand of about 100 mesh. In order to pack the sand properly, the cell was placed in a vertical position, the cathode end plugged, and the sand introduced through the anode end with frequent tapping. In the apparatus shown in figure 2 the packing in one experiment consisted of Pyrex glass wool, as shown by the shading slanting from left to right and, in two other experiments, of

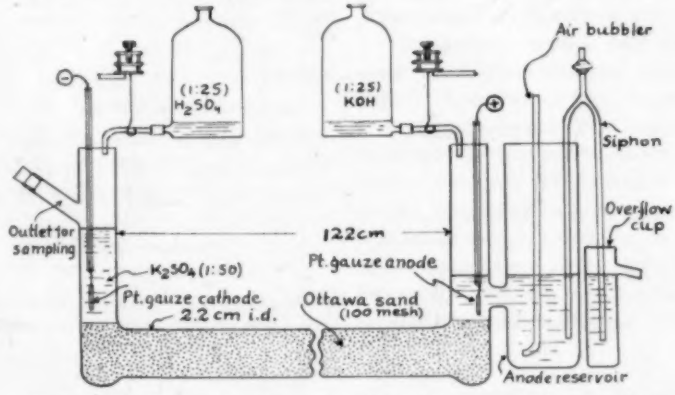

FIGURE 1.—*Electromigration cell packed with 100-mesh Ottawa sand.*

fritted Pyrex glass powder, as shown by the shading slanting from right to left. The glass wool was Corning standard No. 008 grade having a fiber diameter of 0.0002 to 0.0003 inch. It was cut into lengths of 1 to 2 cm and rammed into the cell through an opening at *A*, after which the opening was sealed. In preparing the fritted packing

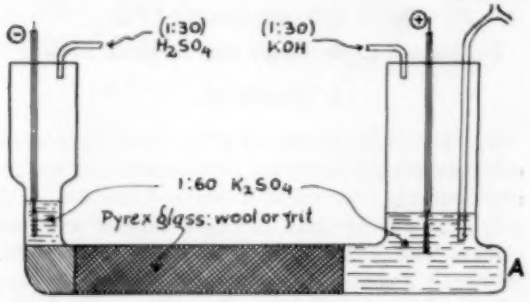

FIGURE 2.—*Electromigration cell packed with Pyrex glass wool (shading slanting from left to right) or fritted glass (shading slanting from right to left).*

a straight tube was plugged with asbestos at the lower end and filled with glass powder 100 to 140 mesh. The tube was then packed in sand in a vertical position, heated in an electric furnace to 715° C and kept at this temperature for 1 hour. The anode and cathode compartments were then sealed on to the packed tube.

The general arrangement of the electromigration cells is shown in figure 1. The restituent liquids [3] were added to the electrode compartments by means of droppers. These droppers were made from thick-walled capillary tubes bent at a right angle. The ends were ground flat to insure uniformity in the drop size. The drop rates were controlled by means of Hoffman screw clamps. Methyl red was used as indicator and the rates were such that the liquid in the electrode compartments changed color between drops. The anode was provided with a siphon and overflow cup. The electrodes consisted of platinum gauze 2 by 2 cm attached to platinum wires enclosed in glass tubes. In one experiment, when high voltage was used, a 2,000-v motor generator was employed. In the other experiments the source of current was a 220-v d-c line. The cell was kept in a bath to prevent sudden changes of temperature.

[3] "Restituent liquid" is a liquid that helps to restore the original chemical composition of the electrolyte in the cell.

3. Electrolytes and Restituent Solutions

Potassium sulfate was the electrolyte used in all the experiments. The electrode reactions involved are $2K^+ + H_2SO_4 = K_2SO_4 + H_2$ at the cathode, and $SO_4^{--} + 2KOH = K_2SO_4 + H_2O + \frac{1}{2}O_2$ at the anode. Thus the anode receives a continuous fresh supply of K^+, and the initial ratio $^{39}K/^{41}K$ is kept constant in the anode compartment. In order to maintain the concentration of the electrolyte in the cell at its original value, the concentration of the restituent solutions, KOH and H_2SO_4, must be adjusted to the transport numbers of the respective cation and anion of the electrolyte. For the sake of simplicity, it is convenient to designate the electrolyte itself, as well as the restituent solutions, on the basis of equivalent ratios solute: Water, rather than on the basis of normality. In the experiments described in this paper, concentration ratios $1/2K_2SO_4 : H_2O = 1:50$ and $1:60$ were used. The transport numbers of K^+ and $1/2SO_4^{--}$ at the above concentrations are about equal, and the H_2SO_4 and KOH solutions were made up each in the equivalent ratios 1:25 and 1:30 for the 1:50 and 1:60 K_2SO_4 experiments, respectively.

Concentrations, densities, and normalities of all the solutions employed in this work are given in table 1.

TABLE 1.—*Solutions employed in the electromigration experiments*

Solute	Ratio solute: H_2O	Concentration	Density [a] at 25° C	Normality
		Percent		
$1/2K_2SO_4$	1:50	8.82	1.070	1.083
$1/2K_2SO_4$	1:60	7.46	1.059	0.906
$1/2H_2SO_4$	1:25	9.82	1.063	2.128
$1/2H_2SO_4$	1:30	8.32	1.053	1.785
KOH	1:25	11.07	1.102	2.176
KOH	1:30	9.40	1.086	1.821

[a] Values for KOH are at 15° C.

The amount of restituents added, in grams per ampere hour (0.0373 equivalent) in the case, for example, of $1:60 K_2SO_4$ were as follows:

To cathode		To anode	
$1/2H_2SO_4$	1.830	KOH	2.092
$30H_2O$	20.164	$30H_2O$	20.164
Total	21.994	Total	22.256

4. Calculation of Separation Coefficient

The results obtained in the experiments on concentrating ^{39}K can be interpreted in terms of the separation coefficient ϵ by using eq 10, section I. Rearranging and substituting numerical values, eq 10 can be written

$$\epsilon - 1 = 0.02882 \frac{V_c C}{I^+ t_1} \times \frac{R_n - 14.20}{R_{t_1} + 1},$$

where t_1 is time in hours, and I^+ is positive current.

The cathode volume, V_c, is the free liquid in the cathode compartment down to the packing where it recedes into the horizontal tube, as in the case when fritted glass is used. However, where the packing extends into the cathode compartment, for example, when sand or glass wool is used, the cathode volume is the free liquid above the packing plus the liquid in the packing directly below the cathode cup, as the latter liquid is in thermal exchange with the free liquid due to the heat developed in the packing. Details of cells and experimental conditions are given in table 2.

TABLE 2.—*Experimental conditions*

Experiment No.	Packing [a]		Current		Ratio: 1/2 K_2SO_4: H_2O	Cathode volume	Bath temperature
	Type and mesh	Length					
		cm	v	amp		ml	°C
3	Ottawa sand, 100	122	800	0.5	1:50	30	25 to 30
7	do	10.3	78	.7	1:60	16	25 to 30
9	Pyrex wool	15.5	46	1.0	1:60	6.5	25 to 30
10	Pyrex frit, 100 to 140	12.0	96	0.7	1:60	6.5	4
13	do	6.0	54	.7	1:60	6.5	4

[a] The diameter of the packing was 2.2 cm in all the experiments.

5. Experiments

(a) Preliminary Experiments

Some preliminary experiments were carried out with normal K_2SO_4 as the electrolyte and 2 N H_2SO_4 and KOH as the restituents. In one experiment the packing was 2.1 cm in diameter, 27 cm long, and consisted of 60-mesh Ottawa sand. The cell was operated for 8 hours during the daytime with a current of 0.3 amp. At the end of this period, an approximately 1 ml sample was drawn from the cathode compartment for analysis and the operation discontinued overnight. This was repeated without renewing the electrolyte for a number of days. Analysis showed a value for R varying between 14.8 and 15. On continued operation, the concentration of ^{39}K in the cathode remained at this value. This must have been caused by too much sampling and too long intervals intervening between operating periods, which permitted the accumulated ^{39}K to diffuse from the cathode compartment into the packing.

A U-shaped tube of the same cross section and with the same kind and length of packing, and operated under similar conditions as the straight packed cell for four 8-hour periods, gave similar results.

A cell 30 cm long packed with parallel lengths of capillaries having bores 0.75 to 1 mm was operated with 1-amp current. The result was negative. A similar cell was packed with tubes of 2-mm inside diameter and 3-mm outside diameter, and the bores as well as the spaces between the tubes were filled with 60-mesh Ottawa sand. It was operated at 0.2 amp, the first day for 12 hours and the second day for 14 hours. The isotope ratios were 14.60 and 14.80, respectively, for the 2 days of operation. This experiment points to the necessity of having a packing in which the pores are small and uniform.

A cell of the same length and cross section was packed loosely with acid-washed asbestos wool and operated at 0.4 amp for 12 hours the first day and for 14 hours the next day. Analysis showed ratios of 14.70 and 14.85, respectively, for the two days.

(b) Ottawa-Sand-Packed Cells

Experiments 3 and 7 were carried out in a cell shown in figure 1. The packing was 122 cm long in experiment 3, and 10.3 cm in experiment 7. The bath temperature in both experiments was maintained at 25° to 30° C. In experiment 3 the operation during the first 272 hours was interrupted every night for periods ranging from 8 to 12 hours. The rest of the operation was

continuous. The time counted was that of actual operation. Experiment 7 and the experiments described below were continuous throughout. Small samples for mass spectrometer analysis were drawn from the cathode compartments at about 50-hour intervals.

In order to check on the constancy of operation the cathode samples in experiment 3, before they were used for mass spectrometric analysis, they were analyzed for K_2SO_4 content. This was done by weighing the sample, evaporating it to dryness, and weighing the K_2SO_4 residue. The results of these analyses are shown in table 3. As seen from this table, the K_2SO_4 content in the cathode compartment varied little during 295 hours of operation.

Anode samples were analyzed similarly for K_2SO_4 in both experiments. The analyses, as seen from table 4, show little change in concentration of the electrolyte.

TABLE 3.—*Cathode analysis in experiment 3*

Time	K_2SO_4
Hours	*Percent*
0	8.82
52	8.61
102	8.65
152	8.61
244	8.33
295	8.83

TABLE 4.—*Anode analysis*

Experiment 3		Experiment 7	
Period of operation	K_2SO_4	Period of operation	K_2SO_4
Hours	*Percent*	*Hours*	*Percent*
0	8.82	0	7.46
107	8.79	19	7.84
176	8.70	42	7.51
		218	7.20
Experiment 10		Experiment 13	
0	7.46	0	7.46
45	7.98	45.5	7.76
91	7.74	92.5	7.97
139	7.73	144.5	7.70
211	7.78	188.5	7.70
260	7.89	212.5	7.65
309	8.18	254.5	7.66
354	7.70	309.5	7.73

The mass spectrometer analyses of cathode samples are shown in column 3 of table 5. In column 4, values of the separation factor, S, which is equal to R_T/R_0, are shown. Column 5 shows values of $\epsilon-1$ calculated by means of the equation shown above.

TABLE 5.—*Concentration of* ^{39}K *and separation coefficient*

Experiment No.	Time, T_1	Ratio. $^{39}K/^{41}K$, R_T	Separation factor, S	$(\epsilon-1)\times10^3$
	Hours			
3	52	14.70	1.035	0.229
	102	15.20	1.070	.227
	152	15.70	1.105	.221
	202	16.20	1.141	.215
	244	16.65	1.172	.213
	295	17.00	1.197	.197
	335	17.40	1.225	.194
7	50	14.95	1.052	.112
	150	16.50	1.162	.105
	250	16.70	1.176	.067
	300	17.00	1.197	.062
	350	17.35	1.222	.059
	408	17.75	1.250	.055
9	12.5	14.60	1.028	.070
	31.5	15.00	1.056	.054
	100.5	15.60	1.098	.028
	194.0	17.90	1.260	.034
10	94	14.60	1.028	.013
	152	14.90	1.049	.014
	203	17.50	1.232	.041
	259	20.50	1.443	.055
	360	17.20	1.211	.022
13	191	17.30	1.218	.043
	354	17.75	1.250	.026

(c) Glass-Wool-Packed Cell

Experiment 9 was carried out in a glass-wool-packed cell, as illustrated in figure 2. Details of design and operation are shown in table 2. No analyses were made of K_2SO_4 content in the cathode or anode liquids during operation. Cathode samples were analyzed for ^{39}K concentration, and the results are shown in table 5. The $\epsilon-1$ values are rather low, most likely because of channelling and nonuniformity of porosity in the packing.

(d) Fritted-Glass-Packed Cells

Originally four cells were started: Two cells, each having a 12-cm-long packing, were operated, one at 25° C (expt. 11) and the other at 50° (expt. 12); two other cells, having packings 12 cm long (expt. 10) and 6 cm long (expt. 13) were operated at 4° C. The first two cells showed signs of rapid deterioration of the fritted packing

at the cathode end soon after the operation was started, and the experiments were discontinued. The other two cells, operated at a lower temperature, stood up well, and the operation was continued for a number of days. Details of cells used in experiments 10 and 13 are shown in table 2.

Anode samples were checked for K_2SO_4 content, and the results are shown in table 4. These results indicate little change in the concentration of the electrolyte throughout the operation. Cathode samples were analyzed for concentration of ^{39}K, and the results are shown in table 5.

Figure 3 shows abundance ratio plotted against time for all five experiments.

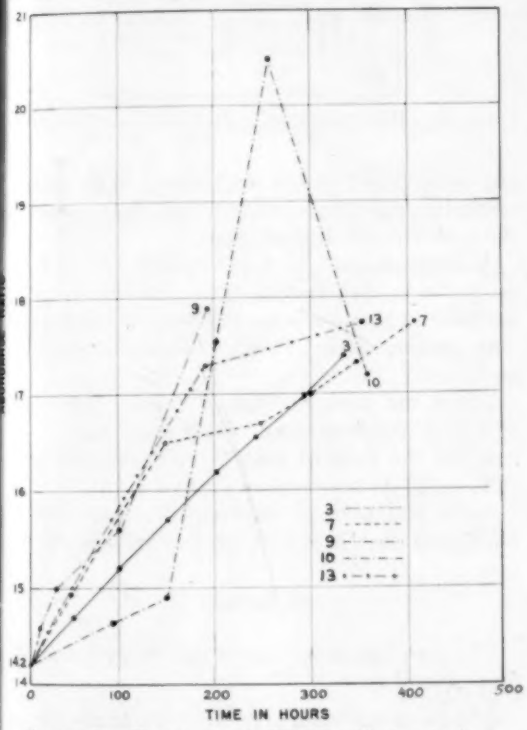

FIGURE 3.—*Change of ratio $^{39}K/^{41}K$ with time in five experiments.*

(e) Distribution of ^{39}K in Packing

Diffusion of ^{39}K from the cathode compartment into the packing and disturbances incidental to the operation, such as may be caused by irregularities in metering the restituents, would tend to lower the separation coefficient. Aside from this, the value of the cathode volume, V_c, cannot be measured accurately as it is not known how far it extends into the packing. In experiment 3, in which a very long packing was used, any losses of ^{39}K concentrate from the cathode volume into the packing could be recovered at the end of the operation.

When experiment 3 was discontinued after 335 hours of operation, 20 ml of liquid was first drawn from the cathode compartment, then the liquid was allowed to seep into this compartment, and successive samples of 25 ml each were drawn. The position of each sample in the packing near the cathode end before it was drawn is shown in figure 4. It should not be assumed that figure 4 gives a true picture of the distribution of ^{39}K concentrate in the packing, because of mixing of successive samples with some of the liquid left in the cathode compartment, as well as in the packing from the previous samples. However, it shows that the concentrate was mostly confined to the cathode end of the packing, and that all the ^{39}K concentrate was removed with the first four samples.

By adding the samples drawn at the end of the operation, as well as the samples drawn during the operation, we get a total of all the ^{39}K concentrate obtained in 335 hours of operation in experiment 3. Table 6 gives the volume and R_t values for all samples. All the samples add up to a total cathode volume of 96.65 ml of an average $R_{t_1}=15.53$. On the basis of 0.5-amp, total current, or 0.25-amp, positive current used in this experiment,

$$\epsilon-1=\frac{0.0288\times96.65\times1.083\times1.33}{0.25\times335\times16.53}=0.00290.$$

TABLE 6.—*Distribution of ^{39}K in the packing in experiment 3*

Period of operation	Volume of cathode sample	R_T
Hours	*ml*	
52	0.326	14.70
102	.222	15.20
152	.345	15.70
202	.243	16.20
244	.231	16.65
295	.283	17.00
335	20	17.40
335	25	16.30
335	25	14.73
335	25	14.35
Total and average	96.65	15.53

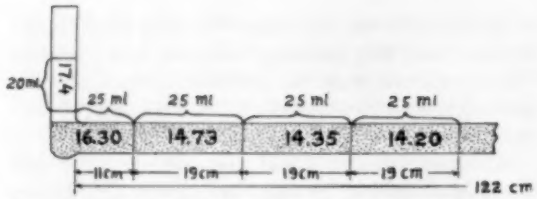

FIGURE 4.—*Distribution of* ^{39}K *concentrate in the packing.*

6. Conclusions

The data presented show the feasibility of concentrating ^{39}K by the electromigration method. Packings made of fine sand proved to be superior to those made of fritted glass, glass wool, asbestos, or glass capillary tubes. Concentration of the electrolyte in the electrode compartments remained practically constant through the entire operation of the cells. Experiment 3, which was carried out in a long tube packed with sand, gave the highest and longest sustained values of $\epsilon-1$. This is explained on the ground that the long packing held any losses of ^{39}K from the cathode compartment caused by irregularities in operation, such as those caused by variation in rates of addition of restituents, by loosening of the packing or by diffusion. The value of $\epsilon-1=0.0029$, obtained by taking into consideration the ^{39}K concentrate in the packing, at the end of experiment 3, should be taken as the best value for the experiments described.

III. Detailed Investigation of Method

By A. Keith Brewer, Samuel L. Madorsky, John Keenan Taylor, and Vernon H. Dibeler

1. Introduction

In view of the success attained in concentrating ^{39}K described in section II, a detailed investigation was initiated to test the various contributing factors described in section I. The results of some 170 experiments run under controlled operating conditions are summarized in this section.

2. Experimental Details

(a) General Assembly

A complete layout for a typical experimental setup is shown in figure 5. The cell illustrated is

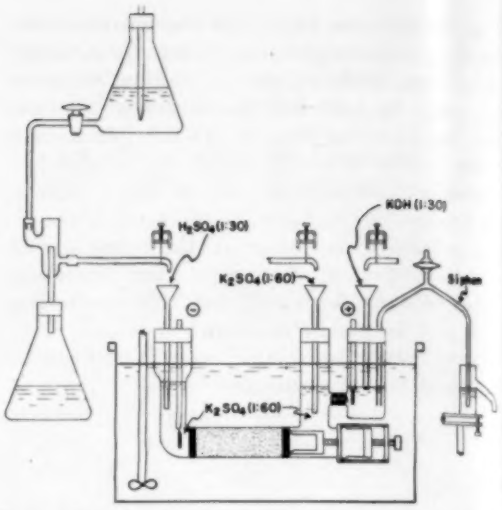

FIGURE 5.—*Experimental setup for the concentration of* ^{39}K.

one using K_2SO_4 as the electrolyte. The cathode control is manually operated; the anode control is the constant pH flushed type.

A large number of modifications of the basic design have been tested. The cells illustrated in figures 5 to 10 are representative of the most common designs used. These cells can be classified as follows:

1. On the basis of type of control—pH (figs. 5, 6, 7, 9) and boundary (figs. 8 and 10, B).
2. On the basis of packing—packed (figs. 5, 6, 7, 8, 9, 10, A) and unpacked (figs. 10, B).
3. On the basis of direction of stream flow—horizontal (figs. 5, 6, 7, 8, 10) and vertical (fig. 9).

(b) Packings

The packings investigated can be grouped into four general types:

1. Granular: Sand, glass ballotini beads, silicon carbide.
2. Fibrous: Glass wool, asbestos, absorbent cotton, etc.
3. Rigid: Glass frits, Alundum, etc.
4. Close clearance: Concentric tubes.

The dimensions of the packings studied were varied over a wide range. A convenient size of cell used in testing the various pertinent variables was made with packings 14 mm in diameter and 8 cm long.

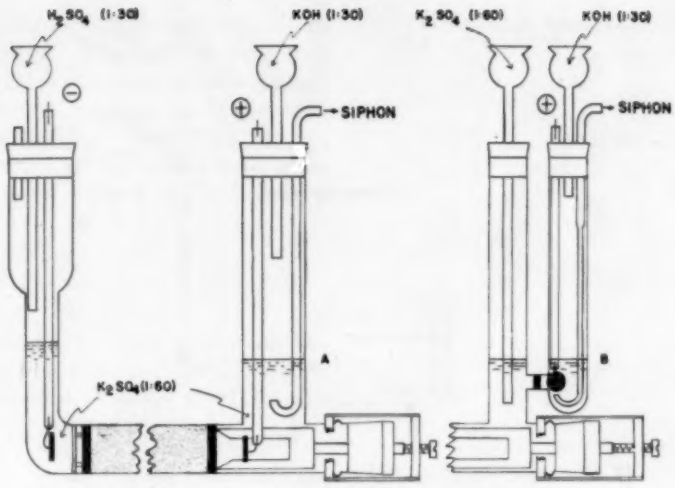

FIGURE 6.—*Cell used in* K_2SO_4 *experiments.*

A. Anode neutralized with KOH; *B*, anode neutralized with KOH and flushed with K_2SO_4 (1:60).

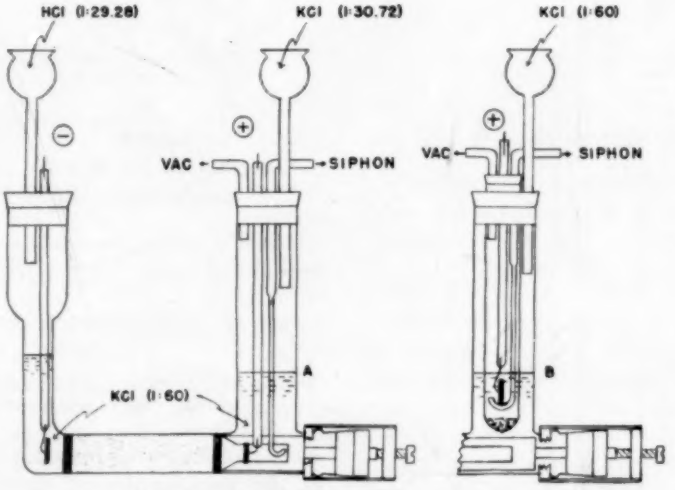

FIGURE 7.—*Cell used in* KCl *experiments.*

A, Single-cup anode flushed with KCl (1:30.72); *B*, double-cup anode flushed with KCl (1:60).

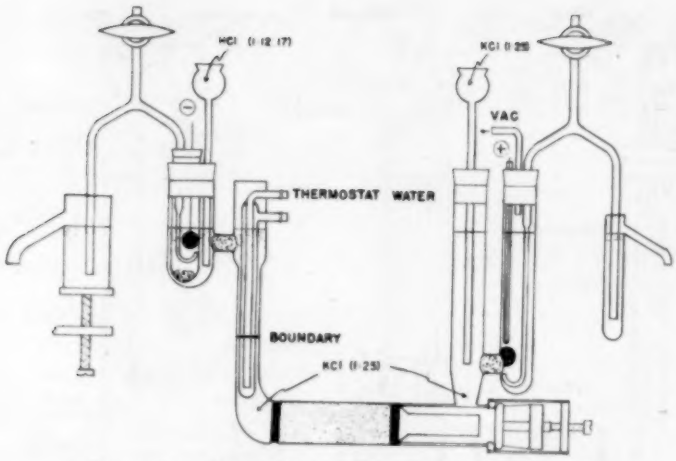

FIGURE 8.—*Cell used in boundary experiments with* KCl.

Anode is of the double-cup, flushed type.

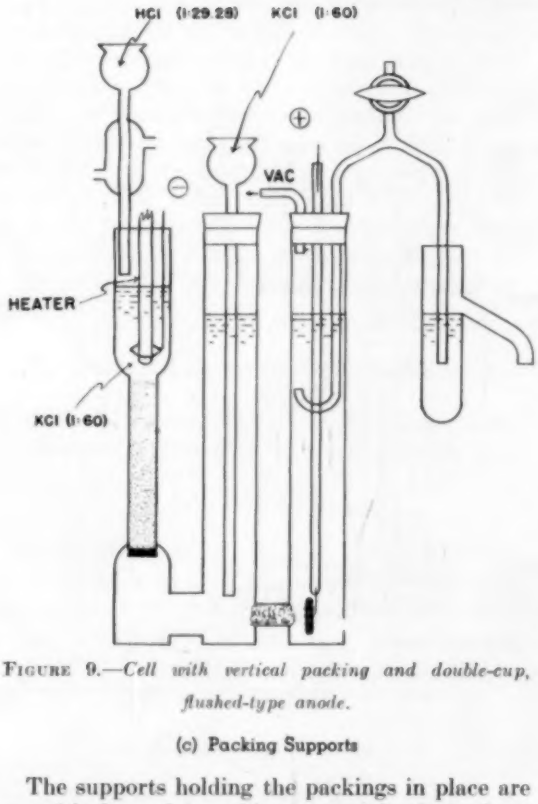

FIGURE 9.—*Cell with vertical packing and double-cup, flushed-type anode.*

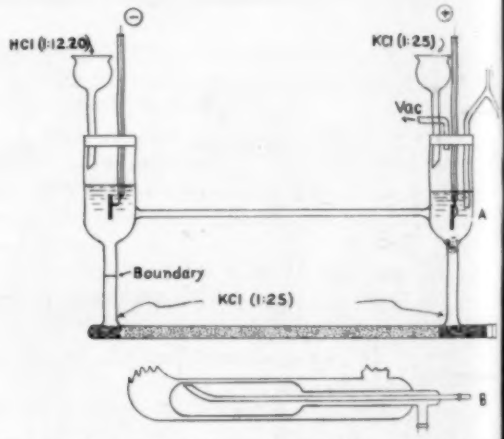

FIGURE 10.—*Cells designed to facilitate the dissipation of heat.*

A, Cell with small diameter of packing used in boundary experiments; B, cell with circular capillary space in place of packing.

(c) Packing Supports

The supports holding the packings in place are as critical as the packing materials themselves. The problem has been one of finding a thin, porous, rigid material to which sufficient pressure can be applied to prevent loosening or channeling of the packing during operation. Another requirement is that it should not distort the potential distribution across the face of the packing or cause an uneven electrolyte stream flow through the packing. Various supporting materials were tested, including sealed-in frits, Alundum plates, finely perforated Bakelite, and thin frits made from No. 47 ballotini beads; the latter proved to be the most satisfactory.

The ballotini frits were cast in graphite molds

and heated to a point to insure rigidity without impairing the porosity. The best cathode frits were about 2.5 mm thick and were tapered slightly at the edge to fit tightly into the cell as shown in figure 8. The anode frits were about 5 mm thick and were calked at the edges with glass thread or glass cloth to prevent the fine packing from leaking out.

(d) The Electrodes

Platinum-gauze electrodes were used in all the experiments. Care was taken to place the electrodes in such a position that the potential distribution across the packing was uniform at all points.

(e) Source of Potential

A 100-volt storage battery was used. The battery was kept charged by floating on a d-c generator line, the generator current being slightly in excess of that drawn from the battery.

3. Electrolytes and Controls

(a) Electrolytes

Experiments were carried out with potassium chloride and potassium sulfate. The choice of electrolyte was based on the type of control mechanism used to maintain the counterflow. The concentrations were varied over a wide range; a 1:60 ratio was adopted as most convenient for general use.

The restituent solutions, i. e., the solutions that were added to the cathode and anode compartments in order to maintain the original composition of the electrolytes, were in the case of 1:60 K_2SO_4, 1:30 H_2SO_4, and 1:30 KOH for the cathode and anode, respectively. For KCl, more accurate values of the K^+ were used in the calculations, and the cathode restitutent for 1:60 electrolyte ratio was 1:29.28 HCl. The anode restitutent was either 1:30.72 KCl or 1:60 KCl, depending on the type of control used, as will be explained later. The concentrations, densities, and normalities of the varioussolutions are shown in table 7.

TABLE 7.—*Solutions employed in electromigration experiments*

Solute	Ratio Solute:H_2O	Concentration	Density [a] at 25° C	Normality
		Percent		
KCl	1:25	14.20	1.090	2.077
KCl	1:30.72	11.87	1.075	1.711
KCl	1:60	6.45	1.038	0.898
KCl	1:12.20	14.23	1.067	4.162
KCl	1:29.28	6.47	1.029	1.823
$1/2K_2SO_4$	1:60	7.46	1.059	0.906
$1/2K_2SO_4$	1:30	8.32	1.053	1.785
KOH	1:30	9.40	1.086	1.821

[a] Values for KOH are given at 15° C.

The amounts of restituents added per ampere hour when the electrolyte is 1:60 K_2SO_4 are shown in section II. For 1:60 KCl, the amounts of restituents added were as follows:

To cathode		To anode	
	g		*g*
HCl	1.362	KOH	2.781
$29.28H_2O$	19.680	$30.72H_2O$	20.648
Total	21.042	Total	23.429

(b) Control of Cathode

The pH and the boundary controls used have been devised for both manual and automatic operation. The automatic-control system is described in section VII.

The pH controlled cells were equipped with droppers designed to supply acid to the cathode compartment at a constant rate. The droppers were attached to constant level spillways and were supported near the tips by adjustable screw clamps. Methyl orange and methyl red were used as the indicators to determine the dropping rate. The rate of dropping was adjusted to the point where the cathode solution turned from red to yellow between drops.

A boundary between HCl and KCl was also used as the index of reflux balance. An analysis of the boundary mechanism indicates that a stable boundary should exist when the concentrations C_1 of the HCl solution and C_2 of the KCl solution are in the ratio of their cation transport numbers, i. e., $C_1/C_2 = T_{H^+}/T_{K^+}$.

727972—47——2

In the absence of a counterflow, the passage of 1 Faraday of current causes the boundary to move through a volume $V=T_{K^+}/C_2$. To maintain the boundary stationary a volume, V, of solution must be added to the cathode compartment. This volume must contain 1 equivalent of HCl to neutralize the electrode reaction.

The construction of the boundary cells is shown in figure 8. The internal cooler is desirable as large boundaries are inclined to become diffuse in the center. The height of the column of electrolyte controlling reflux rate is adjusted by a screw under the spillway. The rate of acid addition is not critical in the arrangement illustrated, provided it is sufficient to maintain a constant pH in the acid above the boundary.

(c) Control of Anode

Several types of anode controls have been tested. These are shown in the cells illustrated. In figure 6A, KOH is added to the anode at the stoichiometric rate. A precise regulation is necessary for the dropping rate. Cell 2B is designed to eliminate the need for drop control by employing a flushed-type anode. The electrolyte of the original concentration is added to the anode compartment at a rate sufficient to keep the pH at its initial value. KOH can be added at the anode cup if desired, to lessen the quantity of electrolyte required for flushing. This addition of KOH, when the electrolyte is KCl, is not necessary as chlorine is liberated at the anode.

4. Correlation of Experimental Data

The separation efficiency was determined in terms of the abundance ratio $^{39}K/^{41}K$ in the cathode compartment, as measured by the mass spectrometer. The experiments described in this report were all conducted under conditions where the abundance ratio in the anode compartment was maintained at the value for normal potassium, i. e., $^{39}K/^{41}K=14.20$.

In order to place individual experiments on a comparable basis, it is necessary to consider the current, the cathode volume, and the concentration of the electrolyte. The method chosen was to compare the amounts in milliequivalents of the light isotope ^{39}K transported into the cathode compartment per ampere. This value is designated by q/i, and is calculated from the expression

$$q/i=\frac{V_c C \Delta N}{i},$$

in which

q=milliequivalents of ^{39}K transport into the cathode compartment
i=current in amperes
V_c=volume of cathode liquid in milliliters
C=normality

ΔN is obtained from the abundance ratio as follows:

$$\Delta N=\frac{R_t}{R_t+1}-\frac{R_0}{R_0+1}=\frac{R_t}{R_t+1}-\frac{14.2}{15.2}=\frac{R_t}{R_t+1}-0.9342$$

Here $R_t=^{39}K/^{41}K$ in the cathode compartment at time, t, and R_0=normal ratio 14.20.

The initial slope, q/it_1, obtained by plotting q/i against the time of sampling is related to the separation coefficient ϵ by the equation

$$\epsilon-1=0.876\times q/it_1,$$

where t_1 is time in hours.

5. Results

(a) General Operation

The $^{39}K/^{41}K$ ratio in the cathode compartment as a function of time of operation for six separate experiments is given in figures 11 and 13. These experiments were chosen from the types most regularly used in this research in order to illustrate normal cell operation as well as the effect of various disturbing factors. The separation efficiency (q/i vs t_1) for these same experiments is given in figures 12 and 14.

The pertinent data for the above experiments are given in table 8. The data for two boundary controlled experiments, 134 and 157, are included in table 8 and figures 13 and 14 for comparison.

Experiment 170 was run in a cell of the type illustrated in figure 7, using flushed anode 3B. The cathode was controlled by manual regulation of the drop rate; the indicator was methyl red. This type of cell was the easiest to keep regulated and, in general, represents the most satisfactory arrangement studied. It will be noted that the concentration of ^{39}K in the cathode compartment increases nearly linearly with time. The small deviation observed at the 113 hour is due to the cell becoming out of balance for a short period of time. The slight tapering off in rate is to be

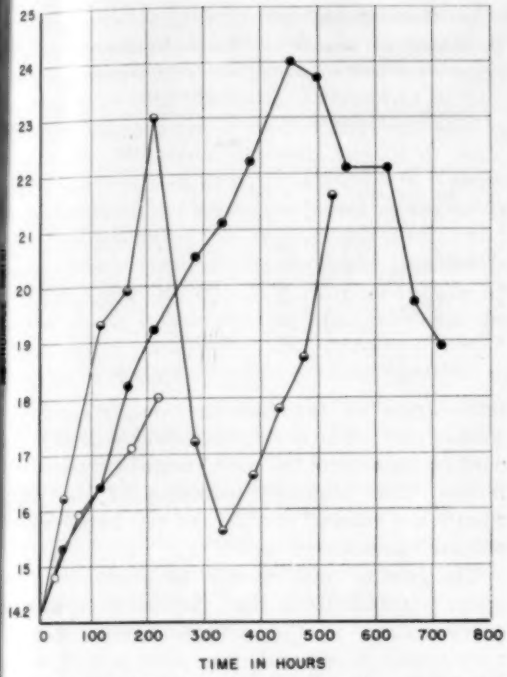

FIGURE 11.—*Ratio of* $^{39}K/^{41}K$ *in the cathode compartment, plotted against time, for three representative experiments.*
◒ 149 vertical; ● 170 horizontal; ○ 186 automatic.

expected as the concentration of light isotope in the packing is not taken into consideration in the efficiency curve.

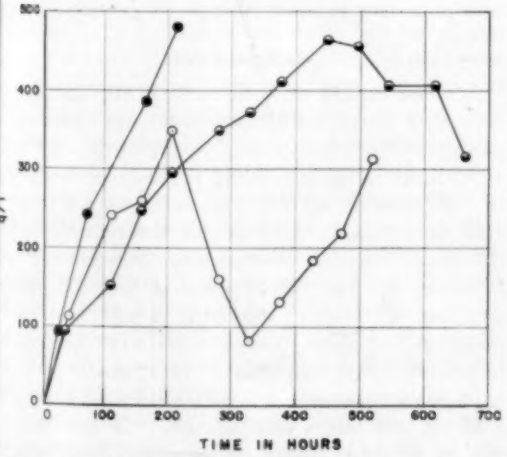

FIGURE 12.—*Milliequivalents of* ^{39}K *transported into the cathode compartment per ampere, plotted against time, for three representative experiments.*
○ 149 vertical; ◒ 170 horizontal; ● 186 automatic

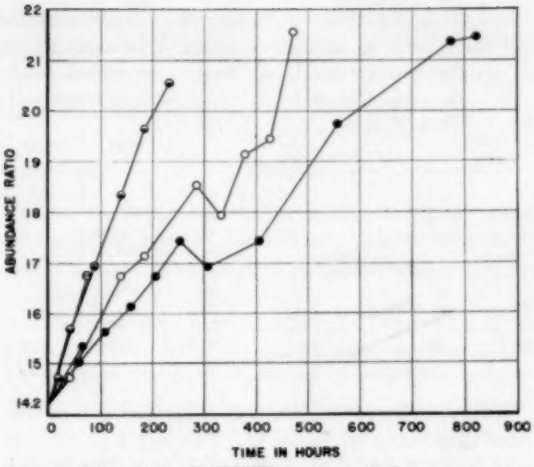

FIGURE 13.—*Ratio of* $^{39}K/^{41}K$ *in the cathode compartment, plotted against time, for five representative experiments.*
⊖ 134 boundary; ⊙ 157 boundary; ○ 158 indicator; ◒ 182 indicator; ● 184 automatic.

Experiment 186 was run under complete automatic control. The anode was the flushed type shown in figure 6, B. The cathode was provided with an automatic acid injector controlled by H_2 versus $PbSO_4$ electrodes in the electrolyte. The automatic arrangement is described in section VII.

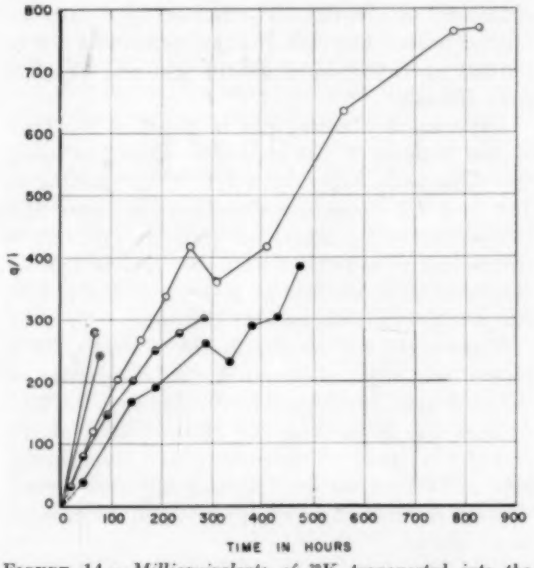

FIGURE 14.—*Milliequivalents of* ^{39}K *transported into the cathode compartment per ampere, plotted against time, for five representative experiments.*
⊙ 134 boundary; ⊖ 157 boundary; ● 158 indicator; ◒ 182 indicator; ○ 184 automatic.

TABLE 8.—*Experimental conditions and separation coefficient*

[H, horizontal. V, vertical. B, boundary. I, indicator. A, automatic. SiC, silicon carbide. S, sand. GB, glass beads.]

Experiment No.	Type of cell	Packing			Cathode volume	Current		Electrolyte		$(\epsilon-1)\times 10^6$
		Mesh	Length	Diameter				Salt	Ratio salt: water	
			cm	*cm*	*ml*	*amp*	*v*			
134	H, B	SiC 150	10	0.4	0.75	0.06	80	KCl	1:25	0.28
149	V, I	S 100	10	1.4	8	.5	87	KCl	1:60	.22
157	H, B	GB 100	7	1.4	15	.5	32	KCl	1:25	.30
158	H, I	GB 100	5	2.5	12	.6	32	KCl	1:60	.06
170	H, I	GB 100	7	1.4	10	.5	93	KCl	1:60	.17
182	H, I	S 60	8	1.4	8	.5	90	KCl	1:60	.13
184	H, A	S 100	8	2.5	20	.5	80	K_2SO_4	1:60	.17
186	H, A	GB 60	10	1.4	16	.4	138	K_2SO_4	1:60	.38

Experiment 149 was run in a vertical cell of the type illustrated in figure 9. The cell was packed with sand held in place by gravity. The barrel of the tube was made from an extra-thin-walled Pyrex tube. The results indicate a rapid concentration at first, disturbed later by an accumulation of gas in the packing. Sometime after 200 hours a bubble of gas formed in the sand and slowly worked its way up and out during the next 100 hours; after this, the sand settled back in place, and the cell resumed its initial rate of operation. This particular cell was equipped with a degassing heater in the cathode compartment, and the gas accumulated after the heater burned out. Replacing the heater, however, did not restore the cell to normal operation until all the gas was expelled from the sand.

Experiment 158 was run in a cell of the type shown in figure 7, the general arrangement being the same as in experiment 170. The packing in 158 had 2.5 times the cross-sectional area and five-sevenths the length of that in 170. It is interesting to note that while the rate in 158 for the first 150 hours, was 75 percent of that in 170, the power input was only 41 percent.

Experiment 184 illustrates the necessity for a precise control of the required rate of addition of the restituent solutions. In this instance the HCl dropper was stopped up for about 1 hour at the end of 260 hours. This resulted in a break in the rate curve between the 250- and 320-hour period. The cell resumed the normal rate when the dropper was repaired.

Experiment 182 shows the results of loosening of the beads near the cathode. The effect began at about the hundredth hour; at the end of 300 hours the channel was of such a size that the entire concentrate in the cathode compartment was washed out. The development of channels in the packing represents the most common cause of cell failure. The slightest loosening of the beads results in a channel of sufficient size to prevent an efficient operation of the cell.

The general conclusion to be drawn from the above experiments is that the change in isotope concentration in the cathode compartment is very nearly linear with time over a wide range. The rate is sensitive to any factor that might disturb the precise point balance between the ion mobility and the countercurrent stream flow. Incorrect rate of addition of the restituent solutions and the accumulation of gas in the packing give rise to effects from which the cells will recover when the disturbance is corrected. Channeling in the packing results in permanent cell failure.

(b) Type of Cell

A large variety of both vertical and horizontal cells were tested for different packings under various operating conditions. Experiments 149 and 170, shown in figures 11 and 12, are representative of each type of cell when operating under reasonably favorable conditions. A comparison of all the data, however, showed some difference in the efficiency for the two types as a function of the packing size. For 100-mesh beads and sand packings the rates of separation were essentially identical; a large number of experiments of each type gave maximum q/i values between 0.35 and 0.40 for 200 hours of operation. In the case of 40- to 80-mesh beads, in contrast, the vertical cells showed very small separation, whereas the q/i value for the horizontal cells was about one-half that for 100-mesh beads.

The general conclusion to be drawn is that the efficiency of the two types of cells is essentially the same under conditions where convection has been reduced to a minimum. The effect of convection, however, is entirely different. In the horizontal cells the convection flow is at right angles to the stream flow. In addition, it is small at the ends of the packing where the surface is uniformly cooled by the cathode and anode solutions. In the vertical cells the convective flow is in the opposite direction to the stream flow, being in the anode to cathode direction through the center of the tube and in the opposite direction along the cooled walls. This necessarily results in a mixing of the solution in the two electrode compartments. In consequence, for successful operation it is essential to use either packings of such fineness that convection becomes negligible, or to adjust conditions so that convection will just counterbalance the excess electrolyte flow in the center of the packing, where the viscosity is lower because of the higher temperature.

(c) Grain Size

The effect of grain size on the separation efficiency of horizontal cells is shown in figure 11.

A number of comparison experiments were run under similar conditions except for the grain size in the packings. Five duplicates were run for each bead size. The type of cell used is illustrated in figure 6, B. The packings were 5 to 10 cm long and 1.4 to 2.4 cm in diameter.

Lines 1, 2, 3, and 4 represent the maximum slope for each set of duplicate runs. In each case a majority of the cells gave values at or near the line as drawn; deviations from the line were due either to imperfect packing or to faulty operation.

It was not found possible to sift beads to exact mesh sizes. Line 1 was taken with commercial 107-mesh beads sifted through a 140-mesh screen. Line 2 was taken with beads that passed a 100-mesh screen but were rejected by a 120-mesh screen. Line 3 was taken with commercial 70-mesh beads sieved between 80 and 100 mesh. Line 4 is for commercial 47-mesh beads sieved between 40 and 80 mesh.

The conslusion to be drawn from the data presented in lines 1, 2, 3, and 4 is that the rate of separation increases with the fineness of the beads, the rate for 140-mesh beads being about twice that for 60-mesh beads. Although the data are inconclusive, these results, combined with those obtained with fine fiber packings, indicate that the final separation to be obtained for various packings increases with the fineness of the pores.

(d) Packing Materials

The various types of packing materials were tested under similar conditions. The results however, are incomplete and to that extent are inconclusive.

Granular packings, in general, were the most satisfactory. Ballotini glass beads were the easiest to pack and were not affected by the electrolyte. Their poor thermal conductivity, however, resulted in a tendency for the cells to boil during operation; this necessitated the use of relatively low current densities. The free space and heating effects have been described in section I. Sand packed almost as well as glass beads; it was superior in that the cells ran slightly cooler. Silicon carbide of the type used in glass grinding did not pack well under pressure. In spite of the fact that it ran appreciably cooler than glass beads, it was more inclined to fill up with gas. In general, spheres are more satisfactory than sharp-edged particles.

Rigid packings were only moderately successful. Glass frits, on the whole, gave high initial rates, but they developed pores or cracks. Alundum plates behaved the same as glass frits, but they were more inclined to plug up with indicator or any suspended material in the acid. Rubber battery separators failed to show sufficient uniformity in porosity for satisfactory use. Filter paper cut in strips and pressed in packs gave rates comparable to the best bead packings. As these packings were difficult to support, their possibilities were not thoroughly investigated. Fiber packings gave high initial values but, in general, deterioration was rather rapid. The values for absorbent cotton shown in line 6 of figure 15 have a comparatively high rate. The length of packing was only 1 cm compared to 8 cm for the beads. The cotton was cut in disks and packed wet, care being taken to keep all the fibers lying in a radial direction. Unfortunately, fully half the tubes so packed proved defective because intimate contact between the cotton and the glass walls could not be obtained at all points. Line 7 is a typical run obtained with glass-wool packings. A number of

glass fibers tested gave about the same results; these included very fine "*A* fibers" of alkali resistant glass, battery-separator fibers, and ordinary glass wool. In each case the fiber packings started off with a high separation rate, only to develop pores at the end of a few hundred hours. Apparently the systems became alkaline for sufficient time throughout the operation to cause the fibers to disintegrate. It is possible that glass fibers can be made to operate on the automatically controlled experiments, in which the pH variation can be reduced to a minimum.

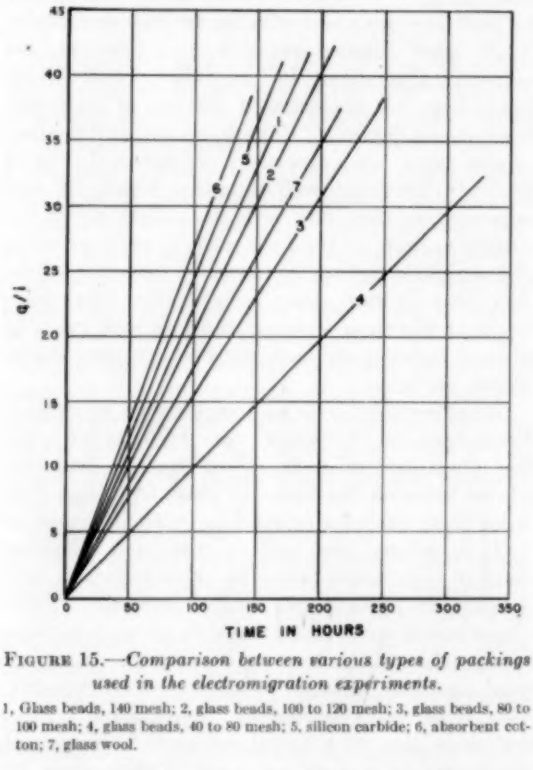

FIGURE 15.—*Comparison between various types of packings used in the electromigration experiments.*

1, Glass beads, 140 mesh; 2, glass beads, 100 to 120 mesh; 3, glass beads, 80 to 100 mesh; 4, glass beads, 40 to 80 mesh; 5, silicon carbide; 6, absorbent cotton; 7, glass wool.

From a consideration of all the packing materials studied it must be concluded that the material itself plays no direct part in the separation process. The choice of packing resolves itself into obtaining uniform porosity combined with mechanical and chemical stability.

(e) Length of Packing

Packing lengths from a few millimeters to 10 cm were investigated. In general, the longer packings gave the higher yields before breaking down. A study of the isotope distribution throughout the packing, however, revealed that high concentrations should be obtainable in very fine packings of 1 cm in length. The use of short packings necessitates a precise control at all times to prevent washing out of the material concentrated in the packing.

(f) Diameter of Packing

The diameter of the packings in horizontal cells was varied from 0.4 to 3.75 cm. The results showed the rate of concentration of ^{39}K to pass through a broad maximum between 1.2 and 2.5 cm. Results of this type are to be expected. For the small-diameter cells the contact between the glass walls and the beads constitutes an appreciable fraction of the free space. As this contact is not as intimate as between the beads themselves, a nonuniformity of porosity results. The loss of efficiency in large cells is doubtless due to the greater opportunity afforded for convective disturbances.

The packing in vertical tubes was investigated from 1 to 7 cm in diameter. The difficulties involved were confined largely to obtaining sufficient uniformity of porosity across the packing and also in arranging the electrodes to provide a uniform potential distribution while at the same time preventing the accumulation of gas on the under surface. When adequate precautions were taken, the large-diameter cells operated at an efficiency comparable with the horizontal tubes.

(g) The Anion

The effect of the chemical nature of the anion (Cl^- or $SO_4^=$ on separation efficiency is shown in tables 7 and 8 and in figures 11, 13, and 15. These data were taken under similar conditions. Corresponding data have also been taken for other types of cells. Apparently no detectable difference in the efficiency of separation can be attributed to the chemical nature of the anion.

(h) pH of Anode Compartment

Experiments were run in which the pH of the anode was maintained as nearly as possible at 1.5, 3.5, and 6. No difference in the efficiency was detected. In practice, it was found more convenient to use the flushed type of control, in which the anode compartment remained at the pH of the original solution.

(i) Reflux Rate

The effect of the concentration of the HCl added to the cathode compartment was checked with KCl as the electrolyte, two experiments were run in which the restituent solutions were 1:28.28 and 1:31.72, respectively. The resultant rates were indistinguishable. This is to be expected as the cells will automatically adjust themselves to small differences in concentration.

(j) Concentration of Electrolyte

Experiments were performed in which the KCl:H_2O ratios were 1:25, 1:60, and 1:120. The differences in rate were no greater than usually observed between experiments run at the same concentration. For cells with equal cathode volumes, the rate of increase of the abundance ratio, for a given current, was greatest when the electrolyte was the most dilute.

(k) Type of Control

The results signify the necessity for the correct rate of addition of the restituent solutions at all times. Any system of control that permits a wide swing from low to high pH during the control cycle is objectionable. The pH swing is in general lower in the boundary and in the automatic-control experiments than is possible to obtain by manually regulated droppers. For this reason the q/i values for the latter are low on the average. This statement must be made with some reservations, however, because the cathode volume was kept small in most of the manually operated experiments, hence the pH swing is comparatively large. The results as a whole indicate a higher q/i value for the larger cathode volumes, although the rate of change in abundance ratio is in the reverse order.

(l) Potential Gradient

The potential gradient differed by a factor of about five for the various packings, being lowest in fiber packings, i. e., cotton, asbestos, and glass wool, and highest in the silicon-carbide and close-clearance cells shown in figure 10, B. The fact that q/i for cotton was as large as for silicon carbide does not indicate the absence of a potential gradient effect, because convection should also be less in the cotton. The only conclusion to be drawn from the limited data available is that if a gradient effect exists it does not make more than a first-power contribution.

(m) Current Density

The current density has been varied over a wide range without observing marked differences in the value of q/i. The interdependence of such factors as current, temperature, convection, and the like, prevent the drawing of any definite conclusions.

(n) Temperature

The cooling baths were operated at 15°, 25°, and 50° C. The temperature within the packings was measured in representative experiments by means of thermocouples incased in thin glass tubes inserted at various positions in the packing. The bath temperature had little or no influence upon the efficiencies observed. The temperature within the packing was just under the boiling point in experiment 149 and in the neighborhood of 50° C in experiment 186. Figure 12 shows no appreciable difference in rate.

6. Summary

The method of balanced electromigration has been shown to be very efficient for the concentration of the ^{39}K isotope. Its successful utilization rests upon the establishment of a local as well as an over-all balance between the electrolyte stream flow in one direction and the ion transport in the opposite direction, as a result of which the net transport of K^+ ions at all points is reduced to zero. When this has been realized, $^{39}K^+$ ions will make headway toward the cathode compartment, whereas the $^{41}K^+$ ions are washed back. To attain such a balance it is necessary to conduct the electrolysis through a packing of uniform porosity or through a capillary tube to reduce mixing to a minimum.

The separation efficiency has been found to be affected very little if any by the size and shape of the electrolytic cell, the composition of the packing material, the chemical nature of the anion, the electrolysis current, or the temperature of the cooling bath.

The most common causes of cell failure are channeling and nonuniformity of porosity in the packing. Other common causes of faulty operation are improper rates for the addition of the

resistant solutions and gas-bubble formation in the packing.

The mechanism described in this paper should prove an effective means for the continuous separation of isotopes of most of the elements or of any two substances (i. e., Ra and Ba), whose ions have different transport velocities.

The authors express their indebtedness to Marvin Schwartz, Murray Nash, Thaddeus Sterling, Albert Lewis, and Ellen Dawson for their efforts in keeping the experiments under control; to H. W. Bond, Edward C. Wise, Dorothy Thompson, and R. J. Prosen, who prepared most of the solutions used in this research.

IV. Concentration of ^{41}K

By John Keenan Taylor and Vernon H. Dibeler

1. Method and Apparatus

A slight Modification of the apparatus and method used in the separation of ^{39}K can be utilized for the concentration of ^{41}K. In this case a stationary boundary is set up at the anode side of the packing. In an arrangement of this type the more mobile ^{39}K ions migrate toward the cathode, whereas the ^{41}K ions accumulate in the anode compartment between the packing and the boundary.

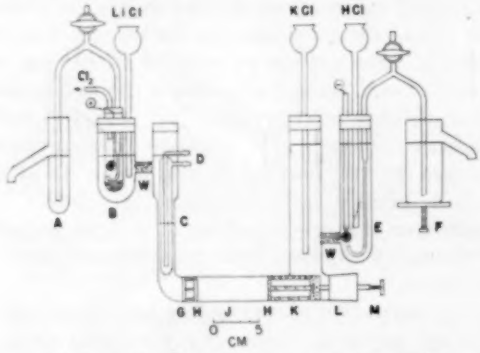

FIGURE 16.—*Cell for the concentration of* ^{41}K.

A, anode overflow; *B*, anode compartment; *C*, boundary; *D*, boundary temperature regulator; *E*, cathode compartment; *F*, reflux adjuster; *G*, *H*, *K*, packing supports; *J*, packing; *M*, screw device to apply pressure to packing; *W*, glass-wool plugs.

The cell is shown in figure 16. It is similar to that used in the concentration of ^{39}K, except that the cathode and anode are interchanged. The electrolytes were lithium chloride above the boundary and potassium chloride in the rest of the cell.

The cell was filled in the following manner. Potassium chloride solution that had been boiled to free it of gas was introduced while still warm until it stood at level *C* in both ends of the cell. Suitable rubber stoppers were placed in the openings, and the cell was evacuated with a water pump until no more bubbles of gas were evolved. The last traces of air were removed from the packing by pouring hot water over the cell. The vigorous boiling that took place at the reduced pressure effectively swept out remaining traces of trapped gas. The cell was then placed in a thermostated water bath, and lithium chloride and potassium chloride were introduced dropwise into their respective funnels. The former was made to seep through the glass-wool plug so that a fairly sharp density boundary resulted. This boundary became exceedingly sharp when the current was turned on.

A number of experiments were carried out with a 2.08 *N* potassium chloride solution containing 1 equivalent of salt to 25 moles of water (14.19% KCl). The lithium chloride solution used with the above solution was 1.22 *N* (5.03% LiCl). In later experiments a solution containing 1 equivalent of the potassium salt to 60 moles of water was used (0.90 *N*) with a lithium chloride solution of 0.55 *N* (2.31% LiCl).

Sodium chloride was tried in place of lithium chloride, but the boundary was difficult to observe because the refractive indices of the two solutions were so nearly identical.

The anode and the cathode compartments were continuously flushed with lithium chloride and potassium chloride solutions, respectively, of the above-mentioned concentrations to remove the products of electrolysis and maintain a constant composition of the solutions on both sides of the boundary. For a current of 0.5 amp, an addition rate of 100 g/hr was found to be adequate. It was also found advisable to add hydrochloric acid to the cathode at a rate sufficient to keep the electrode compartment neutral or slightly acid.

2. Results

(a) Single-Boundary Experiments

Four experiments were performed for the concentration of ^{41}K; the details are given in table 9.

TABLE 9.—*Specifications of cells used in concentration of* ^{41}K

Experiment No.	Concentration of electrolyte (equivalent of KCl per mole of P_2O)	Cathode volume	Current	Length of run	Minimum ratio $^{39}K/^{41}K$
		ml	*amp*	*hr*	
2	1:25	17	0.50	193	13.0
2	1:25	17	.50	1,061	10.9
7	1:60	8	.25	574	9.1
3	1:25	13	.40	338	12.1

Samples for mass spectrometric analysis were taken at approximately 50-hour intervals in the following manner. A thin-walled capillary tube was carefully inserted below the boundary, and the required amount of solution (about 0.2 ml) was withdrawn. The mass spectromatic technic and apparatus are described in section VI.

The treatment of the experimental data is similar to that used in section III. From the observed values of the abundance ratio $^{39}K/^{41}K$ and the constants of the cells, values of q/i were calculated and are plotted in figure 17. The irregularities of the curves are mainly due to mechanical difficulties, such as power failures, clogging of glass-wool plugs, loosening of the packing, etc. These

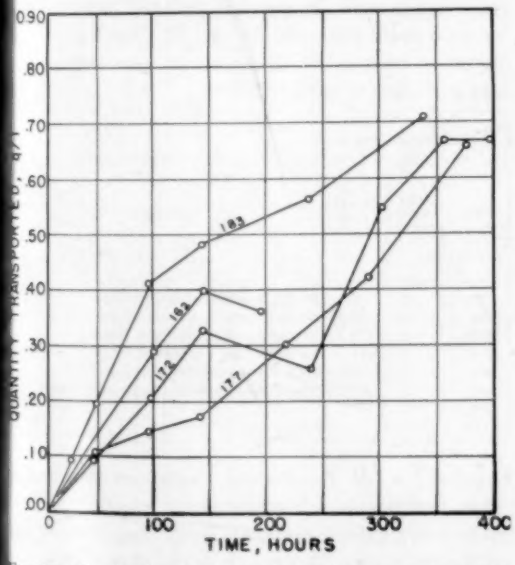

FIGURE 17.—*Performance of cells used to concentrate* ^{41}K.

produce disturbances that may result in the remixing of the isotopes. The maximum value for the slope is the one to be used in the calculation of ϵ for the separation process. The initial slope in experiment 183 gives, for the ratio of the mobilities, $\epsilon = 1.0039$, a value in substantial agreement with that found previously for ^{39}K (sections II and III).

(b) Double-Boundary Experiment

It is possible to construct a cell with both an anode and cathode boundary so that the simultaneous concentration of ^{39}K and ^{41}K is accomplished. Such a cell was set up, in which the anode

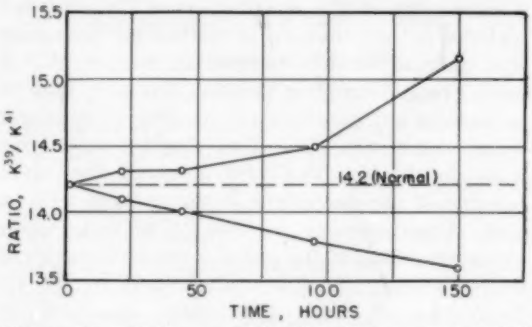

FIGURE 18.—*Performance of cell used to concentrate* ^{39}K *and* ^{41}K.

boundary consisted of lithium chloride above potassium chloride, whereas the cathode boundary was composed of hydrochloric acid above potassium chloride. The potassium chloride was thus confined in the middle of the cell. It is evident that the concentrations of the solutions must be accurately adjusted to the theoretical values if both boundaries are to remain stationary. This was not attained, and the experiment had to be discontinued after 160 hours as the cathode boundary rose slowly while the anode boundary was held in a fixed position. Nevertheless, mass spectrometric analysis of the samples taken during the life of the experiment showed that the predicted isotope concentration changes took place. These values are plotted in figure 18. The method is thus practical and should prove useful for further isotopic concentration of small amounts of enriched potassium salts.

V. Distribution of ^{39}K in Packing

By John Keenan Taylor and A. Keith Brewer

1. Method

In section I it is pointed out that an ideal column packed with 100-mesh granuals could be expected to give up to 200 theoretical units per centimeter when operating at equilibrium under total reflux, and the various factors which affect the height of theoretical unit are discussed. A mathematical analysis of the problem is presented in RP1766 [10].

In practice, it is possible to determine the height of theoretical units of a reflux column from a knowledge of the distribution of the enriched material in the packing. A method for measuring this distribution is described in section II. A more precise sampling technic, however, had to be worked out for the short packing experiments reported in section III. Two sampling procedures were developed. The first involved the rapid freezing of the electrolyte in the packing with as little disturbance as possible. The material in various portions of the packing was then removed and analysed. The second, devised by R. G. VanName, of Yale University, consisted in placing rubber tips at various positions along the barrel of the tube, which could be punctured by a hypodermic needle.

In the first method the electrolyte of the cell was frozen by placing the vessel in a bath of dry ice and acetone. After the electrolyte had solidified, the glass envelop surrounding the packing was broken away to expose the packing as a solid plug. This plug was then sawed into thin disks with a clean hacksaw blade. The thickness of each disk, as well as the distance from its center to the cathode end of the packing, was measured as accurately as possible.

It is necessary to minimize flow of electrolyte from the cathode to the anode compartment during the freezing procedure. The method adopted was as follows: All clamps holding the apparatus in the bath were loosened while the electrolysis was still in progress. At the moment the current was shut off, a pipette was inserted in the cathode compartment, and the liquid level was adjusted as closely as possible to that in the anode compartment. The cell was immediately removed from the bath and placed in the freezing mixture. Some disturbance of the electrolyte in the packing undoubtedly took place during this process.

2. Results

Distribution studies were made on a number of the experiments described in section III. The pertinent data for the various cells are given in table 10. The free space for the packing material was computed by using 38 percent voids for the glass beads and 34 percent for the sand. Data for two cells designed by R. G. VanName, and operated under his direction at the Bureau are also included in table 10.

TABLE 10.—*Characteristics of the electrolysis cells*

Experiment No.	Packing				Current		Time	Cathode volume	Free volume of packing	Remarks
	Material	Mesh	Diameter	Length						
			cm	*cm*	*amp*	*v*	*hr*	*ml*	*ml*	
121	Glass beads	100 to 140	2.5	5	0.60	30	1320	15	9.9	800 hours past equilibrium value.
164	do	100 to 140	2.5	3	.50	34	748	15	9.9	200 hours past equilibrium value.
170	do	100 to 140	1.4	7	.50	93	713	10	3.9	300 hours past equilibrium value.
181	Sand	60 to 100	1.4	8	.50	90	332	5	4.2	100 hours past equilibrium value.
184	do	100 to 140	2.5	8	.50	80	874	20	14.1	150 hours past equilibrium value.
I (VanName)	do	80 to 100	3.75	18	.90	100	101	15	67.7	VanName equilibrium value not attained.
II (VanName)	do	100 to 140	3.75	16	1.00	105	100.5	14	60.1	Do.

The results obtained are summarized in table 11. The first column gives the distance, d, from the center of the packing slice to the cathode end of the packing; the second column gives the isotope abundance ratio, and the third column gives the number, n, of theoretical units per centimeter. This number was computed by plotting the enrichment against distance from the cathode end of the packing. A smooth curve was then drawn through the points, and the slope of the curve at

various points was measured by graphically drawn tangents. From these slopes the equivalent enrichment per centimeter, S, was estimated. The number of theoretical plates per centimeter was computed by the equation $R_c/R_a=S=\epsilon^n$ (eq 8, section I), using $\epsilon=1.006$ for the separation coefficient. The values given in column four are the reciprocal of those in column three and represent values for the height of a theoretical unit for the various experiments.

TABLE 11.—*Efficiency of electrolysis cells*

d	$R=^{39}K/^{41}K$	n (unit cells/cm)	Height of theoretical unit
EXPERIMENT 121			
cm			*cm*
0	18.6	63	0.016
.4	17.2	20	.050
1.3	15.9	11	.091
2.2	15.4	8	.125
3.1	14.7	6	.167
4.0	15.3	3	.333
4.9	14.2	0	
EXPERIMENT 164			
0	20.8	42	0.024
.4	19.4	29	.034
1.2	17.5	16	.063
2.0	17.1	11	.091
2.8	16.3	9	.111
3.6	15.0	9	.111
4.4	14.3	6	.167
EXPERIMENT 170			
0	18.9	34	0.029
.5	17.5	20	.050
1.5	16.0	11	.091
EXPERIMENT 181			
0.6	18.8	11	0.091
1.7	18.3	8	.125
2.8	17.2	6	.167
EXPERIMENT 184			
0	21.0	43	0.023
.5	19.6	12	.083
1.5	18.7	9	.111
2.5	18.3	8	.125
3.5	16.9	7	.143
4.5	16.2	6	.167
5.5	15.9	6	.167
6.5	15.0	5	.200
7.5	14.5	4	.250

TABLE 11.—*Efficiency of electrolysis cells*—Continued

d	$R=^{39}K/^{41}K$	n (unit cells/cm)	Height of theoretical unit
EXPERIMENT I (VANNAME)			
cm			*cm*
0	16.7	14	0.071
2.9	15.16	2	.500
7.0	14.66	1	1.000
10.7	14.56	1	1.000
14.8	14.67	0	
EXPERIMENT II (VANNAME)			
0	16.63	9	0.111
2.5	15.28	4	.250
6.3	14.38	1	1.000
10.4	14.25	0	
14.5	14.2	0	

3. Discussion of Results

The data presented in table 11 show that the abundance ratio drops very rapidly with distance from the cathode end of the packing. In contrast, the gradient is small through the midportion of the packing and is negligible at the anode end. The height of theoretical unit computed from the abundance gradient increases rapidly from the cathode end of the packing. It is interesting to note that this is very low near the cathode, showing that a high value of n can be realized, as is pointed out in section I.

An exact interpretation of the data presented in table 11 should not be made at this time as it is probable that all the packings tested loosened slightly during operation. The steep gradient at the cathode end of the packing, and the negligible gradient at the anode reservoir end, are to be expected in a reflux column in initial stages of operation. If this were the case, the gradient adjacent to the cathode would be indicative of the equilibrium gradient to be expected across the entire packing. Thus experiment 184, for instance, would reach equilibrium when the abundance ratio in the cathode compartment was $^{39}K/^{41}K=112$. In reality, the cell failed to concentrate after reaching an abundance ratio of 21. This suggests that either the height of theoretical unit was not uniform through the packing or that the packing developed a defect when this ratio was reached. Without doubt, both conditions occurred. As the midportion of the packing has been shown to be materially hotter than the ends, the various con-

trolling factors described in section I will tend to increase the height of theoretical unit in this region. This will account in part for the observed decrease in the number of theoretical plates per centimeter in the center of the packing, but it does not account for the absence of a gradient at the anode. The absence of an anode gradient, combined with the fact that the concentration in the cathode compartment increased linearly with time until a ratio of 21 was attained, when it suddenly ceased to increase, indicates that a packing defect developed at this stage in the operation.

In view of what has just been said, the results presented in tables 10 and 11 cannot be considered as defining the operation of an ideal packing. These data are important, however, in that they show conclusively that very small values for the height of theoretical unit are possible, and that the abundance concentration in the packing is in general analogous to that found in conventional reflux columns operating under total reflux.

The writers are particularly indebted to R. G. VanName for his interest in and contributions to this investigation, and to V. H. Dibler for constructing many of the cells used.

VI. Mass Spectrometric Analysis of Isotope Abundance Ratios

By Paul Bradt, O. Lee Parham, and A. Keith Brewer

1. Mass Spectrometer

The mass spectrometer used in measuring the isotope abundance ratios has been described previously [12]. A number of minor changes were made for the present work, the most conspicuous being the substitution of power packs for *B* batteries as a source of high potential. This, however, resulted in no improvement in the operation of the instrument.

The instrument, as modified, was of the 180-degrees type with a focusing radius of 3.6 cm. The side walls of the analyzing chamber were made of Swedish iron to serve as pole pieces. These were soldered into a brass block, as illustrated in figure 19.

The free space between the pole pieces was ⅜ in. This space opened on three sides into a ¾-in. channel drilled in the brass block. The channel not only served as a well to prevent the reflection of ions, but facilitated evacuation. The faces of the pole pieces were chromium plated and burnished to minimize the formation of insulating deposits that might become charged and distort the resolved ion beams. The analyzing chamber was mounted between the pole pieces of a large electromagnet.

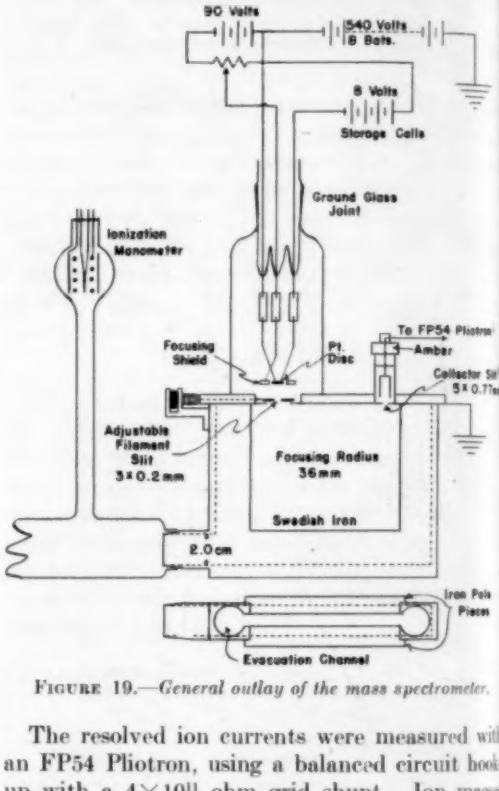

FIGURE 19.—*General outlay of the mass spectrometer.*

The resolved ion currents were measured with an FP54 Pliotron, using a balanced circuit hookup with a 4×10^{11} ohm grid shunt. Ion masses could be brought in by varying either the accelerating potential or the current energizing the electromagnet. The latter was used almost exclusively as positive-ion emission currents do not exhibit perfect saturation, hence it is preferable to keep the ion-acceleration potential constant.

2. Positive-ion Source

The ion source was of the thermionic type. The positive ions were emitted from a platinum disk impregnated with the sample. The disk, 2 mm in diameter, was spot-welded to a hairpin tung-

en filament, and was mounted from 6 to 8 mm bove the entrance slit to the analyzing chamber. ccelerating potentials from 500 to 600 volts ere used.

In order to obtain precision results it was es-ntial to bring the thermionic beam to focus on he entrance slit. This was accomplished by eans of an electrostatic focusing shield in the rm of a washer with the disk symmetrically cated in the eye. In general, a positive potential the washer of about 60 v with respect to the isk was required to bring the beam to a sharp cus on the filament slit. The slit was made ovable to permit adjusting for maximum re-olved ion currents. This position usually is dentical to that for minimum background.

The platinum disk was prepared for impreg-ation by glowing at white heat in vacuum until ll residual potassium was removed. Impreg-ation was accomplished by pasting a small uantity of a potassium containing material on he disk with distilled water and heating to red-ess for about 30 minutes. During the heating rocess the platinum absorbed sufficient potassium o serve as a positive-ion source. For high resolu-ion, it is essential to remove all adhering deposits rom the platinum by scraping it with a sharp nife. Salt or ash deposits on the platinum result ot only in a nonuniform work function over the urface but become charged in operation, and ons-quently, introduce an appreciable back-round between the isotope peaks.

The positive-ion emission from impregnated ources always passes through a definite cycle ith respect to time. The ion current at first ncreases with temperature until a fairly flat pla-eau is reached. Thereafter, the emissivity de-reases, approaching zero when all the alkali is emoved. Consecutive measurements of the eights of the isotope peaks taken when the mission is increasing slowly or when it has reached he plateau give the same abundance ratio. Meas-rements taken when the emission is decreasing sually give a ratio that is too low.

The mechanism resulting in a decrease in the bundance ratio when the source is near exhaus-ion has been discussed in a previous article [13]. n addition, it was pointed out that the emission f positive ions from impregnated sources can be xpressed by an equation of the Richardson type aving the form

$$N^+ = n(kT/2\pi m)^{1/2} e^{-\phi/kT},$$

where N^+ is the number of K^+ ions escaping per unit surface at temperature T, n is the K atom density per unit volume at the surface, m is the atomic weight, and ϕ is the work function. The escape of positive ions at a given temperature is seen to be the product of two variable terms, the first, n, being a direct proportionality, and the second, ϕ, being a negative exponential. As positive ions on the surface behave as a positive grid to depress their own emissivity, it follows that the work necessary to remove an ion decreases rapidly with a decrease in n. Thus, the initial increase in emissivity can be explained as a result of a decrease in ϕ brought about by the concomitant decrease in n. When the surface in the final stages of exhaustion is largely denuded of potassium, ϕ will undergo little further change, and the emissivity will drop as n approaches zero.

3. Preparation of Samples

Although any potassium-containing material can be used to impregnate the platinum disks, crystalline salts like potassium chloride and potassium sulfate are difficult to use as the coatings are inclined to peel off during the initial heating. To overcome this difficulty, it has been found advantageous to convert such salts to phosphates.

As only 10^{-8} g of potassium is required for analysis, sample-taking becomes a problem of using a small quantity that can be handled conveniently. The smallest possible samples were preferred as the operation of the electromigration cells should be checked as nearly as possible under conditions of total reflux. The technic adopted was to remove a drop of solution from the cathode compartment and to place it in a 2-ml platinum crucible that had been boiled in nitric acid and washed in distilled water. A drop of dilute phosphoric acid and a little powdered quartz were added, and the mass was evaporated to dryness and heated to dull redness. The quartz, which had been boiled for 2 days in nitric acid, was used simply as a carrier for the potassium phosphate.

In preparing the sample for the mass spectrometer, a little quartz was scraped out of the crucible and placed on the platinum disk. The disk was then heated to dull redness in a vacuum, after which all the quartz and adhering phosphate were carefully removed. It was then spot-welded to

the mass-spectrometer filament and placed in the instrument for analysis.

4. Potassium Isotope Abundance Ratio

The abundance ratio for the isotopes of potassium has been shown to be constant in nature, except where base exchange or perhaps certain vital processes have taken place. This ratio is $^{39}K/^{41}K = 14.20 \pm 0.02$ [14]. As commercial salts all have the normal ratio, it was not necessary in the present experiments to check during the operations the solutions flowing through the anode compartment when ^{39}K was being concentrated or the cathode solution when ^{41}K was being concentrated. All isotope concentrations reported in the present paper represent a change in abundance from the normal ratio of 14.20.

VII. An Automatic Reflux Control

By Roy J. Britten and J. Gilman Reid, Jr.

1. Introduction

In the electromigration method of isotope separation, conditions of reflux balance must be maintained over long periods of time. Manual control of operating conditions proved satisfactory when the cell was kept under continual observation. A virtually self-regulating system was controlled by the pH of the cathode solution. This provided greater convenience and reliability, and, in addition, reduced the amplitude of cyclic departures from conditions of exact reflux balance.

In potassium cells, the pH of the cathode solution was found to be a sensitive and reliable criterion of reflux balance. The rate at which restituent acid was added to the cathode volume proved an effective means of controlling the reflux rate. Here the pH was indicated by the emf of a hydrogen electrode against a lead-sulfate or silver-chloride reference electrode. This emf operated through a d-c amplifier to actuate an electric valve in the acid supply line.

The cathode compartment of a small K_2SO_4 separation cell with associated control elements is shown in figure 20. The hydrogen electrode and the lead-sulfate electrode were located side by side in a relatively field-free region above the cathode. Nascent hydrogen evolved in the cathode reaction saturated the hydrogen electrode. The feed line for the restituent acid (H_2SO_4, 1:30) entered the cathode solution and was curved to point up at the hydrogen electrode. The valve in the acid line, was attached to a Mariotte supply bottle and was held open or closed under control of the electric relay in the amplifier output circuit. Polarity of connections was such that an increase in cathode pH above a chosen reference value caused the valve to open and feed more restituent acid.

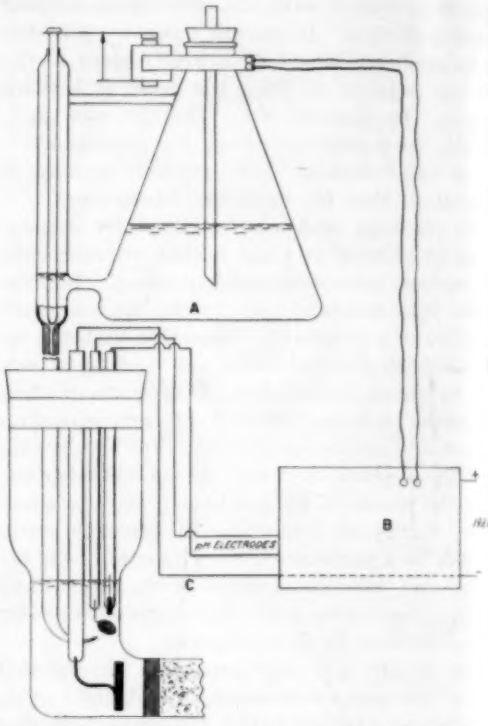

FIGURE 20.—*Cathode compartment and control equipment.*
A, Restituent acid; *B*, amplifier; *C*, cathode.

2. Control Electrodes

The reversible hydrogen electrode consisted of a 1-cm disk of platinized platinum gauze. This was located directly above the cathode of the cell so as to receive a plentiful supply of nascent hydrogen.

The reference electrode of lead-lead sulfate was a projecting length, about 0.3 cm^2 in surface area, of a pure lead wire waxed into the end of a protective glass sleeve. Previously, the wire had been anodized for about 15 minutes in a dilute sulfuric acid solution at a current density of 0.1 amp/cm^2, and with several subsequent polarity

versals. Electrodes of this type were used in sulfate solutions.

In chloride solutions, the reference electrode was of silver-silver chloride with a built-in salt bridge. This electrode was housed in a 4-mm Pyrex tube with a porous frit sealed in one end. The tube was filled for several centimeters above the frit with an agar gel saturated with KCl. A silver wire with a drop of AgCl cast on its end was immersed in the gel. The open end of the tube was sealed with wax around the silver wire.

bility of less than 0.1 pH. Neither the hydrogen electrode nor the lead-sulfate electrode showed any deterioration during extended operation. Although the silver-chloride electrode was expected to be subject to deterioration due to the leaching of KCl from the gel, no such difficulty was encountered.

3. Amplifier

The amplifier is shown schematically in figure 21. It consisted of an input stage with 6SF5

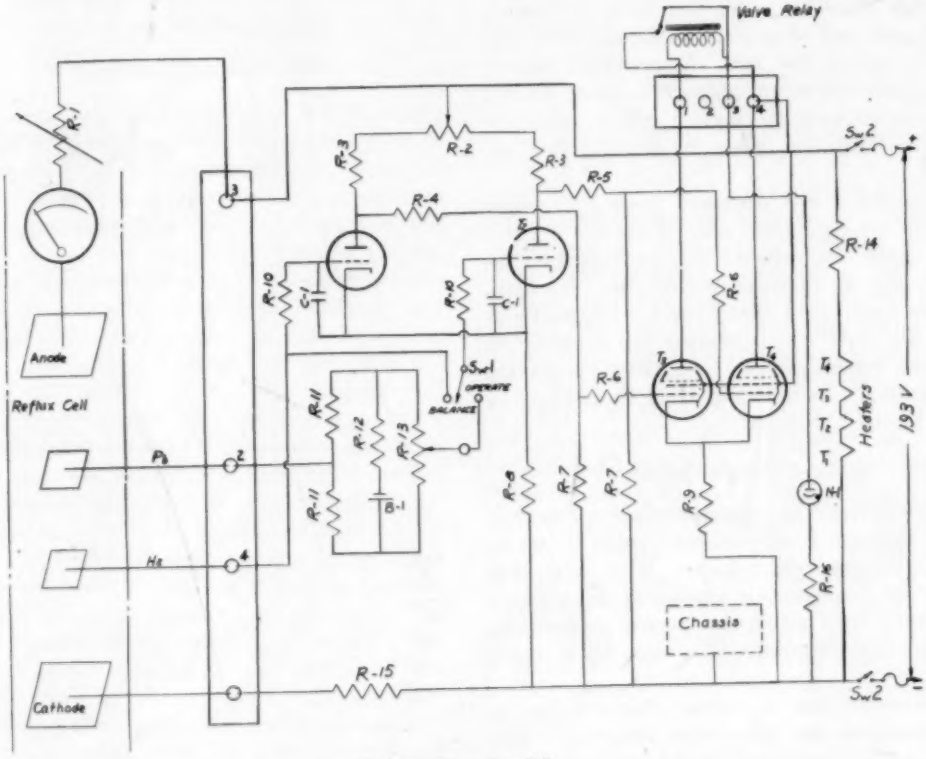

FIGURE 21.—*Amplifier.*

R-1, 2,000 ohm power rheostat (external to amplifier); *R*-2, 50,000 ohm potentiometer, *R*-3, 200,000 ohm resistor; *R*-4, 150,000 ohm resistor, *R*-5, 100,000 ohm resistor; *R*-6, 25,000 ohm resistor; *R*-7 1 megohm resistor; *R*-8, 35,000 ohm resistor; *R*-9, 2,000 ohm resistor, 10 watt, wire wound; *R*-10, 100,000 ohm resistor; *R*-11, 50,000 ohm resistor; *R*-12, 20,000 ohm resistor; *R*-13, 10,000 ohm potentiometer wire wound; *R*-14, 500 ohm resistor, 100 watt, wire wound, adjustable (adjusted to 440 ohms). *R*-15, 75 ohm resistor, 25 watt, wire wound, adjustable. (Adjusted for 20 to 25 volt drop at operating current of cell); *R*-16, 100,000 ohm resistor; all resistors ½ watt carbon, except where otherwise specified; *C*-1, 0.05 mf. Paper capacitor; *R*-1, neon lamp, 1/25 watt; *T*-1 and *T*-2, vacuum tubes 6SF5; *T*-3 and *T*-4, vacuum tubes 25L6.

The hydrogen electrode against either reference electrode developed a change in emf of about 60 mv per unit of pH. The electrodes operated without polarization into the 10-megohm input circuit of the amplifier. Random drift was a few millivolts and corresponded in all cases to an insta-

triodes (T_1 and T_2) and a power stage with 25L6 beam tetrodes (T_3 and T_4). In each stage, reversed phase coupling of the two tubes was developed by the high resistance (R_8, R_9) in their common cathode circuit. The amplifier responded to potential variations between the two input

grids but was only slightly affected by variations in their common potential relative to ground. The resistance offered by the input grids was about 10 megohms. The grid-circuit filters (R_{10}, C_1) provided a bypass of transient and alternating potentials picked up by the leads and electrode which could not easily be shielded.

The output load was the coil of a relay that actuated the acid valve. This was in the plate circuit of T_3. Between this point and the input grids the amplifier has a transconductance of 150 ma/v. Amplitude response was linear over an input range of 250 mv. R_{13} permitted application to the input emf of a positive or negative bias adjustable up to 250 mv. R_2 provided adjustment of quiescent output current between 15 and 35 ma approximately. Switch SW–1 could be thrown to short the input for making this adjustment.

The amplifier was operated from the power supply for the separation cell. This was a 180-v stack of heavy lead cells which were floated on the 220-v d-c line at a charge rate of about 0.2 amp. This gave a source of about 193 v with good stability. Alternatively it should be possible to operate the system directly on a 220-v line having good stability. In this case R–14 should have a value of about 550 ohms.

4. Acid Supply System

The acid supply system comprised a reservoir that fed through a ball-and-cone valve to an injector in the cathode volume. The valve was actuated by the armature motion of an ordinary electric relay from which the electric contact elements had been removed. The assembly is shown in figure 20.

The reservoir was a 4-liter Mariotte bottle, which supported the glass-valve assembly. The valve stem was a 32-cm length of 3-mm rod ground round at its lower end and with a head at its upper end for support by the lifting arm. The conical valve seat was ground in a length of heavy-walled capillary tube which was sealed into the lower end of the valve housing. The length of capillary tubing was adjusted to limit the acid flow to the desired maximum. The injector was a length of 5-mm tube curved and drawn into a nozzle at the discharge end.

The valve assembly is shown in greater detail in figure 22. The relay coil had a resistance of 850 ohms for normal actuation at about 20 m
The relay was supported by a brass clamping str
from the neck of the Mariotte bottle. The lifti
arm was a light brass strip, 15 mm wide and creas
lengthwise for stiffness. It was attached wi
screws to the relay armature and projected 8 c
beyond the pivot axis. A notch in the open e

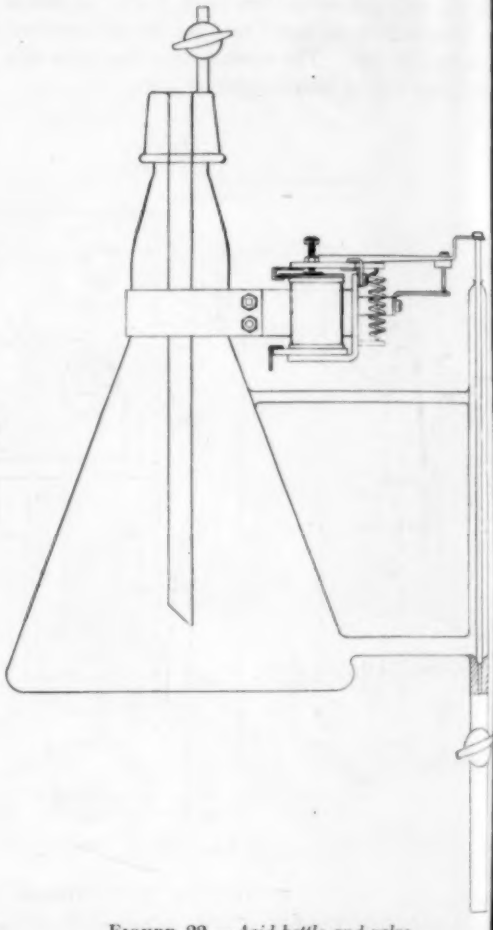

FIGURE 22.—*Acid bottle and valve.*

engaged the valve rod just below its head. Tw
4–40 machine screws threaded through the arm
ture served as adjustable stops on closure.

Mechanical adjustment of the relay was n
critical. In a typical case, the stops for open a
close position were set so that the relay closed
a 2-mm air gap at 30-ma current and opened to
3-mm air gap at 25-ma current. The valve r
was lifted about 3 mm when the relay was ene

zed. This adjustment maintained itself for an peration period of over 800 hours. The 5-ma fference in relay currents corresponded to 30 mv the amplifier input. As the total instability of mplifier and pH electrodes was equivalent to ss than ±10 mv at the input, the quiescent lay current could be set at 25 ma with no risk of tuation from a random surge.

Contacts consisting of short lengths of brass re were attached to the valve lift arm and to the lay frame so as to close when the valve arm ted. These were connected to a small neon mp that served as an indicator of valve position.

5. Cathode Compartment

The character of the regulation was critically fluenced by the shape of the cathode compartent and the placement of the cathode, of the pH ctrode, and of the injector, as well as the rate acid injection. The time required for the jected acid to mix completely through the caode solution was determined by the compartent shape, the placement of the cathode, and e rate of hydrogen evolution through its mixing tion. The dominant factor in establishing the riod of the control cycle was the time interval tween the opening of the valve and the contact the injected volume of concentrated acid with e hydrogen electrode. This interval depended the acid release rate and a placement of the jector relative to the hydrogen electrode.

During the part of the operating cycle when id was not being added, the pH of the cathode lution continually increased as hydrogen was olved in the cathode reaction. The emf from e pH electrode and the output current of the mplifier consequently increased. At the pretermined current level, the valve opened and en remained open until the concentrated acid rculated into the contact with the hydrogen ctrode. During the ensuing interval, in which e hydrogen electrode was recovering from the ntact of concentrated acid, the valve remained sed and the injected pulse of concentrated acid s thoroughly mixed through the solution. pon recovery, the potential of the hydrogen elecde again represented the average pH of the thode compartment, and the cycle was repeated. In a typical case, the period of the operating cle was maintained with stability at 10 seconds. Acid injection was at about three times the required average rate for approximately one-third of the cycle. The time required for thorough admixing of the injected acid was about 5 seconds. The emf of the hydrogen electrode indicated a total pH swing of from four to five units during the cycle.

The tip of the acid injector was located about 3 mm from the hydrogen electrode and was aimed directly at it from below. A closer placement of the injector reduced the period of the cycle, but this offered no particular advantage and decreased the stability of operation.

6. Adjustment Procedure

Initial adjustment of the self-regulating cell was made in the following manner: The current and the rate of addition of the restituent solution to the anode compartment were adjusted to the proper values. The control amplifier, which had meanwhile warmed up (with switch *SW*–1 thrown to short the input grids, was adjusted for a current output slightly below that for valve closure. Then, with *SW*–1 thrown to the operating position, a small quantity of a selected chemical indicator was added to the cathode solution and the potentiometer *R*–13 adjusted to open the valve coincidently with the indicator color change. Where necessary, acid was manually added to the cathode solution for bringing its pH into the chosen operating range. After the control cycle of operation had been established, *R*–13 was readjusted for more precise agreement of relay actuation and indicator color change. The neon lamp, *N*–1, was a pilot for valve operation and permitted easy observation of the cycle adjustment.

7. Results

Several potassium sulfate and potassium chloride cells were maintained in self-regulated operation for periods of, in some cases, more than 800 hours. Representative experiments are included in table 8. The automatic control was of principal value in making the operation of cells more convenient and reliable by eliminating their need for continual attention. From available data the separation efficiency of a cell was in no case impaired upon its conversion to self-regulation.

727972—47——3

VIII. References

[1] F. A. Lindemann, Proc. Roy. Soc. (London) [*A*] **99,** 103 (1921).

[2] Robert S. Mulliken and W. D. Harkins, J. Am. Chem. Soc. **44,** 37 (1922).

[3] James Kendall and E. C. Crittenden, Proc. Nat. Acad. Sci. **9,** 75 (1923).

[4] James Kendall, Science **67,** 163 (1928).

[5] J. E. G. Pilley, Phil. Mag. [6] **49,** 889 (1925).

[6] Eric R. Jette, Phil. Mag. [7] **3,** 58 (1927).

[7] A. Keith Brewer, S. L. Madorsky, and J. W. Westhaver, Science **104,** 156 (1946).

[8] T. I. Taylor and H. C. Urey, J. Chem. Phys. **6,** 429 (1938).

[9] A. Keith Brewer, Ind. Eng. Chem. **61,** 1597 (1939).

[10] J. W. Westhaver, The concentration of ^{39}K by counter current electromigration, some theoretical aspects of the operation, J. Research, NBS **38,** 169 (1947) RP1766.

[11] A. Keith Brewer, J. Ind. Eng. Chem. **30,** 893 (1938); Phys. Rev. **46,** 894 (1934); J. Am. Chem. Soc. **58,** 365 (1936).

[12] A. Keith Brewer, J. Chem. Phys. **4,** 350 (1936).

[13] A. Keith Brewer, J. Am. Chem. Soc. **58,** 370 (1936); **61,** 1597 (1939).

WASHINGTON, March 14, 1946.

U. S. Department of Commerce
National Bureau of Standards

Research Paper RP1766
Volume 38, February 1947

Part of the Journal of Research of the National Bureau of Standards

Concentration of Potassium[39] by Countercurrent Electromigration: Some Theoretical Aspects of the Operation[1]

By James W. Westhaver [2]

Equations are derived which describe the operations (*A*), for the early stages of the run, (*B*), after infinite time with no production, and (*C*), after infinite time at fixed production. The formulas under (*A*) enable evaluation of the elementary separation coefficient, ϵ. Those under (*B*) enable calculation of the maximum separation in terms of various channeling factors which determine the length of theoretical unit cell, h. The formulas under (*C*) enable calculation of optimum production conditions. When measured by the smallness of h, the analysis depicts the fractionator as one which is about 100 times more powerful than a modern laboratory distillation column.

I. Introduction

A mathematical analysis of various factors pertinent to the operation of countercurrent electrolysis [1, 2][3] in capillary tubes, packings, and sheets is presented. Special emphasis is given to the adverse effects of channeling. Although the discussion is applied to the specific problem of concentrating ^{39}K, it is applicable to open and packed reflux columns in general merely by changing the definition of terms.

The factors involved in the analysis are (1) The separation coefficient. This is defined as the ratio of the mobilities or velocities of the ^{39}K and ^{41}K isotopes, $\epsilon = v_1/v_2$. The actual mechanism giving rise to a difference in mobility is not involved in the discussion. (2) The length of column, h, required to give a separation of ϵ. In the discussion the term h takes the place of the conventional height of elemental theoretical plate or height of theoretical unit. The various experimental conditions limiting h are considered individually. (3) Factors for continuous production. Calculations based on (1) and (2) are given for the most efficient length of tube, the holdup, and the yield in grams per kilowatt hour, when the product is $^{39}\mathrm{K}/^{41}\mathrm{K} = 21.3$.

1. Symbols and abbreviations

A = cross-sectional area of packing, cm^2
a = lateral spacing between a velocity crest and a velocity trough, cm
c_1, c_2 = concentrations of ^{39}K, and ^{41}K, moles/cm^3
C = normality, moles/liter
D, D_1, D_2 = isotropic, lateral and longitudinal coefficients of pure diffusion, cm^2/sec
D' = over-all or effective longitudinal coefficient of remixing by both pure diffusion and convection remixing, cm^2/sec
$\epsilon = v_1/v_2$ = elementary process separation factor
F = Faraday constant = 96,500 coulombs/equivalent
h = length of theoretical unit, as defined in text, cm
η = viscosity of solution, poise
I^+ = total current times positive-ion transference number, amperes
l = length of packing or fractioning path, cm
γ = equivalent conductivity of solution
N_1, N_2 = mole fractional concentrations of ^{39}K and ^{41}K

[1] This paper will be included in volume 6, division III, of the Manhattan Project Technical Series.
[2] Patent Examiner, U. S. Patent Office, and Consultant to Mass Spectrometer Section, National Bureau of Standards.
[3] Figures in brackets indicate the literature references at the end of this paper.

n = dimensionless exponent

q = valence of positive ion = 1 for K

r, r_0 = radial coordinate and radius of tube, cm

$R = V_a/\Delta V_a$ = reflux ratio during production

S_t, S_e = over-all separation factor at time t and at equilibrium

t = time, sec

v_1, v_2 = velocity of ^{39}K and ^{41}K relative to the solution, cm/sec

V_a = mean countervelocity of solution for total reflux, cm/sec

v = local point counter velocity of solution, cm/sec

ΔV_a = mean departure from total reflux mean countervelocity, with reference to production, cm/sec

Δv = local point departure from exact ion-velocity, solution-velocity balance under total reflux equilibrium, cm/sec

V_c = cathode volume, cm^3

x, w = thickness coordinate and semithickness between parallel walls, cm

z = distance from anode face of packing, cm.

II. Significance of ϵ

In an electrolytic cell of the type discussed in RP1765 [2], the transport mole/cm^2/sec of the light ^{39}K isotope due to the electric current before the liquid counterflow is superimposed is

$$\frac{c_1 v_1}{c_1 v_1 + c_2 v_2} \frac{I^+}{qFA},$$

in which c_1 and c_2 are mole concentrations of ^{39}K and ^{41}K per milliliter at time t; v_1 and v_2 are their velocities; I^+ is the positive-ion current equal to the total current times the cation transference number; $F = 96{,}500$ is the Faraday constant; A is the effective cross-sectional area; and q is the valence of the positive ion, being unity for K^+.

When liquid counterflow is superimposed at a rate intermediate between the velocities of the ^{39}K and ^{41}K, these are transported in opposite directions and an isotope concentration gradient builds up. This gradient begins adjacent to the cathode and works its way to the anode, finally reaching an equilibrium value. When this equilibrium is reached, the stream flow plus the back diffusion and convection remixing just balances the ^{39}K ion current. If the potential is then removed, the flow of ^{39}K in the anode direction is $V_a c_1 + D'(dc_1/dz)_{t=\infty}$ moles per square centimeters a second, where V_a is the mean liquid velocity, D' is the over-all or effective coefficient of remixing by both diffusion and convection processes, and z refers to length along the tube.

When the average K ion is static against the moving stream, as is the case during perfect operation, and when equilibrium is reached for the entire tube, conditions in the system are expressed by

$$\frac{c_1 v_1}{c_1 v_1 + c_2 v_2} \frac{I^+}{qFA} = V_a c_1 + D'(dc_1/dz)_{t=\infty}, \quad (1)$$

where $(dc_1/dz)_{t=\infty}$ represents the maximum attainable gradient.

The liquid countervelocity, V_a, is so adjusted at the cathode end that the net forward transport of positive ions by the current is balanced by the backward transport of the stream, so that $I^+/(qFA) = V_a(c_1 + c_2)$. Hence there is no net positive-ion current after this adjustment. The small currents of ^{39}K and ^{41}K that cause the tube to build up a gradient are equal and opposite, and finally disappear when the equilibrium gradient is reached. Hence, under proper conditions, the entire current is carried by the negative ions throughout the run. V_a is maintained constant throughout the run and has the value

$$V_a = \frac{I^+}{qFA(c_1 + c_2)}. \quad (2)$$

Substituting eq 2 in eq 1 and collecting

$$\frac{I^+}{qFA} \frac{c_1 c_2 (v_1 - v_2)}{(c_1 + c_2)(c_1 v_1 + c_2 v_2)} = D'(dc_1/dz)_{t=\infty}. \quad (3)$$

As v_1 and v_2 are nearly equal, it is sufficiently accurate to write $(c_1 v_1 + c_2 v_2) = (c_1 + c_2) v_2$ and, also, to express isotope concentrations as mole fractions by $N_1 = c_1/(c_1 + c_2)$, $N_2 = c_2/(c_1 + c_2)$, and $dc_1 = (c_1 + c_2) dN_1$. With these relations, eq 3 becomes

$$\frac{I^+ (v_1 - v_2)}{qFAD'(c_1 + c_2) v_2} dz = \frac{dN_1}{N_1 N_2}. \quad (4)$$

As $N_1 + N_2 = 1$, and hence $dN_1 = -dN_2$, it follows that

$$dN_1/N_1 N_2 = dN_1/N_1 - dN_2/N_2 = d \ln(N_1/N_2),$$

and the integration of eq 4 over the length, l, of the tube, assuming uniform salt concentration, gives

$$\frac{I^+(v_1-v_2)l}{qFAD'(c_1+c_2)v_2}=\ln\frac{(N_1/N_2)_{z=l}}{(N_1/N_2)_{z=0}}. \quad (5)$$

This is the equilibrium equation for the tube and applies only after the gradient ceases to rise in any part of the tube.

The elementary process separation coefficient is defined as the ratio of the mobilities or velocities, of the light to the heavy-isotope ions, thus

$$\epsilon=v_1/v_2 \quad \text{or} \quad \epsilon-1=\frac{v_1-v_2}{v_2}.$$

The over-all equilibrium separation factor is defined as the ratio of the abundance ratio at the cathode to the abundance ratio at the anode, thus

$$S_e=\frac{(N_1/N_2)_{z=l}}{(N_1/N_2)_{z=0}}. \quad (6)$$

As ϵ is close to unity, $\epsilon-1$ can be replaced by $\ln\epsilon$. Equation 5 therefore can be written

$$\ln S_e=\frac{I^+(\epsilon-1)l}{qFAD'(c_1+c_2)}=\frac{I^+l\ln\epsilon}{qFAD'(c_1+c_2)}, \quad (7)$$

or

$$S_e=(\epsilon)^{l/h}, \quad (8)$$

where h is the height of theoretical unit and equals $qFAD'(c_1+c_2)/I^+=D'/V_a$, and l/h is the number of theoretical units contained in the length l.

All quantities are measurable in eq 7 and 8 with the exception of the over-all remixing coefficient D'; this can be calculated under certain simplified experimental conditions, for example, those prevailing in a single vertical capillary tube. Equations 7 and 8 thus make it possible to calculate the maximum separation attainable.

At the beginning of the run there is no remixing as $dc_1/dz=0$, and the total transport of light isotope is concentrated in the cathode compartment. The initial transport, in moles of ^{39}K per second, from eq 3 is

$$\frac{I^+}{qF}\frac{N_1N_2(v_1-v_2)}{v_2}=\frac{I^+N_1N_2(\epsilon-1)}{qF}. \quad (9)$$

The initial rate of rise in concentration at the cathode is inversely proportional to the cathode volume. When ΔN_1 is the mole fraction gain in concentration of the light isotope in t seconds; V_c, the cathode volume; and C, the normality; the moles of light isotope accumulated is $V_cC\Delta N_1 10^{-3}$ moles ^{39}K. This is equal to the rate given by eq 9 times the time. Hence

$$V_cC\Delta N_1 10^{-3}=\frac{I^+N_1N_2(\epsilon-1)t}{qF},$$

or

$$\epsilon-1=\frac{V_cCqF}{1000I^+t}\frac{\Delta N_1}{N_1N_2}. \quad (10)$$

As ΔN_1 is small compared to N_1 during initial operation,

$$\frac{\Delta N_1}{N_1N_2}=\Delta\ln(N_1/N_2)=\ln(N_1/N_2)_t-\ln(N_1/N_2)_{t=0}=\ln S_t.$$

Equation 10 now becomes

$$\epsilon-1=\frac{V_cCqF\ln S_t}{1000I^+t}. \quad (11)$$

With eq 11 it is possible to calculate the ratio of mobilities from the initial slope of the curve of $\ln S_t$ plotted with respect to t. If S_t is near unity, it is sufficiently accurate to write $\ln S_t = S_t-1$ and plot this with respect to t. Also N_1/N_2 may be plotted, but in this case the initial slope must be divided by (N_1/N_2) (mean) in making the calculation of ϵ.

Equation 10 or 11 applies regardless of whether the light isotope is rare or abundant. In cases involving the concentration of the heavy isotope, N_1 and N_2 are interchanged, and S_t is defined as $(N_2/N_1)_t/(N_2/N_1)_{t=0}$. The definition of ϵ then remains the same, namely, the ratio of the light to the heavy-ion mobilities.

III. Calculation of h

The factor h is defined for the present process as that segmental length of tube or cell that will boost the abundance ratio by a factor ϵ when the concentration gradient has built up to a steady state under "total reflux", i.e., cathode sampling rate is zero. It is important that h be kept small as the power requirement, holdup, and time to reach equilibrium are each proportional to it. This section discusses conditions under which a small h can be realized, as well as other conditions that will lead to a large h.

According to eq 2, 7, and 8, the length h is given by

$$h=D'/V_a, \quad (12)$$

where D' is the over-all longitudinal remixing coefficient, and V_a is the mean liquid counter-

velocity that balances the mean drift velocity of the K ions. In all cases met in practice the effective coefficient D' is made up of both pure molecular back diffusion and convective remixing. The latter is due to convection of K resulting from the fact that the point liquid countervelocity is not in exact balance with the point ion velocity over the entire flow cross section, being higher than the ion velocity in one region and lower than the ion velocity in another. It is necessary to evaluate this latter remixing effect to arrive at a value for D' or h. As convective remixing depends not only on the longitudinal velocity of the K but is diminished by the cross diffusion between the counterflowing streams of K, it is necessary to analyze the steady state in terms of the profiles of longitudinal velocity and lateral diffusivity. This can be done rigorously only for cases involving geometrical symmetry, in a manner now to be discussed.

Consider a round tube that may be either a single narrow capillary or a much larger packed tube. Assume that the mean liquid countervelocity is held in exact balance with the mean ion velocity, notwithstanding that the center of the tube has a liquid velocity greater, and the periphery a liquid velocity less, than the ion velocity in these regions. Assume further that the profile of the velocity departure is symmetrical to the center of the tube. Then, for the point difference between liquid countervelocity, v, and ^{39}K ion velocity v_1

$$\Delta v = v_1 - v, \tag{13}$$

where the point velocity departure, Δv, is a symmetrical function of r.

Also, as there is a net balance of transport with respect to average values,

$$\bar{v}_1\bar{c}_1 + \bar{v}_2\bar{c}_2 = V_a(\bar{c}_1 + \bar{c}_2), \tag{14}$$

where $\bar{v}_1$ and $\bar{v}_2$ are the averaged point ^{41}K ion velocities and the c's are the averaged point concentrations of the two isotopes.

As by definition, $\epsilon = v_1/v_2$, which is closely $\bar{v}_1/\bar{v}_2$, and as $\epsilon - 1$ is quite small compared to unity, eq 14 may be written

$$\bar{v}_1 - V_a = V_a\bar{c}_2(\epsilon - 1)/(\bar{c}_1 + \bar{c}_2). \tag{15}$$

Equations 13 and 15 will be returned to, it now being necessary to consider the differential and integral equations that describe the steady state operation of the tube.

Let $\partial\bar{c}_1/\partial z$ be the longitudinal concentration gradient finally established after very prolonged running, $\bar{c}_1$ being the average ^{39}K concentration over the cross section at level z. This gradient is also the gradient for each point in the cross section because the distribution curves for concentration along the wall, along the axis, or along an intermediate cylinder, are closely parallel in all cases to be considered.

Consider an element of volume at a point r, z. Due to such lack of equality as may exist between ion and liquid velocity, the ^{39}K is removed longitudinal from the element at a rate $(v_1 - v)\partial\bar{c}_1/\partial z$ moles sec^{-1} cm^{-3}. But as point concentrations in the tube have reached a steady state, this removal must be exactly compensated by a lateral diffusion of ^{39}K into the element at a rate $(d/dr)(D_1 r\, dc_1/dr)$ moles sec^{-1} cm^{-3}, in which D_1 is the radial coefficient of diffusion. Hence the steady state requires

$$\frac{d(D_1 r dc_1/dr)}{rdr} = (v_1 - v)\partial\bar{c}_1/\partial z. \tag{16}$$

A second equilibrium condition, assuming zero sampling rate at the cathode, is that the integrated transport of ^{39}K is zero. This is expressed by

$$\int_0^{r_0} [(v_1 - v)c_1 - D_2\partial\bar{c}_1/\partial z]\, 2\pi r dr = 0, \tag{17}$$

where $(v_1 - v)c_1$ is the moles/cm^2/sec transported at the point r,z due to the velocity departure, and $D_2\partial\bar{c}_1/\partial z$ is the moles cm^{-2} sec^{-1} diffusing back, D_2 being the longitudinal coefficient of pure diffusion.

Equations 16 and 17 can be combined after suitable transformation as follows: Integration of eq 16 gives

$$dc_1 = \partial\bar{c}_1/\partial z\left[\int_0^r (v_1 - v) r dr\right] dr/D_1 r, \tag{18}$$

whereas integration of eq 17 by parts gives

$$\bar{c}_1\int_0^{r_0}(v_1 - v)2\pi r dr - \int_0^{r_0}\int_0^r (v_1 - v)2\pi r dr dc_1 = \pi r_0^2 \bar{D}_2\partial\bar{c}_1/\partial z. \tag{19}$$

For dc_1 in eq 19 is substituted the expression given by eq 18, giving

$$\bar{c}_1\int_0^r (v_1-v)2rdr=\left[2\int_0^r\left[\int_0^r (v_1-v)rdr\right]^2 dr/D_1r+\bar{D}_2r_0^2\right]\partial\bar{c}_1/\partial z. \quad (20)$$

But

$$\int_0^r v_1 2rdr=\bar{v}_1r_0^2 \text{ and } \int_0^r v2rdr=V_a r_0^2.$$

Hence returning to eq 13 and 15, and combining these with eq 20,

$$\frac{\bar{c}_1\bar{c}_2V_a(\epsilon-1)r_0^2}{\bar{c}_1+\bar{c}_2}=\left[2\int_0^r\left[\int_0^r (\Delta v)rdr\right]^2 dr/D_1r+\bar{D}_2r_0^2\right]d\bar{c}_1/dz. \quad (21)$$

Now let $dz=h$. Then by definition of h the corresponding longitudinal increase in the abundance ratio is by a factor ϵ, where

$$\epsilon=\frac{\bar{c}_1+d\bar{c}_1}{\bar{c}_2+d\bar{c}_2}\div\bar{c}_1/\bar{c}_2.$$

As $d\bar{c}_1=-d\bar{c}_2$, and is small, this last expression can be written

$$\epsilon-1=\frac{(\bar{c}_1+\bar{c}_2)dc_1)}{\bar{c}_1\bar{c}_2},$$

and substitution in eq 21 gives

$$h=dz=\frac{2\int_0^r\left[\int_0^r (\Delta v)rdr\right]^2 dr/D_1r}{V_a r_0^2}+D_2/V_a. \quad (22)$$

Equation 22 is the general result sought. It enables the calculation of h for any round tube whether packed or open, provided Δv and D_1 are known symmetrical functions of the radial coordinate, r.

In a similar fashion it can be shown that h for a long, thin packing or film, contained between parallel walls, where flow is lengthwise and a uniform balance can be assumed breadthwise, is given by

$$h=\frac{\int_0^w\left[\int_0^x (\Delta v)dx\right]^2 dx/D_1}{V_a w}+\bar{D}_2/V_a, \quad (22a)$$

where Δv is the symmetrical velocity departure as a function of the thickness coordinate, x, the origin of the latter being midway of the walls, and w is the semispacing. In general, the upper and lower limits of x should be chosen such that $dc_1/dx=0$ at both limits.

Five special cases under eq 22 and two under eq 22a will now be considered in detail.

Case I. The Isothermal Capillary.—Consider a single narrow capillary tube and assume an inappreciable rise in axial temperature relative to the wall temperature. Then the ion velocity is uniform over the cross section so that $v_1=\bar{v}_1$. But the liquid countervelocity is a symmetrical parabolic function of r, and this is true even if the flow is aided or impeded by electro-osmosis, as it is known that the latter type of flow also has a parabolic profile [3].

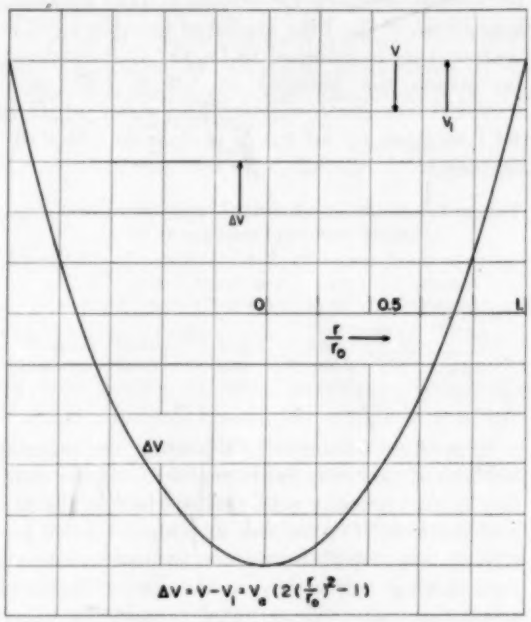

FIGURE 1.—*Profile of isothermal capillary tube.*

The profile of the velocity departure is illustrated in figure 1 and is given by

$$\Delta v=v_1-v=v_1-v=V_a[2(r/r_0)^2-1]. \quad (23)$$

This is to be substituted in eq 22. The profile of the radial diffusion coefficient D_1 is a horizontal line in this case, and hence D_1 may be brought outside the integral sign. The diffusion coefficient vertically will be the same as radially, and both will be designated D.

For the first operation indicated by eq 22,

$$\left[\int_0^r (\Delta v)rdr\right]=(V_a^2r_0^4/4)[(r/r_0)^8-2(r/r_0)^6+(r/r_0)^4].$$

The remaining integration with limits r_0, and 0 leads to

$$h=(V_a r_0^2/2D)(1/8-1/3+1/4)+D/V_a$$
$$=(1/48)V_a r_0^2/D+D/V_a. \quad (24)$$

From this result it is seen that the minimum value of h is $r_0/2\sqrt{3}$, and that the liquid countervelocity to achieve this minimum is

$$V_a=(D/r_0)4\sqrt{3}.$$

The values of h for a 1.0-mm inside diameter isothermal capillary for several voltage gradients lengthwise of the tube are listed in table 1. The temperature is assumed to be 18° C throughout, for which the mobility in 1.0 N KCl [6] is 0.000498 cm sec^{-1} volt^{-1}. The value of D in KCl solution up to 1.0 N is close to 1.55×10^{-5} cm^2/sec.

TABLE 1.—*Height of theoretical unit of 1.0-mm inside diameter isothermal capillary at 18° C*

Potential	V_a	(1/48) $V_a r_0^2/D$	D/V_a	h
v/cm	*cm/sec*			*cm*
1	0.000498	0.00168	0.03110	0.0328
4.31	.00215	.00722	.00722	.0144 min.
10	.00498	.0168	.00311	.0199

In practice, because of I^2R heating, the assumed isothermal condition is not realized. If the capillary is set vertically with cathode feed at the top, and say a 40° C axial rise in temperature is permitted, it is possible to so select the inside diameter that thermal convection up the center and down along the walls will partially balance the excess and deficiency of the countervelocity. The resultant profile, illustrated in figure 2, is a closer approach to ideal point balance than figure 1. In consequence, h will be less than the values indicated in table 1. Calculations indicate that a vertical capillary under perfect control with an inside diameter of 0.7 mm, and a gradient of 15 v/cm, can yield an h of 0.002 cm, or 500 theoretical units per centimeter length.

If the capillary is set horizontally, the effect of heating results in a lateral convective mixing. This increases the value of D in the first term of eq 24. Hence the value of h will be somewhat lower than indicated in table 1, provided the increased back diffusion represented by the term D/V_a is unimportant, as is the case for voltage gradients higher than about 10.

The foregoing calculations apply only to a sing capillary tube. To be applicable to a bundle tubes it would be necessary for the mean ion a liquid velocities to balance in each. The exac ness of this individual tube balance will be realiz when it is considered that maximum separati can occur in each tube only when the mean liqu velocity has a value lying between the velociti of the ^{39}K and ^{41}K ions. As, for a given liqu head, the liquid velocity varies as the square capillary bore, and as the two ions differ in velo

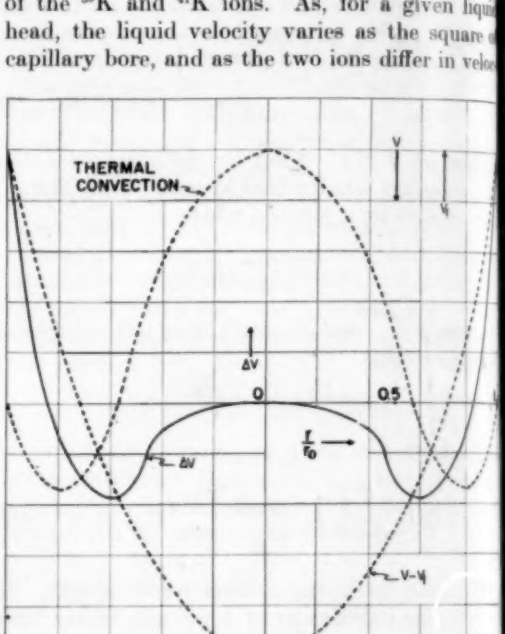

FIGURE 2.—*Profile improved by thermal convection.*

ity by only about 0.3 percent, a suitable bundl must consist of tubes with variations in bore o less than 0.2 percent. Such a requirement can not be met by selection of ordinary glass tubing, although extruded tubes might have the required uniformity. However, a further requirement is that the tubes be at nearly the same temperature, and this is difficult to achieve as the solution has a negative temperature coefficient of resistance.

In contrast, if the above bundle is provided with numerous lateral communications between the tubes, the resulting cross diffusion will greatly compensate for lack of individual tube balance, and it becomes possible to achieve a reasonably low h. This action, though on a larger lateral

cale, is similar to the effect of radial diffusion in he single capillary, which partially compensates or the point lack of balance over the cross section nd gave rise to the reasonably small first term n eq 24.

A tube packed with sand, beads, etc., is analoous to a capillary tube bundle having cross ommunication between passages. It will be lear, therefore, that isotope separation in other han an ideal packing is possible only because of ross diffusion. Various cases of nonideal packngs will be treated hereinafter, but first it appears esirable to discuss the ideal, though as yet nonxistent, packing in order to show the ultimate ossibilities of this method of fractionation.

Case II. The Ideal Packing.—The perfect packng should have the properties of an ideal tube undle. This requires that the pores be small nd nearly identical in shape, cross-sectional size, nd length. The ideal case must exclude the resence of a temperature gradient normal to the irection of liquid counterflow because fluidity of he solution increases with a somewhat greater emperature coefficient than does the mobility of he ions. This last consideration suggests that he ideal packing must be a face-cooled diaphragm.

In order to maintain maximum temperatures elow 100° C, calculations indicate that the diaphragm should have a thickness not exceeding bout 1 cm. Where one diaphragm is insufficient o give the desired separation factor, a series can e used with intermediate spaces for insertion of ooling elements.

A further requirement is that thermal convection cross the thickness of the diaphragm must be liminated. Consider a frit made from 50-mesh eads. With the faces vertical, a convection urrent will occur inwardly from both faces at he bottom, up the midsection, and outwardly oward both faces at the top. The convection t top and bottom will cause remixing. On the ther hand, with the diaphragm horizontal, the pper half will comprise cool liquid overlying hot nd the thermal instability will result in convection urrents toward and away from the upper face. alculations indicate that if thermal convections re to be reduced to negligible velocity the frit hould be made from beads of about 200 mesh er inch or finer. This corresponds to a mean ore radius of 0.002 cm or less.

In summary, it appears that the ideal packing should be a face cooled diaphragm of extremely uniform thickness and porosity with mean pore radius of less than 0.002 cm. For such a diaphragm the first term of eq 24, using for r_o the mean pore radius, is negligible; hence, $h=D/V_o$, where D is the longitudinal diffusion coefficient of the free liquid and V_o the mean liquid countervelocity in the pore. The following are the values of h under the ideal conditions assumed when V_o is taken as 0.00498 cm/sec, corresponding to a 1.0 N KCl solution and an applied gradient of 10 v/cm at 18° C:

Values of D at temperatures other than 18° C were estimated by assuming proportionality to absolute temperature times the fluidity of the water for that temperature [8].

At 18° C; $D=1.55\times10^{-5}$ cm²/sec; $h=0.0031$cm.

At 40° C; $D=2.68\times10^{-5}$ cm²/sec; $h=0.0054$cm.

At 80° C; $D=5.57\times10^{-5}$ cm²/sec; $h=0.0112$cm.

The h at 18° C would apply to diaphragm regions close to either face. The h at 80° C would be encountered across the midplane of a frit having this maximum temperature. As the mobility increases toward the midplane, the voltage gradient across this plane will drop to a value such that the ion velocity and liquid countervelocity are in balance.

Case III. Packed Tube With Uniform Porosity and Hot Core.—Assume first that the packing has a pore radius of about 0.002 cm or less, so that thermal convection is negligible. The value of h will be D/V_o at the cooled end faces of the packing just as in case *II*. At points remote from the ends, however, the ion velocity and liquid velocity are not in point balance over the cross section due to the fact that the temperature coefficient for fluidity is somewhat higher than for mobility. The bulk profile of the velocity departure will approximate the appearance shown in figure 3, and will be assumed to be parabolic, as given by the relation

$$\Delta v=\Delta r_m\,[2(r/r_0)^2-1], \qquad (25)$$

where all velocities and diffusion coefficients are now to be considered as superficial. The superficial values are obtained by multiplying the mean pore values by the fraction voids.

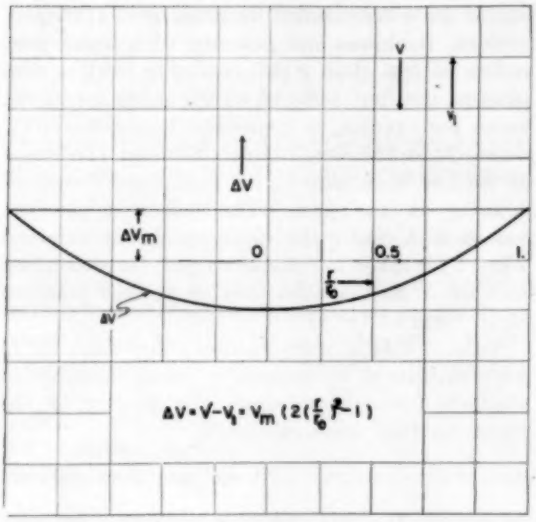

FIGURE 3.—*Profile of packed tube, uniform porosity, hot core.*

Equation 22 is applicable. A rigorous solution requires that the lateral diffusivity D_1 be expressed in terms of r, as D_1 increases with temperature and has its maximum value at the point of maximum temperature, $r=0$. It is sufficiently accurate for our purpose here to consider D_1 as having a uniform value based on the mean temperature between wall and axis. The result of the integration is then

$$h=(1/48)\ (\Delta v_m/V_a)^2 V_a r_0^2/\overline{D}_1+\overline{D}_2/V_a, \quad (26)$$

where V_a is equal to the superficial mean ion velocity based on the mean temperature.

As eq 26 involves ratios of velocity to diffusivity, each of which is to multiplied by the fraction voids to obtain superficial values, it is just as proper to use mean pore values. Further, as V_a is adjusted to balance the mean ion velocity, and as the latter is closely the same function of temperature as is the diffusivity, calculations can be based on KCl solution at 18°, for which, at 1.0 normal, $V_a=0.000498$ cm sec^{-1} $volt^{-1}$, and $D_1 \cong \overline{D}_2 = 1.55\times10^{-5}$ cm^2/sec.

Consider a tube packed with 200-mesh sand and having an applied gradient of 10 v/cm. The maximum permissible temperature rise is assumed to be 80° C. For this rise, due to the fact that fluidity increases more rapidly with temperature than mobility, the ratio $\Delta v_m/V_a$ is calculated to be 0.10. Table 2 lists the values of h for various tube sizes.

TABLE 2.—*Packed tube with uniform porosity, 80° temperature (rise, 10 v/cm)*

Inside diameter of tube	h
cm	*cm*
0.5	0.0073
1.0	.0198
2.0	.0701
4.0	.271
8.0	1.07

It should be emphasized here that the values in table 2 are for an extreme case, remote from the ends of the packing, and with no thermal convection. If the tube is set vertically, and instead of 200-mesh sand, a coarser packing of about 100 mesh is used, calculations indicate that thermal convection will largely overcome the lack of point balance indicated in figure 3. If a tube of 100-mesh sand is set horizontally, thermal convection will be sufficient to markedly increase the effective lateral diffusion coefficient, $\overline{D}_1$. For these reasons it is possible to obtain lower values for h than are indicated by table 2. On the other hand, if the packing contains gas bubbles, the effective value of $\overline{D}_1$ is decreased; hence, h will be increased.

Case IV. Packed Tube With Wall Channeling.—Uniform porosity was assumed in case III. Actually, when a tube is packed with beads or sand, the porosity adjacent the wall, and for a width of about half a bead, is about 50 percent greater than elsewhere. This fact can usually be disregarded when the beads are very small and held under pressure. In the case of frits the higher porosity at the wall can be eliminated with suitable cement. It is of interest, however, to calculate the value of h for cases in which, due to failure of one kind or another, a wall channel makes its appearance.

Consider first a wall channel of uniform thickness over the entire circumference. A suitable function for Δv is

$$\Delta v=\Delta v_m-(\Delta v_w+\Delta v_m)(r/r_0)^{2n}, \quad (27)$$

where Δv_w is the maximum velocity departure near the wall. The parameter, n, determines the extent of the flat portion of the velocity profile and for large values of this parameter the profile

flat over the major portion of the cross section, as illustrated in figure 4.

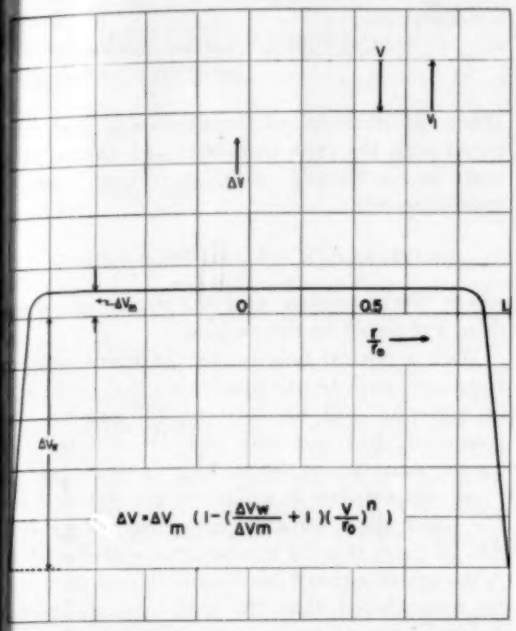

FIGURE 4.—*Packed tube with symmetrical wall channeling.*

Equation 27 must satisfy the condition for average balance,

$$\int_0^{r_0} (\Delta v) 2\pi r dr = 0,$$

from which it is found that

$$n = \Delta v_w / \Delta v_m.$$

From eq 22, neglecting the $\overline{D}_2/V_a$ term, it is found that

$$h = (\Delta v_m^2 r_0^2 / 2 V_a \overline{D}_1)[1/4 - 1/(n+2) + 1/4(n+1)], \quad (28)$$

and for those cases in which the wall velocity departure is 10 or more times the departure in the packing, this becomes

$$h = 0.1(\Delta v_m r_0 / V_a)^2 V_a / \overline{D}_1. \quad (29)$$

In terms of the channel thickness, d, this can be written

$$h = 0.1(\Delta v_m d / V_a)^2 V_a / \overline{D}_1. \quad (29a)$$

It is seen from eq 29 that the values of h will be about five times those for case *III* for the same values of Δv_m, thus showing the adverse effect of abrupt as compared with gradual departure from point balance. A symmetrical wall channeling sufficient to cause a velocity departure in the packing of 10 percent will lead to a value of h of 0.12 cm for a 1.0-cm inside diameter tube operating with an applied voltage gradient of 10 v/cm.

From eq 29a it is seen that if the thickness of the wall channel is the same, the h for various tube sizes will remain the same. This is because the wall-velocity departure for a given head depends only on the channel thickness.

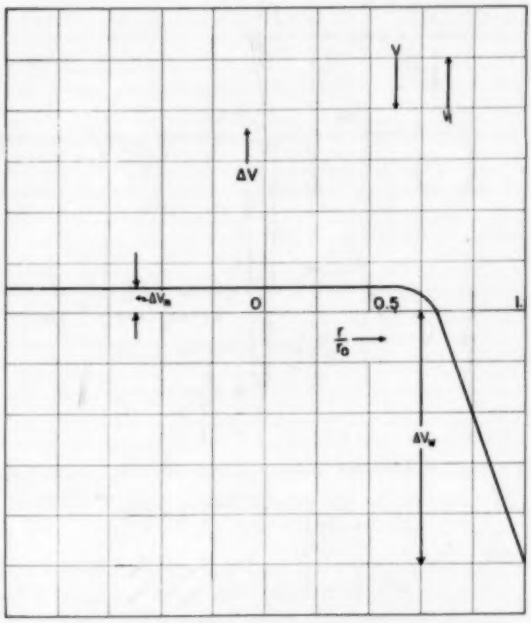

FIGURE 5.—*Packed tube—unsymmetrical wall channeling.*

Although a rigorous treatment cannot be given for cases involving unsymmetrical channeling, such as illustrated in figure 5, it can be stated that for the same Δv_m the value of h will be much higher than in the symmetrical case. Thus, in the general case, h varies as the square of the average diffusion distance between the channel and the interior of the packing and inversely as the lateral diffusion area between the channel and the packing. Hence, a wall channel due to a localized breakthrough may easily result in such

a large h that isotope separation for a 10-cm length of packing will be inappreciable.

Case V. Core Channeling.—Assume the formation of a single narrow round channel of radius r_1 and coaxial with the packed tube. The profile of the velocity departure will be parabolic in the channel and essentially uniform in the surrounding packing, as illustrated in figure 6. Hence

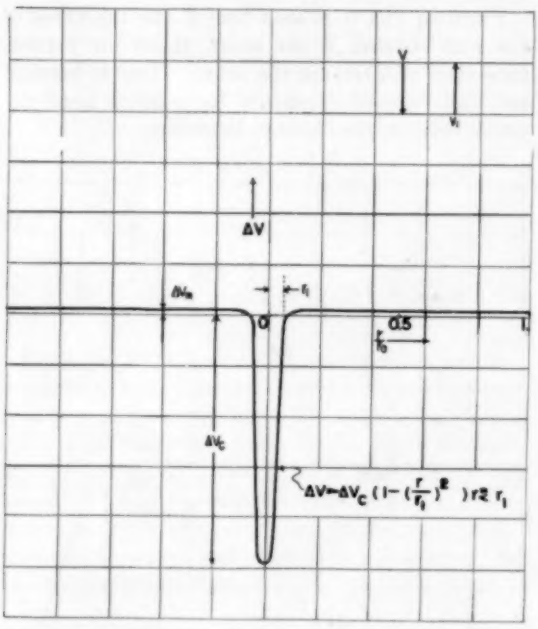

FIGURE 6.—*Packed tube—symmetrical core channeling.*

$$\Delta v = -\Delta v_c[1-(r/r_1)^2],\ 0<r<r_1$$

and

$$\Delta v = \Delta v_m,\ r_1<r<r_0.$$

As an over-all balance is maintained,

$$\int_r^{r_0}(\Delta v)rdr = -\int_0^r(\Delta v)rdr,$$

and therefore eq 22, neglecting the $\overline{D}_2/V_a$ term, and assuming uniform lateral diffusivity, can be put in the form

$$h=(2/\overline{D}_1V_ar_0^2)\left\{\int_{r_1}^{r_0}\left[-\int_r^{r_0}(\Delta v)rdr\right]^2dr/r+\int_0^{r_1}\left[\int_0^r(\Delta v)rdr\right]^2dr/r\right\}.$$

This is integrated after substitution of the above expressions for Δv, and the result is

$$h=(2/\overline{D}_1V_ar_0^2)\{(\Delta v_m^2r_0^4/4)[\ln r_0/r_1-3/4+(r_1/r_0)^2-(r_1/r_0)^4/4]+(19/768)\Delta v_c^2r_1^4\}$$

When the diameter of the channel is small compared with the tube diameter, such that $r_a>10$ and $\Delta v_cr=2\Delta vmr_0^2$, this expression becomes approximately,

$$h=0.5(\Delta v_mr_0/V_a)^2(V_a/\overline{D}_1)(\ln r_0/r_1-0.7),\quad (30)$$

where the velocities and diffusivity are superficial and apply to the packing.

With a central hole having an inside diameter from one-tenth to one-hundredth that of the tube, $\ln r_0/r_1-0.7$ will lie between 1.6 and 3.9. On comparing this case with case *IV*, it is seen that for the same Δv_m in the packing, meaning that the total channel flow in milliliters per second is also the same, the h for axial core channeling is from 8 to 20 times that for symmetrical wall channeling. Although this result may seem surprising, it is to be remembered that the axial channel presents far less area to the packing through which the compensating effect of cross diffusion can occur.

From Poiseuille's law, the mean liquid velocity in the channel relative to the mean liquid velocity in the average pore within the packing is proportional to $(r_1/r_p)^2$, where r_p is the equivalent pore radius. Hence, for a bead packing with 38 percent of void space,

$$\frac{V_a+\Delta v_c/2}{V_a/.38-\Delta v_m}=(r_1/r_p)^2,$$

or, approximately,

$$\Delta v_c/2V_a=(\Delta v_m/V_a)\ (r_o/r_1)^2=2.63(r_1/r_p)^2-1,$$

when $\Delta V_m/V_a<0.1$.

The equivalent pore radius for a bead packing has been determined experimentally to be 0.165 bead diameter [2].

Table 3 gives the values of h computed from eq 30 for a 2-cm inside diameter tube packed with beads of 100-mesh per inch, $r_p=0.0042$ cm, assuming 1.0 KCl at 18° C and a voltage gradient of 10 v/cm. For these conditions, $V_a=0.0049$ cm/sec and $\overline{D}_1=1.55\times10^{-5}$ cm²/sec.

TABLE 3.—*Core channeling in 2-cm inside diameter tube, 100-mesh beads, 10 v/cm*

Core channel radius / Equivalent pore radius r_1/r_p	Core channel radius, r_1	h
	cm	*cm*
4	0.0168	0.068
6	.0252	1.6
8	.0336	15
10	.0420	92

Table 3 shows that when a single continuous core channel has reached a size about five times the mean pore size of the packing, the resultant h will be about 1.0 cm. In such a case isotope separation between ends of a 10-cm length of tube would be negligible. This result assumes, however, that the radial diffusion coefficient has the value indicated, this being the minimum value corresponding to molecular diffusion. Actually, when the tube is set horizontally, $\overline{D}_1$ will have a much larger effective value than assumed because of thermal convections in planes normal to the axis. Hence, the values of h in table 3 should be regarded as maximum. They show merely that very poor results can be due to a single relatively small core channel. It is for this reason that bead packings should be held under pressure.

Case VI. Face-Cooled Diaphragm, Non Uniform Porosity.—The diaphragm of uniform porosity was considered under case *II*. When the diaphragm is not uniformly porous, various regions can be found in which the porosity is above or below a mean porosity. Two factors of equal importance determine the performance of the packing, the first being the magnitude of the velocity departure due to the porosity departure; the second is the lateral distance across the face of the diaphragm between a velocity crest and a velocity trough.

The general case does not permit a rigorous treatment. However, the order of magnitude of h can be gotten by assuming an equivalent diaphragm in which the regions of porosity departure are parallel, the mean velocity departure and the mean crest-trough spacing of the actual case and the equivalent case being the same.

The profile of the equivalent case is shown in figure 7 and is expressed analytically by

$$\Delta v = -\Delta v_m \cos(\pi x/a).$$

Equation 22a is applicable. As lateral diffusion vanishes at limits a and 0, as indicated in figure 5, the integration should be made between these limits. The result is

$$h = 0.0505(\Delta v_m a/V_a)^2 V_a/\overline{D}_1 + \overline{D}_2/V_a, \qquad (31)$$

this being the h for each symmetrical pair of strips, and therefore the h for the entire diaphragm.

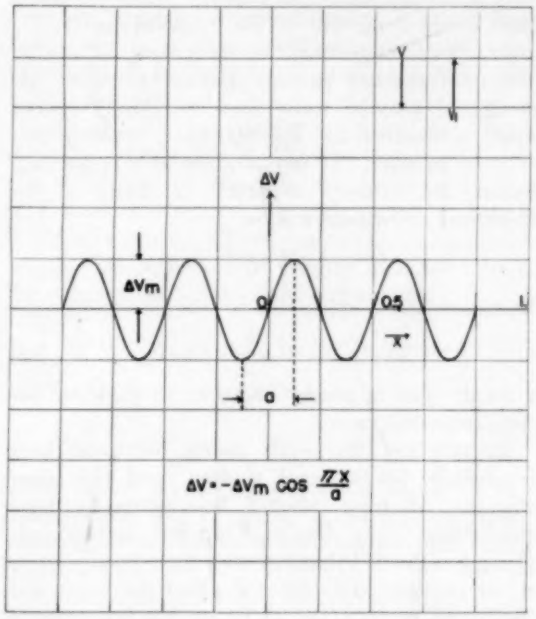

FIGURE 7.—*Profile of a diaphragm with variable porosity.*

From this result it is apparent that small values of h can be achieved only when the product, (velocity departure) times (crest-trough spacing), is small.

Consider two diaphragms wherein the velocity departures are 10 percent of V_a in one and 2 percent of V_a in the other. Assume a voltage gradient for each of 10 v/cm at 18° C, so that $V_a/\overline{D}_1 = 322$ and $\overline{D}_2/V_a = 0.0031$ for 1.0 N KCl solution. The resulting values of h are given in table 4 for various crest-trough spacings, a.

From the results in table 4 it can be seen that a nonideal diaphragm will enable appreciable isotope separation even though the centers of the regions of porosity departure are laterally a fraction of a centimeter apart, but, if several centimeters apart,

TABLE 4.—*Diaphragms with variations in porosity, 10 v/cm*

$\delta\epsilon_m/V_a$	a	h	$\delta\epsilon_m/V_a$	a	h
	cm	cm		cm	cm
0.10	0.5	0.044	0.02	0.5	0.0047
.10	1.0	.17	.02	1.0	.0096
.10	2.0	.65	.02	2.0	.029
.....	.....	.....	.02	4.0	.12
.....	.....	.....	.02	8.0	.48

only when the maximum velocity departure is less than about 2 percent of the countervelocity, V_a.

Case VII. Isothermal Capillary Film.—Consider the unobstructed passage formed between two elongated parallel walls that are closely spaced apart a distance $2w$, are extremely smooth, and strictly parallel. If temperature effects be neglected, the velocity departure in terms of the thickness coordinate will be

$$\Delta v = (V_a/2)[3(x/w)^2 - 1].$$

Equation 22a is applicable to this case and gives

$$h = (2/105)V_a w^2/D + D/V_a, \qquad (32)$$

a result that is nearly identical to that for the capillary tube, case *I*.

In practice, the walls should be good heat conductors for external cooling, and the inner surfaces, at least, should be electrically nonconductive. The film will run hot at the midplane, but the fact that viscosity times conductance is not precisely constant will affect the numerical coefficient in equation 32 by only a few percent and can be disregarded. Calculations for h can be based on values of V_a and D at 18° C.

Thermal convection can be used to advantage to avoid a breadthwise velocity departure by arranging the walls so that length is horizontal and breadth vertical. A value of h calculated as in case *III* should be added to eq 32 when a breadthwise departure is present. The effective diffusion coefficient breadthwise can be found from eq 12 and 22a.

In a second arrangement the film can be confined by vertical concentric cylinders. In this case, one of the cylinders should be rotated to avoid circumferential variations in composition and temperature. By proper selection of spacing the profile would be analogous to figure 2, the theory permitting lower values of h than indicated by eq 32.

IV. Production Conditions

Economical production of enriched materi depends primarily on the values of ϵ and h di cussed in sections II and III of RP1765 [2]. Th larger the ϵ and the smaller the h, the lesser wi be the power requirement per unit rate of pro duction. In general, the method is applicable though not necessarily more economical tha other methods, when ϵ exceeds unity by as littl as 0.1 percent and when h is less than 0.1 cm In the following discussion a specific example wi be worked through for $\epsilon = 1.0030$ and $h = 0.020$ cm.

The simplest procedure for continuous produc tion is to maintain constant anode composition b exchange with an unlimited supply of normal K After a build-up period, material enriched in ^{39}K can then be very slowly bled from the cathode. Another procedure, analogous to continuous frac tional distillation, is to feed normal material to a point intermediate to the ends and to withdraw from both anode and cathode compartments. In this case the apparatus provides a stripping sec tion yielding material at the anode enriched in ^{41}K. The enriching section for ^{39}K may be treated as though an anode were located at the point of feed and is thus equivalent to the first procedure. The following treatment will be focused on the ^{39}K enrichment.

1. Build-up Period

In bringing the cathode to the desired enrich ment, the procedure is to operate at zero sampling rate (total reflux) while maintaining at the cathode end an exact balance between counterflow of solu tion and K ion migration. Other factors remain ing constant, it follows that the countervelocity must slightly increase as the enrichment increases; thus the maximum fractional increase in going from normal abundance to 100 percent ^{39}K would be $(\epsilon - 1)/15.2$, which is the difference between the mean ion velocity of normal K and the ion velocity of pure ^{39}K. This increase is well within the limits of the control and of no actual importance. However, assuming a uniform normality and a precise balance at the cathode, it follows that the countervelocity will be too high at the anode end by the same fraction. The result is a slight wash ling out of salt, the voltage gradient increasing slightly toward the anode, and the tube thus balances itself throughout. More important is

the tendency of increased temperature to increase gas speed and destroy the balance, but here also the balance throughout the tube is restored by a change in normality of salt and voltage gradient. Hence it is strictly correct to suppose an exact mean balance for all sections of the tube, but it is not correct to assume uniform normality of salt except when temperature effects at the ends of the tube may be neglected.

The velocity balance at any section requires $v_1+v_2c_2=V_a(c_1+c_2)$ or $v_1-V_a=(v_1-v_2)c_2/(c_1+c_2)$. The net transport of light isotope across any section is $(v_1-V_a)c_1-D'\partial c_1/\partial z$ or $(v_1-v_2)c_1c_2/(c_1+c_2)-D'\partial c_1/\partial z$ mole cm^{-2} sec^{-1}. Each factor in the foregoing is an average for the cross section, distant z from the anode.

The exact differential equation governing the total reflux build-up of concentration as a function of time and distance, and applying to a tube having nonuniform temperatures lengthwise, is

$$\frac{\partial(D'\partial c_1/\partial z)}{\partial z^2}-\frac{\partial(v_1-v_2)c_1c_2/(c_1+c_2)}{\partial z}=\partial c_1/\partial t. \quad (33)$$

In a very long packed tube it would be permissible to neglect temperature nonuniformities at the ends. In this case the effective diffusivity, D', the difference in the velocity of the ionic isotopes, v_1-v_2, and total concentration, c_1+c_2, can be considered invariant. Equation 33 in terms of mole fractions then takes the form

$$\partial^2N_1/\partial z^2-\frac{\epsilon-1}{h}\partial N_1N_2/\partial z=\frac{1}{D'}\partial N_1/\partial t, \quad (34)$$

which involves the close approximation $h=D'/V_a\cong D'/v_2$.

Attempts to obtain an exact solution of eq 34 in order to obtain the dependence of N_1 on distance at the time the cathode has reached a desired enrichment have not been successful. This solution is necessary to obtain the exact preliminary holdup of ^{39}K and the exact time at which production can be commenced. However, as it would apply only to a long tube, and since relatively short tubes or diaphragms are ample for ^{39}K concentration, this failure is of secondary importance to the present problem.

Returning to eq 33, which applies to a short tube, integration over the equivalent length V_c/A of the cathode volume gives

$$\partial c_1/\partial z=(v_1-v_2)c_1c_2/D'(c_1+c_2)-(V_c/AD')\partial c_1/\partial t, z=l, \quad (35)$$

showing that the concentration gradient at the front of the cathode volume is less than its maximum possible value at the concentrations by the amount $(V_c/AD')\partial c_1/\partial t$. This fact will be considered in the subsequent approximation for the build-up time of a short packed tube.

2. Production Equilibrium

When the cathode reaches the desired enrichment, withdrawal is begun at such a rate as to maintain the enrichment constant. Thereafter, the concentration distribution along the tube undergoes a further change until a steady distribution is reached.

Let ΔV_a be the departure from the "total reflux" countervelocity, V_a, this departure being due to continuous sampling at the cathode at a rate holding the cathode enrichment constant. When a steady distribution is reached a transport balance taken across the tube at distance z from the anode gives for the light component

$$(v_1-V_a+\Delta V_a)c_1-D'dc_1/dz=\Delta V_ac_{1-cath}, \quad (36)$$

and for the heavy component,

$$(v_1-V_a+\Delta V_a)c_2-D'dc_2/dz=\Delta V_ac_{2-cath}, \quad (36a)$$

where the c's and D' refer to mean values for the cross section, and c_{1-cath}, c_{2-cath} refer to the moles per cubic centimeter of the two components in the product.

Equation 36 is divided by c_1 and eq 36a by c_2, the latter is subtracted from the former, and the terms arranged to give

$$dz=\frac{D'(dc_1/c_1-dc_2/c_2)c_1c_2}{c_1c_2(v_1-v_2)-\Delta V_a(c_2c_{1-cath}-c_1c_{2-cath})}. \quad (37)$$

To proceed further, the approximation that temperature does not depend on z is assumed. The normality of salt is invariant and eq 37 can be written in terms of mole fractions as

$$dz=\frac{RhdN_1}{-R(\epsilon-1)N_1^2+[R(\epsilon-1)+1]N_1-N_{1-cath}}, \quad (38)$$

where $v_1-v_2=v_2(\epsilon-1)\cong V_a(\epsilon-1)$, $h=D'V_a\cong D'/v_2$, and $R=V_a/\Delta V_a\cong v_2/\Delta V_a$. The integral of eq 38 is had by a well-known formula. The result is

$$z=\frac{hR}{\sqrt{q}}\ln\left[\frac{2aN_1+b-\sqrt{q}}{2aN_1+b+\sqrt{q}}\cdot\frac{2aN_{1-anode}+b+\sqrt{q}}{2aN_{1-anode}+b-\sqrt{q}}\right], \quad (39)$$

where $a=-R(\epsilon-1)$, $b=R(\epsilon-1)+1$, $c=-N_{1-cath}$, and $q=b^2-4ac$. Equation 39 gives the relation between distance from anode, z, and mole fraction light, N_1, when the distribution has reached a steady state after prolonged production at reflux ratio, R.

Example.—Consider the production of material having an abundance ratio greater than normal by 50 percent; $^{39}K/^{41}K=N_1/N_2=21.3$ at the cathode. Provided sufficient quantities can be produced, this enrichment would suffice for many purposes such as experiments for tracing potassium metabolism. It is desired to know (1) the length of packing and reflux ratio for maximum efficiency, (2) the efficiency of the yield in grams of total enriched potassium per kilowatt-hour, (3) the required build-up time under total reflux operation.

The case chosen is for a bead-packed tube, 1 cm inside diameter with anode abundance maintained normal at 14.2. The cathode volume, V_c is 1.0 ml, and the equivalent length of cathode volume based on a packing of 38 percent voids is 3.35 cm. The solution is taken as 1.0 N KCl. The temperature, normality, and voltage gradient will be assumed invariant with distance for purposes of this approximate calculation. The applied voltage is chosen to be 10 v/cm; the current is 0.50 amp and the input is 5.0 w/cm (a higher input would result in boiling).

The value of ϵ, based on the consideration of section II of RP1765 [2], together with experimental data reported in other papers of this series, is assumed to be 1.003. This is a conservative value.

The value of h is taken to be 0.020 cm, a value which appears conservative for the optimum conditions of operation discussed under case *III* of section III.

Equation 39, with the above values of ϵ and h, is shown plotted in figure 8, for various values of R and corresponding lengths of packing, l. The Rl versus l curve is also shown.

As seen in figure 8, the minimum packing length, l, required to give the assumed enrichment is 2.7 cm, under total reflux equilibrium, i. e., $R=\infty$ and $t=\infty$. The required reflux ratio for a packing of infinite length is 114.

The power requirement is proportional to length of packing whereas the production in grams of enriched material per unit time is proportional to $1/R$. Hence, maximum efficiency is had when Rl is a minimum. The Rl versus l curve of figure 6 shows a fairly broad minimum at about 4.6 cm for which $R=170$; these are the values of packing length and reflux ratio which will give the most efficient yield although the curve shows that considerable latitude is permissible in the direction of greater packing length and lower reflux ratio.

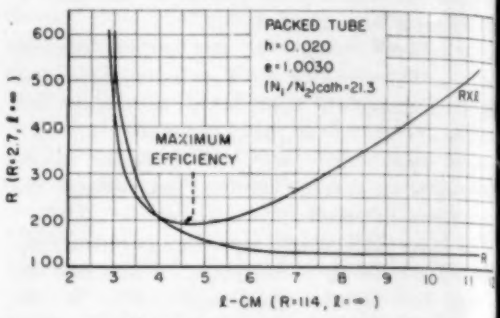

FIGURE 8.—*Relation between reflux ratio, R, and length of packing, l, for fixed cathode enrichment.*

The total potassium arriving at the cathode when counterflow is zero is I^+/F moles/sec, where I^+ is the total current times the transport number; the latter in this case is close to 0.50. At reflux ratio R, the production is $(I^+/FR$ moles/sec. For the present example the yield is

$$\text{yield}=\frac{0.50\times0.50}{96{,}500\times170}=1.5\times10^{-6}\text{ mole of 21.3 K/sec}=5.5\times10^{-5}\text{ mole of 21.3 K/hr.}$$

The power input to the 4.6 cm-packing is $4.6\times5=23$ w. By allowing 7 w for electrode losses, the power, exclusive of that for the control equipment, is about 0.030 kw. Hence

$$\text{yield efficiency}=5.5\times10^{-5}/0.030=1.8\times10^{-3}$$

mole of 21.3 K/kwhr $=7.2\times10^{-2}$ g of 21.3 K/kwhr. The corresponding energy requirement is 14 kwhr/g of 21.3 K. The energy charges against the production are thus seen to be quite nominal.

The solid curve, 1, of figure 9 shows the abundance ratio vs distance from the anode, z, as related by equation 39. This is the production equilibrium. Curve 2 is a rough sketch of the solution of eq 33 at the time the cathode reaches the production enrichment; this curve has a slope at $z=l$ that is less than curve 1, as was seen in eq 35. As at the time of curve 2 the build-up is still

diffusing toward the anode and is less near the anode than for curve 1, it follows that curve 2 must cross curve 1.

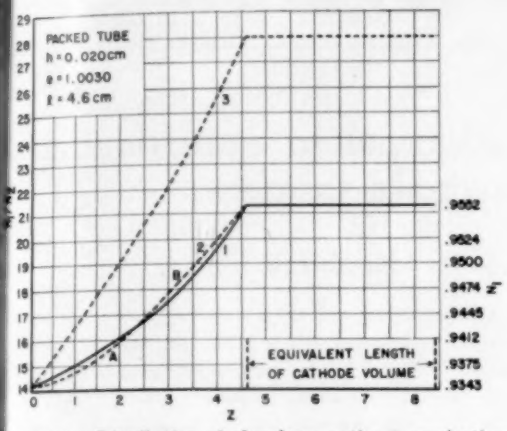

FIGURE 9.—*Distribution of abundance ratio: 1, production equilibrium; ($R=170$, $t=\infty$); 2, end of build-up timer; ($R=\infty$, $t=13$ hr); 3, total reflux equilibrium; ($R=\infty$, $t=\infty$).*

The difference between areas A and B of figure 9 represents the hold-up of ^{39}K yet to be accumulated in the packing after the production has begun. This difference is negligible in the present case because of the relatively large hold-up at the cathode. In consequence, the approximate hold-up for both curves 1 and 2 is given closely by graphical integration under curve 1. This procedure gives: hold-up of packing plus cathode volume equals 2.2×10^{-5} mole of ^{39}K in excess of normal abundance.

As the concentration gradient at the anode remains zero for a large part of the build-up time, it is a good approximation to assume the hold-up of ^{39}K to have been transported at the maximum rate $I^+ (N_1N_2)_{anode} (\epsilon-1)/F$ moles ^{39}K/sec, from the anode into the packing. This rate is in accordance with eq 9 of section 1 of RP1765 [2] and gives for the present example, 0.5×0.5 $(14.2/15.2)$ $(1/15.2)\times0.003/96{,}500 = 4.8\times10^{-10}$ mole ^{39}K/sec. Hence total-reflux build-up time

$$= 2.2\times10^{-5}/4.8\times10^{-10}$$
$$= 4.6\times10^{4} \text{ sec.}$$
$$= 13 \text{ hr.}$$

V. References

[1] A. Keith Brewer, S. L. Madorsky, and J. W. Westhaver, Science **104,** 156 (1946).

[2] A. Keith Brewer, S. L. Madorsky, etal., The concentration of isotopes of potassium by the counter-current electromigration method, J. Research NBS **38,** 137 (1947) RP1765.

[3] J. A. V. Butler, Electrocapillarity, p. 98 (Chemical Publishing Co., New York, N. Y., 1940).

[4] Int. Critical Tables **6,** 234 and 310 (1929).

[5] Int. Critical Tables **5,** 68 (1929).

[6] R. E. Powell, W. E. Roseveare, and H. Eyring, Ind. Eng. Chem. **33,** 430 (1941).

WASHINGTON, July 29, 1946.

72707—47—4

U. S. Department of Commerce
National Bureau of Standards

Research Paper RP1767
Volume 38, February 1947

Part of the Journal of Research of the National Bureau of Standards

Concentration of Isotopes of Chlorine by the Countercurrent Electromigration Method[1]

By Samuel L. Madorsky and Sidney Straus

The isotope ^{35}Cl was concentrated in the anode compartment of an electromigration cell, with NaCl as the electrolyte. The operation was regulated by means of a stationary boundary between solutions of NaOH and NaCl as the lower and upper liquids, respectively. A concentration of ^{35}Cl from the normal value of 75.76 percent to a maximum value of 80.7 percent was obtained in 474 hours. The maximum initial separation coefficient, $\epsilon-1$, was 0.207×10^{-2}.

I. Introduction

Kendall and Crittenden [1][2] attempted to separate the isotopes of chlorine by the ionic-migration method. They transported chlorine ions in a tube filled with agar-agar through a distance of 100 feet by means of a moving boundary. An atomic-weight determination of chlorine in the forward section of the gel failed to detect any change in the isotope ratio. More recently, a new method [2] based on the principle of countercurrent electromigration, has been developed at the National Bureau of Standards for the separation of isotopes. The successful application of this method to the concentration of ^{39}K and ^{41}K [3] from solutions of K_2SO_4 and KCl suggested the possibility of concentrating the isotopes of chlorine by this method. The present paper describes some experiments designed to concentrate ^{35}Cl from a solution of NaCl.

II. Outline of Problem

Chlorine appears in nature as a mixture of 75.4 percent ^{35}Cl and 24.6 percent ^{37}Cl [4]. In an electromigration cell $^{35}Cl-$ can be concentrated in the anode compartment, provided the original isotopic ratio is maintained in the cathode compartment. However, if the chloride ion is allowed to react at the anode to form chlorine gas, it will escape. This reaction was prevented by interposing a solution of sodium hydroxide around the anode to form a boundary between the chloride and hydroxide solutions.

Sodium chloride in the ratio $NaCl:H_2O=1:30$ was used as the electrolyte. As the transport numbers of Na^+ and Cl^- are approximately 0.40 and 0.60, respectively, the anode restituent was 1:18 NaOH, whereas the cathode restituent was 1:12 HCl. Characteristic properties of the solutions employed are shown in table 1. As seen from this table, 1:18 NaOH has a greater density than 1:30 NaCl, and, therefore, the alkali solution should be the lower layer, and the salt solution should be the upper layer at the anode boundary. Such an arrangment is shown in the gooseneck-shaped anode compartment in figure 1.

TABLE 1.—*Solutions employed in the chlorine electromigration experiments*

Solute	Ratio solute·H_2O	Concentration	Density at 25° C	Normality
		Percent		
NaCl	1:30	9.76	1.067	1.782
NaOH	1:18	10.98	1.118	3.067
HCl	1:12	14.43	1.068	4.225

[1] This paper will appear in volume 6, division III, of the Manhattan Project Technical Series.
[2] Figures in bracket indicate the literature references at the end of this paper.

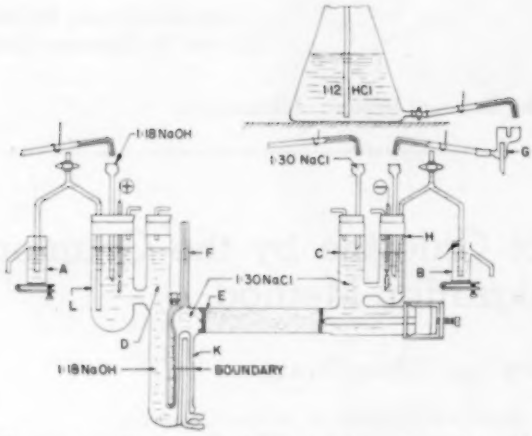

FIGURE 1.—*Diagram of electromigration cell used in the chlorine experiments.*

III. Apparatus and Experimental Procedure

The apparatus is shown diagrammatically in figure 1 and photographically in figure 2. The packing was 2 cm in diameter and 10 cm long. It consisted of No. 107 ballotini glass beads in experiment 1 and of 60- to 100-mesh Ottawa sand in the other experiments. The packing supports

FIGURE 2.—*Electromigration cell assembly showing dropper and constant level devices.*

were No. 40 bead frits. At the anode end t
frit was held in place by means of a sealed-in gl
cross, and at the cathode end it was supported
means of a screw and a glass rod passing throu
a rubber stopper. In experiments 2 and 3, fri
similar to those at the ends of the packed colu
were also placed in the packing at intervals
about 3 cm in order to impart greater rigidity
the compressed sand. The wall thickness of t
packed tube was 1 mm. The electrode secti
were supplied with manually controlled droppe
siphons, and manually controlled overflow cu
(*A* and *B*, fig. 1). The cathode was of the flush
type receiving 1:30 NaCl solution in addition to
stoichiometric amount of 1:12 HCl. The ele
trodes were made of platinum gauze, about
cm^2 in area.

The boundary was maintained between 1:
NaCl and 1:18 NaOH as the upper and low
liquids, respectively, in an annular space, *K*, b
tween the outer tube and the inside cooler,
shown in figure 1. The boundary ring had an i
side diameter of 13 mm, was 1.5 mm wide, a
had a total area of 0.6 cm^2. The anode volum
i. e., the volume of liquid between the boundar
and the packing, was about 10 ml. The boundar
is shown in figure 3. Pertinent data of all t
experiments are shown in table 2.

TABLE 2.—*Experimental details and results*

Experiment No.	Packing	Potential	Anode volume	Initial (e−1/x
		amp	*ml*	
1	100-mesh ballotini glass beads, with no intermediate frits.	0.430	10.4	0.1
2	60- to 100-mesh sand, 3 intermediate frits.	.430	10.4	.2
3	do	.430	11.0	.9
4	60- to 100-mesh sand, no intermediate frits	.500	11.0	.2
5	do	.500	11.0	.9

In filling the cell, 1:18 NaOH solution was firs
poured into the anode compartment to the lev
where the boundary was expected. Sodium chlo
ide solution (1:30) was then poured into th
cathode compartment and allowed to seep through
the packing into the anode volume space *E* (fig. 1).
Further additions of NaOH solution kept th
junction between the two liquids in the neighbor
hood where the boundary was desired. After th
cell was filled to the proper levels, the curren
was turned on and the addition of restituents

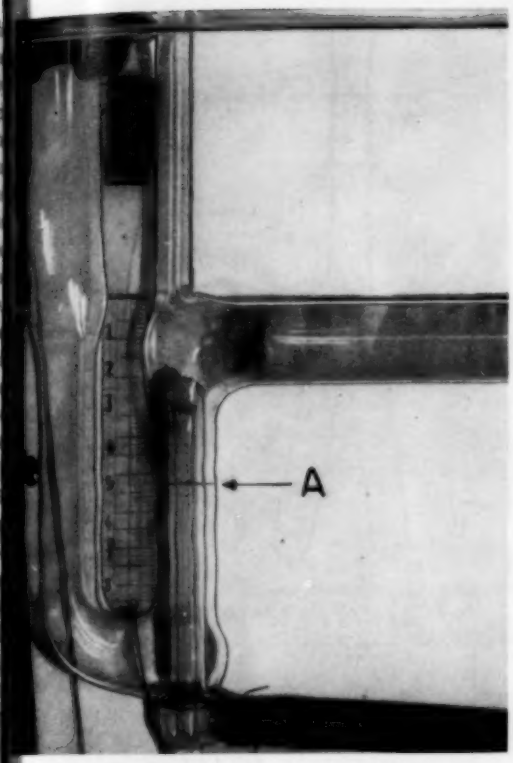

FIGURE 3.—*Details of cathode compartment.*
A, Boundary.

arted. A sharp boundary appeared within a w minutes.

The current in all the experiments was about .5 amp and the voltage between the electrodes bout 80.

The operation was continuous, requiring little ttention. In the daytime, drop rates were adusted two to three times, while during nights the ells were left without attention. Fluctuations of he boundary level during off-duty periods were enerally within 1 cm, but occasionally it would each a maximum of 2 cm. As the cross section f the annular space, *K* (fig. 1), was 0.6 cm², a - to 2-cm variation of the boundary level corresponded to about 5 to 10 percent in anode volume, %. Variations of drop rates were chiefly caused y changes in room temperature.

The chlorine electromigration cells seemed to e more sensitive to the pH condition of the athode, i. e., to the rate of addition of HCl than o the rate of addition of NaOH or NaCl. In order to control the acid rate more closely, it was first fed into a constant overflow cup, *G* (fig. 1), and from there into the cathode compartment *H* through manually controlled droppers. The cells operated best when the cathode overflow from *B* was slightly acid, as was indicated by methyl red introduced with the HCl restituent. The stoichiometric amounts of HCl and NaOH solutions required per ampere hour are 9.4276 and 13.5902 g, respectively. The actual amount of HCl added was slightly in excess of that required theoretically. For NaOH an excess of about 20 g per ampere hour was used. This excess was bypassed through a siphon, as shown in figure 1. The amount of cathode flushing restituent, NaCl, added was 24 g per ampere hour. The cells under normal operation ran slightly alkaline above the boundary and through the packing column, as was indicated by methyl red fed into the anode with the NaOH restituent.

As a check on the operation of the cells, analyses of the anode and cathode overflow liquids, as well as of samples drawn from various parts of the cell, were made at intervals. Overflow liquid from *A* (fig. 1) and samples drawn from *D* were analyzed for NaOH. Overflow liquid from *B* was analyzed for NaCl and HCl, and samples drawn from *C* were analyzed for NaCl and NaOH. No chlorine was found either in cup *D* or in the anode overflow

TABLE 3.—*Analysis of cell and overflow liquids in experiments 2 and 3*

Hours after start	Overflow from *A*, NaOH	Liquid from cup *D*, NaOH	Overflow from *B*		Liquid in cup *C*	
			NaCl	HCl	NaCl	NaOH
EXPERIMENT 2						
	%	%	%	%	%	%
0	10.95	10.95	9.76	0	9.76	0
65	10.15	.....	9.93	.21	10.87	.24
137	9.34	10.58	.....	.....	.....	.....
209	10.24	.....	10.02	.40	10.91	.23
305	10.30	.....	10.05	.30	10.86	.22
411	10.09	.....	9.94	.43	10.88	.22
EXPERIMENT 3						
0	10.95	10.95	9.76	0	9.76	0
69	10.88	.....	9.77	.93	9.76	.52
93	10.55	10.64	.....	.....	.....	.....
237	10.57	.....	9.87	.25	10.43	.22
309	10.39	.....	9.75	.48	10.31	.20
405	10.31	.....	9.79	.32	10.25	23
501	10.53	.....	9.99	.17	.....	.....

liquid. As an illustration, analyses for experiments 2 and 3 are shown in table 3.

As seen from this table, there was little change in the composition of the liquids in the cells during operation.

IV. Mass-Spectrometer Analysis And Interpretation of Resulrs

A sample of liquid weighing about 0.2 g was drawn from the anode volume, E, by inserting a capillary through a small tube, F (fig. 1). In preparing the sample for analysis in the mass spectrometer, it was placed through A in leg B of the specially designed sampler shown in figure 4 and evaporated to dryness. About 0.3 to .05 ml of concentrated H_2SO_4 was then placed in leg C of this sampler, the latter connected to a vacuum system through ground-glass joint E, and highly evacuated. Stopcock D was then closed and the sampler removed from the vacuum system. Before attaching the sampler to the mass spectrometer by means of E, it was tilted so as to allow the H_2SO_4 to flow from leg C into leg B. The HCl formed in the reaction between NaCl and H_2SO_4 was then analyzed for the isotopes of chlorine. The analyses were carried out in a Consolidated mass spectrometer.

Concentration of ^{35}Cl in ordinary chlorine was measured in five samples of chemically pure NaCl as follows:

Analysis No.	^{35}Cl
	Percent
1	75.74
2	75.73
3	75.79
4	75.74
5	75.79
Average	75.76

From the above ratio, $R_0=N_1/N_2=^{35}Cl/=3.12$

The results are shown in table 4 in terms of percentage of ^{35}Cl, ratio $R_t=N_1/N_2$ at time t and separation factor R_t/R_0. Figure 5 shows concentration of ^{35}Cl plotted against time in hours.

The separation coefficient, ϵ, was calculated by means of eq 10 of RP1765 [3].

$$\frac{I^- t(\epsilon-1)N_1N_2}{F}=\frac{V_e C}{1{,}000}\times\frac{R_t-R_o}{(R_t+1)(R_o+1)},$$

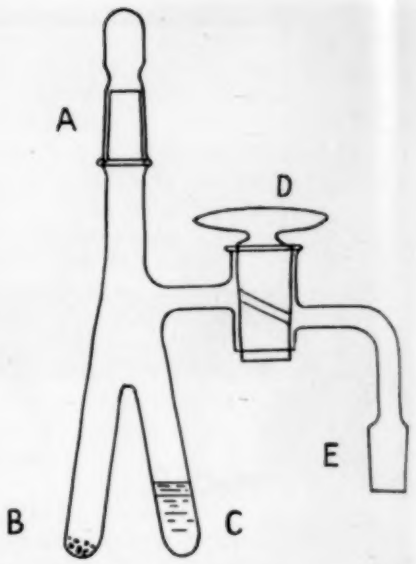

FIGURE 4.—*Sample tube used in mass-spectrometer analysis of ratio of chlorine isotopes.*

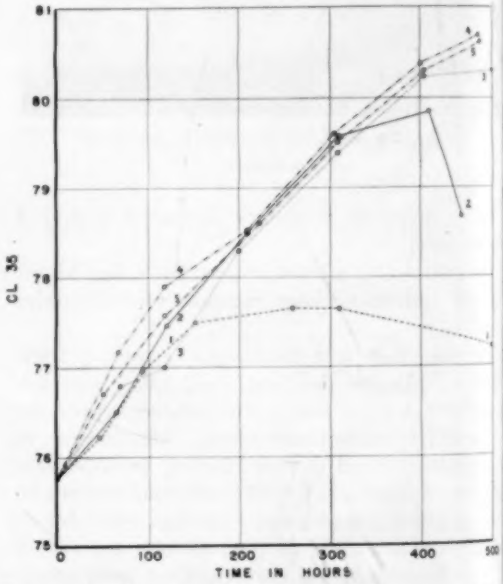

FIGURE 5.—*Curves showing increase in percentage of ^{35}Cl with time in five similar experiments.*

where

I^- = negative current = total current I times chlorine transport number T_{Cl}, which in this case is 0.6

t = time in seconds

V_a = anode volume
C = normality of NaCl solution = 1.782
F = Faraday constant.

The above equation can be written in the following simplified form:

$$\epsilon - 1 = 0.03543 \frac{V_a C}{I t_1} \times \frac{R_{t_1} - 3.12}{R_{t_1} + 1},$$

where t_1 is time in hours. The values for $\epsilon - 1$ are shown in the last column of table 4.

TABLE 4.—*Concentration of* ^{35}Cl *and separation coefficient*

Experiment No.	Hours after start	^{35}Cl	$R_t = {}^{35}Cl/{}^{37}Cl$	Separation factor, R_t/R_0	$(\epsilon-1)\times 10^2$
		Percent			
	0	75.76	3.12	1.000	
	46	76.22	3.21	1.029	0.115
	92.5	76.96	3.34	1.071	.136
	152	77.50	3.44	1.103	.117
	259	77.65	3.47	1.112	.075
	312	77.64	3.48	1.115	.064
	499	77.21	3.39	1.087	.031
	65	76.50	3.26	1.045	0.128
	120	77.47	3.44	1.103	.152
	209	78.50	3.65	1.170	.138
	310.5	79.57	3.89	1.247	.128
	411	79.85	3.96	1.269	.104
	450	78.68	3.69	1.183	.068
	69	76.80	3.31	1.061	0.180
	117	77.00	3.35	1.074	.127
	200	78.30	3.61	1.157	.150
	309	79.39	3.85	1.234	.137
	405	80.23	4.06	1.301	.129
	501	80.31	4.08	1.308	.106
	66.5	77.17	3.38	1.083	0.207
	118	77.90	3.52	1.128	.174
	209	78.52	3.66	1.173	.128
	305	79.60	3.90	1.250	.121
	402	80.38	4.10	1.314	.111
	474	80.70	4.18	1.340	.100
	50	76.71	3.29	1.055	0.183
	118	77.58	3.46	1.109	.150
	222	78.61	3.68	1.180	.125
	309	79.51	3.88	1.244	.117
	405	80.30	4.08	1.308	.108
	477	80.63	4.16	1.333	.98

V. Conclusions

Glass-bead packing did not stand up well because of the alkaline nature of the anode, as seen from results of experiment 1. Sand, on the other hand, stood up well, as shown by the result of experiments 2 to 5, inclusive. Inserting fritted disks in the packing in experiments 3 and 4 did not seem to make any difference, as is evident by comparing the results of these experiments with those of experiments 4 and 5. Results of all the experiments (in case of experiment 1, up to 150 hr) are in good agreement. At about 400 hours, the curves (fig. 5) begin to drop. This is due to the accumulation at the anode end of the packing of silica gel resulting from the action of NaOH on the glass. A close examination of figure 3 shows a jelly-like mass in front of the anode end of the packing. The highest separation was obtained in experiment 4, where the concentration of ^{35}Cl changed from 75.76 to 80.70 percent, after 474 hours of operation, representing an increase of 4.94 percent.

The initial ϵ^{-1} for the first 50 to 70 hours varies from 0.0115 to 0.0207. There is in every case a tapering off of these values with time, due undoubtedly to the accumulation of ^{35}Cl in the packing caused by diffusion and fluctuation of the boundary.

The authors thank V. H. Dibeler and Dorothy Thompson for making the mass-spectrometer analyses reported in this paper.

VI. References

[1] James Kendall, Science **67,** 163 (1928).
[2] A. Keith Brewer, Samuel L. Madorsky, and James W. Westhaver, Science **104,** 156 (1946).
[3] A. Keith Brewer, S. L. Madorsky, et al., The concentration of isotopes of potassium by the countercurrent electromigration method, J. Research NBS **38,** 137 (1947) RP1765.
[4] Sixth Report of the Committee on Atoms of the International Union of Chemistry (1941–42).

WASHINGTON, August 5, 1946.

U. S. Department of Commerce
National Bureau of Standards

Research Paper RP1768
Volume 38, February 1947

Part of the Journal of Research of the National Bureau of Standards

Normal Coordinate Analysis of the Vibrational Frequencies of Ethylene, Propylene, *cis*-2-Butene, *trans*-2-Butene, and Isobutene[1]

By John E. Kilpatrick[2] and Kenneth S. Pitzer[3]

The secular equations for the vibrations of ethylene, propylene, *cis*-2-butene, *trans*-2-butene, and isobutene have been derived and have been factored to the greatest possible extent. A potential expression has been fitted to an assignment of vibrational frequencies for ethylene and deuteroethylene. Some of the constants so determined have been used in deriving approximate potential expressions for propylene, *cis*-2-butene, *trans*-2-butene, and isobutene. With the vibrational frequencies calculated from these potential expressions as a guide, frequency assignments have been made for propylene, *cis*-2-butene, *trans*-2-butene, and isobutene.

I. Introduction

This investigation was undertaken to obtain a reasonably complete understanding of the forces operating around an olefinic double bond, so that reliable statistical thermodynamic calculations could be made. The various force constants obtained will, of course, be of interest in other connections.

The number of internal degrees of freedom in the molecules of propylene, *cis*-2-butene, *trans*-2-butene, and isobutene is so large that a complete vibrational assignment from spectral data alone would be unreliable. The 1-butene molecule presents an even more difficult problem because of the complete lack of symmetry and the presence of an unbalanced rotation in the molecule.

A satisfactory assignment is available, however, for ethylene [1].[4] A potential expression was determined that would reproduce the vibrational frequencies of C_2H_4 and C_2D_4. These constants were used, either directly or with reasonable modifications, and with the addition of potential constants from other molecules, to calculate the vibrational frequencies of propylene and the three rigid-frame butenes (*cis*-, *trans*-, and *iso*).

The assignments of many, though of course not all, of the vibrational frequencies of these molecules were obvious from spectral data alone. The uncertain potential constants (involving structural relations not found in either ethylene or any of the simple paraffins) were adjusted to fit the definitely assigned frequencies. This procedure would not have been satisfactory had the problem not involved several molecules containing the same type of bonds.

II. Derivation of the Secular Equations

Wilson has devised a very useful system for setting up the secular equation for the vibrations of a molecule [2]. This procedure has been used in the calculations of this report.

The secular equation is derived from the inverse of the kinetic-energy matrix (G) and the potential-energy or force-constant matrix (F). Wilson's

[1] This investigation was performed at the National Bureau of Standards as part of the work of the American Petroleum Institute Research Project 44 on the "Collection, analysis and calculation of data on the properties of hydrocarbons."

[2] Research Associate on the American Petroleum Institute Research Project 44 at the National Bureau of Standards.

[3] Associate Supervisor on the American Petroleum Institute Research Project 44, Professor of Chemistry at the University of California, Berkeley, Calif.

[4] Figures in brackets indicate the literature references at the end of the paper.

method is particularly well adapted to the use of internal coordinates (bond stretchings and angular distortions). The physical interpretation of the potential constants corresponding to these coordinates is simple. Furthermore, potential constants determined for a given structure in one molecule are found to hold fairly well in other similar molecules.

For a given internal coordinate R_k, a vector $\mathbf{S}_{kt}$ is defined for each atom t of the molecule, so that for an arbitrary displacement $\mathbf{p}_t$,

$$R_k = \sum_{t=1}^{n} \mathbf{S}_{kt} \cdot \mathbf{p}_t. \tag{1}$$

The $\mathbf{S}_{kt}$ may be calculated by rules given by Wilson. As the direction of $\mathbf{S}_{kt}$ is the displacement of atom t, which produces the maximum change in R_k, the various $\mathbf{S}_{kt}$ can usually be written down by inspection.

The elements of G, the inverse kinetic-energy matrix, are given by the expression

$$G_{kk'} = \sum_{t=1}^{n} \mu_t \mathbf{S}_{kt} \cdot \mathbf{S}_{k't}, \tag{2}$$

where μ_t is the reciprocal of the mass of the atom t.

If the coordinates R_k are properly chosen with respect to the symmetry of the molecule, the matrix G will be factored into a series of blocks along its diagonal. The coordinates of each block will correspond to vibrations of the same symmetry type. The F matrix will be factored at least as much as the G matrix. The coordinates that produce this factorization are always linear combinations of the individual bond stretchings and angular distortions, and are designated by the symbol $\mathfrak{R}_k$. G and F in terms of $\mathfrak{R}_k$ are given the symbols $\mathfrak{G}$ and $\mathfrak{F}$.

III. Ethylene

1. The Secular Equation

The ethylene molecule has the symmetry of the point group V_h. This group contains eight irreducible representations, or symmetry types. Application of standard group theoretical methods [3, 4] leads to the general conclusions as to the symmetry and activity of the 12 vibrations summarized in table 1.

TABLE 1.—*Symmetry characteristics of ethylene*

V_h	E	C_2^z	C_2^y	C_2^x	I	σ_z	σ_y	σ_x	Number of vibrations	Activity
A_{1g}	1	1	1	1	1	1	1	1	3	$R(p)$
B_{1g}	1	1	−1	−1	1	1	−1	−1	2	$R(dp)$
B_{2g}	1	−1	1	−1	1	−1	1	−1	1	$R(dp)$
B_{3g}	1	−1	−1	1	1	−1	−1	1	0	$R(dp)$
A_{1u}	1	1	1	1	−1	−1	−1	−1	1	in
B_{1u}	1	1	−1	−1	−1	−1	1	1	1	$IR(z)$
B_{2u}	1	−1	1	−1	−1	1	−1	1	2	$IR(y)$
B_{3u}	1	−1	−1	1	−1	1	1	−1	2	$IR(x)$

The coordinates chosen to describe the planar motions of this molecule are the increases in the lengths of the four C—H bonds (d_1, d_2, d_3, d_4), the increases of the four C=C—H angles (α_1, α_2, α_3, α_4) and the two H—C—H angles (β_1, β_2), and the increase in the length of the C=C bond (r). The internal coordinates are numbered as in figure 1.

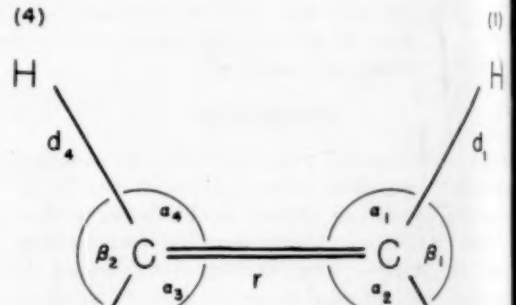

FIGURE 1.—*Nomenclature of the coordinates used in ethylene.*

In order to utilize fully the symmetry of the molecule, 11 linear combinations of the internal coordinates were formed. A fourth-order symmetry matrix was applied to the d's and one of the sixth order to the α's and β's. Two of the angle combinations are identically zero because of the geometric relation of the angles around each carbon atom. There remain nine symmetry coordinates, which agrees with the fact that there are nine planar vibrations. The symmetry com-

nations, each identified with its irreducible representation, are

$$\mathfrak{R}_1 = \tfrac{1}{2}(d_1+d_2+d_3+d_4) \quad (3a)$$

$$\mathfrak{R}_2 = \tfrac{1}{2}(d_1+d_2-d_3-d_4) \quad (3b)$$

$$\mathfrak{R}_3 = \tfrac{1}{2}(d_1-d_2+d_3-d_4) \quad (3c)$$

$$\mathfrak{R}_4 = \tfrac{1}{2}(d_1-d_2-d_3+d_4) \quad (3d)$$

$$\mathfrak{R}_5 = \tfrac{1}{6}\sqrt{6}(\beta_1+\alpha_1+\alpha_2+\beta_2+\alpha_3+\alpha_4) \equiv 0 \quad (3e)$$

$$\mathfrak{R}_6 = \tfrac{1}{6}\sqrt{6}(\beta_1+\alpha_1+\alpha_2-\beta_2-\alpha_3-\alpha_4) \equiv 0 \quad (3f)$$

$$\mathfrak{R}_7 = \tfrac{1}{6}(-2\beta_1+\alpha_1+\alpha_2-2\beta_2+\alpha_3+\alpha_4) = \tfrac{1}{2}(\alpha_1+\alpha_2+\alpha_3+\alpha_4) \quad (3g)$$

$$\mathfrak{R}_8 = \tfrac{1}{6}(-2\beta_1+\alpha_1+\alpha_2+2\beta_2-\alpha_3-\alpha_4) = \tfrac{1}{2}(\alpha_1+\alpha_2-\alpha_3-\alpha_4) \quad (3h)$$

$$\mathfrak{R}_9 = \tfrac{1}{2}(\alpha_1-\alpha_2+\alpha_3-\alpha_4) \quad (3i)$$

$$\mathfrak{R}_{10} = \tfrac{1}{2}(\alpha_1-\alpha_2-\alpha_3+\alpha_4) \quad (3j)$$

$$\mathfrak{R}_{11} = \tau \quad (3k)$$

If the two β's had been ignored and the four α's combined with a fourth-order symmetry matrix, the same symmetry coordinates would have been obtained. However, a large α_1,α_2 interaction term would then have been necessary in the potential expression in order to account for the β bending energy.

The coordinates chosen to describe the out-of-plane vibrations are the angle of torsion, ϕ, between the two CH_2 groups and the two angles, γ' and γ'', between the C=C bond and the bisectors of the two CH_2 groups. The proper symmetry coordinates are then: $\mathfrak{R}_{12}=\phi$, A_{1u}; $\mathfrak{R}_{13}=\sqrt{\tfrac{1}{2}}(\gamma'-\gamma'')$, B_{2g} (chair, or *trans*, bending); $\mathfrak{R}_{14}=\sqrt{\tfrac{1}{2}}(\gamma'+\gamma'')$, B_{1u} (boat, or *cis*, bending).

The symmetry coordinates were used to set up the inverse kinetic-energy matrices ($\mathfrak{G}$) and the potential-energy matrices ($\mathfrak{F}$) for each symmetry type. The roots λ of each equation

$$\|\mathfrak{G}\mathfrak{F}-\lambda E\|=0 \quad (4)$$

yield the several vibrational frequencies by means of the equation $\lambda=4\pi^2\nu^2$.

Such determinantal equations can readily be expanded into the usual secular equations. In matrix notation, the nature of the kinetic coupling of the several symmetry coordinates in each irreducible representation can be seen by inspection. The elements of the $\mathfrak{F}$ matrices are the coefficients of the potential-energy expression as a quadratic function of the symmetry coordinates. Furthermore, no choice of potential interaction terms need be made until the final expansion of the matrix equations to the secular equations.

Gallaway and Barker [1] found the H−C−H angle of C_2H_4 and of C_2D_4 to be 119°55′ ±30′. We have used the even value of 120°. In the following equations, μ_H and μ_C are the reciprocals of the masses of the hydrogen and carbon atoms. ϵ and τ are the reciprocals of the equilibrium C−H and C=C bond lengths, respectively.

The $\mathfrak{G}$ and $\mathfrak{F}$ matrices for the seven symmetry types of vibration in ethylene are given in table 2. Each matrix is symmetric about the main diagonal, so only the upper half is written.

TABLE 2.—*Secular matrices for ethylene*

Symmetry types	Coordinates	$\mathfrak{G}$ matrices	$\mathfrak{F}$ matrices
A_{1g}	$\mathfrak{R}_1$	$\mu_H+\frac{1}{2}\mu_C$ $\frac{1}{2}\sqrt{3}\,\epsilon\mu_C$ $-\mu_C$	$\mathfrak{F}_{11}$ $\mathfrak{F}_{12}$ $\mathfrak{F}_{13}$
	$\mathfrak{R}_7$	$\epsilon^2(\mu_H+\frac{1}{2}\mu_C)$ $-\sqrt{3}\,\epsilon\mu_C$	$\mathfrak{F}_{22}$ $\mathfrak{F}_{23}$
	$\mathfrak{R}_{11}$	$2\mu_C$	$\mathfrak{F}_{33}$
B_{1u}	$\mathfrak{R}_2$	$\mu_H+\frac{1}{2}\mu_C$ $-\frac{1}{2}\sqrt{3}\,\epsilon\mu_C$	$\mathfrak{F}_{44}$ $\mathfrak{F}_{45}$
	$\mathfrak{R}_8$	$\epsilon^2(\mu_H+\frac{1}{2}\mu_C)$	$\mathfrak{F}_{55}$
B_{1g}	$\mathfrak{R}_3$	$\mu_H+\frac{1}{2}\mu_C$ $-\frac{1}{2}\sqrt{3}\,(\epsilon+4\tau)\mu_C$	$\mathfrak{F}_{66}$ $\mathfrak{F}_{67}$
	$\mathfrak{R}_9$	$\epsilon^2\mu_H+\frac{1}{2}(\epsilon+4\tau)^2\mu_C$	$\mathfrak{F}_{77}$
B_{1u}	$\mathfrak{R}_4$	$\mu_H+\frac{1}{2}\mu_C$ $-\frac{1}{2}\sqrt{3}\,\epsilon\mu_C$	$\mathfrak{F}_{88}$ $\mathfrak{F}_{89}$
	$\mathfrak{R}_{10}$	$\epsilon^2(\mu_H+\frac{1}{2}\mu_C)$	$\mathfrak{F}_{99}$
A_{1u}	$\mathfrak{R}_{12}$	$\frac{1}{4}\epsilon^2\mu_H$	$F_{\phi\phi}$
B_{2g}	$\mathfrak{R}_{13}$	$2\epsilon^2\mu_H+4(\epsilon+\tau)^2\mu_C$	$F_{\gamma\gamma}-f_{\gamma\gamma}$
B_{1u}	$\mathfrak{R}_{14}$	$2\epsilon^2\mu_H+4\epsilon^2\mu_C$	$F_{\gamma\gamma}+f_{\gamma\gamma}$

The symmetry force constants $\mathfrak{F}_{ij}$ are related to the individual valence force constants by means of a congruent transformation with the same matrix that relates the original internal and the symmetry coordinates. As the transformation actually used—an orthonormal (symmetry) matrix with two rows altered by the factor $\sqrt{3}$—is not normalized, the following relations must be used:

$$\mathfrak{R}=UR \quad (5a)$$

$$\mathfrak{G}=UG\tilde{U} \quad (5b)$$

$$\mathfrak{F}=\tilde{U}^{-1}FU^{-1}, \quad (5c)$$

where U is the matrix of the transformation of eq 3, and $\tilde{U}$ is its transpose.

The elements of $\mathfrak{F}$ for the planar vibrations (symmetry types A_{1g}, B_{2u}, B_{1g}, B_{2u}) are

$$\mathfrak{F}_{11}=K_{CH}+k_{CH12}+k_{CH13}+k_{CH14} \quad (6a)$$

$$\mathfrak{F}_{44}=K_{CH}+k_{CH12}-k_{CH13}-k_{CH14} \quad (6b)$$

$$\mathfrak{F}_{66}=K_{CH}-k_{CH12}+k_{CH13}-k_{CH14} \quad (6c)$$

$$\mathfrak{F}_{88}=K_{CH}-k_{CH12}-k_{CH13}+k_{CH14} \quad (6d)$$

$$\mathfrak{F}_{22}=(H_\alpha+2H_\beta-4h_{\alpha\beta})+h_{\alpha12}+h_{\alpha13}+h_{\alpha14} \quad (6e)$$

$$\mathfrak{F}_{55}=(H_\alpha+2H_\beta-4h_{\alpha\beta})+h_{\alpha12}-h_{\alpha13}-h_{\alpha14} \quad (6f)$$

$$\mathfrak{F}_{77}=H_\alpha-h_{\alpha12}+h_{\alpha13}-h_{\alpha14} \quad (6g)$$

$$\mathfrak{F}_{99}=H_\alpha-h_{\alpha12}-h_{\alpha13}+h_{\alpha14} \quad (6h)$$

$$\mathfrak{F}_{33}=K_{CC} \quad (6i)$$

$$\mathfrak{F}_{12}=l_{H\alpha}-2l_{H\beta} \quad (6j)$$

$$\mathfrak{F}_{45}=l_{H\alpha}-2l_{H\beta} \quad (6k)$$

$$\mathfrak{F}_{67}=l_{H\alpha} \quad (6l)$$

$$\mathfrak{F}_{89}=l_{H\alpha} \quad (6m)$$

$$\mathfrak{F}_{13}=2k_{HC} \quad (6n)$$

$$\mathfrak{F}_{23}=2(l_{C\alpha}-l_{C\beta}) \quad (6o)$$

Typical coordinates involved in each elementary force constant are

K_{CH}	$(d_i)^2$	$h_{\alpha12}$	$(\alpha_1)(\alpha_2)$
K_{CC}	$(r)^2$	$h_{\alpha13}$	$(\alpha_1)(\alpha_3)$
H_α	$(\alpha_i)^2$	$h_{\alpha14}$	$(\alpha_1)(\alpha_4)$
H_β	$(\beta_i)^2$	$h_{\alpha\beta}$	$(\alpha_1)(\beta_1)$
k_{H12}	$(d_1)(d_2)$	$l_{C\alpha}$	$(r)(\alpha_i)$
k_{H13}	$(d_1)(d_3)$	$l_{C\beta}$	$(r)(\beta_i)$
k_{H14}	$(d_1)(d_4)$	$l_{H\alpha}$	$(d_1)(\alpha_1)$
k_{HC}	$(d_i)(r)$	$l_{H\beta}$	$(d_1)(\beta_1)$

The most general quadratic potential for the planar vibrations of ethylene therefore contains 15 constants. All quadratic interactions between symmetry coordinates in different representations are identically zero. We have resolved the 15 constants into linear combinations of 16 elementary principal and interaction force constants. Five interactions involving C—H stretching and angular distortion in different ends of the molecule have been neglected. They can readily be added by inspection or by means of a matrix operation should their consideration ever become necessary.

It is necessary to remember that in matrix notation two interactions, F_{ij} and F_{ji}, are counted as distinct, though equal in magnitude. The total interaction is the sum of the two constants.

If all of the interaction constants are set equal to zero the above matrix equations can readily be expanded to the set of secular equations given by Herzberg [5].

The vibrational assignment of Gallaway and Barker [1] was adopted for C_2H_4 and C_2D_4. These data are given in table 3. The bond lengths given by the same authors have been used. They are equilibrium C=C bond length, 1.353 A, and equilibrium C—H bond length, 1.071 A.

TABLE 3.—*Observed fundamental frequencies and their symmetry types*

	C_2H_4	C_2D_4
	cm^{-1}	cm^{-1}
A_{1g}	3019.3	2251
	1623.3	1515
	1342.4	981
B_{2u}	2989.4	2300.2
	1443.9	1077.9
B_{1g}	3069	2304
	1055	800
B_{2g}	3105.5	2345
	995.0	740
A_{1u}	[a](825)	[b](583)
B_{1g}	943	780
B_{1u}	949.2	720.0

[a] Calculated from its second harmonic, 1654 cm^{-1}.
[b] Calculated from the corresponding C_2H_4 frequency by means of the product rule.

A choice of potential constants for the totally symmetric vibrations (type A_{1g}) presents the most difficult problem. It is not possible to find real and positive values for $\mathfrak{F}_{11}$, $\mathfrak{F}_{22}$, and $\mathfrak{F}_{33}$ (with the off-diagonal elements of $\mathfrak{F}$ set equal to zero), which will yield either the three frequencies of C_2H_4 or of C_2D_4. On the basis of experience and a few trial calculations, it was decided to set $\mathfrak{F}_{12}$ and $\mathfrak{F}_{13}$ equal to zero and to find values of $\mathfrak{F}_{11}$, $\mathfrak{F}_{22}$, $\mathfrak{F}_{33}$, and $\mathfrak{F}_{23}$ that would most accurately yield the six observed A_{1g} frequencies of C_2H_4 and C_2D_4.

No exact solution is possible even with the most

general potential expression with six constants. The observed A_{1g} frequencies of the two molecules fail to satisfy the product rule exactly.

Values of the above four constants that yielded the three A_{1g} C_2H_4 frequencies exactly and that gave the closest approach to the corresponding C_2D_4 frequencies did so with a total error of 1.5 percent.

2. Correction for Anharmonicity

As the values of $\mathcal{F}_{22}$ and $\mathcal{F}_{33}$ were quite sensitive to the value of $\mathcal{F}_{23}$ assumed, it was decided to attempt to correct the equations for anharmonicity in order to make a closer approach to the true potential expression. However, the data on overtones and combination tones are far from sufficient to permit a complete treatment of anharmonicity. Consequently, the method proposed by Tchang [6] was used. The masses of the hydrogen and deuterium atoms were replaced by effective masses according to the equations.

$$M'_H = M_H(1+CM_H^{-1/2}) \tag{7a}$$

$$M'_D = M_D(1+CM_D^{-1/2}). \tag{7b}$$

The product-rule quotient is in every case the ratio of the determinants of the $\mathcal{G}$ matrices for the symmetry type in question for the two isotopic molecules. In the case of A_{1g} for C_2H_4 and C_2D_4 the equation is simply

$$\frac{M_D^2}{M_H^2} = \frac{\lambda_1\lambda_2\lambda_3}{\lambda'_1\lambda'_2\lambda'_3}, \tag{8}$$

where the umprimed λ's are for C_2H_4 and those primed for C_2D_4.

The value of $C=+0.0578$ yields values of M'_H and M'_D, which satisfy the product rule. With this accomplished, there is a much greater possibility of finding potential constants consistent with the six observed A_{1g} frequencies of the two molecules.

This correction has some theoretical basis in that it is just the form derived from the energy-level expression for a diatomic anharmonic oscillator when only first-order anharmonicity is considered. In that case, when the potential is given by $V=1/2kx^2+ax^3+bx^4+\ldots$, we have

$$(\epsilon_1-\epsilon_0)/h=\nu=\frac{k^{1/2}}{2\pi M^{1/2}}\left(1+\frac{3hb}{8\pi k^{3/2}M^{1/2}}\right) \tag{9}$$

$$C\approx -(3hb)/(4\pi k^{3/2}). \tag{10}$$

In a polyatomic molecule the significance of C is obscure, but it can be interpreted as a sort of composite anharmonicity coefficient.

With the hydrogen and deuterium masses corrected in this manner for anharmonicity, the force constants should be of the zeroth order, but the equations should yield the observed frequencies.

3. Working Units for G and F Matrices

Before the final results are presented, a convenient numerical transformation will be discussed. The secular equations are much easier to handle when all the elements are of the order of magnitude of unity. To achieve this end, all masses are expressed in atomic-weight units and bond lengths in angstrom units. Force constants (in cgs units) are multiplied by the factors in table 4.

TABLE 4.—*Conversion factors for force constants, cgs units to atomic-weight units*

Type of force constant	Factor [a]
Principal stretching	$10^{-5}Z$
Principal bending	$10^{+11}Z$
Stretching-stretching interaction	$10^{-5}Z$
Stretching-bending interaction	$10^{+1}Z$
Bending-bending interaction	$10^{+11}Z$

[a] Explanation of symbols:

$$Z=1.69765=\frac{N_0 10^5}{4\pi^2c^2 10^8}.$$

N_0 = Avogadro's number.

c = velocity of light.

The roots λ of the secular equation are then related to the frequencies of vibration, in wave numbers, centimeters^{-1}, through the equation

$$\bar{\nu}=1000\lambda^{1/2}. \tag{11}$$

The elements of $\mathcal{F}$ in cgs units will be designated by $\mathcal{F}_{ij}$ and in the above-mentioned units by, $\mathcal{F}'_{ij}$.

4. Potential Constants for Ethylene

A preliminary calculation determined that $\epsilon\mathcal{F}'_{23}\cong 1.0$. A series of values in this neighborhood were chosen for $\mathcal{F}'_{23}$, and then by means of successive approximations the unique values of $\mathcal{F}'_{11}$, $\epsilon^2\mathcal{F}'_{22}$, and $\mathcal{F}'_{33}$ that would yield the three A_{1g} frequencies of C_2H_4 were found. The three corresponding C_2D_4 frequencies were then calculated and compared with the observed values. The error in each of the three calculated frequencies was

plotted against $\mathcal{F}'_{23}$. The three curves intersected very nearly at a single point, which lies very nearly on the zero error axis. The data are presented in table 5.

TABLE 5.—*Calculation of force constants for the symmetry type A_{1g} of ethylene*

$\mathcal{F}'_{22}$	$\mathcal{F}'_{11}$	$\mathcal{F}'_{12}$	$\mathcal{F}'_{33}$	Calculated λ's of C_2D_4		
				λ_1	λ_2	λ_3
(a) 1.10	9.139	2.0032	16.74	5.07234	2.31406	0.95350
(b) 1.05	9.141	2.0254	16.50	5.06778	2.30076	.95988
(c) 1.00	9.143	2.0523	16.23	5.06223	2.28485	.96760
(d) 0.90	9.151	2.1558	15.35	5.04149	2.22065	.99070
(e) 0.80*						
(f) 1.031	9.142	2.0351	16.46	5.06586	2.29488	.96270
Observed λ's of C_2D_4				5.06700	2.29523	.96236
Calculated ν of C_2D_4				2250.7	1514.9	981.2
Observed ν of C_2D_4				2251	1315	981

* No solution.

If the validity of the anharmonicity correction is granted, the essentially perfect agreement of the six calculated and six observed frequencies justifies the use of only four symmetry potential constants.

For the symmetry types B_{3u}, B_{1g}, and B_{2u} the off-diagonal symmetry potential constants were neglected as they are of the type found negligible in A_{1g}. In these cases it was possible to solve directly for the two constants in each case that would yield the C_2H_4 frequencies exactly. The corresponding C_2D_4 frequencies were then calculated. The agreement with the observed C_2D_4 frequencies is fair. When the anharmonicity correction from A_{1g} is included the agreement is not essentially changed.

The lack of perfect agreement may be due to several causes. The assignments of these 12 frequencies is not as certain as is the case in A_{1g}. The off-diagonal potential constants may be too important to neglect. The anharmonicity correction probably has a different value in each case, although it certainly has the same sign as in A_{1g}. In all three symmetry types the agreement with the product rule was improved by the inclusion of the anharmonicity correction with the value of C found in A_{1g}.

Probably a more elaborate treatment of anharmonicity is needed, involving different apparent masses for the motion of hydrogen atoms in the three different directions (parallel to the CH bond, perpendicular to the bond in the plane of the molecule and perpendicular to plane of the molecule). However, in order to evaluate all of these constants, good assignments for the mixed deuteroethylenes would probably be necessary. It was not thought that the problem was of sufficient interest to warrant further attention at the present time.

In table 6 are presented the elements of $\mathcal{F}$ and F' determined without correction for anharmonicity, together with a comparison of the calculated and observed frequencies of C_2D_4. As has been previously stated, these constants give the observed frequencies of C_2H_4 exactly. The same information, but with the corrections for anharmonicity, is given in table 7. No attempt was made to correct the three out-of-plane vibrations for anharmonicity.

TABLE 6.—*Force constants calculated from the frequencies of ethylene without consideration of anharmonicity*

[Comparison of calculated with observed frequencies for deuteroethylene]

Force constants *	C_2D_4 Calculated frequency	C_2D_4 Observed frequency
	cm^{-1}	cm^{-1}
A_{1g} $\begin{bmatrix} 8.678 & \\ & 2.2853 \quad 0.924 \\ & 0.924 \quad 15.667 \end{bmatrix}$	2249.1	2251
	1503.0	1315
	974.4	981
B_{3u} $\begin{bmatrix} 8.634 & \\ & 2.1536 \end{bmatrix}$	2160.9	2261
	1098.8	1077
B_{1g} $\begin{bmatrix} 8.376 & \\ & 0.7866 \end{bmatrix}$	2306.4	2294
	848.7	880
B_{2u} $\begin{bmatrix} 8.629 & \\ & 1.1041 \end{bmatrix}$	2317.3	2345
	713.4	740
A_{1u} [0.590]	584	
B_{2g} [0.339]	781	780
B_{1u} [0.446]	718	720

$K_{CH}=8.580$
$k_{H12}=0.077$
$k_{H13}=-.053$
$k_{H14}=0.077$

$K_{CC}=15.667$
$l_{C\alpha}-l_{C\beta}=0.462$

$H_\alpha+H_\beta-h_{\alpha\beta}=1.5824$
$H_\alpha-2h_{\alpha\beta}+h_{\alpha12}=0.6371$
$h_{\alpha12}=-.0465$
$h_{\beta14}=0.1123$
If $h_{\alpha\beta}=h_{\alpha12}=0$,
$H_\alpha=0.9453$
$H_\beta=0.6371$

$F_{\alpha\alpha}=0.590$
$F_{\gamma\delta}=0.393$
$F_{\gamma\gamma}=0.054$

* These force constants are expressed in angstrom—atomic weight units as previously described.

TABLE 7.—*Force constants calculated from the frequencies of ethylene with approximate correction for anharmonicity*

[Comparison of calculated with observed frequencies for deuteroethylene]

Force constants	C_2D_4 Calculated frequency	C_2D_4 Observed frequency
	cm^{-1}	cm^{-1}
B_{1g} $\begin{bmatrix} 9.142 & \\ & 2.3343 \quad 1.104 \\ & 1.104 \quad 16.40 \end{bmatrix}$	2250.7	2251
	1514.9	1515
	981.2	981
A_g $\begin{bmatrix} 9.108 & \\ & 2.2645 \end{bmatrix}$	2167.6	2200.2
	1066.9	1077.9
B_{2g} $\begin{bmatrix} 8.796 & \\ & 0.8161 \end{bmatrix}$	2296.7	2304
	860.9	860
B_{3u} $\begin{bmatrix} 9.008 & \\ & 1.1656 \end{bmatrix}$	2308.5	2345
	717.0	740(?)

K_{CH}= 9.029 $\quad$ $H_\alpha+H_\beta-h_{\alpha\beta}$= 1.6451

k_{H12}= 0.097 $\quad$ $H_\alpha-h_{\alpha\beta}+h_{\alpha12}$= 0.6543

k_{H13}= −.079 $\quad$ $h_{\alpha11}$= −.0699

k_{H14}= 0.077 $\quad$ $h_{\alpha14}$= 0.1048

if $h_{\alpha\beta}=h_{\alpha12}=0$

K_{CC}=16.40 $\quad$ H_α= 0.9909

$l_{C\alpha}-l_{C\beta}$= 0.552 $\quad$ H_β= 0.6543

Anharmonicity constant: C=0.0578.

Some interesting conclusions can be drawn from the values of these force constants. The 13 interactions, both for C—H stretching and for bending, are negative but are about the same absolute magnitude as the corresponding 14 (and in the case of C—H stretching) and 12 interactions.

IV. Propylene, *cis*-2-Butene, *trans*-2-Butene, and Isobutene

1. Normal Equations for *cis*-2-Butene, *trans*-2-Butene, and Isobutene

As the first step in the formulation of the complete equations for these molecules, the equations for the skeletal models, including the pair of olefinic hydrogens, were set up. The methyl groups were considered as point masses.

The numbering of the various coordinates is similar to that used for ethylene and is presented in figure 2.

The symmetry classifications and the selection rules of the three rigid frame butenes are given in table 11. The two symmetry types that are symmetrical with respect to the plane of the carbon skeleton are A_1 and B_2 for symmetry C_{2v}, and A_g and B_u for symmetry C_{2h}. Linear combinations of elementary stretchings of bonds and expansions of angles having these symmetries were formed for use as symmetry coordinates.

The coordinates that were used are the two C—H stretchings, the two C—C stretchings, the two C=C—H bendings, the two C=C—C bendings, and the C=C stretching.

The proper symmetry combinations are the symmetric and antisymmetric combinations of like pairs of coordinates, written in the numerical order of their index numbers.

It was assumed that, as in ethylene, the skeletal angles are all 120°. The reciprocals of the C=C, C—H, and C—C equilibrium bond lengths have been designated by τ, ϵ and δ, respectively. The reciprocals of the masses of hydrogen, carbon of a methyl group, and carbon from the olefinic group are denoted by μ_H, μ_C, and $\mu_{C'}$, respectively. In the case of isobutene, the reciprocal mass of the carbon of the CH_2 is denoted by $\mu_{C''}$ and that of the other olefinic carbon by $\mu_{C'}$.

The vibrations unsymmetrical to the skeletal plane of the molecule are A_u and B_g for C_{2h} and A_2 and B_1 for C_{2v}. The coordinates used to describe these motions are analogous to those used for ethylene. In the case of *cis*- and *trans*-butene, symmetric and antisymmetric combinations of the two γ bendings (=C$\langle^{CH_3}_{H}$ against the

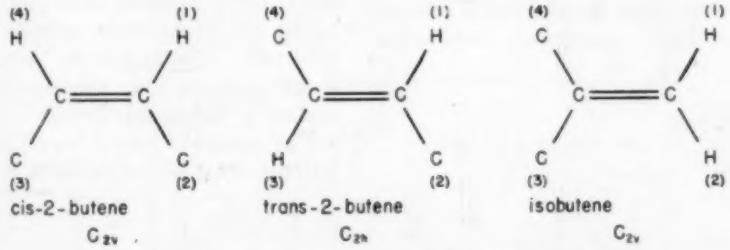

FIGURE 2.—*Numbering of the coordinates for the three butenes.*

olefinic C=C group) were used. In isobutene the two angles were used separately.

In the early stages of this work, it was hoped that a satisfactory analysis could be completed without a detailed treatment of the methyl groups. It soon became apparent, however, that the kinetic coupling between the rocking or wagging motions of the methyl groups and the remainder of the molecule was great enough that this coordinate, at least, must be included in the normal coordinate analysis.

The $\mathfrak{G}$ matrix of the skeleton of a molecule is a submatrix of the $\mathfrak{G}$ matrix for the whole molecule. It is not necessary to orient the methyl groups that replace single particles so that the symmetry of the molecule is unchanged, although such might seem to be the case at first sight.

The additional elements of $\mathfrak{G}$ from each methyl group are of two kinds (1) those from the eight degrees of freedom of each methyl group, and (2) those arising from the coupling of methyl and skeletal motions.

The elements of $\mathfrak{G}$ arising purely from each methyl are the same as those first calculated by Wilson for CH_3X. The symmetry classification of the vibrations may be changed, however. For example, the doubly degenerate (E) vibrations usually will separate into different symmetry classes.

Of the eight modes of vibration of a methyl group, two are parallel to the methyl axis. These are (1) symmetric C—H stretching, (2) symmetric CH_3 deformation. The six remaining modes are perpendicular to the methyl axis. These are a mutually perpendicular pair each of (3) unsymmetric C—H stretching, (4) unsymmetric CH_3 deformation, and (5) methyl wagging.

Let α_{ij} be the change in an H^iCH^j angle, β_i the change in an XCH^i angle, and d_i the change in a CH^i bond. X is the atom to which the methyl group is attached. Eight appropriate coordinates are then:

(1) $(1/\sqrt{3})(d_1+d_2+d_3)$
(2) $(1/\sqrt{3})(\alpha_1+\alpha_2+\alpha_3)$
} parallel to CH_3 axis.

(3) $(1/\sqrt{6})(2d_1-d_2-d_3)$
(4) $(1/\sqrt{6})(2\alpha_1-\alpha_2-\alpha_3)$
(5) $(1/\sqrt{6})(2\beta_1-\beta_2-\beta_3)$
(3)′ $(1/\sqrt{2})(d_2-d_3)$
(4)′ $(1/\sqrt{2})(\alpha_2-\alpha_3)$
(5)′ $(1/\sqrt{2})(\beta_2-\beta_3)$
} perpendicular to C[illegible] axis.

The elements of G from each methyl group are

parallel vibrations:

$$\begin{array}{c} \\ (1) \\ (2) \end{array} \begin{array}{c} \begin{array}{cc} (1) & (2) \end{array} \\ \begin{bmatrix} \mu_H+\frac{1}{3}\mu_C & -\frac{2}{3}\sqrt{2}\rho\mu_C \\ & \rho^2(\mu_H+\frac{2}{3}\mu_C) \end{bmatrix} \end{array}$$

perpendicular vibrations:

$$\begin{array}{c} \\ (3) \\ (4) \\ (5) \end{array} \begin{array}{c} \begin{array}{ccc} (3) & (4) & (5) \end{array} \\ \begin{bmatrix} \mu_H\frac{4}{3}+\mu_C & \frac{4}{3}\sqrt{2}\rho\mu_C & -\sqrt{2}(\delta+\frac{1}{3}\rho)\mu_C \\ & \rho^2(\frac{2}{3}\mu_H+\frac{2}{3}\mu_C) & \frac{1}{2}\rho^2\mu_H-2\rho(\delta+\frac{1}{3}\rho)\mu_C \\ & & \rho^2\mu_H+\frac{3}{2}(\delta+\frac{1}{3}\rho)^2\mu_C+\frac{1}{2}\gamma^2\mu_H \end{bmatrix} \end{array}$$

where ρ is the reciprocal C—H bond length and δ is the reciprocal C—X bond length. The factor γ is unity when only one methyl group is attached to the atom X. When this is not the case, as in isobutene, the symmetry S vector for the atom X may have a different length than it does in the above simple case. The factor γ is proportional to the number of methyl groups attached to atom X and to the square of the relative change in S from its usual value for a single methyl group.

Coupling terms between two modes of vibration can arise only through an atom, t, which has S_t vectors that are nonperpendicular. Consequently, the methyl group can couple with the skeletal motions only through the methyl carbon or the atom to which the methyl group is attached. Vector $\mathbf{S}_{kt}$ for the methyl carbon is nonzero for all eight methyl motions and is parallel or perpendicular to the methyl axis, according to the type of vibration. For the atom to which the methyl group is attached, $\mathbf{S}_{kt}$ is zero except for the rocking motion of the methyl group.

The complete matrix equations for these three butenes are given in tables 8, 9, and 10.

72762-47—5

TABLE 8.—$\mathbf{G}$ *matrices for propylene out-of-plane, cis- and trans-2- butene in-plane vibrations*

PROPYLENE, A''

Unsym. me. v	$\mu_H+\frac{1}{2}\mu_C$	$\frac{3}{4}\sqrt{2}\rho\mu_C$	$-\sqrt{2}(\delta+\frac{1}{2}\rho)\mu_C$	0	$-\frac{3}{4}\sqrt{3}\,\delta\mu_C$	$\frac{3}{4}\delta\mu_C$
Unsym. me. δ		$\rho^2(\frac{3}{4}\mu_H+\frac{3}{2}\mu_C)$	$\frac{1}{2}\rho^2\mu_H-2\rho(\delta+\frac{1}{2}\rho)\mu_C$	0	$-\frac{3}{4}\sqrt{6}\,\rho\delta\mu_C$	$\frac{3}{4}\sqrt{2}\,\rho\delta\mu_C$
Me. rocking			$\rho^2\mu_H+\frac{3}{2}(\delta+\frac{1}{2}\rho)^2\mu_C+\frac{3}{2}\delta^2\mu_{C'}$	$-\frac{1}{2}\sqrt{3}\,\delta\tau\mu_C$	$\frac{1}{2}\sqrt{6}\,\delta(\delta+\frac{1}{2}\rho)\mu_C+\frac{1}{2}\sqrt{6}\,\delta(\epsilon+\delta+\tau)\mu_{C'}$	$-\delta(\delta+\frac{1}{2}\rho)\mu_C+\delta\epsilon\mu_{C'}$
CH_2 rocking				$2\epsilon^2\mu_H+(2\epsilon+\tau)^2\mu_{C''}+\tau^2\mu_{C'}$	$-\tau(2\epsilon+\tau)\mu_{C''}-\tau(\epsilon+\delta+\tau)\mu_{C'}$	$-\frac{1}{2}\sqrt{3}\,\tau(\epsilon-\delta)\mu_{C'}$
$CH(CH_3)$ rocking					$\epsilon^2\mu_H+\delta^2\mu_C+(\epsilon+\delta+\tau)^2\mu_{C'}+\tau^2\mu_{C''}$	$\frac{1}{2}\sqrt{3}\,(\epsilon^2\mu_H-\delta^2\mu_C+(\epsilon-\delta)(\epsilon+\delta+\tau)\mu_{C'})$
C=C twisting						$\epsilon^2\mu_H+\frac{1}{2}\delta^2\mu_C+\frac{1}{2}(\epsilon-\delta)^2\mu_{C'}$

cis-2-BUTENE, A_1; *trans*-2-BUTENE, B_a, TO VERTICAL LINE

Sym. me. v	$\mu_H+\frac{1}{2}\mu_C$	$-\frac{3}{4}\sqrt{2}\,\rho\mu_C$	0	0	0	0	$-\frac{1}{2}\sqrt{3}\,\mu_C$	0	0	0
Sym. me. δ		$\rho^2\mu_H+\frac{3}{2}\rho^2\mu_C$	0	0	0	0	$\frac{3}{4}\sqrt{6}\,\rho\mu_C$	0	0	0
Unsym. me. v			$\mu_H+\frac{1}{2}\mu_C$	$\frac{3}{4}\sqrt{2}\,\rho\mu_C$	$-\sqrt{2}(\delta+\frac{1}{2}\rho)\mu_C$	0	0	0	$-\frac{3}{4}\sqrt{3}\,\delta\mu_C$	0
Unsym. me. δ				$\frac{3}{2}\rho^2\mu_H+\frac{3}{2}\rho^2\mu_C$	$\frac{1}{2}\rho^2\mu_H-2\rho(\delta+\frac{1}{2}\rho)\mu_C$	0	0	0	$-\frac{3}{4}\sqrt{6}\,\delta\rho\mu_C$	0
Me. rocking					$\rho^2\mu_H+\frac{3}{2}(\delta+\frac{1}{2}\rho)^2\mu_C+\frac{3}{2}\delta^2\mu_{C'}$	$\frac{1}{4}\sqrt{2}\,\delta\mu_C$	0	$\frac{1}{4}\sqrt{6}\,\epsilon\delta\mu_{C'}$	$\frac{1}{2}\sqrt{6}\,\delta(2\delta+\frac{1}{2}\rho)\mu_C$	$-\frac{1}{2}\delta\mu_{C'}$
CH v						$\mu_H+\mu_{C'}$	$-\frac{1}{2}\mu_{C'}$	0	$\frac{1}{2}\sqrt{3}\,\delta\mu_{C'}$	$-\frac{1}{2}\sqrt{2}\,\mu_{C'}$
CC v							$\mu_C+\mu_{C'}$	$\frac{1}{2}\sqrt{3}\,\epsilon\mu_{C'}$	0	$-\frac{1}{2}\sqrt{2}\,\mu_{C'}$
H wagging								$\epsilon^2(\mu_H+\mu_{C'})$	$\frac{1}{2}\epsilon\delta\mu_{C'}$	$-\frac{1}{2}\sqrt{6}\,\epsilon\mu_{C'}$
Skeletal δ									$\delta^2(\mu_C+\mu_{C'})$	$-\frac{1}{2}\sqrt{6}\,\delta\mu_{C'}$
C=C v										$2\mu_{C'}$

TABLE 8.—**G** *matrices for propylene out-of-plane, cis- and trans-2- butene in-plane vibrations*—Continued

	trans-2-BUTENE, A_g; *cis*-2-BUTENE, B_b, TO VERTICAL LINE									
Sym. me. v	$\mu_H+\frac{1}{4}\mu_C$	$-\frac{1}{4}\sqrt{2}\rho\mu_C$	0	0	0	0	$-\frac{1}{4}\sqrt{3}\mu_C$	0	0	0
Sym. me. δ	$\rho^2\mu_H+\frac{1}{8}\rho^2\mu_C$		0	0	0	0	$\frac{3}{8}\sqrt{6}\rho\mu_C$	0	0	0
Unsym. me. v		$\mu_H+\frac{3}{4}\mu_C$	$\frac{1}{4}\sqrt{2}\rho\mu_C$	$-\sqrt{2}(\delta+\frac{1}{4}\rho)\mu_C$		0	0	0	$-\frac{3}{4}\sqrt{6}\delta\mu_C$	0
Unsym. me. δ			$\frac{3}{8}\rho^2\mu_H+\frac{3}{8}\rho^2\mu_C$	$\frac{1}{8}\rho^2\mu_H-2\rho(\delta+\frac{1}{4}\rho)\mu_C$		0	0	0	$-\frac{3}{8}\sqrt{6}\delta\rho\mu_C$	0
Me. rocking				$\rho^2\mu_H+\frac{3}{2}(\delta+\frac{1}{2}\rho)^2\mu_C+\frac{3}{2}\delta^2\mu_{C'}$		$\frac{3}{4}\sqrt{2}\delta\mu_{C'}$	0	$-\frac{1}{4}\sqrt{6}\delta(2\tau-\epsilon)\mu_{C'}$	$\frac{1}{4}\sqrt{6}(\delta(\delta+\frac{1}{2}\rho)\mu_C+\delta(\tau+\delta)\mu_{C'})$	$-\frac{1}{2}\delta\mu_{C'}$
CH v						$\mu_H+\mu_{C'}$	$-\frac{1}{2}\mu_{C'}$	$-\sqrt{3}\tau\mu_{C'}$	$\frac{1}{4}\sqrt{3}(\delta+2\tau)\mu_{C'}$	$-\frac{1}{2}\sqrt{2}\mu_{C'}$
CC v							$\mu_C+\mu_{C'}$	$\frac{1}{2}\sqrt{3}(\epsilon+2\tau)\mu_{C'}$	$-\sqrt{3}\tau\mu_{C'}$	$-\frac{1}{2}\sqrt{2}\mu_{C'}$
H wagging								$\epsilon^2\mu_H+(\epsilon^2+2\epsilon\tau+4\tau^2)\mu_{C'}$	$\frac{1}{4}(\epsilon\delta-2\epsilon\tau-2\delta\tau-8\tau^2)\mu_{C'}$	$-\frac{1}{2}\sqrt{6}\epsilon\mu_{C'}$
Skeletal δ									$\delta^2\mu_C+(\delta^2+2\delta\tau+4\tau^2)\mu_{C'}$	$-\frac{1}{2}\sqrt{6}\delta\mu_{C'}$
C=C v										$2\mu_C$

TABLE 9.—**G** *matrices for isobutene in-plane vibrations*

ISOBUTENE, A_1

TABLE 9.—*F matrices for isobutene-like planar vibrations*

ISOBUTENE, A_1

Sym. me. v	$\mu_H+\frac{1}{3}\mu_C$	$-\frac{2}{3}\sqrt{2}\,\rho\mu_C$	0	0	0	0	$-\frac{1}{3}\sqrt{3}\,\mu_C$	0	0	0
Sym. me. δ		$\rho^2\mu_H+\frac{8}{3}\rho^2\mu_C$	0	0	0	0	$\frac{2}{3}\sqrt{6}\,\rho\mu_C$	0	0	0
Unsym. me. v			$\mu_H+\frac{4}{3}\mu_C$	$\frac{1}{3}\sqrt{2}\,\rho\mu_C$	$-\sqrt{2}\,(\delta+\frac{1}{3}\rho)\mu_C$	0	0	0	$-\frac{2}{3}\sqrt{3}\,\delta\mu_C$	0
Unsym. me. δ				$\frac{8}{3}\rho^2\mu_H+\frac{8}{3}\rho^2\mu_C$	$\frac{1}{3}\rho^2\mu_H-2\rho(\delta+\frac{1}{3}\rho)\mu_C$	0	0	0	$-\frac{2}{3}\sqrt{6}\,\delta\rho\mu_C$	0
Me. rocking					$\rho^2\mu_H+\frac{2}{3}(\delta+\frac{1}{3}\rho)^2\mu_C+\frac{2}{3}\delta^2\mu_{C'}$	0	$\frac{2}{3}\sqrt{2}\,\delta\mu_{C'}$	0	$\frac{1}{3}\sqrt{6}\,(\delta(\delta+\frac{1}{3}\rho)\mu_C+\frac{1}{3}\delta^2\mu_{C'})$	$-\frac{1}{3}\delta\mu_{C'}$
C–H v						$\mu_H+\frac{1}{3}\mu_{C'}$	0	$\frac{1}{3}\sqrt{3}\,\epsilon\mu_{C'}$	0	$-\frac{1}{3}\sqrt{2}\,\mu_{C'}$
C–C v							$\mu_C+\frac{1}{3}\mu_{C'}$	0	$\frac{1}{3}\sqrt{3}\,\delta\mu_{C'}$	$-\frac{1}{3}\sqrt{2}\,\mu_{C'}$
H wagging								$\epsilon^2(\mu_H+\frac{2}{3}\mu_{C'})$	0	$-\frac{1}{3}\sqrt{6}\,\epsilon\mu_{C'}$
Skeletal δ									$\delta^2(\mu_C+\frac{2}{3}\mu_{C'})$	$-\frac{1}{3}\sqrt{6}\,\delta\mu_{C'}$
C=C v										$\mu_{C'}+\mu_{C''}$

ISOBUTENE, B_2

Sym. me. v	$\mu_H+\frac{1}{3}\mu_C$	$-\frac{2}{3}\sqrt{2}\,\rho\mu_C$	0	0	0	$-\frac{1}{3}\sqrt{3}\,\mu_C$	0	0
Sym. me. δ		$\rho^2\mu_H+\frac{8}{3}\rho^2\mu_C$	0	0	0	$\frac{2}{3}\sqrt{6}\,\rho\mu_C$	0	0
Unsym. me. v			$\mu_H+\frac{4}{3}\mu_C$	$\frac{1}{3}\sqrt{2}\,\rho\mu_C$	$-\sqrt{2}\,(\delta+\frac{1}{3}\rho)\mu_C$	0	0	$-\frac{2}{3}\sqrt{3}\,\delta\mu_C$
Unsym. me. δ				$\frac{8}{3}\rho^2\mu_H+\frac{8}{3}\rho^2\mu_C$	$\frac{1}{3}\rho^2\mu_H-2\rho(\delta+\frac{1}{3}\rho)\mu_C$	0	0	$-\frac{2}{3}\sqrt{6}\,\delta\rho\mu_C$
Me. rocking					$\rho^2\mu_H+\frac{2}{3}(\delta+\frac{1}{3}\rho)^2\mu_C+\frac{2}{3}\delta^2\mu_{C'}$	0	$-\frac{2}{3}\sqrt{2}\,\delta\mu_{C'}$	$\frac{1}{3}\sqrt{6}\,\delta\tau\mu_{C'}$	$\frac{1}{3}\sqrt{6}\,(\delta(\delta+\frac{1}{3}\rho)\mu_C+\frac{1}{3}\delta(\delta+2\tau)\mu_{C'})$
C–H v						$\mu_H+\frac{1}{3}\mu_{C'}$	0	$-\frac{1}{3}\sqrt{3}\,(\epsilon+2\tau)\mu_{C'}$	$-\sqrt{3}\,\tau\mu_{C'}$
C–C v							$\mu_C+\frac{2}{3}\mu_{C'}$	$-\sqrt{3}\,\tau\mu_{C'}$	$-\frac{1}{3}\sqrt{3}\,(\delta+2\tau)\mu_{C'}$
H wagging								$\epsilon^2\mu_H+\frac{1}{3}(\epsilon+2\tau)^2\mu_{C''}+2\tau^2\mu_{C'}$	$\tau(\epsilon+2\tau)\mu_{C''}+\tau(\delta+2\tau)\mu_{C'}$
Skeletal δ									$\delta^2\mu_C+\frac{1}{3}(\delta+2\tau)^2\mu_{C'}+2\tau^2\mu_{C''}$

TABLE 10.—*G matrices for cis-2-butene, trans-2-butene, and isobutene and out-of-plane vibrations*

ISOBUTENE, B_1

Unsym. me. v	$\mu_H+\frac{1}{2}\mu_C$	$\frac{1}{2}\sqrt{2}\rho\mu_C$	$-\sqrt{2}(\delta+\frac{1}{2}\rho)\mu_C$	0 / $\frac{1}{2}\sqrt{6}\delta\mu_C$
Unsym. me. δ		$\rho^2(\frac{1}{2}\mu_H+\frac{1}{2}\mu_C)$	$\frac{1}{2}\rho^2\mu_H-2\rho(\delta+\frac{1}{2}\rho)\mu_C$	0 / $\frac{1}{2}\sqrt{3}\rho\delta\mu_C$
Me. rocking			$\rho^2\mu_H+\frac{3}{2}(\delta+\frac{1}{2}\rho)^2\mu_C+3\delta^2\mu_{C'}$	$-\sqrt{3}\delta\tau\mu_{C'}$ / $\sqrt{3}\delta(\delta+\frac{1}{2}\rho)\mu_C+\sqrt{3}\delta(2\delta+\tau)\mu_{C'}$
CH_3 rocking				$2\epsilon^2\mu_H+(2\epsilon+\tau)^2\mu_{C''}+\tau^2\mu_{C'}$ / $-\tau(2\epsilon+\tau)\mu_{C''}-\tau(2\delta+\tau)\mu_{C'}$
Skeletal δ				$2\delta^2\mu_C+(2\delta+\tau)^2\mu_{C'}+\tau^2\mu_{C''}$

ISOBUTENE, A_2

Unsym. me. v	$\mu_H+\frac{1}{2}\mu_C$	$\frac{1}{2}\sqrt{2}\rho\mu_C$	$-\sqrt{2}(\delta+\frac{1}{2}\rho)\mu_C$	$\frac{1}{2}\sqrt{2}\delta\mu_C$
Unsym. me. δ		$\rho^2(\frac{1}{2}\mu_H+\frac{1}{2}\mu_C$	$\frac{1}{2}\rho^2\mu_H-2\rho(\delta+\frac{1}{2}\rho)\mu_C$	$\frac{1}{2}\rho\delta\mu_C$
Me. rocking			$\rho^2\mu_H+\frac{3}{2}(\delta+\frac{1}{2}\rho)^2\mu_C$	$-\delta(\delta+\frac{1}{2}\rho)\mu_C$
C=C twisting				$\frac{3}{2}(\epsilon^2\mu_H+\delta^2\mu_C$

cis-2-BUTENE, A_2; *trans*-2-BUTENE, B_2 TO VERTICAL LINE

Unsym. me. v	$\mu_H+\frac{1}{2}\mu_C$	$\frac{1}{2}\sqrt{2}\rho\mu_C$	$-\sqrt{2}(\delta+\frac{1}{2}\rho)\mu_C$	$-\frac{1}{2}\sqrt{3}\delta\mu_C$	$\frac{1}{2}\sqrt{2}\delta\mu_C$
Unsym. me. δ		$\rho^2(\frac{1}{2}\mu_H+\frac{1}{2}\mu_C)$	$\frac{1}{2}\rho^2\mu_H-2\rho(\delta+\frac{1}{2}\rho)\mu_C$	$-\frac{1}{2}\sqrt{6}\rho\delta\mu_C$	$\frac{1}{2}\rho\delta\mu_C$
Me. rocking			$\rho^2\mu_H+\frac{3}{2}(\delta+\frac{1}{2}\rho)^2\mu_C+\frac{1}{2}\delta^2\mu_{C'}$	$\frac{1}{2}\sqrt{6}\delta(\delta+\frac{1}{2}\rho)\mu_C+\frac{1}{2}\sqrt{6}\delta(\epsilon+\delta+2\tau)\mu_{C'}$	$-\delta(\delta+\frac{1}{2}\rho)\mu_C+\delta(\epsilon-\delta)\mu_{C'}$
Chair δ				$\epsilon^2\mu_H+\delta^2\mu_C+(\epsilon+\delta+2\tau)^2\mu_{C'}$	$\frac{1}{2}\sqrt{6}(\epsilon^2\mu_H-\delta^2\mu_C)+\frac{1}{2}\sqrt{6}(\epsilon-\delta)(\epsilon+\delta+2\tau)\mu_{C'}$
C=C twisting					$\frac{3}{2}(\epsilon^2\mu_H+\delta^2\mu_C)+\frac{3}{2}(\epsilon-\delta)^2\mu_{C'}$

trans-2-BUTENE, A_u; *cis*-2-BUTENE, B_1 TO VERTICAL LINE

Unsym. me. v	$\mu_H+\frac{1}{2}\mu_C$	$\frac{1}{2}\sqrt{2}\rho\mu_C$	$-\sqrt{2}(\delta+\frac{1}{2}\rho)\mu_C$	$-\frac{1}{2}\sqrt{3}\delta\mu_C$	$\frac{1}{2}\sqrt{2}\delta\mu_C$
Unsym. me. δ		$\rho^2(\frac{1}{2}\mu_H+\frac{1}{2}\mu_C)$	$\frac{1}{2}\rho^2\mu_H-2\rho(\delta+\frac{1}{2}\rho)\mu_C$	$-\frac{1}{2}\sqrt{6}\rho\delta\mu_C$	$\frac{1}{2}\rho\delta\mu_C$
Me. rocking			$\rho^2\mu_H+\frac{3}{2}(\delta+\frac{1}{2}\rho)^2\mu_C+\frac{1}{2}\delta^2\mu_{C'}$	$\frac{1}{2}\sqrt{6}\delta(\delta+\frac{1}{2}\rho)\mu_C+\frac{1}{2}\sqrt{6}\delta(\epsilon+\delta)\mu_{C'}$	$-\delta(\delta+\frac{1}{2}\rho)\mu_C+\delta(\epsilon-\delta)\mu_{C'}$
Boat δ				$\epsilon^2\mu_H+\delta^2\mu_C+(\epsilon+\delta)^2\mu_{C'}$	$\frac{1}{2}\sqrt{6}(\epsilon^2\mu_H-\delta^2\mu_C)+\frac{1}{2}\sqrt{6}(\epsilon^2-\delta^2)\mu_{C'}$
C=C twisting					$\frac{3}{2}(\epsilon^2\mu_H+\delta^2\mu_C)+\frac{3}{2}(\epsilon-\delta)^2\mu_{C'}$

2. Normal Equations for Nonplanar Vibrations of Propylene

Propylene has only one element of symmetry, the plane through the three carbon atoms. The vibrations therefore fall into only two classes. No attempt was made in this research to treat the planar vibrations by means of normal coordinate analysis. The high order of the matrix involved would be prohibitively laborious to handle. A reasonably certain assignment of these frequencies can be made from the spectral data alone.

The nonplanar frequencies present a somewhat more difficult problem in assignment. Because they are not so numerous as the planar frequencies the normal equations were set up.

The coordinates used are the same as for the butenes. It was not necessary (or desirable) to take some of the symmetry combinations used in the butenes and in ethylene in this case, however.

The nonplanar propylene $\mathfrak{G}$ matrix (symmetry type A'') is given in table 8.

3. Reduction of the Order of Matrix Equations

The matrix equations which have been derived are of an inconveniently high order. Their order may be reduced by the removal of certain relatively constant frequencies. Wilson has shown that the C—H (stretching) frequencies may be removed from the matrix equations by setting their force constants equal to infinity [2]. The $\mathfrak{G}$ matrix is reduced in order by the number of frequencies thus removed and the remaining terms are slightly modified. The modification is equivalent to that produced by a partial triangularization of the original $\mathfrak{G}$ matrix about the diagonal terms corresponding to the frequencies removed. The remaining force constants are not changed. As can be seen from Rayleigh's principle [7], the remaining frequencies are all slightly increased. The increase does not exceed 2 percent for the frequencies in the range 1000 to 1500 cm^{-1} and decreases rapidly for the lower frequencies. Even this small effect could be compensated by a slight decrease in the remaining force constants.

The above reduction was applied to all of the C—H frequencies and to the CH_3 δ frequencies. The reduced equations therefore apply exactly to a hypothetical molecule which can execute all of the usual deformations, with the exceptions (1) the C—H bonds are rigid for stretching and (2) the methyl groups are rigid units for internal deformations. A methyl group may rock, however, against the connecting C—C bond.

This approximation for the methyl group probably has a larger effect on the remaining frequencies than the one for C—H v motions. It is known, however, that methyl deformation frequencies are remarkably constant, whatever the molecule in which they are found. It would seem that there is a relatively slight coupling between a methyl group and the rest of the molecule. In any event, this model is certainly better than a simple skeletal model.

In this way the four $\mathfrak{G}$ matrices for the three rigid frame butenes are reduced from the orders 10, 9, 5, and 4 to 5, 4, 3, and 2, respectively. The matrix for A'' (out of plane) for propylene is reduced in order from 6 to 4.

4. Direct Assignments From Spectral Data

(a) Propylene

The infrared absorption spectrum data used in the present assignment are from the Shell Development Co., Emeryville, Calif. [8] and from Wilson and Wells [9]. The Raman spectral data are from Ananthakrishnan [10]. The symmetry of propylene is very low, that of the point group C_s. Consequently all of its vibrational frequencies are permitted in both the infrared and Raman spectra.

The assignment of the directly observed frequencies of propylene of the present work differs only in minor details from that of Wilson and Wells [9]. No attempt was made to give detailed assignments to the C—H stretching vibrations as there are many modes of almost identical frequency. The C—H v vibrations were assigned the conventional values of 3050 cm^{-1} for the three olefinic CH groups and 2950 cm^{-1} for the three paraffinic CH groups. Symmetric and unsymmetric CH_3 δ vibrations were assigned the values 1370 cm^{-1} and 1444 cm^{-1}, respectively. Some of the other frequencies differ by a few wave numbers from the above authors' assignment, due to small differences between the two sets of infrared data used.

In-plane (A') CH_2 and CH_2 wagging, which Wilson and Wells did not assign, have been

assigned the frequencies 1172 cm^{-1} (*IR*) and 1042 cm^{-1} (*IR*).

(b) *cis*-2-Butene

Gershinowitz and Wilson have reported the infrared and Raman spectra of *cis*-2-butene [11] but unfortunately did not determine the state of polarization of the latter spectrum. The Shell Development Co., Emeryville, Calif., has contributed an infrared spectrogram for this substance to the catalogue of infrared spectrograms of the American Petroleum Institute Research Project 44 [8]. These spectral data were used in the preliminary assignment for *cis*-2-butene.

cis-2-Butene, with the symmetry of the point group C_{2v}, has four symmetry types of vibrations. The selection rules and the symmetry characteristics of the vibrations are presented in table 11. The approximate form of the separate vibrations of each type is given in the complete assignment of table 18.

TABLE 11.—*Symmetry properties of the vibrations, and the selection rules for cis-,[a] trans-,[b] and isobutene [a]*

Characters for the point groups C_{2v} and C_{2h}

C_{2v}	C_{2h}	$\frac{E}{E}$	$\frac{C^2}{C^2}$	$\frac{\sigma'}{\sigma_h}$	$\frac{\sigma''}{I}$
A_1	A_g	1	1	1	1
A_2	A_u	1	1	−1	−1
B_1	B_g	1	−1	−1	1
B_2	B_u	1	−1	1	−1

Selection rules

C_{2v}: Infrared active: A_1, B_1, B_2.
Raman active: A_1, A_2, B_1, B_2.
(A_1 polarized; A_2, B_1, and B_2 depolarized)

C_{2h}: Infrared active: A_u, B_u.
Raman active: A_g, B_g.
(A_g polarized, B_g depolarized)

[a] Symmetry type C_{2v}.
[b] Symmetry type C_{2h}.

The value 2950 cm^{-1} was assigned to the six methyl C—H v vibrations and 3050 cm^{-1} to the two olefinic C—H vibrations. The value 1450 cm^{-1} was assigned to the four unsymmetrical methyl δ vibrations and 1380 cm^{-1} to the two symmetrical methyl δ motions. These motions invariably give rise to frequencies of about these magnitudes and are too numerous in this case to separate definitely.

The strong infrared absorption maximum at 1672 cm^{-1} is obviously the C=C v motion. The three lowest frequencies, 304 cm^{-1} (*R*), 402 cm^{-1} (*R*), and 583 cm^{-1} (*IR*,*R*) are undoubtedly the two planar skeletal δ and the C=C twisting motions, respectively. Normal coordinate analysis confirmed this assignment, indicating 304 cm^{-1} for A_1, 402 for A_2, and 583 for B_2 skeletal deformations, respectively.

The lines at 876 and 978 cm^{-1} are probably A_1 and B_2 C—C v frequencies, respectively. The CH planar waggings (A_1 and B_2) should lie in the neighborhood of 1300 cm^{-1} and the methyl rocking frequencies about 1000 to 1100 cm^{-1}. A definite assignment of these latter motioos and of the C—H out-of-plane (A_2 and B_1) motions was postponed until after the complete normal coordinate treatment.

(c) *trans*-2-Butene

Infrared and Raman spectral data from the same two sources as for *cis*-2-butene were used in the assignment for this molecule. Fortunately Gershinowitz and Wilson have obtained polarization data for the Raman spectrum. It is therefore possible to distinguish certain symmetry types. Frequencies with the symmetries A_g and B_g are Raman active, infrared inactive (table 11), with the former polarized and the latter depolarized. The other two classes, A_u and B_u, are active only in the infrared.

The C—H v and CH_3 δ vibrations were assigned as in *cis*-2-butene. Outside of these two frequency ranges there are four polarized Raman lines: 1681, 1309, 870, and 507 cm^{-1}. These frequencies undoubtedly represent C=C v, C—H wagging, C—C v, and skeletal bending, all of symmetry A_g. There remains, therefore, only one vibration of symmetry A_g unassigned, CH_3 wagging.

Outside of the C—H v and CH_3 δ frequency ranges there are three depolarized Raman lines, at 1043, 746, and 210 cm^{-1}. The first two must be CH_3 and CH wagging, respectively, with the symmetry B_g. The lowest line probably arises from the B_g methyl torsional mode of vibration. This judgment is confirmed by the fact that 210 cm^{-1}, symmetry B_g, corresponds to a restricting potential for the methyl groups of about 2,000 cal/mole, in agreement with the value 1,950 cal/mole determined by calorimetric data [15]. The other CH_3 torsional frequency has the sym-

metry A_u and therefore could appear only in the infrared spectrum.

The strong infrared band centered at 964 cm^{-1} was assigned to A_u CH wagging. It would be expected that such an out-of-plane motion would have a large dipole moment and would show strong P, Q, and R branches. The A_u methyl wagging frequency was not selected from the spectrum, for no band seems certainly to be due to this motion. The other A_u frequency, C=C twisting, should lie at about 250 to 300 cm^{-1}, according to preliminary rough normal calculations. This is below the range of the available infrared data.

In this molecule B_u vibrations appear to exhibit a double minimum in the infrared absorption spectrum. Bands of this nature at 1304 and 1065 cm^{-1} were selected for B_u CH wagging and C—C v. The shoulder, at about 964 cm^{-1}, on the strong A_u band at 973 cm^{-1}, was selected for B_u CH_3 wagging. The other B_u vibration, skeletal bending, should have the value of about 300 cm^{-1}, which is below the range of the spectral data.

(d) Isobutene

Infrared spectral data from the Shell Development Co., Emeryville, Calif. [8] and Raman data from Kirrmann [12] and Telfair and Pielemeier [13] were used in the assignment for isobutene.

The symmetry of isobutene is the same as that of *cis*-2-butene, C_{2v}, and therefore the selection rules are the same. The classifications of the various frequencies among the four symmetry types differ somewhat, however (table 20).

The C—H v and CH_3 δ vibrations were assigned as in *cis*-2-butene. The vibrations with the symmetry A_1 were assigned as follows: The value 1664 $cm^{-1}(IR,R(p))$ was assigned to C=C v, the vibration 800 $cm^{-1}(IR,R(p))$ to C—C v, 1390 cm^{-1} $(IR,R\ (p))$ to CH_3 δ, 1053 $cm^{-1}(IR,R(p))$ to CH_3 wagging, and 378 cm^{-1} (R) to skeletal deformation. This accounts for all the A_1 vibrations and leaves no polarized Raman lines unaccounted for.

In the symmetry class B_2 the assignment is not quite as certain as it is in class A_1. The B_2 skeletal deformation is certainly 431 $cm^{-1}(IR,R)$.[5] Probably 986 cm^{-1} (IR) and 1280 cm^{-1} (IR) are B_2 C—C v and unsymmetrical CH_2 bending, respectively. B_2 CH_3 wagging is left unassigned for the moment.

The weak unpolarized line in the Raman spectrum at 700 cm^{-1} is likely due to A_2 C=C twisting. A_2 methyl rocking will be assigned later.

The very strong infrared band at 888 cm^{-1} is probably due to B_1 CH_2 wagging, as in the analogous cases of *cis*- and *trans*-2-butene. No band is obviously due to methyl wagging. The probable frequency of B_1 skeletal bending lies below the range of the infrared data. There appears to be no line in the Raman spectrum from this source.

5. Potential Constants

(a) In-Plane Motions

The value 1.08 [6] was taken for the methyl rocking constant, F_r, from the work of Stitt [14]. A variety of values were tried for the C—C v constant, F_{CC}, but as one seemed to have no decided advantage over another, the value 7.64 from the work of Wilson and Wells was used in the final computations. The C=C v constant, 16.40, from the present work on ethylene apparently is too high for the butenes. It was reduced to 15.40 in order to fit the observed C=C v frequencies.

The pattern of bending constants determined for ethylene was used as a guide in estimating the bending constants for the butenes. It was not practicable to utilize the full set of interaction bending constants as was done in the case of ethylene.

In table 12 the in-plane bending constants which were used are listed, together with the angle to which each corresponds.

TABLE 12.—*In-plane bending force constants and the associated angles*

Force constant	Angle	Force constant	Angle
H_α	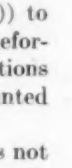	$H_{\beta'}$	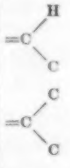
$H_{\alpha'}$		$H_{\beta''}$	
H_β			

Preliminary calculations showed that $H_{\alpha'}$ has a value about 60 percent greater than H_α from

[5] D. C. Smith, U. S. Naval Research Laboratory, reports in a private communication a strong infrared band at 432 ±2 cm^{-1}.

[6] The values of the potential constants given in this section are expressed in angstrom-atomic weight units, as previously described.

ethylene. The following relations were therefore assumed:

$$H_{\alpha'}=1.6H_{\alpha} \tag{12}$$

$$H_{\beta'}=1.3H_{\beta} \tag{13}$$

$$H_{\beta''}=1.6H_{\beta} \tag{14}$$

The interaction between C=C v and C=C−H δ was found to be by no means negligible in ethylene. In the butenes it was assumed that the interaction $l_{C\alpha'}$ is 1.3 greater than the value of $(l_{C\alpha}-l_{C\beta})$ found in ethylene. The value of $l_{C\beta}$ is probably much smaller than that of $l_{C\alpha}$ and was neglected.

The $\mathbf{F}$ matrices for the in-plane vibrations of *cis-*, *trans-*, and isobutene are given in table 13.

TABLE 13.—*Reduced* $\mathbf{F}$ *matrices for the in-plane vibrations of cis-, trans-, and isobutene*

cis-2-Butene, A_1, and *trans*-2-Butene, A_g[a]

$$\begin{bmatrix} F_\tau & & & & \\ & F_{CC} & & & \\ & & H_\alpha+H_\beta' & H_\beta' & \sqrt{2}l_{C\alpha} \\ & & & H_\alpha'+H_\beta' & \sqrt{2}l_{C\alpha'} \\ & & & & K_{CC} \end{bmatrix}$$

Isobutene, A_1

$$\begin{bmatrix} F_\tau & & & & \\ & F_{CC} & & & \\ & & H_\alpha+2H_\beta & & \sqrt{2}l_{C\alpha} \\ & & & H_{\alpha'}+2H_{\beta''} & \sqrt{2}l_{C\alpha'} \\ & & & & K_{CC} \end{bmatrix}$$

Isobutene, B_2

$$\begin{bmatrix} F_\tau & & & \\ & F_{CC} & & \\ & & H_\alpha & \\ & & & H_{\alpha'} \end{bmatrix}$$

[a] The $\mathbf{F}$ matrices for *cis*-2-Butene B_2 and *trans*-2-Butene B_u are the same as the above matrix without the last column (C=C v).

(b) Out-of-Plane Motions

The symbol $F_{\varphi_{ij}}$ is used for the potential constant of torsion between the planes of the groups at either end of the olefinic bond. The subscripts i and j identify the two groups. The subscript 0 is used for $=CH_2$, 1 for $=CH(CH_3)$ and 2 for $=C(CH_3)_2$.

The potential constant for the change in the angle between the C=C bond and the plane of the attached group is designated F_{γ_i}, where i has the values 0, 1, and 2 as above. The symbol $f_{\gamma\gamma}$ is used for the interaction constant between the two γ angles of a molecule.

In order to fit the observed out-of-plane frequencies it was necessary to include an interaction constant $f_{\gamma\varphi}$ between γ_1 and ϕ out-of-plane distortions.

In a preliminary calculation it was found that F_γ and $f_{\gamma\gamma}$ have about the same values in propylene and the butenes as in ethylene but that F_φ exhibits a trend upward with increase in the number of attached methyl groups. Since the order of the matrices involved is small, it was possible then to make further slight adjustments in order to improve the fit with the observed frequencies.

The $\mathbf{F}$ matrices for the out-of-plane frequencies of propylene, *cis-*, *trans-*, and isobutene are given symbolically in table 14.

TABLE 14.—*Reduced* $\mathbf{F}$ *matrices for the out-of-plane vibrations of propylene, cis-, trans-, and isobutene*

Propylene

$$A'' \begin{bmatrix} F_\tau & & \\ & F_{\gamma_0} & f_{\gamma\gamma} \\ & & F_{\gamma_1} \end{bmatrix} \quad \begin{bmatrix} f_{\gamma\phi} \\ F_{\phi_{10}} \end{bmatrix}$$

cis-2-Butene

$$A_2 \begin{bmatrix} F_\tau & \\ & F_{\gamma_1}-f_{\gamma\gamma} \end{bmatrix} \quad \begin{bmatrix} \sqrt{2}f_{\gamma\phi} \\ F_{\phi_{11}} \end{bmatrix} \qquad B_1 \begin{bmatrix} F_\tau & \\ & F_{\gamma_1}+f_{\gamma\gamma} \end{bmatrix}$$

trans-2-Butene

$$A_u \begin{bmatrix} F_\tau & \\ & F_{\gamma_1}+f_{\gamma\gamma} \end{bmatrix} \quad \begin{bmatrix} \sqrt{2}f_{\gamma\phi} \\ F_{\phi_{11}} \end{bmatrix} \qquad B_g \begin{bmatrix} F_\tau & \\ & F_{\gamma_1}-f_{\gamma\gamma} \end{bmatrix}$$

Isobutene

$$B_1 \begin{bmatrix} F_\tau & \\ & F_{\gamma_0} \end{bmatrix} \quad \begin{bmatrix} f_{\gamma\gamma} \\ F_{\gamma_2} \end{bmatrix} \qquad A_2 \begin{bmatrix} F_\tau & \\ & F_{\phi_{20}} \end{bmatrix}$$

For *cis-* and *trans*-2-butene, $F_{\gamma_1}-f_{\gamma\gamma}$ and $F_{\gamma_1}+f_{\gamma\gamma}$ were found to have the values 0.37 and 0.45, respectively. A value of −0.09 was determined for $f_{\gamma\varphi}$ and 1.08 for $F_{\varphi_{11}}$.

In isobutene, F_{γ_0} was set equal to 0.35 in order to fit approximately the observed frequency at 888 cm^{-1}. F_{γ_0} and F_{γ_2} were made to average the same as F_{γ_1} from *cis-* and *trans*-2-butene. Therefore, $F_{\gamma_2}=0.47$. The interaction constant $f_{\gamma\gamma}$ was given the same value as in the two preceding molecules, 0.04. The torsional constant $F_{\varphi_{20}}$ was found to have the value 0.83 by comparison with the observed frequency at 700 cm^{-1}.

In propylene, F_{γ_0} and F_{γ_1} were taken as the mean of the values of F_γ from ethylene and of F_{γ_1} and F_{γ_2} in isobutene giving 0.37 and 0.43, respectively. Giving $f_{\gamma\gamma}$ the usual value of 0.04, we selects $F_{\varphi_{10}}=0.85$ to fit the 580 cm^{-1} frequency in the propylene spectrum.

The increase from $F_{\varphi_{00}}=0.59$ to $F_{\varphi_{10}}=0.85$ to $F_{\varphi_{11}}=1.08$ is reasonably regular. The value of 0.43 for $F_{\varphi_{20}}$ from isobutene seems anomalous, but unless a new line is found in the spectrum there appears to be no alternative.

6. Calculated Frequencies

The values calculated for the in-plane frequencies of *cis-*, *trans-*, and isobutene from the potential constants of section 5 (a) are compared with the observed frequencies in table 15. The observed frequencies marked with an asterisk (*) were not used as guides in the adjustment of the potential constants.

The same comparison for the out-of-plane frequencies is given in table 16.

TABLE 15.—*Comparison of calculated and observed frequencies, in wave numbers, for in-plane vibration*

Compound	Calculated	Observed	Calculated	Observed
	A_1		B_2	
cis-2-Butene	1671	1672	1473	1390
	1242	*1267	1090	*1040
	1016	*1018	972	978
	911	876	586	581
	298	*304	.....	.....
	A_g		B_u	
trans-2-Butene	1693	1681	1353	1304
	1342	1309	1070	1065
	1080	.....	974	973
	920	870	308	.....
	473	507	.....	.....
	A_1		B_2	
Isobutene	1606	1664	1397	1280
	1457	1300	1007	.....
	1002	1053	963	986
	776	800	438	431
	380	378	.....	.....

* This frequency of *cis*-2-butene is observed to be considerably higher than the calculated value. The motion, symmetric in-plane skeletal deformation, involves a rather close approach of the two methyl groups. The additional potential energy from this source probably accounts for the increase in the frequency over the simple calculated value.

TABLE 16.—*Comparison of calculated and observed frequencies, in wave numbers, for out-of-plane vibrations*

Compound	Calculated	Observed	Calculated	Observed
	A_2		B_1	
cis-2-Butene	1049	.....	1028	1046
	951	.....	686	685
	491	402	.....	.....
	A_u		B_g	
trans-2-Butene	1030	.....	1045	1043
	960	964	746	746
	260	.....	.....	.....
	B_1		A_2	
Isobutene	1056	.....	988	.....
	867	888	701	700
	391	.....	.....	.....
	A''			
Propylene	1049	.....	.....	.....
	974	990	.....	.....
	929	911	.....	.....
	573	580	.....	.....

7. The Complete Assignments

The complete vibrational frequency assignments of propylene, *cis-*, *trans-*, and isobutene are presented in tables 17, 18, 19, and 20. The descriptions of the motion are only approximate. Each mode of vibration actually involves a linear combination of all the elementary symmetry modes, but with one type usually predominating. The symbols after each frequency give its origin, according to the following scheme: *IR* for infrared, *R* for Raman, *p* for polarized, *dp* for depolarized, *c* for conventional value and * for calculated.

The two skeletal deformations of *trans*-2-butene were lowered from the calculated values of 260 and 308 cm^{-1} to 240 cm^{-1} and 290 cm^{-1}, respectively, in order that the restricting potential for the rotation of the methyl groups, calculated from calorimetric data and the remainder of the above assignment, should agree with the barrier to methyl rotation calculated from the 210 cm^{-1} Raman line which in turn agrees with the value of the barrier determined for propylene [15].

TABLE 17.—*Vibrational frequency assignment of propylene, in wave numbers*

Type of vibration	A'	A''
C−H ν (ethylenic)	(3) 3050 *c*	....
C−H ν (methyl)	(2) 2950 *c*	2950 *c*
C=C ν	1649 *IR,R(p)*	....
C−C ν	920 *IR,R(p)*	....
CH_2 unsym. δ	1444 *IR,R*—	1444 *IR,R*
CH_3 sym. δ	1370 *c*	....
CH_2 δ	1415 *IR,R(p)*	....
CH_2 wagging	1042 *IR*	1050 (*)
CH_2 wagging	1172 *IR*	911 *IR*
CH wagging	1297 *IR,R(p)*	580 *IR,R(dp)*
Skeletal δ	417 *R(p)*	....
C=CH_2 twisting	....	900 *IR*

TABLE 18.—*Vibrational frequency assignment of cis-2-butene, in wave numbers*

Type of vibration	A_1	A_2	B_1	B_2
C−H ν (ethylenic)	3050 *c*	....	....	3050 *c*
C−H ν (methyl)	(2) 2950 *c*	2950 *c*	2950 *c*	(2) 2950 *c*
C=C ν	1672 *R,IR*	....	....	....
C−C ν	876 *IR*	....	....	978 *R,IR*
CH_3 δ unsym	1450 *c*	1450 *c*	1450 *c*	1450 *c*
CH_3 δ sym	1380 *c*	....	....	1380 *c*
CH_2 wagging	1018 *R,IR*	950 (*)	1040 (*)	1064 *IR*
CH wagging	1267 *R*	1050 (*)	673 *R,IR*	1300 *R,IR*
Skeletal δ	304 *R*	402 *R*	....	583 *R*

TABLE 19.—*Vibrational frequency assignment of trans-2-butene, in wave numbers*

Type of vibration	A_g	A_u	B_g	B_u
C−H ν (ethylenic)	3050 *c*	....	....	3050 *c*
C−H ν (methyl)	(2) 2950 *c*	2950 *c*	2950 *c*	(2) 2950 *c*
C=C ν	1681 *R(p)*	....	....	....
C−C ν	870 *R(p)*	....	....	1065 *IR*
CH_3 δ unsym	1450 *c*	1450 *c*	1450 *c*	1450 *c*
CH_3 δ sym	1380 *c*	....	....	1380 *c*
CH_2 wagging	1080 (*)	1030 (*)	1043 *R(dp)*	973 *IR*
CH wagging	1309 *R(p)*	904 *IR*	746 *R(dp)*	1304 *IR*
Skeletal δ	307 *R(p)*	240 (*)	....	290 (*)

TABLE 20.—*Vibrational frequency assignment of isobutene, in wave numbers*

Type of vibration	A_1	A_2	B_1	B_2
C−H ν (ethylenic)	3050 *c*	....	....	3050 *c*
C−H ν (methyl)	(2) 2950 *c*	2950 *c*	2950 *c*	(2) 2950 *c*
C=C ν	1664 *IR,R(p)*	....	....	....
C−C ν	800 *IR,R(p)*	....	....	986 *IR*
CH_3 δ unsym	1450 *c*	1450 *c*	1450 *c*	1450 *c*
CH_3 δ sym	1380 *c*	....	....	1380 *c*
CH_2	1390 *IR,R(p)*	....	....	....
CH_2 wagging	1053 *IR,R(p)*	988 (*)	1006 *IR*	1007 (*)
CH_2 wagging	....	....	888 *IR,R(dp)*	1280 *IR*
Skeletal δ	378 *R*	700 *R*	301 (*)	431 *IR,R*

V. References

[1] W. S. Gallaway and E. F. Barker, J. Chem. Phys. **10,** 88 (1942).

[2] E. B. Wilson, Jr., J. Chem. Phys. **9,** 76 (1941).

[3] A. G. Meister, F. F. Cleveland, and M. J. Murray, Am. J. Phys. **11,** 239 (1943).

[4] J. E. Rosenthal and G. M. Murphy, Rev. Modern Phys. **8,** 317 (1936).

[5] G. Herzberg, Infrared and Raman spectra of polyatomic molecules (D. Van Nostrand Co., Inc., New York, N. Y.)

[6] Y. L. Tchang, Ann. Soc. Sci. Bruxelles [1] **58,** 87 (1938).

[7] Rayleigh, The theory of sound (The Macmillan Co., New York, N. Y.)

[8] American Petroleum Institute Research Project 44 at the National Bureau of Standards. Catalog of Infrared Spectrograms. Serial Nos. 19, 21, 22, 23; Propylene, *cis*-2-butene, *trans*-2-butene, and isobutene. Contributed by the Shell Development Co., Emeryville, Calif.

[9] E. B. Wilson, Jr. and A. J. Wells, J. Chem. Phys. **9,** 319 (1941).

[10] R. Ananthakrishnan, Proc. Ind. Acad. Sci. **3a,** 527 (1936).

[11] H. Gershinowitz and E. B. Wilson, Jr., J. Chem. Phys. **6,** 247 (1938).

[12] A. Kirrmann, Bul. Soc. Chim. [5] **6,** 845 (1939).

[13] D. Telfair and W. H. Pielemeier, Rev. Sci. Instr. **13,** 122 (1942).

[14] F. Stitt, J. Chem. Phys. **7,** 297 (1939).

[15] J. E. Kilpatrick and K. S. Pitzer, J. Research NBS **37,** (1946) RP1738.

WASHINGTON, May 29, 1946.

U. S. Department of Commerce
National Bureau of Standards

Research Paper RP1769
Volume 38, February 1947

Part of the Journal of Research of the National Bureau of Standards

Infrared Absorption Spectra of Seven Cyclopentanes and Five Cyclohexanes

By Earle K. Plyler, Ralph Stair, and Curtis J. Humphreys

The infrared absorption spectra of seven cyclopentanes and five cyclohexanes have been measured in the region from 2 to 15 microns. The substances were cyclopentane, methylcyclopentane, 1,1-dimethylcyclopentane, *trans*-1,2-dimethylcyclopentane, *trans*-1, 3-dimethylcyclopentane, *cis*-1,2-dimethylcyclopentane, and *cis, trans, cis*-1,2,4-trimethylcyclopentane, also cyclohexane, methylcyclohexane, 1,1-dimethylcyclohexane, *trans*-1,2-dimethylcyclohexane, and *cis*-1,2-dimethylcyclohexane. The wavelengths of all the observed absorption bands are given in a table, and a graph is shown of the percentage transmission over the wavelength region of each substance. The hydrocarbons were highly purified in the Chemistry Division and these spectra will be of value as a check on the purity of these compounds which may be obtained from other sources. Also the more intense bands serve as a means of identification. For each substance the bands that are best suited for distinguishing it are noted.

Of special interest are the four dimethylcyclopentanes which were studied. The structural positions of the substituted methyl groups differ only slightly, but the spectral difference is quite marked. The infrared absorption spectra are well suited to show characteristic differences between isomers.

The measurements were made with a Perkin-Elmer spectrometer with a General Motors amplifier and Brown recorder. A slit control mechanism is described in detail. Although the slit control gear arrangement is relatively simple, the results obtained with it are good. The energy output is held nearly constant from 3.5 to 14.5 microns.

I. Introduction

In the Bureau's cooperative research program with the American Petroleum Institute, many of the constituents of petroleum have been purified to a high degree. Various physical and chemical properties of these constituents are being investigated. The Radiometry Section of the Bureau is contributing to this program by measuring the infrared absorption spectra of a number of these compounds. This report deals with two series of compounds, cyclopentanes and cyclohexanes, that are closely related and which show some interesting properties. The absorption spectra of 1,1-dimethylcyclopentane, *cis*-1,2-dimethylcyclopentane, *cis, trans, cis*-1,2,4-trimethylcyclopentane, and 1,1-dimethylcyclohexane have not been previously measured.

II. Method of Measurement

A Perkin-Elmer model 12A infrared spectrometer with an NaCl prism was used as the dispersing instrument. The prism face is 60 by 75

mm and an off-axis mirror of 27 cm focal length is used as the collimator. More details about the instrument can be found in the article "Small prism infrared spectrometry" [1].[1] It was found that better resolution of the water-vapor band at 6.26μ was obtained when the slits were reduced from 0.05 to 0.02 mm. This demonstrated the high quality of the optical parts.

When the instrument was obtained from the manufacturer, there was no provision for the automatic rotation of the wavelength drum or the slit drum. In order to measure the region from 2μ to 15μ continuously, a synchronous motor with gear reduction was connected to the wavelength drum. The selection of gears made it possible to traverse this region of the spectrum in 45 or 90 minutes. A globar element was used for the source, and for a fixed slit width the maximum radiation was found to occur in the region of 2μ. When the drum was set for wavelengths greater than 2μ, the deflection decreased. In order to keep the deflections approximately constant, it was necessary to open the slits for longer wavelength settings. A graph was plotted of the slit widths required to produce constant energy at various wavelengths. The relationship is not linear, but it was found that three chords closely approximated the curve. The aim of constant-energy output could almost be attained by opening the slits with three different constant speeds. A synchronous motor was used with gears of such ratios that the slits could be opened at the appropriate speeds. Also, a gear shift was installed so that the speed could be changed without stopping the instrument.

With this arrangement, the energy curve is of about the same height above the zero from 3.5μ to 14μ. There are some regions of the spectrum where the energy drops by a few percent. Somewhat better results could be obtained if, in addition to the slit change, the impedance of the output circuit of the amplifier was varied. Variation of the amplifier gain would not be a satisfactory method of control as the energy of the radiating source at 2μ is many times greater than the energy at 14μ.

Figure 1 shows the slit control mechanism. The letters identify the different parts. The gears have the following number of teeth: *A*, 84; *B*, 24; *C*, 18 (1⅛-in-length rod); *D*, 36; *E*, 32; *F*, 28 (⅝-in-length rod); *G*, 24; *H*, 12; *I*, 16; *J*, 24; *K*, 38; *L*, 32; *M*, motor 2 rpm; *N*, gear shift. The gears are standard Boston gears and the rod-gears have the same size teeth.

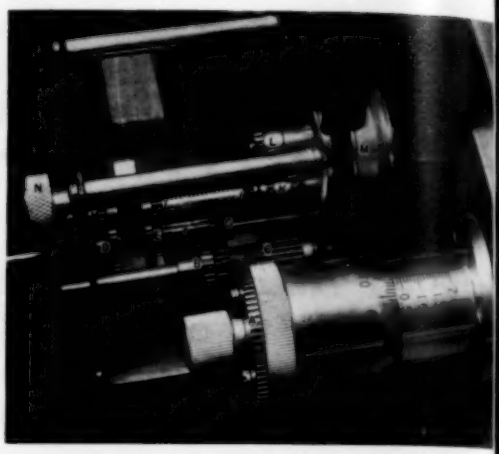

FIGURE 1.—*Slit-control mechanism, showing gears and arrangement.*

The ordinary operating conditions are the globar at 50 volts, the General Motors amplifier [2] gain dial at 2.5, wavelength drum traversed in 45 minutes. The slit micrometer is set at 0.019 mm at 2μ. The wavelength drum is operated to 3μ without engaging the gears. From 3 to 9μ, the low gear, *H*, is used. From 9 to 12μ, gear *I* is used, and from 12 to 15μ, gear *J* is engaged. For different scanning speeds, different gear ratios would be needed. Other features are to be added to the device, such as an automatic stop and a reversing gear for the near infrared region.

The thermocouple is in a housing with a KBr window, and it is kept at pressure below 10^{-4} mm. The pressure is kept low over long periods of time by means of activated charcoal, and pumping is necessary only every 3 or 4 weeks. The thermocouple approaches its final output in about 1½ seconds after it is exposed to radiation. It is connected to a General Motors amplifier that operates a Brown recorder. A smooth tracing is obtained when the amplifier is not operated on too high gains. Under ordinary operating conditions, 1 microvolt produces a full-scale deflection, and the noise level is less than one-fourth of 1 percent of the full scale. The thermocouple contains a

[1] Numbers in brackets indicate the literature references at the end of this paper.

mpensating junction, but this does not completely eliminate the drift. The room temperature is controlled, which is of great help in stabilizing the thermocouple. No change is observed in the zero owing to the opening of the slits, until they become one-half of a millimeter in width. For this and larger openings the zero drift may be considerable.

Under average operating conditions the widths of frequency bands resolved are 16.4 cm^{-1} at 3.0μ, 4 cm^{-1} at 6.4μ, 2.4 cm^{-1} at 11μ, and 3.5 cm^{-1} at 4.3μ. In the region beyond 5μ the wavelength of sharp bands can be repeated to 0.01μ. The instrument is practically free of stray radiation between 4 and 12μ. At 14.5μ the stray radiation produces about 10 percent of the total deflection.

In the measurement of the absorption of the compounds, two cell thicknesses were used, 0.05 mm and 0.4 mm, the thicker cell being used to check weak bands. Even with the 0.05-mm cell, the absorption was 100 percent in the region of 4μ. As some of the liquids under investigation have high vapor pressures at room temperature, it is necessary to use an enclosed cell. The cell was made by using two plates of rock salt, and separating them by a lead shim 0.05 mm in thickness. In one of the rock-salt plates two holes were drilled. This allowed the cell to be filled after it was assembled and placed in a metal holder. The shim was cut out so that the radiation passed through the cell and so that the cell could be filled through the holes in the rock-salt plate. The samples of the materials were in the liquid state, and a small amount was drawn from the container into a medicine dropper, from which the liquid was slowly passed into the cell. At the same time a small tube, connected to the reduced-pressure system, was placed in the other hole of the rock-salt plate, and the liquid was drawn into the cell, completely filling it without bubbles. This method of filling was used in rinsing out the cell, when changing from one liquid to another.

The arbitrary numbers of the wavelength drum were calibrated into wave numbers by observing the settings corresponding to known lines and absorption bands. Lines of cadmium [3] and mercury [4] were used for the visible and near infrared region. The absorption bands of water vapor [5] and carbon dioxide gas [6] occurring as atmosphere constituents were used for calibration of the longer wavelengths. The absorption spectra of ammonia gas [7] and methyl alcohol vapor [8] also were measured by the use of a gas cell. In this way, a fairly large number of calibration points distributed throughout the spectrum was obtained.

The spectrometer is partially enclosed and a drying agent is kept in both the prism and source compartments. This reduces the water-vapor absorption. The complete removal of the water-vapor absorption spectrum requires an enclosed instrument that may be evacuated or filled with dry gas. However, the absorption bands produced by water vapor and carbon dioxide serve the purpose of a constant check on wavelength calibration and the resolution of the instrument.

Figure 2 shows the trace obtained on the Brown recorder of the 6.26μ absorption band due to water vapor in the atmosphere in the region from 4μ to 7μ. The upper curve was obtained by using slits of 0.05 mm at the shorter wavelength end of the spectrum, and opening them with the automatic slit drive. The amount of energy in the transparent regions between the absorption lines is about constant, and the absorption curve as recorded appears similar to a graph which has the percentage transmission plotted as a function of wavelength. The lower trace in figure 2 is for the water-vapor band with the slits at 0.02 mm at the shorter wavelength side. It is readily seen that the resolving power has increased with the nar-

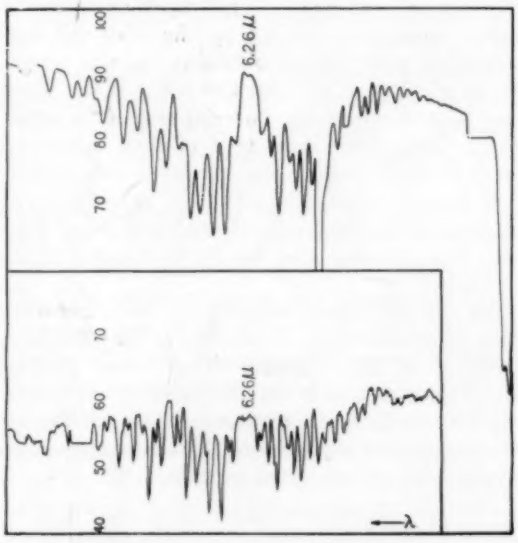

FIGURE 2.—*Two traces for the water-vapor band at 6.26μ observed with different slit widths.*

rower slits. On each side of the center of the band at 6.26μ there is seen one line in the upper curve of figure 2. In the lower curve each of these lines has been separated into two. A comparison of other regions of the spectrum will show that additional lines have been revealed by the higher resolution.

The percentage transmission for the different materials was calculated from the recorded energy curve. At first the absorption spectrum of the substance was obtained by placing the filled cell in front of the entrance slit of the spectrometer. The spectrometer drum was connected to the synchronous motor, and a trace of the region from 2 to 15μ was obtained without removing the cell or using the shutter. This curve showed the wavelength drum readings of the absorption bands. Then a second trace was obtained, and at selected points, in the regions between the absorption bands, the cell was temporarily removed to obtain full-energy values, and similarly, at other convenient points, the shutter was inserted to determine the zero reading. A line was drawn connecting the full-energy values on the trace, and similarly, another was drawn connecting the zero readings. From these two lines and the energy trace with the cell in place, the percentage absorption could be calculated for any point in the spectrum. A correction was made for the radiation loss due to the rock-salt cell windows. In the region of the water-vapor bands, the readings for the filled cell were compared with values obtained for the atmospheric absorption without the cell. Weak bands may be missed because of overlapping of the water-vapor lines. This same type of error is encountered in the region of the carbon-dioxide absorption bands. This difficulty was partially overcome by using thick cells of the liquid being studied, thus causing the bands to become much stronger.

All the substances which have been measured were obtained from F. D. Rossini of the Chemistry Division of the Bureau. They were purified under his direction in connection with the American Petroleum Institute Research Project No. 44. The substances studied and the amount of impurity in each one are given in table 1 [9].

TABLE 1.—*Purity of compounds*

Substance	Impurity
	Mole percent
Cyclopentane	0.05 ±0.0
Methylcyclopentane	.25 ± .0
1,1-Dimethylcyclopentane	.05 ± .0
trans-1,2-Dimethylcyclopentane	.10 ± .1
cis-1,2-Dimethylcyclopentane	.03± .0
trans-1,3-Dimethylcyclopentane	.30 ± .0
cis, trans, cis-1,2,4-Trimethylcyclopentane	.24 ± .1
Cyclohexane	.012± .0
Methylcyclohexane	.36 ± .1
1,1-Dimethylcyclohexane	.10 ± .0
trans-1,2-Dimethylcyclohexane	.08 ± .0
cis-1,2-Dimethylcyclohexane	.024± .0

III. Results and Discussion

Figure 3 shows the percentage transmission o cyclopentane. For a cell thickness of 0.05 mm only four intense bands are observed. Th wavelengths of the bands and their frequencie are given in table 2. The coefficients of absorptio have not been calculated for these bands. How ever, the 12 compounds have been measured wit the same cell thickness, and the relative intensit of absorption of any band of one compound will b directly comparable with that of any band of an of the other 11 compounds. The band at 3.4μ i very intense, which arises from the CH stretchin vibrations. As all these materials contain severa CH bonds, this band will be intense in eac spectrum. The intense absorption at 3.4μ i made up of several bands. With cells of th order of 0.004 mm in thickness the separat bands can be observed. The absorption spectrum in this region was measured with thin cells fo *cis, trans, cis*-1,2, 4-trimethylcyclopentane, cyclo-hexane, *trans*-1,2-dimethylcyclohexane and me-thylcyclohexane. Each substance shows two o three minima of transmission in the region of 3.4μ when a cell of effective thickness 0.004 mm wa used. The thin absorption layers were obtained by diluting these two hydrocarbons with CCl_4 i a cell of 0.05 mm in thickness. When the cel contained only CCl_4, no absorption bands were observed so the entire absorption observed in th mixtures containing the hydrocarbons was attrib-uted to them. The rock-salt prism is not well suited for measurements in this region as its

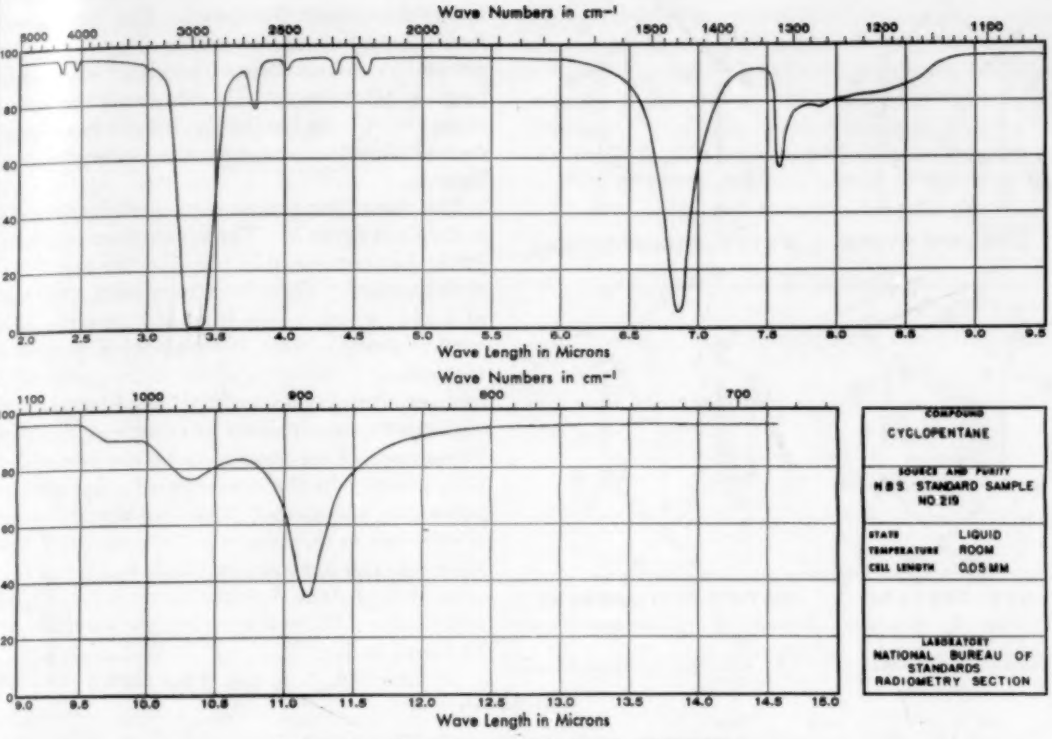
Wave Numbers in cm⁻¹
8000 4000 3000 2500 2000 1500 1400 1300 1200 1100
100 80 60 40 20 0
2.0 2.5 3.0 3.5 4.0 4.5 5.0 5.5 6.0 6.5 7.0 7.5 8.0 8.5 9.0 9.5
Wave Length in Microns
Wave Numbers in cm⁻¹
1100 1000 900 800 700
100 80 60 40 20 0
9.0 9.5 10.0 10.5 11.0 11.5 12.0 12.5 13.0 13.5 14.0 14.5 15.0
Wave Length in Microns
COMPOUND
CYCLOPENTANE
SOURCE AND PURITY
NBS STANDARD SAMPLE NO 219
STATE LIQUID
TEMPERATURE ROOM
CELL LENGTH 0.05 MM
LABORATORY
NATIONAL BUREAU OF STANDARDS
RADIOMETRY SECTION

FIGURE 3.—*Percentage transmission of cyclopentane.*

ispersion is low. With a grating or a lithium uoride prism the bands could have been observed ith better detail. The strong band at 6.86μ rises from the CH bending motion. The intensi- es of the 3.4 and 6.86μ bands vary from one ubstance to the next but the positions remain lmost constant for the cyclopentane and the yclohexane compounds.

The number of fundamental vibrations for a olecule of n atoms is $3n-6$. For cyclopentane here would be 39 fundamental bands. In addi- on to these bands there are possibly many combi- ation and harmonic bands, so that the total umber of absorption bands could be 200 to 300. owever, the observed spectrum does not show uch a large number of absorption bands. The educed number of bands in the observed spectrum ay be due to the fact that a number of the bands re located in the region beyond 15μ and that the ymmetry properties reduce the number of vibra- ons which would be active in the infrared ab- orption.

The structure of the cyclopentane molecule and also that of methylcyclopentane are illustrated in figure 4. A study of the various chemical and physical properties has not yet made it possible to decide if all the carbon atoms are in the same plane. If they are coplanar, a high degree of symmetry would be present. When methyl groups are substituted for the hydrogen atoms, there are a number of new compounds formed. If two methyl groups are substituted on the same side of the carbon plane the configuration is called *cis* and if on opposite sides it is called *trans*. By substituting methyl groups at various positions of the molecule several isomers may be formed.

A distinguishing feature of the absorption spectrum of cyclopentane is the presence of two intense bands at 7.6 and 11.2μ, that occur in addition to the two regions of absorption due to CH vibrations. When substitutions are made in the cyclopentane molecule these bands change in position and intensity.

727972—47——6

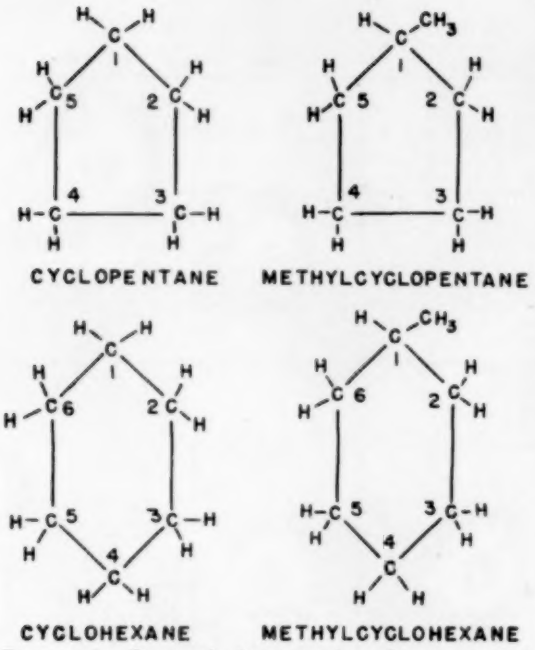

FIGURE 4.—*Structural diagram of cyclopentanes and cyclohexanes.*

Any possible displacements of the carbon atoms from the coplanar arrangement are not indicated.

In table 2 all the bands that have been observed for cyclopentane are listed. The low intensity bands occurring in the region from 2 to 5μ are probably combinations of bands of longer wavelengths. Besides the CH vibrations there are no elements in the molecule which have fundamental vibrations occurring at wavelengths shorter than 5μ.

The absorption spectrum of methylcyclopentane is shown in figure 5. The substitution of a methyl group has considerably changed the spectrum of cyclopentane. There is a strong band in the region of 7.26μ, which arises from the presence of the methyl group. Any vibration of a part of the molecule is a vibration of the entire molecule, but some groups that are tightly bound together may, with good approximation, be considered as separate vibrations. This appears to be the case with the CH_3 group. In the spectrum of other molecules containing the methyl group, an absorption band is observed in this region. Also, methylcyclopentane does not have strong bands at 7.6 and 11.1μ as in cyclopentane, but has bands at 7.4, 8.8, 10.2 and 11.25μ. There are no intense bands between 11.5 and 14.5μ.

In figures 6, 7, 8, and 9 are shown the spectra

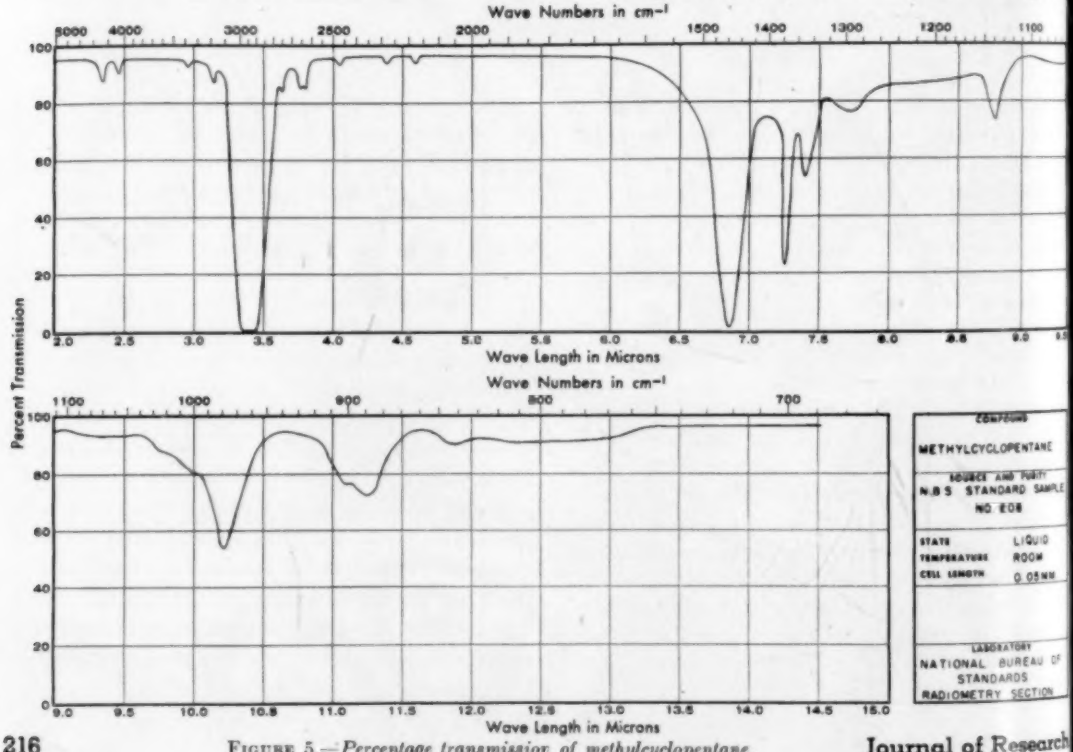

FIGURE 5.—*Percentage transmission of methylcyclopentane.*

the four dimethylcyclopentanes, 1,1-dimethylcyclopentane, *cis*-1, 2-dimethylcyclopentane, *trans*-1,2-dimethylcyclopentane, and *trans*-1,3-dimethylcyclopentane. The 7.3μ band varies very little in wavelength, but the intensity has increased when compared with methylcyclopentane. The greater intensity is due to the presence of two methyl groups in each molecule. In the case of the 1,1-dimethylcyclopentane the absorption in this region shows two maxima. In the region between 7.5 and 11.5μ there is a considerable difference between the spectra of these four isomers. Any one of the group could readily be identified by a study of the spectra in this region. This is a good example of the application of infrared absorption spectra to the problem of identifying isomers. The wavelengths of the absorption bands of the four dimethylcyclopentanes are given in table 20.

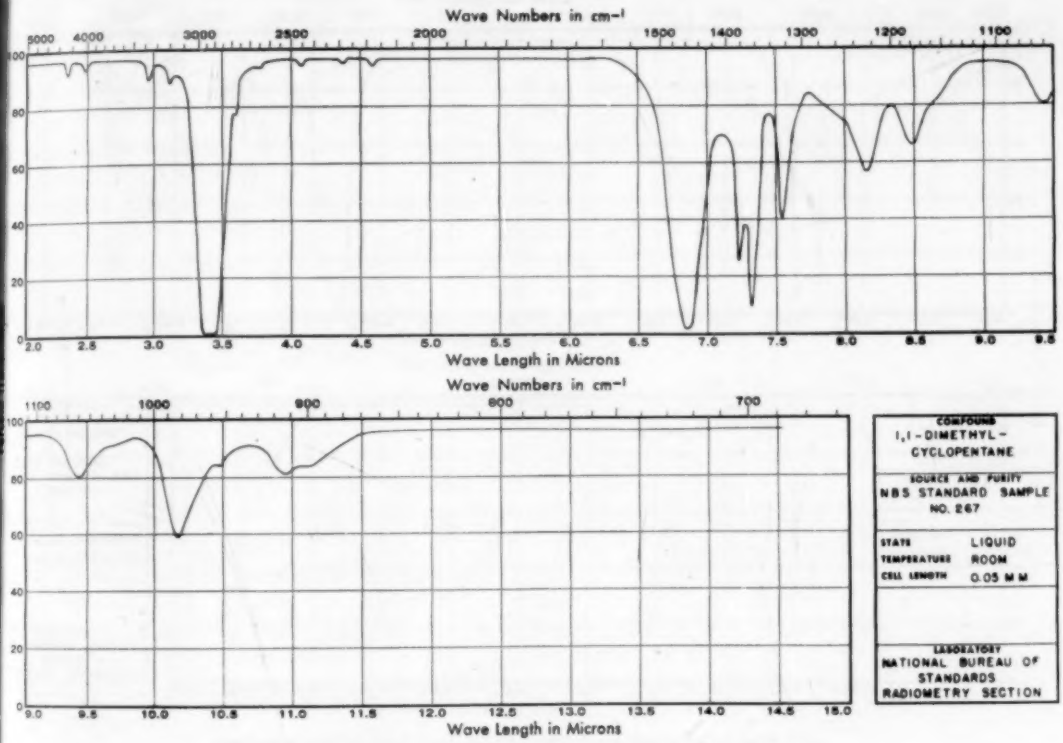
Wave Numbers in cm⁻¹
5000 4000 3000 2500 2000 1500 1400 1300 1200 1100
100 80 60 40 20 0
2.0 2.5 3.0 3.5 4.0 4.5 5.0 5.5 6.0 6.5 7.0 7.5 8.0 8.5 9.0 9.5
Wave Length in Microns
Wave Numbers in cm⁻¹
1100 1000 900 800 700
100 80 60 40 20 0
9.0 9.5 10.0 10.5 11.0 11.5 12.0 12.5 13.0 13.5 14.0 14.5 15.0
Wave Length in Microns
COMPOUND
1,1-DIMETHYL-CYCLOPENTANE
SOURCE AND PURITY
NBS STANDARD SAMPLE NO. 267
STATE LIQUID
TEMPERATURE ROOM
CELL LENGTH 0.05 M M
LABORATORY
NATIONAL BUREAU OF STANDARDS
RADIOMETRY SECTION

FIGURE 6.—*Percentage transmission of 1,1-dimethylcyclopentane.*

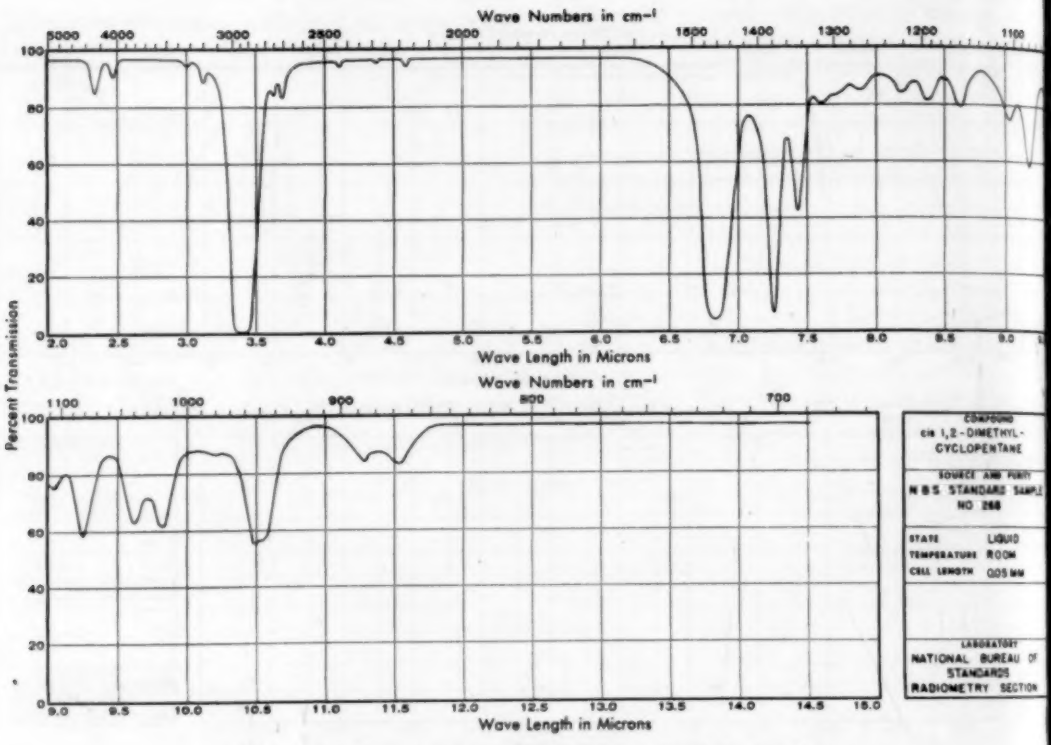

FIGURE 7.—*Percentage transmission of cis-1,2-dimethylcyclopentane.*

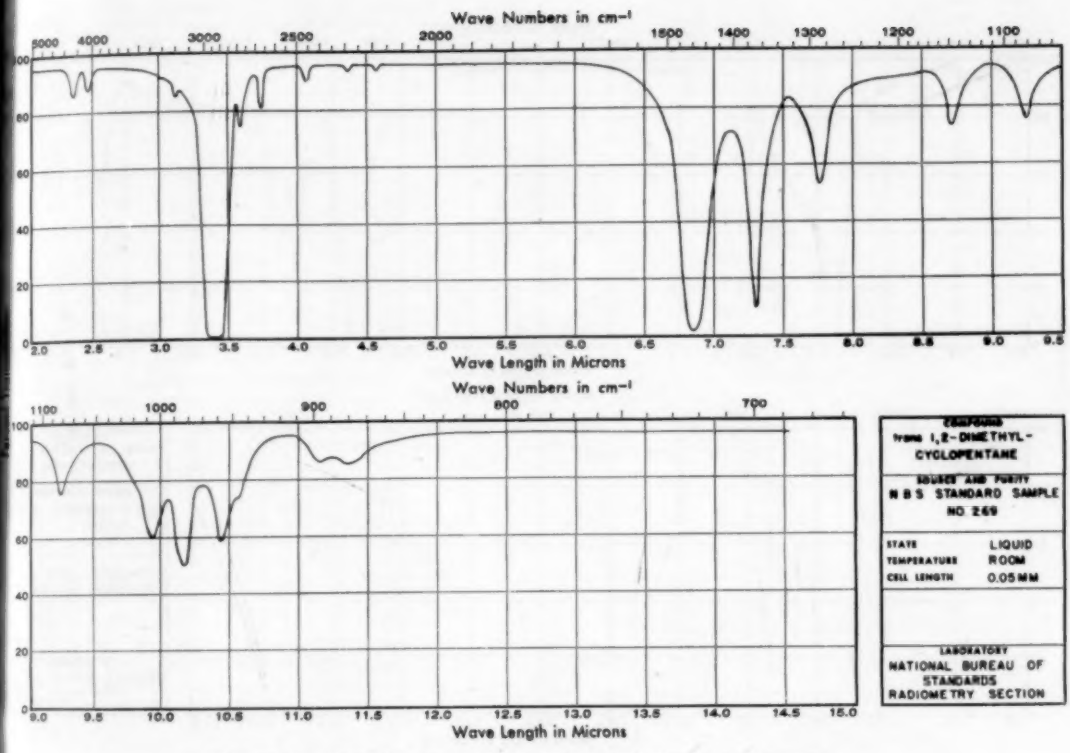
Wave Numbers in cm⁻¹
5000 4000 3000 2500 2000 1800 1400 1300 1200 1100
Wave Length in Microns
2.0 2.5 3.0 3.5 4.0 4.5 5.0 5.5 6.0 6.5 7.0 7.5 8.0 8.5 9.0 9.5
Wave Numbers in cm⁻¹
1100 1000 900 800 700
Wave Length in Microns
9.0 9.5 10.0 10.5 11.0 11.5 12.0 12.5 13.0 13.5 14.0 14.5 15.0
trans 1,2-DIMETHYL-CYCLOPENTANE
NBS STANDARD SAMPLE NO 249
STATE LIQUID
TEMPERATURE ROOM
CELL LENGTH 0.05 MM
NATIONAL BUREAU OF STANDARDS
RADIOMETRY SECTION

FIGURE 8.—*Percentage transmission of trans-1,2-dimethylcyclopentane.*

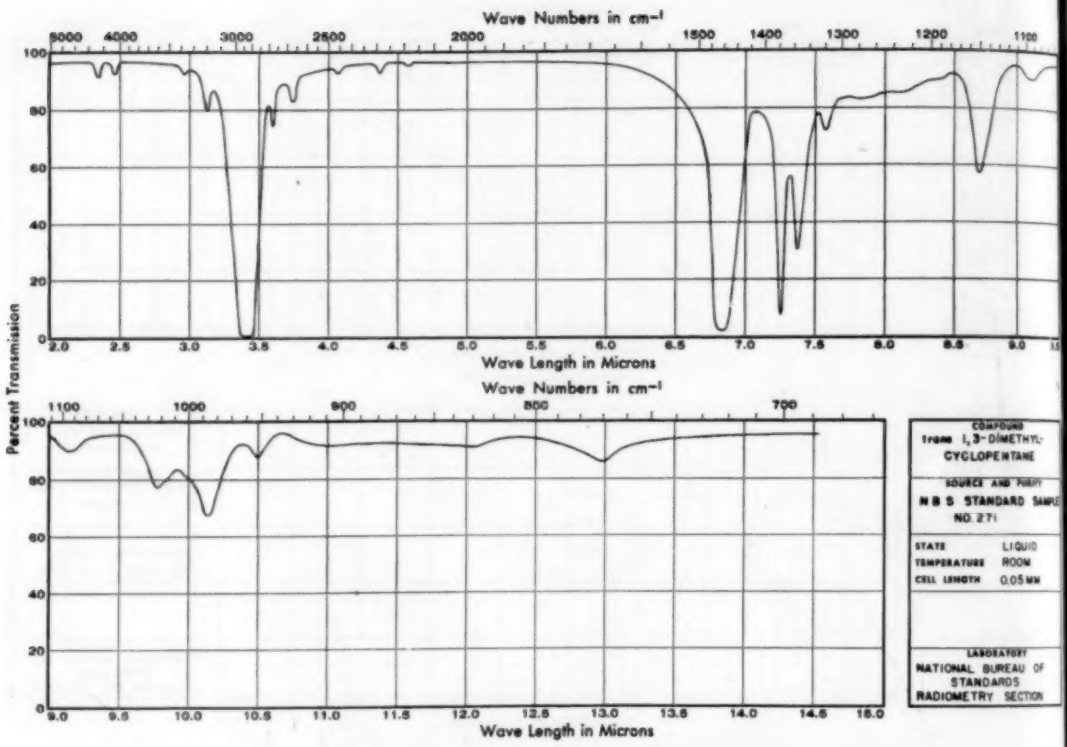
Wave Numbers in cm⁻¹
5000 4000 3000 2500 2000 1500 1400 1300 1200 1100
Percent Transmission
100 80 60 40 20 0
2.0 2.5 3.0 3.5 4.0 4.5 5.0 5.5 6.0 6.5 7.0 7.5 8.0 8.5 9.0
Wave Length in Microns
Wave Numbers in cm⁻¹
1100 1000 900 800 700
100 80 60 40 20 0
9.0 9.5 10.0 10.5 11.0 11.5 12.0 12.5 13.0 13.5 14.0 14.5 15.0
Wave Length in Microns
COMPOUND
trans 1,3-DIMETHYL-CYCLOPENTANE
SOURCE AND PURITY
N B S STANDARD SAMPLE NO. 271
STATE LIQUID
TEMPERATURE ROOM
CELL LENGTH 0.05 MM
LABORATORY
NATIONAL BUREAU OF STANDARDS
RADIOMETRY SECTION

FIGURE 9.—*Percentage transmission of trans-1,3-dimethylcyclopentane.*

TABLE 2.—*Location of infrared absorption bands*

Wavelength	Frequency	Wavelength	Frequency
CYCLOPENTANE			
Microns	cm^{-1}	*Microns*	cm^{-1}
2.34	4274	4.37	2288
2.46	4065	4.59	2179
3.01	3322	6.85	1460
3.38	2959	7.59	1318
3.78	2646	7.88	1269
4.02	2488	10.31	970
----	----	11.16	896
METHYLCYCLOPENTANE			
2.34	4274	4.59	2179
2.46	4065	6.86	1458
2.96	3378	7.26	1377
3.14	3185	7.40	1351
3.43	2915	7.72	1295
3.63	2755	8.78	1139
3.76	2660	10.21	979
3.80	2632	11.09	902
4.05	2469	11.25	889
4.39	2278	11.87	842
1,1-DIMETHYLCYCLOPENTANE			
2.34	4274	6.85	1460
2.48	4032	7.23	1383
2.96	3378	7.32	1366
3.12	3205	7.54	1326
3.41	2933	8.15	1227
3.59	2786	8.48	1179
3.77	2653	9.43	1060
4.07	2457	10.17	983
4.37	2288	10.47	955
4.59	2179	10.95	913
----	----	11.13	898
***cis*-1,2-DIMETHYLCYCLOPENTANE**			
2.33	4292	7.60	1316
2.47	4049	7.89	1267
3.00	3333	8.18	1222
3.12	3205	8.37	1195
3.41	2933	8.62	1160
3.63	2755	9.04	1106
3.69	2710	9.25	1081
4.11	2433	9.62	1040
4.37	2288	9.82	1018
4.59	2179	10.49	953
6.83	1464	10.55	948
7.26	1377	11.28	887
7.43	1346	11.53	867
***trans*-1,2-DIMETHYLCYCLOPENTANE**			
2.35	4255	7.30	1370
2.46	4065	7.76	1289
3.12	3205	8.71	1148
3.40	2941	9.25	1081
3.59	2786	9.94	1006

TABLE 2.—*Location of infrared absorption bands*—Continued

Wavelength	Frequency	Wavelength	Frequency
***trans*-1,2-DIMETHYLCYCLOPENTANE**			
Microns	cm^{-1}	*Microns*	cm^{-1}
3.74	2674	10.17	983
4.07	2457	10.44	958
4.36	2294	10.57	946
4.57	2188	11.15	897
6.85	1460	11.35	881
***trans*-1,3-DIMETHYLCYCLOPENTANE**			
2.34	4274	6.84	1462
2.46	4065	7.26	1377
2.96	3378	7.38	1355
3.12	3205	7.57	1321
3.40	2941	8.69	1151
3.60	2778	9.15	1093
3.75	2667	9.77	1024
4.07	2457	10.14	986
4.37	2288	10.50	952
4.57	2188	12.97	771
***cis-trans-cis*-1,2,4-TRIMETHYLCYCLOPENTANE**			
2.30	4348	7.27	1376
2.33	4292	7.35	1361
2.45	4082	7.46	1340
3.00	3333	7.66	1305
3.13	3195	7.80	1282
3.43	2915	8.02	1247
3.63	2755	8.67	1153
3.77	2653	9.26	1080
4.05	2469	9.77	1024
4.11	2433	9.97	1003
4.66	2146	10.37	964
4.79	2088	10.67	937
4.98	2008	11.38	879
6.86	1458	13.00	769
CYCLOHEXANE			
2.30	4348	4.61	2169
2.34	4274	4.68	2137
2.38	4202	4.84	2066
2.42	4132	5.01	1996
2.51	3984	5.09	1965
2.90	3448	5.23	1912
3.00	3333	5.44	1838
3.12	3205	5.62	1779
3.41	2933	5.93	1686
3.52	2841	6.90	1449
3.67	2725	7.41	1350
3.70	2703	7.95	1258
3.77	2653	8.60	1163
3.93	2545	9.03	1107
3.99	2506	9.61	1041
4.11	2433	9.84	1016
4.29	2331	11.05	905
4.42	2262	11.61	861

TABLE 2.—*Location of infrared absorption bands*—Continued

Wavelength	Frequency	Wavelength	Frequency
METHYLCYCLOHEXANE			
Microns	cm^{-1}	*Microns*	cm^{-1}
2.32	4310	4.80	2083
2.36	4237	4.96	2016
2.41	4149	5.26	1901
2.45	4082	5.56	1799
2.49	4016	6.86	1458
2.53	3953	7.27	1376
2.56	3907	7.33	1364
2.87	3484	7.43	1346
2.97	3367	7.66	1305
3.06	3268	7.92	1263
3.14	3185	8.01	1248
3.20	3125	8.57	1167
3.42	2924	9.02	1109
3.62	2762	9.15	1093
3.69	2710	9.43	1060
3.79	2639	9.68	1033
4.02	2488	10.34	967
4.09	2445	10.99	910
4.41	2268	11.47	872
4.51	2217	11.86	843
4.60	2174	12.76	784
4.71	2123	12.96	772
1,1-DIMETHYLCYCLOHEXANE			
2.30	4348	5.52	1812
2.32	4310	6.85	1460
2.43	4115	7.22	1385
2.48	4032	7.32	1366
2.62	3817	7.55	1325
2.87	3484	7.70	1299
2.98	3356	7.80	1282
3.08	3247	7.91	1264
3.13	3195	8.02	1247
3.40	2941	8.40	1190
3.63	2755	8.50	1176
3.68	2717	8.69	1151
3.90	2564	9.11	1098
3.99	2506	9.25	1081
4.08	2451	9.53	1049
4.38	2283	9.74	1027
4.51	2217	10.15	985
4.56	2193	10.39	962
4.71	2123	10.67	937
4.92	2033	10.83	923
4.99	2004	10.88	919
5.12	1953	11.59	863
5.24	1908	11.78	849
		12.81	781
cis-1,2-DIMETHYLCYCLOHEXANE			
2.29	4367	7.25	1379
2.31	4329	7.31	1368
2.44	4098	7.47	1339
2.58	3876	7.58	1319
3.15	3175	7.68	1302
3.41	2933	7.96	1256
3.64	2747	8.02	1247
3.70	2703	8.18	1222
3.79	2639	8.62	1160
4.01	2494	9.14	1094

TABLE 2.—*Location of infrared absorption bands*—Continued

Wavelength	Frequency	Wavelength	Frequency
cis-1,2-DIMETHYLCYCLOHEXANE			
Microns	cm^{-1}	*Microns*	cm^{-1}
4.09	2445	9.48	1055
4.37	2288	9.79	1021
4.58	2183	9.94	1006
4.67	2141	10.22	978
4.82	2075	10.60	943
4.90	2041	10.86	921
4.99	2004	11.35	881
5.19	1927	11.89	841
5.39	1855	12.07	829
5.62	1779	12.43	805
6.68	1458	13.70	730
trans-1,2-DIMETHYLCYCLOHEXANE			
2.26	4425	5.57	1795
2.30	4348	6.87	1456
2.38	4202	7.28	1374
2.85	3509	7.46	1340
2.95	3390	7.66	1305
3.04	3289	7.97	1255
3.13	3195	8.18	1222
3.42	2924	8.50	1176
3.62	2762	9.03	1107
3.69	2710	9.43	1060
3.80	2632	9.59	1043
3.92	2551	9.95	1005
4.02	2488	10.33	968
4.12	2427	10.56	948
4.34	2304	10.82	924
4.44	2252	11.31	884
4.55	2198	11.66	858
4.89	2045	12.07	829
4.96	2016	12.20	820

The absorption spectrum of *cis*, *trans*, *cis*-1,2,4-trimethylcyclopentane was measured and the results are shown in figure 10. The CH vibrations at 3.4μ and 6.86μ are about the same in location and intensity as in the other cyclopentanes. The methyl group has a very strong band at 7.27μ. The intensity of the band is greater than that of the dimethylcyclopentanes, but its position is the same. From structural relations this trimethylcyclopentane should have some bands in common with *trans*-1,3-dimethylcyclopentane. There is a band at 13.0μ which is present only in these two cyclopentanes. An intense band also occurs at 8.68μ in the spectrum of both these substances. In like manner the trimethylcyclopentane spectrum and that of *trans*-1,2-dimethylcyclopentane should have some common features. There are

bands at 9.24 and 11.38μ in each spectrum. The bands at 7.78, 8.70, 9.94, and 10.38μ in the spectrum of *trans*-1,2-dimethylcyclopentane are observed also in the spectrum of *cis, trans, cis*-1,2,4-trimethylcyclopentane at approximately the same wavelengths. The other dimethylcyclopentanes do not show as close a relation in their spectra to the trimethylcyclopentane as the two compared here.

The infrared absorption spectra of five cyclohexanes have been measured. In figure 11 is shown the percentage transmission of cyclohexane. Five intense bands are located at wavelengths greater than 7μ and are characteristic of this molecule. These bands make it possible to readily distinguish cyclohexane from other hydrocarbons. Also, there are a large number of low-intensity bands in the region from 2 to 6μ. This is quite different from the spectrum of cyclopentane in this region. By the presence of so many active infrared bands, it is likely that there is not a high degree of symmetry of this molecule. A structural diagram is shown in figure 4 of cyclohexane and methylcyclohexane. The dimethylcyclohexanes are formed by substituting the methyl groups for the hydrogen atoms at different positions of the molecule. Although in the diagram the carbon atoms are placed in a plane for simplicity of representation, the present indications from various chemical and physical properties point to the carbon atoms not being in a plane but in a chair-like arrangement. That is, the carbons in positions 1, 2, and 3 form a plane, the carbons 1, 3, 4, and 6 form another plane, and carbons 4, 5, and 6, a third plane. As has been mentioned, the 30 combination and harmonic bands, observed in the near infrared with a cell thickness of 0.05 mm, indicate an irregular rather than a planar arrangement of the carbons. The region from 14 to 15μ was studied with different cell thicknesses up to 1 mm and no band was found. Because of the decrease in energy due to rock-salt absorption and the presence of the carbon-dioxide absorption band, the accuracy is somewhat less than at shorter wavelengths. A KBr prism was also used in the instrument, but no absorption band

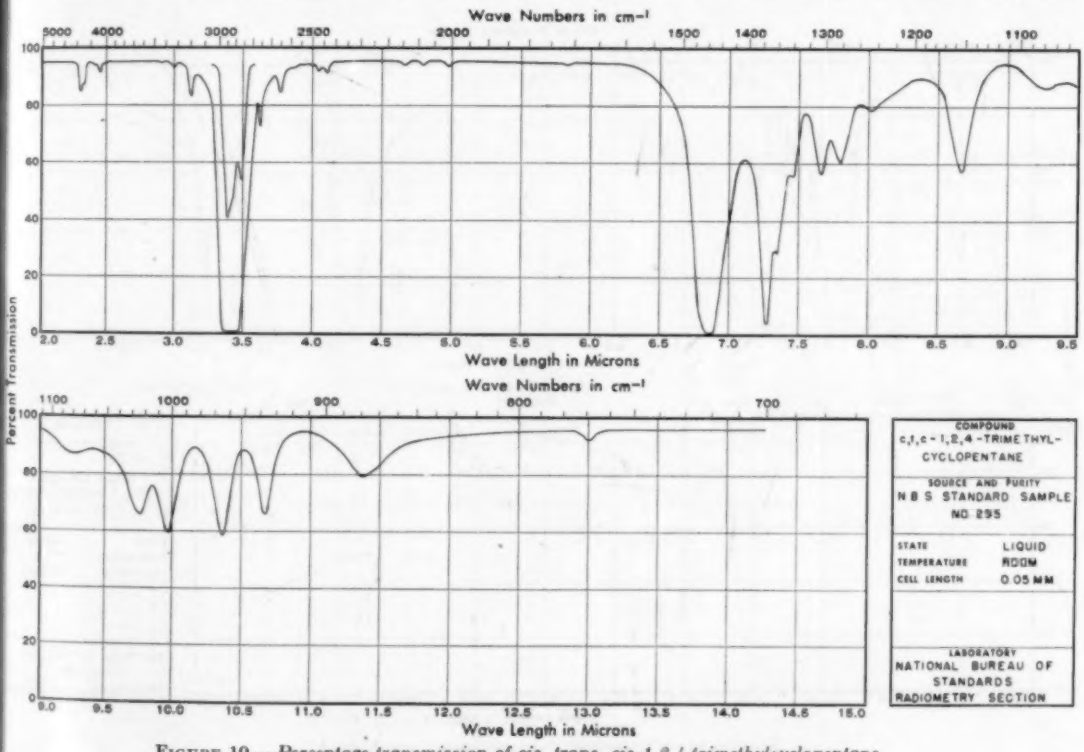
Wave Numbers in cm⁻¹
5000 4000 3000 2500 2000 1500 1400 1300 1200 1100
Percent Transmission
100 80 60 40 20 0
2.0 2.5 3.0 3.5 4.0 4.5 5.0 5.5 6.0 6.5 7.0 7.5 8.0 8.5 9.0 9.5
Wave Length in Microns
Wave Numbers in cm⁻¹
1100 1000 900 800 700
100 80 60 40 20 0
9.0 9.5 10.0 10.5 11.0 11.5 12.0 12.5 13.0 13.5 14.0 14.5 15.0
Wave Length in Microns
COMPOUND
c,t,c-1,2,4-TRIMETHYL-CYCLOPENTANE
SOURCE AND PURITY
N B S STANDARD SAMPLE NO 295
STATE LIQUID
TEMPERATURE ROOM
CELL LENGTH 0.05 MM
LABORATORY
NATIONAL BUREAU OF STANDARDS
RADIOMETRY SECTION

FIGURE 10.—*Percentage transmission of cis, trans, cis-1,2,4-trimethylcyclopentane.*

Extra curves at 3.4μ obtained with cell of 0.004-mm equivalent thickness.

was found in this region for cyclohexane in the liquid or vapor state. Rasmussen [10] found evidence for a band near 14.6μ. In previous studies Kettering and Sleator [11] found a strong absorption band in this region. The absorption band detected by these investigators may have been due to an impurity in the compound which was studied. However, when the measurements were extended to longer wavelengths two bands were observed at 19.12 and 21.8μ. In the vapor state the 19.12μ absorption band shows a strong zero branch. There is some doubt as to the type of the band located at 21.8μ. These curves will be shown in another article dealing with the region from 15 to 25μ.

In figure 12 the absorption spectrum of methylcyclohexane is shown. There has been a considerable change from the spectrum of cyclohexane in the region at wavelengths greater than 7μ. In the methylcyclohexane, strong bands are located at 9.16, 9.68, 10.36, 11.00, 11.47, and 11.86μ. The most intense of these bands at 10.36μ is not present in the spectrum of cyclohexane.

In figures 13, 14, and 15 are shown the absorption spectra of 1,1-dimethylcyclohexane, *trans*-1,2-dimethylcyclohexane, and *cis*-1,2-dimethylcyclohexane. In the spectrum of 1,1-dimethylcyclohexane there is a double band at 7.3μ. This may be caused by the interaction between the two methyl groups. The double band has much the same appearance as that found in 1,1-dimethylcyclopentane and the two minima occur at 7.22 and 7.32μ. The average value of these bands is 7.27μ, which is the position of the band of methylcyclohexane. The absorption bands of *cis*-1,2-dimethylcyclohexane extend to 13.68μ. Eleven intense bands exist beyond 7.5μ. For use in identification, the two bands at 8.62 and 9.14μ are the best suited. The other two dimethylcyclohexanes do not have bands in this region. The *trans*-1,2-dimethylcyclohexane has several intense bands in the region from 10 to 12μ. However, it is best identified by the intense bands at 7.97 and 9.04μ. These two bands readily distinguish it from the spectra of the other cylohexanes that have been measured.

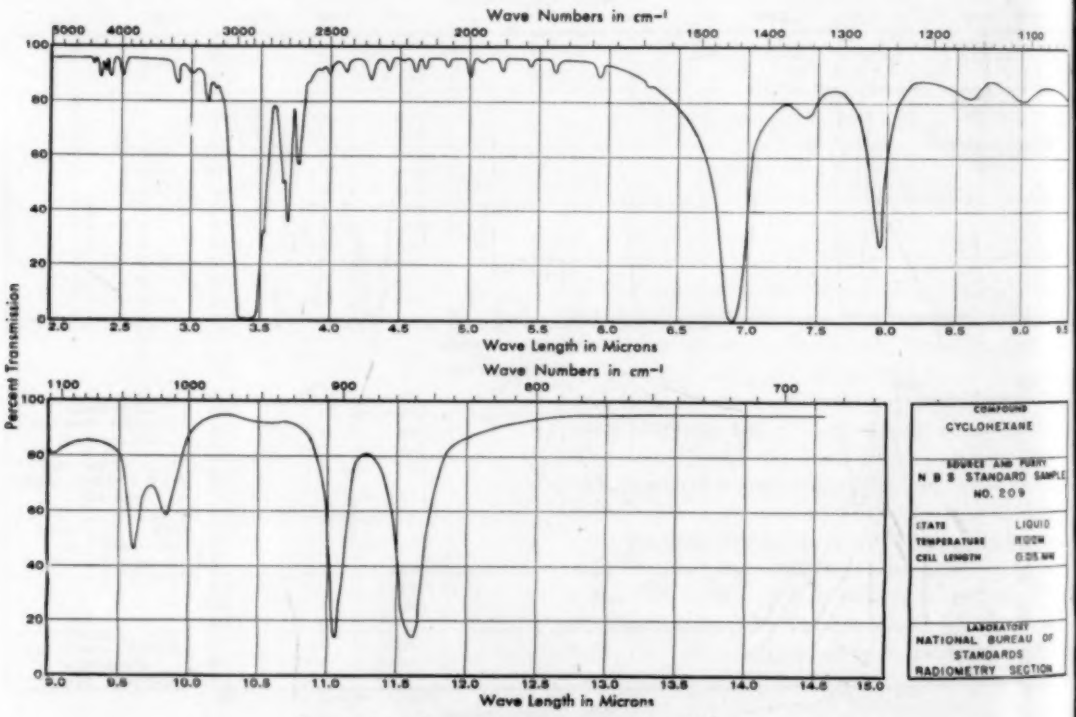

FIGURE 11.—*Percentage transmission of cyclohexane.*

The samples of the 12 compounds whose spectra are reported here are materials of high purity. The spectra should be of value in looking for impurities in compounds of this nature and also in identifying these compounds as impurities in other substances. The wavelengths given in table 2 are of good accuracy for results obtained with a prism spectrometer. Some of these substances have been measured on other spectrometers. The results shown here check well with those obtained on instruments containing larger prisms and having higher resolution. A comparison of our measurements with results obtained at the Texas Oil Co. laboratory at Beacon, N. Y., reveals that the location of the majority of the bands of a substance check within 0.01μ, and scarcely any bands differ by more than 0.03μ. Instances of greater discrepancy occur only in the case of broad bands, that do not have a well-defined minimum.

The absorption spectra may be of value to other laboratories as a secondary check on the calibration of their infrared spectrometer. This work is to be continued on other hydrocarbons as they become available in a high degree of purity.

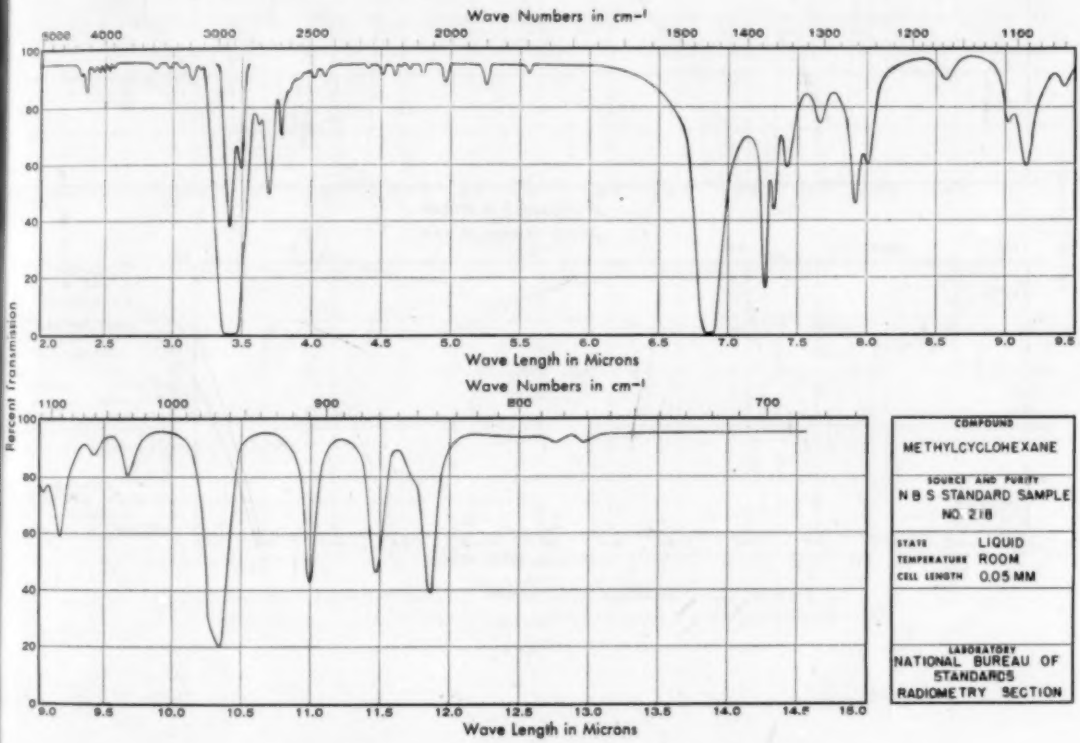
Wave Numbers in cm⁻¹
5000 4000 3000 2500 2000 1800 1600 1400 1300 1200 1100
Percent Transmission
100 80 60 40 20 0
2.0 2.5 3.0 3.5 4.0 4.5 5.0 5.5 6.0 6.5 7.0 7.5 8.0 8.5 9.0 9.5
Wave Length in Microns
Wave Numbers in cm⁻¹
1100 1000 900 800 700
100 80 60 40 20 0
9.0 9.5 10.0 10.5 11.0 11.5 12.0 12.5 13.0 13.5 14.0 14.5 15.0
Wave Length in Microns
COMPOUND
METHYLCYCLOHEXANE
SOURCE AND PURITY
N B S STANDARD SAMPLE
NO. 218
STATE LIQUID
TEMPERATURE ROOM
CELL LENGTH 0.05 MM
LABORATORY
NATIONAL BUREAU OF STANDARDS
RADIOMETRY SECTION

FIGURE 12.—*Percentage transmission of methylcyclohexane.*

Extra curve at 3.4μ obtained with cell of 0.004-mm equivalent thickness.

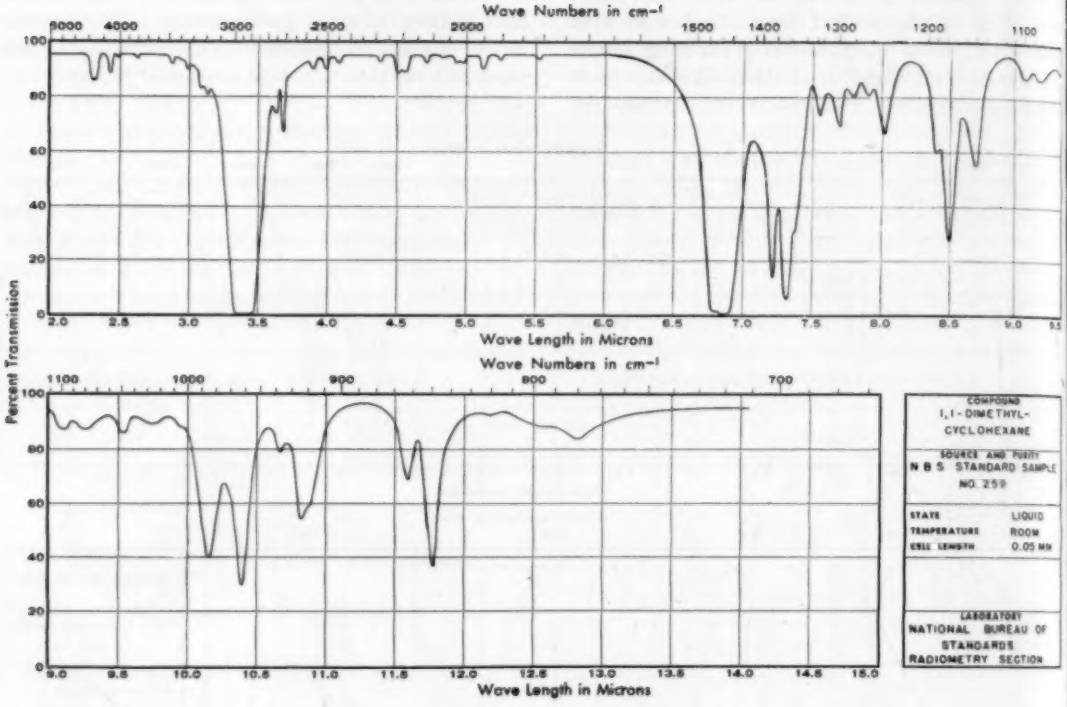
Wave Numbers in cm⁻¹
5000 4000 3000 2500 2000 1500 1400 1300 1200 1100
Percent Transmission
Wave Length in Microns
2.0 2.5 3.0 3.5 4.0 4.5 5.0 5.5 6.0 6.5 7.0 7.5 8.0 8.5 9.0
Wave Numbers in cm⁻¹
1100 1000 900 800 700
9.0 9.5 10.0 10.5 11.0 11.5 12.0 12.5 13.0 13.5 14.0 14.5 15.0
Wave Length in Microns
COMPOUND
1,1-DIMETHYL-CYCLOHEXANE
SOURCE AND PURITY
N B S STANDARD SAMPLE NO. 259
STATE LIQUID
TEMPERATURE ROOM
CELL LENGTH 0.05 MM
LABORATORY
NATIONAL BUREAU OF STANDARDS
RADIOMETRY SECTION

FIGURE 13.—*Percentage transmission of 1,1-dimethylcyclohexane.*

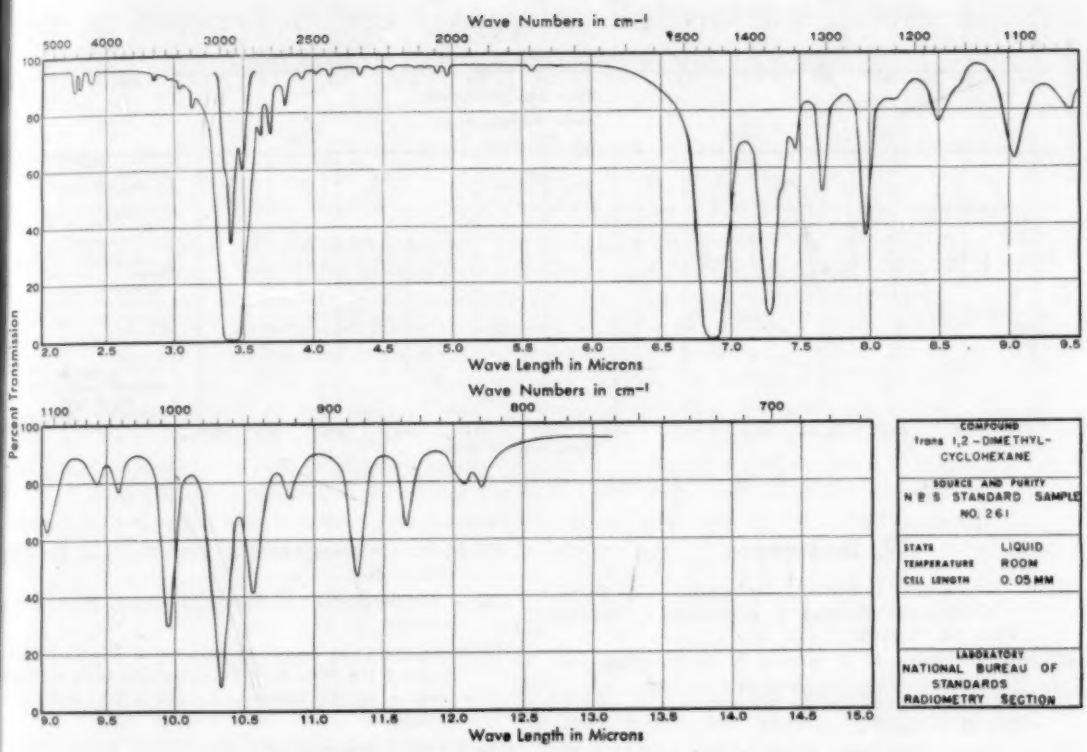

FIGURE 14.—*Percentage transmission of trans-1,2-dimethylcyclohexane.*

The extra curve at 3.4μ was for a cell of 0.004-equivalent thickness.

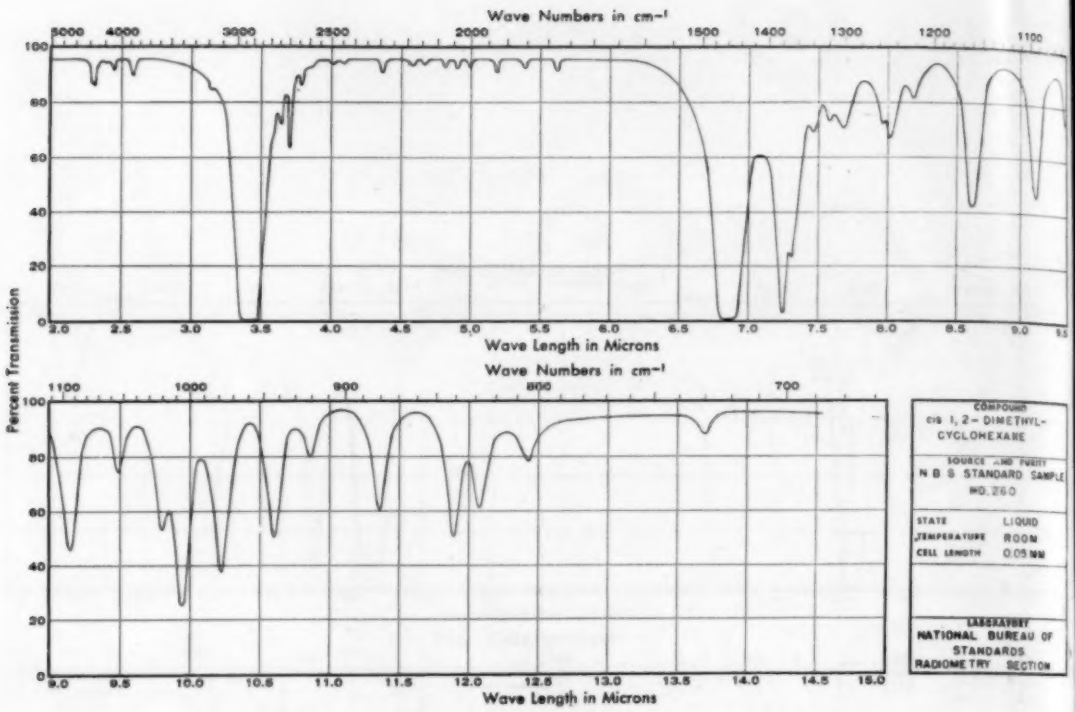
Wave Numbers in cm⁻¹
5000 4000 3000 2500 2000 1500 1400 1300 1200 1100
Percent Transmission
100 80 60 40 20 0
2.0 2.5 3.0 3.5 4.0 4.5 5.0 5.5 6.0 6.5 7.0 7.5 8.0 8.5 9.0
Wave Length in Microns
Wave Numbers in cm⁻¹
1100 1000 900 800 700
100 80 60 40 20 0
9.0 9.5 10.0 10.5 11.0 11.5 12.0 12.5 13.0 13.5 14.0 14.5 15.0
Wave Length in Microns
COMPOUND
CIS 1, 2- DIMETHYL-CYCLOHEXANE
SOURCE AND PURITY
N B S STANDARD SAMPLE NO. 260
STATE LIQUID
TEMPERATURE ROOM
CELL LENGTH 0.05 MM
LABORATORY
NATIONAL BUREAU OF STANDARDS
RADIOMETRY SECTION

FIGURE 15.—*Percentage transmission of cis-1,2-dimethylcyclohexane.*

IV. References

[1] R. B. Barnes, Robert S. McDonald, Van Zandt Williams, and Richard F. Kinnaird, J. Applied Phys. **16,** 77 (1945).

[2] Max D. Liston, C. E. Quinn, W. E. Sargeant, and G. G. Scott, Rev. Sci. Instr. **5,** 194 (1946).

[3] H. Kayser, Handbuch der Spectroscopie **8,** part 1, 380 (S. Hirzel, Leipzig, 1932).

[4] H. Kayser, Handbuch der Spectroscopie **7,** 648 (S. Hirzel, Leipzig, 1934).

[5] W. W. Sleator, Astrophys. J. **48,** 125 (1918); E. K. Plyler and W. W. Sleator, Phys. Rev. **37,** 1493 (1931).

[6] P. E. Martin and E. F. Barker, Phys. Rev. **41,** 291 (1932).

[7] D. M. Dennison and J. D. Hardy, Phys. Rev. **39,** 938 (1932).

[8] A. Borden and E. F. Barker, J. Chem. Phys. **6,** 553 (1938).

[9] Supplement to National Bureau of Standards Circular C398, Standard Samples Issued or in Preparation by the National Bureau of Standards, p. 6 (1946).

[10] Robert S. Rasmussen, J. Chem. Phys. **11,** 249 (1943).

[11] C. F. Kettering and W. W. Sleator, Physics **4,** 39 (1933).

WASHINGTON, September 5, 1946.

U. S. Department of Commerce
National Bureau of Standards

Research Paper RP1770
Volume 38, February 1947

Part of the Journal of Research of the National Bureau of Standards

Elastic Behavior and Creep of Refractory Bricks Under Tensile and Compressive Loads

By Lewis E. Mong

Nine brands of firebrick, including two high alumina, four fire clay, two siliceous, and one silica, were subjected to creep tests. Specimens were cut from 9-inch bricks. Creep tests, with either tensile or compressive stresses, were made at 11 temperatures from 25° to 950° C, inclusive. Durations of tests were approximately 240 days. Small length changes, independent of stress direction,[1] occurred at the lower temperatures. Lowest temperatures at which creep was significant were high alumina, 700° to 850° C; fire clay, 600° to 700° C; siliceous and silica, 950° C. Creep results with compressive stresses could not be correlated with results with tensile stresses. At 950° C, specimens of different brands showed greatly different capacities to carry load. Repeated heatings caused growth of silica brick. Moduli of elasticity at room temperature were determined before and after the various heat treatments, and resultant changes in moduli are recorded. The changes were large for silica brick and small for the fire-clay brick.

I. Introduction

The lowest temperature at which firebrick exhibit appreciable permanent deformation or creep[2] as a result of working stresses maintained for long periods of time is of interest in many modern uses of refractory materials where a definite shape must be maintained under load and at elevated temperatures. In interpreting thermal spalling performance [1],[3] it is necessary to determine the range of temperature over which the material remains rigid and is subject to cracking. It is important also to have a knowledge of flow characteristics at the lower temperatures to determine the amount of stress relief such flow might allow [2]. It was the purpose of this investigation to provide some information on these properties as well as to provide some data indicating the stresses that may safely be used in tension [3].

II. Materials

Firebrick representing nine brands were submitted by eight manufacturers. The laboratory identification numbers are identical with those assigned the same brands in an earlier report [4]. Brick of these brands were selected because their compositions represent a wide range in the silica-alumina ratio. For convenience, the type of brick, the method of manufacture, pyrometric cone equivalent, porosity, and the maturing temperature [5] are given in table 1, together with the chemical analysis.

[1] "Stress direction" is used in this paper to indicate either tensile or compressive loading.

[2] The definition of "creep," from Webster's New International Dictionary (1939), is "to undergo permanent deformation from prolonged exposure to high temperatures or stress." However, "creep" is used in this report to indicate only deformations caused by combined temperature and stress.

[3] Figures in brackets indicate the literature references at end of this paper.

TABLE 1.—*Properties of firebrick*

Brand	Type of brick	Method of manufacture [1]	Pyrometric cone equivalent	Porosity	Matured at cone—	Chemical composition				
						SiO_2	Al_2O_3	Total flux	$Fe_2O_3+TiO_2$	P_2O_5
				Percent		*Percent*	*Percent*	*Percent*	*Percent*	*Percent*
19	High alumina	DP		26.8		14.9	79.3	5.7	4.1	0.2
18	do	DP	35	19.8		36.8	55.7	7.4	3.8	.2
1	Fire clay	DP	34	16.2		47.8	44.4	7.8	3.1	1.6
6	do	SM	32-33	21.5	9	52.0	41.2	6.8	4.4	0.3
11	do	DP	32-33	18.7	14	56.9	37.8	5.3	2.5	.2
7	do	HM	32	25.1	9	58.5	34.8	6.7	4.1	.3
15	Siliceous	SM	31-32	25.4	13	65.3	29.4	5.3	3.5	.6
16	do	HM	29-30	29.9		80.7	16.1	3.2	2.4	.2
17	Silica	HM	32-33	29.3	16	96.0				

[1] DP, SM, and HM refer to dry press, stiff-mud, and handmade, respectively.

III. Specimens and Apparatus

1. Preparation of Specimens

Specimens were cut from standard 9-inch straight brick as received from the manufacturers. Two specimens were obtained from a single brick and the dimensions are shown at *A* in figure 1. This type of specimen has been described [4], and it was used in this work in all the tests in which the material was stressed for extended periods. Specimens having such defects as visible laminations, unusually large voids, or having exceptionally low moduli of elasticity were discarded.

Only five specimens were used in tests without stress. They were 1-inch square and 9 inches long, and were taken from one brick of brand 17.

Two pairs of gage marks were placed on each specimen, as shown at *B* in figure 1. One pair faced the original edge of the brick and the other pair, diametrically opposite faced the original middle of the brick.

The gage marks consisted of silicon-carbide particles, grit No. 180, cemented to the specimen with Alundum cement. The silicon carbide and cement were mixed with water to a thin creamy consistency, and a small drop of the material was placed on the specimen. After the drop was partially dry, it was washed with single drops of water to expose the outlines of several silicon-carbide particles.

The specimens that were stressed in the tests were subjected to a preliminary heating and cooling to mature the cement around the gage marks, to relieve residual stresses in the machined specimens, and to provide a similar cooling treatment for all specimens. This heating and cooling (which will be referred to in this paper as preheating) consisted in raising the temperature of the specimens to 900° C in an electric furnace in 5 hours, maintaining this temperature for one-half hour, and then permitting the specimens to cool with the furnace.

2. Apparatus for Modulus of Elasticity Tests

The modulus of elasticity in tension of the specimens at room temperature was determined with the apparatus previously described [4], using a 6-inch gage length. The gage mountings were placed on the specimens so that the Tuckerman gages indicated strains for the same gage lengths shown at *B* in figure 1.

3. Apparatus for Creep Tests

(a) Description

Figure 1 shows a sectional view of the apparatus and the assembly of parts used for the testing of one specimen in compression, and also the assembly of parts for loading a specimen in tension. The entire apparatus and furnace for compressive loading accommodated 10 specimens in a single furnace, and a similar furnace for tensile loading accommodated 7 specimens. However, the space for one test specimen in the compressive apparatus was occupied by a reference bar of fused quartz with gage marks similar to those on the test specimens. An invar bar, marked and measured to an accuracy of ± 0.00002 in., was used as the reference length at room temperature. The telescope eyepieces were equipped with green filters (Wratten No. 57 A) to avoid loss of contrast resulting

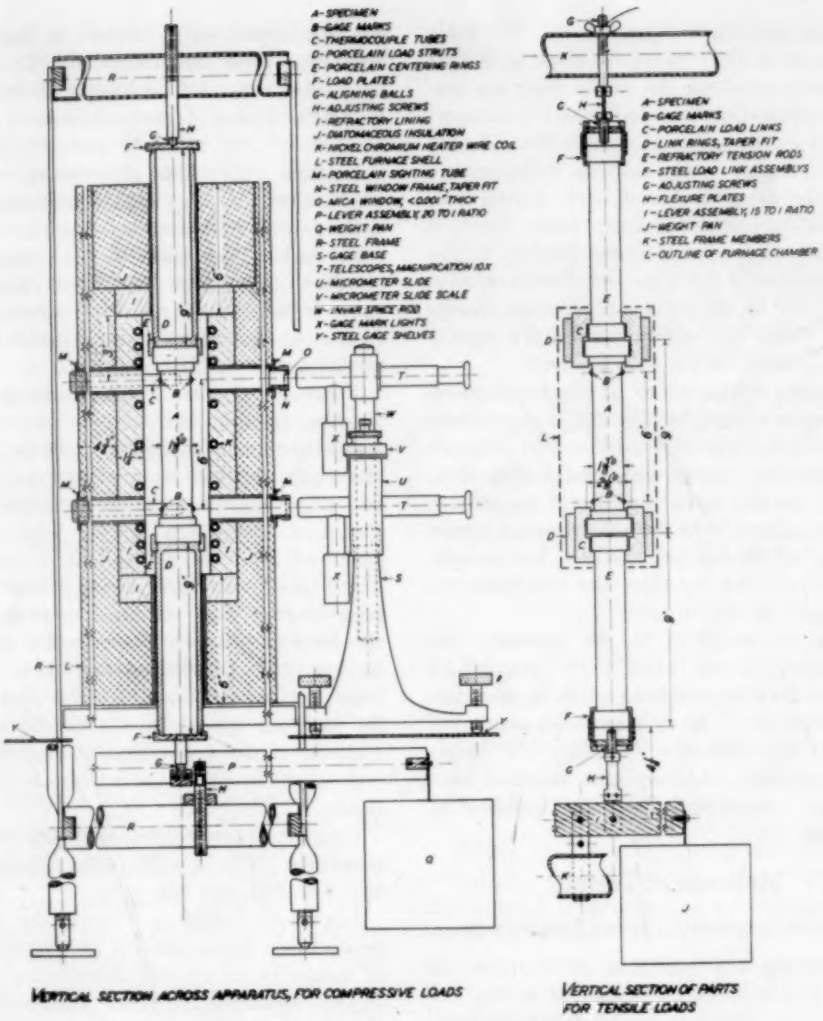

FIGURE 1.—*Apparatus used for compressive and tensile creep tests.*

from light radiated by the specimens at test temperatures of 850° C and above.

The porcelain, refractory, and steel parts transmitting loads to the specimens were finished to obtain a common axis for each assembly. The combination of links and rod to transmit tensile loads to the specimen was found to be the best of three different styles because it proved to be the most economical in time and materials to manufacture, and the alinement obtained was most satisfactory.

Temperatures within the furnace were indicated by six base-metal thermocouples placed at the ends and at the middle of the furnace at heights shown in figure 1. One thermocouple in each furnace operated a galvanometer that controlled the action of a double-throw relay. This in turn connected high or low voltages from a tapped transformer to the furnace to maintain a constant temperature.

(b) Precision of Measurement

The error for the determination of the tensile modulus of elasticity at room temperature was

727972—47——7

± 2 percent, as previously reported [4]. The scale of the micrometer slide could be read to 0.0002 cm. However, errors of the entire gage system, such as those caused by the window of the furnace, lack of sharp outline of gage marks, loss of contrast at the higher temperatures, temperature changes of the telescopes and slide during use, and play within the micrometer slide, made it impossible to repeat length measurements within tolerances less than ± 0.001 cm, which was equivalent to $\pm 6 \times 10^{-5}$ in./in., or to a percentage change of ± 0.006. When the windows were not tightly sealed much greater errors were evident.

The controlled temperature of the furnaces [6] varied less than ± 3 deg C, but the temperatures indicated by the six thermocouples differed by as much as 9 deg C after the heating units had deteriorated. Temperatures at the upper and lower gage-mark levels were equalized by a rheostat shunted across the upper half of the heating element, but no control was available to equalize the temperatures along the length of the furnace.

Pan loads are weighed to the nearest one-sixteenth ounce. Lever ratios were obtained by calibrating the lever assembly in a testing machine. Frictional errors of the lever assemblies amounted to less than 0.1 percent. Considerably larger errors in the applied load may have resulted from the vibration transmitted from the building to the apparatus.

IV. Methods of Testing

1. Modulus of Elasticity at Room Temperature

In determining the modulus of elasticity in tension, the specimen load was limited so that the maximum strain did not exceed 0.007 percent. The modulus of elasticity was obtained for each specimen after it had been preheated and again after it had been subjected to a creep test. It was determined also for some specimens before the preheating and for others after various periods of storage at room temperature.

Modulus of elasticity in compression was determined for only two specimens of each of eight brands, and values were obtained only after the preheating.

2. Creep Tests

Gage lengths were determined after the specimens were assembled in the furnace and before the specimens were loaded or heating started. Telescope cross hairs were alined on single particles of silicon carbide having sharp outlines and a sketch drawn of each gage mark showing the position of the selected particle. This particle was used in subsequent measurements. The exact specimen gage length was calculated from the known reference-bar length and the two readings, on the scale of the micrometer slide, obtained when the telescopes were alined on the reference bar or on the specimen gage marks. A similar procedure was followed for the gage marks diametrically opposite.

Following the exact determination of the gage lengths, the temperature was raised to the test temperature at approximately 40 deg C per hr, and after holding this temperature at least 3 hours, the gage lengths were determined again. The specimen was then loaded and gage lengths observed immediately and at approximately 30-day intervals for the duration of the test. Lastly, gage lengths were obtained after the removal of the load at the test temperature and also after cooling the specimen to room temperature. Some additional length values were taken while the stressed specimen was at the elevated temperature if there were indications that the specimen might break in the interim between observations.

Creep tests were made at the following temperatures (°C): 25, 125, 250, 350, 450, 600, 700, 800, 850, 900, and 950.

For those tested in tension the stress applied to each specimen was 7×10^{-5} times the modulus of elasticity in tension determined on that particular specimen at room temperature, and for those tested in compression, the stress was double the stress used in the tension test. This scheme was followed because it had been found [4] that, at room temperature, strength is approximately proportional to modulus of elasticity and, therefore, the load on each specimen was nearly proportional to its strength.

The stress factor[4] of 7×10^{-5} was selected because preliminary tests indicated this value to be the greatest that could be used in tension for brick of all brands without rupture when loaded at room temperature. Specimens in compression

[4] In this paper, "stress factor" is the ratio of the stress for a specimen in a creep test to the tensile modulus of elasticity at room temperature for that specimen.

ordinarily fail at stresses far greater than 7×10^{-5} times the modulus of elasticity, and, therefore, the factor was doubled to accentuate the creep. Other tensile stresses were used in supplementary tests at 950° C.

Specimens were used in more than one creep test if their moduli of elasticity had not changed more than 7.5 percent when compared to the value obtained following the preheating or if their overall length change did not exceed 15×10^{-5} in./in. If the change was greater than either of these limits, the specimen was considered no longer representative of the brand and a new specimen was used in the next test.

Each brand was represented in the creep test at a given temperature by only one specimen. Creep tests were repeated only at 450° C in tension, using a different lot of specimens.

3. Specimens Without Load

Lengths of 1-inch-square specimens of brand 17 subjected to heating without loading were obtained at room temperature only. The measurements were made on untreated specimens and again after each heating. The length changes resulting from each heating were calculated in percent and the cumulative changes recorded.

V. Results and Discussion

1. Modulus of Elasticity

(a) Variations Along Width of Brick

In the determination of the modulus of elasticity, the strains indicated by the gage facing the original middle of the brick, and the gage facing the original edge of the brick, were usually different. These total differences, more than 100 percent when based on the average strain for some specimens, indicated variation across the section of the specimen in a direction parallel to the width of the original brick. Larger center strains, indicating "soft cores," were found for brick of brands 6, 7, and 15. These bricks were manufactured either by the handmade repressed or the stiff-mud repressed method. The high-silica handmade bricks (brands 16 and 17) had larger edge strain, possibly due to deep surface cracks, which were visible on some specimens of brand 16.

(b) Variations in Specimens and Changes From Preheating

Table 2 gives the maximum, minimum, and average values of modulus of elasticity and the coefficient of variation[5] obtained for specimens following the preheating. The large ranges of the average values for the different brands and the range in values for specimens of each brand indicated the necessity of adjusting the stresses for the creep tests.

TABLE 2.—*Tensile moduli of elasticity of firebrick at room temperature after preheating at 900° C for one-half hour, and percentage change caused by preheating*

Brand No.	Modulus of elasticity after preheating					Change caused by preheating [a]		
	Number of specimens tested	Maximum	Minimum	Average	Coefficient of variation	Number of specimens	Decrease in modulus	
							Average	Standard deviation
		1,000 lb/in.²	*1,000 lb/in.²*	*1,000 lb/in.²*	*Percent*		*Percent*	*Percent*
19	14	5,280	3,690	4,280	10.9	10	2.3	2.0
18	2	2,750	2,700	2,725	.....	0	.....	.....
1	16	2,340	1,130	1,915	17.5	8	1.1	2.3
6	4	1,740	1,650	1,695	2.5	2	4.1	.....
11	12	1,450	320	615	64.3	4	2.7	2.1
7	10	1,610	705	1,185	28.6	6	3.5	1.8
15	10	1,965	1,390	1,725	12.8	4	13.8	1.4
16	27	415	175	275	20.5	13	31.8	9.0
17	24	615	310	435	21.3	14	19.7	4.6

[a] The modulus of elasticity was not determined on all specimens before preheating. Therefore, the percentage decrease is given only for those specimens for which the modulus had been determined both before and after preheating.

When the tensile moduli of elasticity were obtained both before and after the preheating, the change (expressed in percentage of the original value) was always a reduction, and the average values for each brand are given in table 2. Similar changes were observed by Heindl and Pendergast [7]. These changes probably indicated partial fracture of the specimens, resulting in decreased effective cross sections. The high-silica bricks (brands 15, 16, and 17) had the largest changes, and the remaining brands of brick had comparatively small changes.

(c) Comparison of Elasticity in Tension and in Compression

At room temperature the modulus in compression was greater than the modulus in tension, as measured on two specimens from each of eight brands. These differences ranged from 3 to 18 percent and averaged 8 percent.

[5] Manual for interpretation of refractory test data, ASTM Standards on Refractory Materials (Feb. 1935).

(d) Changes With Age of Specimens

The tensile modulus of elasticity of prepared specimens changed slightly as the result of storage for periods up to 5 years at room temperature. The moduli of elasticity of specimens for brand 17 decreased an average of 0.8 percent during an average storage time of 308 days, possibly because of localized expansion and pitting resulting from hydration of uncombined lime. The moduli of specimens of brands 15 and 16 increased approximately 5 percent as the result of storage for about 2 years, whereas those of specimens of the remaining brands increased from 1.3 to 3.4 percent for similar aging periods. There was no definite relation between storage time and amount of change.

(e) Changes Resulting From Creep Tests

The changes in modulus of elasticity in tension at room temperature resulting from creep tests were plotted for single specimens from creep tests in compression in figure 2,B and for single specimens from creep tests in tension in figure 3,B.

These changes in moduli of elasticity indicated a characteristic behavior for brick of each brand. The changes in moduli of elasticity resulting from creep tests at all test temperatures for specimens of brands 15 and 18 were small, although their compositions were widely different. The decrease in moduli of elasticity for specimens of brand 16 used in creep tests at all test temperatures, except the test at 950° C in compression, were large. The decrease in moduli of specimens of brand 17 used in creep tests at temperatures ranging from 125° to 700° C also were large, although the moduli of specimens used in the range from 800° to 950° C increased. After creep tests at temperatures of 125° to 850° C, moderate alterations of moduli of elasticity were observed for specimens of fire-clay brick; of these the specimens for brands 6, 7, and 11 from the compressive creep tests at 900° and 950° C had notable increases in moduli. Alterations in moduli were not determined for specimens of brand 1 from creep tests at 900° and 950° C, nor for the specimen of brand 7 from the tensile creep tests at 950° C, due to breaking or warping of the specimens during the tests. However, a specimen of brand 1 tested in tension at 950° C with a stress factor of only 1×10^{-5} had a small increase in modulus of elasticity. The high-alumina brick, brand 19, had its greatest reduction in modulus of elasticity at 800° C during both tensile and compressive creep tests, but moderate changes occurred during tests at other temperatures.

The changes in modulus of elasticity, plotted in figures 2,B and 3,B, resulted from the combination of the time, temperature, and stress conditions of each creep test. These conditions should change the moduli only so far as they affect the physical texture (crystal and glass phases) of the specimens. For a creep test at a particular temperature, whether in tension or compression, the temperature and time factors are constant, and, therefore, the stress is the only variable. Subtracting the change in modulus that occurred during a test in tension from the change in modulus

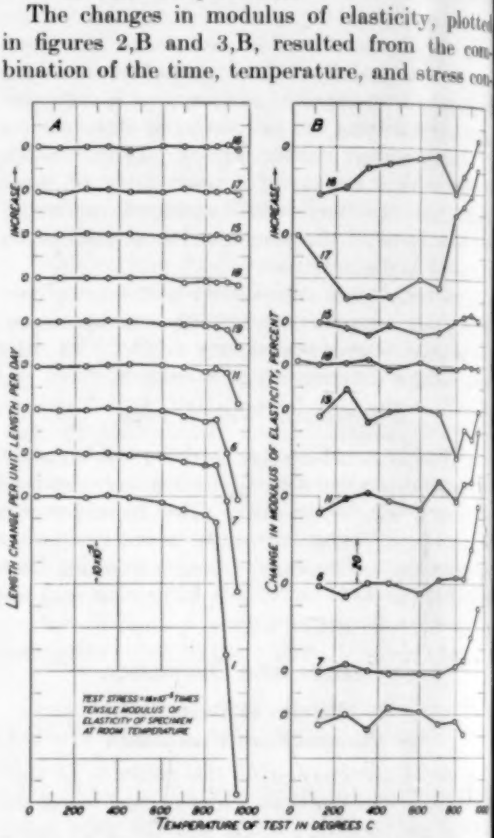

FIGURE 2.—*Changes effected by creep tests in compression.*

The numbers accompanying the curves designate the brand numbers. *A* shows the average length change occurring per day, during approximately 240 days, while the specimens were loaded and at the test temperature indicated. *B* shows the percentage change in tensile moduli of elasticity determined at room temperature before and after the creep test, resulting from a creep test at the indicated temperature. Moduli of elasticity of specimens of brand 1 were not obtained following tests at 900° and 950° C because the specimens were deformed during the creep tests.

that occurred during a corresponding test in compression may supply an indication of the extent to which the direction of stress either supplemented or hindered the volume changes resulting from textural changes. As data on textural changes are not available, the only observation possible at this time is that the changes in moduli during compression were not consistently greater or less than those during tension. This applies

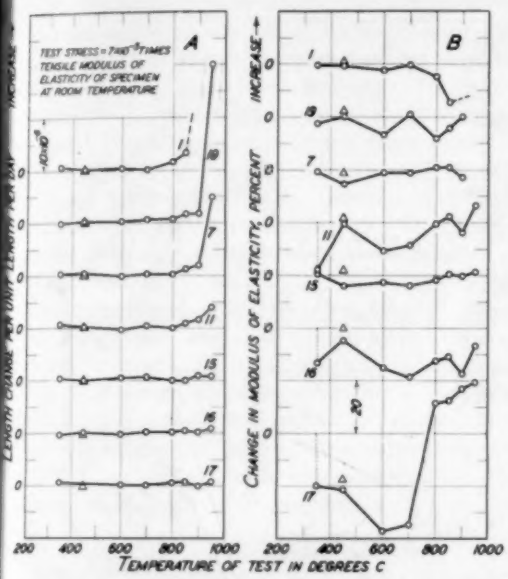

FIGURE 3.—*Changes effected by creep tests in tension.*

The numbers accompanying the curves designate the brand numbers. Data, indicated by triangles, were obtained from duplicate tests. *A* shows the average length change occurring per day, during approximately 240 days, while the specimens were loaded at the test temperature indicated. *B* shows the percentage change in tensile modulus of elasticity, determined at room temperature before and after the creep test, resulting from a creep test at the indicated temperature. The changes in moduli were not obtained for specimens that broke during creep tests, and for these specimens the creep values are for time intervals as follows: Brand 1 at 900° C broke after 4 days and no creep values were obtained; brand 1 at 950° C broke after 6 days, and the creep per day during the first 3 days was 923×10^{-4}; brand 19 at 950° C broke after 35 days, and the creep rate shown applies to the first 5 days; brand 7 at 950° C broke after 123 days, and the creep rate shown applies to the first 95 days.

either for specimens of one composition at the several test temperatures or for the several compositions at one temperature.

As the sense of the sustained stress in the creep tests did not have a consistent effect on the changes of the moduli of elasticity, these changes were apparently the result of the heat treatment. The lack of similarity of the changes from the preheating at 900° C (unstressed and heated one-half hour, see table 2) and the changes following the creep tests at 900° C (stressed for 240 days, see figs. 2,B and 3,B) indicated that the duration of the exposure at the high temperature was an important factor. Preheating decreased the average moduli of the specimens representing all brands, whereas the combined effects of the stress and the longer exposure at 900° C in the creep tests increased the moduli of brand 17, both when subjected to tensile stress and to compressive stress, and of brands 6, 7, 11, and 15 when subjected to compressive stress.

2. Length Changes

(a) Length Changes and Time

Graphs of length changes and time for the duration of a creep test are plotted in figure 4. The graphs for the specimens of brands 7 and 17 tested at 900° C only are given. Results from compressive tests are shown at *A* and *C* and from tensile tests at *B* and *D*. Corresponding graphs for all of the specimens tested were similar.

The thermal-expansion values of several specimens of a given brand were seldom in agreement. These differences, for example, ranged from 0.02 to 0.065 percent at 950° C for specimens of those brands having a total thermal expansion of approximately 0.6 percent between 25° and 950° C. Also, irregular curves were obtained when the total thermal-expansion values from the several creep tests were plotted against the test temperatures. This was true whether the data were obtained with one specimen, or with more than one specimen.

The thermal-expansion and thermal-contraction values for any one specimen were rarely equal, and for all specimens the contraction ranged from 0.075 percent greater to 0.085 percent less than the expansion.

Deformations observed during the 15 minutes following the application or removal of the load were considered as primarily elastic. As the creep tests probably altered the specimens, the elastic deformations resulting from loading and from unloading were not necessarily equal.

Figure 4 shows marked differences in the creep (m), or change in length during the time loads were applied, for brands 7 and 17. The curve for the specimen of brand 7 in compression illustrated the type of curves [8, 9, 10] associated with brands

of brick having comparatively large creep rates during loading at constant temperature. For bricks of this type the rate of creep is large during the first 20 to 40 days and considerably smaller and practically constant for the remainder of the 240 days. Graphs showing little total creep, only a few times the precision of measurement, were obtained for specimens of most of the brands of brick, as illustrated by results for brand 17.

(b) Creep and Test Temperature

Graphs obtained by plotting test temperature and the creep per day, with compressive stress equal to 14×10^{-5} times the tensile modulus of elasticity at room temperature of the specimen, are shown in figure 2,A. Figure 3,A shows similar graphs when tensile stresses equal to 7×10^{-5} times the tensile modulus of elasticity of each specimen were used. Each point on the

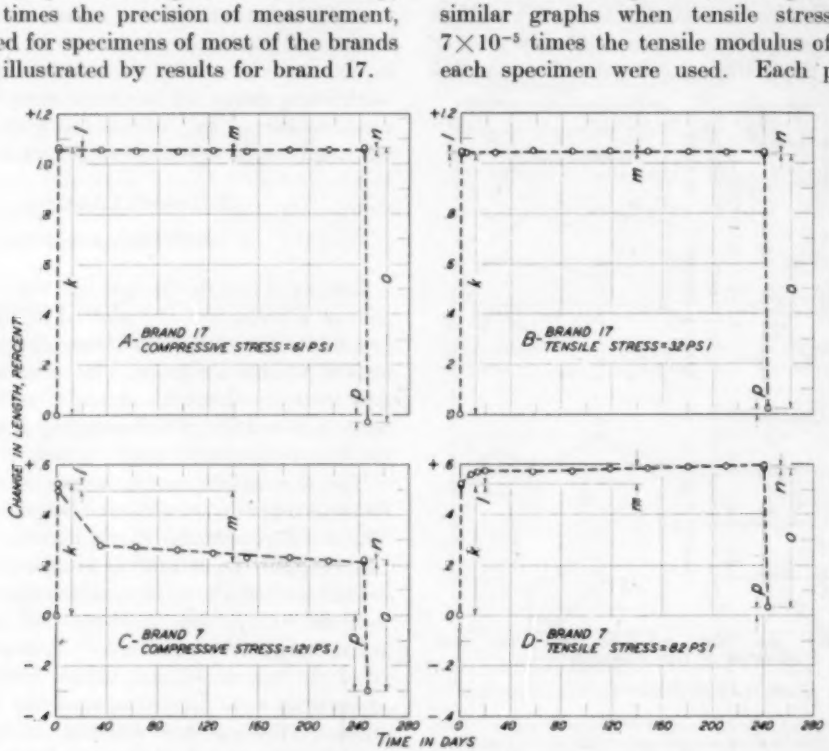
A- BRAND 17 COMPRESSIVE STRESS = 61 PSI
B- BRAND 17 TENSILE STRESS = 32 PSI
C- BRAND 7 COMPRESSIVE STRESS = 121 PSI
D- BRAND 7 TENSILE STRESS = 82 PSI
CHANGE IN LENGTH, PERCENT
TIME IN DAYS

FIGURE 4.—*Length changes occurring during the course of compressive and tensile creep tests at 900° C for two brands of firebrick.*

k, Thermal expansion resulting from heating from room temperature to the test temperature; *l*, the elastic deformation at 900° C due to loading; *m*, total creep occurring during stressing and heating at 900° C; *n*, elastic deformation due to removal of load; *o*, thermal contraction resulting from cooling from the test temperature to room temperature; and *p*, over-all length change.

Values of total creep and over-all length change, for the same specimen and test temperature, were rarely equal. The over-all change included not only creep but also differences between thermal expansion and contraction and between elastic deformations caused by loading and unloading.

The durations of the various creep tests were about 240 days, as shown in figure 4, but were not identical, and therefore the creep per day was calculated (total creep divided by loading time in days), and the results are plotted in figures 2,A and 3,A.

curves represents data from a single specimen. Data from tests in tension at room temperature, at 125° and 250° C are not reported. The following discussion applies to both figures 2,A and 3,A.

Indicated changes in length, which averaged less than 0.00016 percent per day, probably result from internal changes in the specimen because, for a given temperature, they may be either increases or decreases regardless of the direction of the applied stress. The presence of these changes, when larger than the precision of measurement, obscured a determination of the minimum temper-

ature at which the length changes may be assigned definitely to creep caused by the applied stress [11]. However, it is obvious that the curves in figure 2,A for specimens of brands 1 and 7 indicate some creep at test temperatures as low as 600° C, whereas for specimens of brands 16 and 17, creep was not definite below 950° C.

Specimens of brand 1 had the greatest rate of creep under compressive stress at 950° C and ruptured while under tensile stress. An examination of the properties of this brand (table 1) indicates it to be unique in that it contained over 1 percent of P_2O_5 and had the lowest porosity. Its pyrometric cone equivalent (pce) was 34, yet specimens for brand 1 had 85 times as much creep as specimens for brand 16, which had a pce of 29–30. Specimens for fire-clay bricks, brands 1, 6, 7, and 11, all had large creep values at 950° C. Specimens for bricks containing the higher percentages of silica (brands 15, 16, and 17) had small creep values. Specimens for the 55-percent-alumina brick, brand 18, also had small creep values, probably because the predominant phase was mullite. However, specimens for the 80-percent-alumina brick, brand 19, in which the predominant phase was corundum, had moderate creep values at 950° C. Brick of both brands contained an intermediate amount of glassy bond.

(c) Creep and Direction of Stress

Compressive stresses, although twice the tensile stresses, caused approximately the same creep as the tensile stresses for specimens for brands 15, 16, and 17 at 950° C. At the same temperature, specimens for brands 7 and 11 had creep values for compressive tests about twice the values for tensile tests, even though the specimen of brand 7 broke in the tensile test after 123 days of loading. The tensile specimen of brand 19 had a creep value about five times larger than the compressive specimen in the tests at 950° C. Specimens of brand 1 had an extreme difference in tensile and compressive creep, the tensile value (before the specimen broke) being approximately 13 times the compressive value at 950° C. This weakness in tension of specimens of both brands 1 and 19 at 950° C was indicated by breakage during the tensile creep tests (see legend to fig. 3).

(d) Creep at 950° C and Tensile-Stress Factor

Rates of creep in tension at 950° C, obtained from tests with single specimens, are plotted in figure 5 with respect to stress factor. The curves indicate an enormous difference in the reaction of the specimens of different brands to different stresses.

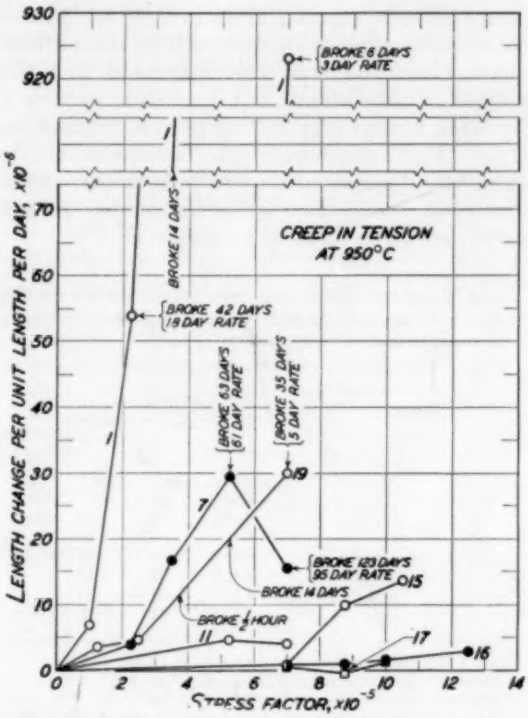

FIGURE 5.—*Creep at 950° C with respect to tensile-stress factor.*

The stress for each creep specimen is the product of the stress factor and its tensile modulus of elasticity. The numbers accompanying the curves designate the brand numbers. The number of days of loading included in the daily rate from the beginning of the test is noted for some of the specimens that broke. Creep rates were not determined for the specimen of brand 1 that broke after 14 days, and specimens of brand 19 that broke after one-half hour and after 14 days. Two specimens, not indicated, of brand 17 tested with stress factors equal to 17.5×10^{-4} and 25×10^{-4} broke within one-half minute.

Variations between specimens of brand 19 were shown by decreases in time before breakage as the stress factor was reduced from 7×10^{-5} to 3.75×10^{-5}. Also, variation in specimens of brand 7 was shown by a greater creep rate for a stress factor equal to 5.25×10^{-5} than for a factor equal to 7×10^{-5}.

(e) Comparative Stresses for Equal Creep Rates at 950° C

For the purpose of evaluating the brands of brick, "comparative stresses" causing equal creep rates in tension at 950° C were calculated. The

comparative stress is the product of the stress factor causing a creep rate of 1×10^{-6} per day (obtained from the curves in fig. 5), and the average modulus of elasticity. The stress factors and comparative stresses are given in table 3. As the comparative stresses are derived from results from one specimen and large errors may result from the method of calculation, the values given in table 3 for some brands may be 300 percent or more in error. For comparison, the minimum tensile strengths of specimens broken in the tests, or the maximum stresses used for specimens that did not break, are given in table 3, column 4.

TABLE 3.—*Stress factors and comparative stresses causing creep rates equal to* 1×10^{-6} *(in./in.)/ day, and strengths of firebrick at 950° C in tension*

Brand	Stress [1] factor	Comparative [2] stress	Tensile strength	Time loaded before breaking
	$\times10^{-6}$	*psi*	*psi*	
19	0.35	15	[3] 175	½ hr.
1	.15	3	[3] 32	42 days.
11	1.1	7	[4] 30	
7	0.55	6	[3] 65	63 days.
15	7.0	120	[4] 205	
16	8.5	23	[4] 45	
17	9.6	42	[3] 65	½ min.

[1] Taken from curves in figure 5 for a creep rate of 1×10^{-6}.
[2] Product of stress factor and average modulus of elasticity.
[3] Minimum specimen stress causing breakage at 950° C.
[4] Maximum specimen stress used in tests at 950° C; specimen not broken after 240 days.

These comparative stresses indicated great differences in the load-bearing capacities of the specimens of different brands. Specimens of brand 15 were superior because they had the highest comparative stress, resulting from a low creep rate at a relatively high stress, and also because they had the highest tensile strength. Specimens of brands 16 and 17, having high silica content, had moderate comparative stresses because of low strength, even through their resistance to creep at a relatively low stress was high. However, for specimens of these brands the comparative stresses are such a large fraction of the tensile strengths as to leave little provision for temporary overloads. Specimens of the fire-clay bricks, brands 1, 7, and 11, had comparatively small comparative stresses and their strengths fell in the same range with the strengths of the specimens of the high-silica brick. Specimens of the high-alumina brick, brand 19, had an intermediate comparative stress resulting from their large creep rate, but they had a large reserve in strength.

(f) Growths and Shrinkages Other Than Creep

If the creep were the only permanent change occurring during a creep-test cycle, then p would be equal to m (fig. 4). However, thermal expansion (k) and contraction (o), and elastic deformation following loading (l) and elastic deformation following unloading (n), were not equal. The difference between m and p is a measure of these combined inequalities. This difference may result in either growth or shrinkage.

The growths were largest for specimens of silica brick, brand 17 [12]. As creep was negligible for this brick, any over-all change in the length between the gage marks was attributed to growth or shrinkage. These over-all changes, plotted in figure 6,A, were appreciable even for the test at 125° C, in compression, and greatest for the tensile test at 700° C. Growths for these particular specimens were considerably greater than growths for compressive tests at all temperatures except 450° C.

The characteristic texture and mineral composition of silica brick [13] may account for these comparatively large over-all changes, which are associated with decreases in modulus of elasticity for tests at and below 700° C. Sintering and decomposition of partially rehydrated, uncombined lime may be factors in the limited over-all changes and increases in modulus of elasticity for tests at and above 800° C.

To determine the extent of the growth of unstressed specimens during repeated heat treatments, five 1-inch-square specimens from one brick of brand 17 were included in the creep furnaces for the tests indicated in figures 6,B and C. Excepting the pronounced effect of the first heat treatments (specimens 2 and 5, fig. 6,B, and 4, fig. 6,C, at 350° C; and specimens 1, fig. 6,B, and 3, fig. 6,C, at 600° C), the curves have sufficient similarity to indicate that they are real and reproducible. The cumulative growths resulting from the series of heat treatments for these five specimens range from 0.231 to 0.268 percent.

Creep specimens of the remaining brands had much smaller growths, or shrinkages, than were found for brand 17. Specimens of the high-

alumina brick, brand 19, had growth resulting from the creep tests at 700° C only. The fire-clay bricks had little tendency to grow or shrink. For brands 15 and 16 the over-all length-change curves were somewhat similar to those for brand 17, but the changes were less than half as large.

VI. Summary of Results

The changes in moduli of elasticity in tension of preheated specimens as the result of storage at room temperature for periods as long as 5 years were small. These changes fell in the range from about 1-percent decrease in moduli to 5-percent increase. The changes were not proportional to time.

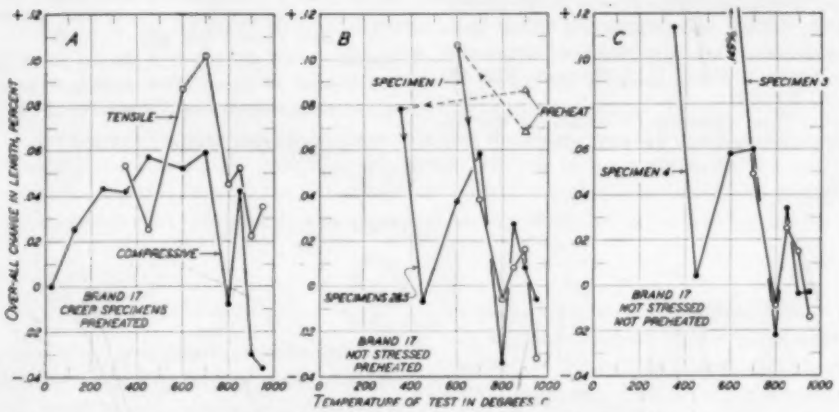

FIGURE 6.—*Over-all, or net, length change of silica brick observed after heating from room temperature to indicated test temperature, maintaining test temperature approximately 240 days and cooling to room temperature.*

Solid circles show values for specimens treated in the furnace for compressive tests; open circles show values for specimens treated in the furnace for tension tests. All values in figures *A*, *B* and *C* for a given temperature and furnace apply to specimens tested simultaneously. *A*, Over-all length changes for preheated specimens used in creep tests. Each point is for a new specimen; *B*, over-all length changes for three unstressed specimens heated at progressively higher temperatures after having been preheated at 900° C for one-half hour. The triangles indicate the length changes resulting from this preheating; *C*, over-all length changes for two unstressed specimens heated at progressively higher temperatures. The specimens had not been preheated.

The average tensile moduli of elasticity at room temperature of the different brands ranged from 275,000 to 4,280,000 psi, with coefficients of variation ranging from 2.5 to 64.3 percent. Indications of variations within individual specimens were noted.

At room temperature the compressive moduli of elasticity of preheated but not creep-tested specimens averaged 8 percent greater than the tensile moduli.

At room temperature significant reductions occurred in the tensile moduli of elasticity of siliceous bricks containing 81 or 96 percent of silica as the result of either tensile or compressive creep tests at and below 700° C. For brick containing 96 percent of silica and a majority of the fire-clay bricks, increases in tensile moduli at room temperature resulted from compressive creep tests at and above 800° C.

Small changes in length were found at test temperatures of 450° C and lower, but the changes did not depend on the direction of the stress and were attributed to internal adjustments of the specimens. Deformations were small also at all test temperatures for specimens of two brands of siliceous, one silica, and one high-alumina brick. Large deformations were obtained at test temperatures from 850° to 950° C for fire-clay bricks and a high-alumina brick containing 80 percent of alumina.

Creep values for specimens tested in compression were not proportional to creep values for specimens tested in tension.

The stress that would produce a 1×10^{-6} (in./in.)/ day tensile creep at 950° C ranged from 3 psi for a fire-clay brick containing 48 percent of SiO_2 to 120 psi for one containing 65 percent of SiO_2.

Unstressed specimens of silica brick showed

growths as large as 0.27 percent resulting from repeated heatings at several temperatures without load.

VII. References

[1] A. C. Elliot and R. J. Montgomery, A new type of thermal shock, J. Can. Ceram. Soc. **6,** 44 (1937).

[2] Shin-ichi Suzuki, Modulus of elasticity and spalling. I, J. Japan. Ceram. Assn. **47,** 230 (1939).

[3] J. H. Partridge and C. F. Adams, Creep of refractory materials at high temperatures and its bearing on the performance of glasshouse pots, J. Soc. Glass Tech. **23,** 141 (1939).

[4] R. A. Heindl and L. E. Mong, Young's modulus of elasticity, strength and extensibility of refractories in tension, J. Research NBS **17,** 463 (1936) RP923.

[5] Raymond A. Heindl and William L. Pendergast, Deformation and Young's modulus of fire-clay brick in flexure at 1,220° C, J. Research NBS **19,** 353 (1937) RP1030.

[6] F. H. Norton, New apparatus for measuring the viscosity of glass, Glass Ind. **16,** 143 (1935).

[7] Raymond A. Heindl and William L. Pendergast, Young's modulus of elasticity at several temperatures for some refractories of varying silica content, J. Research NBS **13,** 851 (1934) RP747.

[8] F. H. Norton, Flow of ceramic bodies at elevated temperatures, J. Am. Ceram. Soc. **19,** 129 (1936).

[9] F. H. Norton, Critical examination of load test of refractories, J. Am. Ceram. Soc. **22,** 334 (1939).

[10] F. H. Clewes, H. M. Richardson, and A. T. Green, The behavior of refractory materials under stress at high temperatures, parts I and II, Trans. Brit. Ceram. Soc. **43,** 223 (1944). Ceram. Abs. **23,** 85 (1944).

[11] G. A. Kirkendale and R. J. Montgomery, A proposed gloss firing cycle based upon the temperature of plastic flow of the body, J. Can. Ceram. Soc. **3,** 25 (1934).

[12] G. R. Rigby, A. E. Dodd, R. P. White, and A. T. Green, Investigation of the permanent expansion of silica products containing cristobalite, Trans. Brit. Ceram. Soc. **42,** 11 (1943).

[13] W. A. Semple and R. J. Montgomery, Spalling resistance of fused silica vs. quartz and calcined fire-clay grog, J. Can. Ceram. Soc. **9,** 40 (1940).

WASHINGTON, June 13, 1946.

U. S. Department of Commerce
National Bureau of Standards

Research Paper RP 1771
Volume 38, February 1947

Part of the Journal of Research of the National Bureau of Standards

Surface Tensions of Some Optical Glasses

By Leo Shartsis and Alden W. Smock

The surface tension of a number of optical glasses made at the National Bureau of Standards was measured by a modification of the anchor-ring method. At 1,300° C, the values for the flint glasses were in the range 210 to 230 dynes/cm; those for the barium-crown glasses were 260 to 310; the other types of glasses had intermediate values. Most of the glasses had positive temperature coefficients of surface tension. The surface-tension values increased with increasing periods of time that the glasses were maintained at elevated temperatures immediately prior to measurement. Positive rank correlation coefficients of statistical significance were found between seed quality of optical glasses and such factors as surface tension, pot attack, and amount of gas liberated during the melting process.

I. Introduction

For all optical elements, freedom from bubbles, known technically as seeds, is desirable, and for some elements, such as reticles, bubble-free glass is absolutely essential to secure satisfactory performance. As bubbles have a glass-gas interface, it seems reasonable to suppose that the surface tension of the glass has a bearing on the stability of the bubble, although it is believed the exact effect of surface tension on the elimination of seeds has not been completely explained.

Bubbles in molten glass may be eliminated either by their rising to the surface and being expelled or by being absorbed as the glass is cooled. The absorption of a bubble in a cooling glass is facilitated by several mechanisms, which at constant volume would lower the gas pressure inside the bubble. Among these may be mentioned (1) the normal lowering in pressure of a gas with decrease in temperature, (2) the lowering in pressure caused by condensation of certain constituents, such as volatilized alkali, lead oxide, etc., (3) absorption of gases, such as CO_2 and SO_2 by the condensed alkali, and (4) the normal increase in solubility of gases in glass as the temperature is lowered. As the surface tension of the glass acts to decrease the size of the bubble, the volume becomes smaller as the opposing gas pressure becomes less. The pressure on a bubble, due to surface tension, is given by the expression $2\sigma/r$, where σ is the surface tension, and r is the radius of the bubble [1] [1]. Therefore, as the bubble contracts, the pressure due to surface tension increases until it is balanced by the gas pressure, which also increases as the bubble shrinks. This brings into play the increase in gas solubility normally associated with increasing pressure. The net effect is that bubbles below a certain critical size are reabsorbed as the glass is cooled. This phenomenon has been noted by practical glassmakers when taking samples. The sample while hot may show many small seeds that disappear upon cooling. Thus, as concerns reabsorption of small seeds, high surface tension, when accompanied by an increased gas solubility as the glass is cooled, is a favorable factor.

For the elimination of bubbles by rising to the

[1] Figures in brackets indicate the literature references listed at the end of this paper.

surface, low surface tension would seem to be favorable, since, other things being equal and for a given amount of gas in a bubble, the glass with the lower surface tension will have the larger bubble. As, according to Stokes' law, the rate of rise varies as the square of the radius of the bubble, this effect is important. The influence of viscosity on the elimination of bubbles has not been included in this discussion because this property, in contrast to surface tension, changes markedly with temperature and thus may be controlled almost at will.

An experimental approach to the study of the effect of surface tension on the fining rate, i. e., the rate of removal of bubbles by rising to the surface, was attempted by A. A. Appen [2], who used sirups of different surface tensions but of the same viscosity. He found a positive correlation between fining time and surface tension, i. e., the sirups with higher surface tension took longer to fine.

II. Experimental Method and Calculations

The pull-on-cylinder method, used by Harrison and Moore [3], was adopted tentatively as the most convenient for measuring the surface tension of glasses. In this method the pull is measured on a hollow vertical cylinder whose lower edge is kept at the level of the undisturbed surface of the test liquid. In working with optical glasses, however, this method was not entirely successful, apparently because some of these glasses do not completely wet the cylinder.

The second method tried involved the maximum pull-on-cylinder principle used by Babcock [4]. In this method the maximum pull is measured on a hollow vertical cylinder, the bottom edge of which is in contact with the molten glass. For accurate results with this method, a correction was applied that involves the density of the glass at the temperature of test. A high accuracy for the density value, however, is not necessary because the correction term usually amounts to only about 3 to 5 percent of the total surface tension value. The following equation developed by Verschaffelt [1] was used in the present investigation:

$$\sigma=\frac{F}{4\pi R}\left[1-\left\{2.8284+0.6095\sqrt{\frac{h}{R}}\right\}\frac{\delta}{\sqrt{hR}}+\left\{3+2.585\sqrt{\frac{h}{R}}+0.371\frac{h}{R}\right\}\frac{\delta^2}{hR}\right],$$

σ = surface tension
F = maximum extra force
R = mean radius of cylinder
$h=\frac{F}{\pi R^2\rho g}$
ρ = density of glass
2δ = thickness of cylinder wall.

For purposes of computation, the expression $F/4\pi R$ is equivalent to $W_{max}\ (g/4\pi R)$, where W_{max} is the maximum weight observed, and g is the acceleration of gravity. Then, as R varies with temperature, a table of $g/4\pi R$ was set up for different temperatures.

Periodic measurements of the diameter of the platinum cylinder showed that it increased with use. In the early experiments the value for $g/4\pi R$ was 60.66 at 1,300° C, and this slowly changed to 60.25 in the later experiments.

The densities of some of the glasses at high temperatures had been measured previously by the use of a platinum volumenometer. These data were used to deduce densities for related glasses. In general, it was found sufficiently accurate to compute the correction term for any glass at one temperature only, and then to apply this correction to the measurements at other temperatures.

III. Apparatus and Procedure

Figure 1 shows in diagrammatic form the apparatus used. An ordinary analytical balance was used to measure the pull on the cylinder. To counteract the effect of the strong damping action that the viscous glass exerted, the balance was equipped with a sensitive optical lever. The light beam from a galvanometer lamp was directed toward a small front-surface mirror mounted at the center of the balance beam. The reflected beam was focused on a scale at a distance of approximately 30 inches from the mirror. The scale was viewed by means of a small telescope mounted near the balance.

The vertical-tube furnace was wound with 80 percent platinum-20 percent rhodium resistance wire. A small auxiliary heater, separately controlled, was situated at the bottom of the furnace and an Alundum disk, directly above this heater, constituted the floor of the furnace. A noble metal thermocouple projected through a hole in

the center of the furnace floor and came almost in contact with the platinum dish, 3-in. in diameter, which held the molten glass. Two additional thermocouples were inserted through holes in the split plug that capped the furnace. One of these thermocouples was connected to a potentiometer controller that maintained the temperature of the furnace within ±5 deg C while surface tension measurements were being made.

In making a determination, several lumps of glass were placed in the dish and lowered gradually into the furnace, which had previously been heated to 700° or 800° C. The platinum cylinder

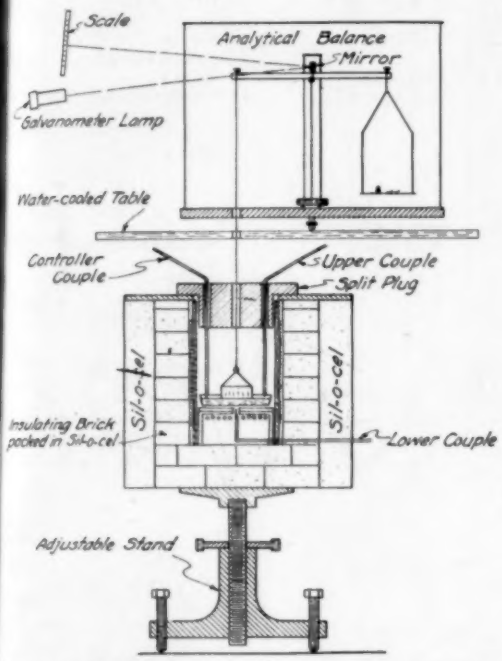

FIGURE 1.—*Schematic diagram of surface-tension apparatus.*

then was lowered into a position some distance above the glass and the furnace plugs were inserted. Next, the temperature was increased to 1,300° C, and the auxiliary heater current was adjusted so that the spread in temperature indicated by the upper and lower thermocouples was within 5 deg C. The cylinder was then weighed, after which the furnace was raised until the bottom edge of the cylinder made contact with the glass. The moment at which contact was made was clearly indicated by the instantaneous damping of the chain vibration.

After contact was established, weights somewhat less than that necessary to balance the downward force exerted by the glass were placed on the weight pan and the balance beam released. By turning the handwheel of the adjustable stand, the furnace was then lowered several millimeters to allow for the stretching of the glass adhering to the cylinder. More weights were slowly added and the furnace position lowered further as the glass continued to stretch, the aim being to have the balance pointer near the scale zero at the time the maximum force was attained. As this point was approached, weights were added in 1-mg steps, sufficient time being allowed for equilibrium to be established. The response of the balance became more pronounced as the end point approached, until, upon the addition of an excess milligram, the balance pointer moved relatively rapidly without coming to equilibrium, indicating that the glass was incapable of supporting the additional weight. This maximum force was remeasured frequently by reestablishing contact and observing the maximum weight the glass could support indefinitely. Measurements were made at 100-deg-C intervals of decreasing temperature until the glass was too viscous to yield in a reasonable time, and the path retraced until 1,300° C was again reached.

IV. Data and Discussion

Table 1 gives the chemical composition, as computed from the batch materials, of the optical glasses studied in this investigation. The data obtained on surface tension are given in table 2.

TABLE 1.—*Compositions of glasses, computed from batch*

[F=flint, BaC=barium crown, LC=light crown, BaF=barium flint, BSC=borosilicate crown, CF=crown flint]

Glass	Melt No.	Component oxides—weight percent									Other oxides
		SiO_2	PbO	BaO	B_2O_3	Na_2O	K_2O	ZnO	As_2O_3	Sb_2O_3	
F 5725/42.2	5820	55.1	31.7	1.0		5.0	6.9		0.3	0.5	
F 5795/40.9	6993	53.1	35.5	0.6		0.4	9.6		.3		
F 605/37.9	4194	47.6	40.9			2.2	8.8		.5		
F 617/36.6	6984	45.6	43.1			4.7	6.1		.5		
F 620/36.2	6841	45.6	45.2			3.0	5.7		.5		
F 649/33.8	6934	41.2	51.1			0.7	6.5		.5		
F 666/32.4	6937	39.3	54.4				6.0		.3		
F 6725/32.2	4316	38.8	55.4				5.5		.3		
F 720/29.3	6860	34.1	62.4				3.2		.3		
F 750/27.7	6397	31.2	66.2				2.3		.3		
BaC 541/59.8	6990	58.8		19.9	3.4	3.2	10.3	4.1	.3		
BaC 5725/57.4	6822	45.2		28.7	6.2	1.4	7.0	7.5	.3	.7	Al_2O_3 3.0
BaC 611/58.8	6980	38.3	0.2	42.8	10.7				.4	.2	Al_2O_3 2.9; CaO 4.5
BaC 617/55.0	6903	37.3	1.4	44.8	4.4	0.2	0.4	5.6	.3	.7	Al_2O_3 4.9
BaC 620/60.0	6495	37.2		41.6	11.0				.3	.2	BeO 4.2; CaO 3.8; ZrO_2 2.0
BaF 584/46.0	6494	49.8	18.8	13.4		1.6	8.2	7.8	.5		
BaF 588/53.4	4848	45.8	10.0	25.9	8.8	0.8	6.7		.5		ZrO_2 1.5
BaF 604/43.5	4411	45.7	23.3	13.6			8.9	8.1	.4		
BSC 511/63.5	6292	68.8			8.5	7.8	14.7		.2		
BSC 517/64.5	6929	66.4			12.4	8.2	12.0	0.5	.5		
BSC 536/64.5	6471	63.4			13.0		6.2		.4		BeO 2.0; SrO 10.0; Li_2O 5.0
LC 5125/60.5	6931	71.9			5.0	14.7	5.0			1.2	CaO 2.2
LC 5145/59.5	5767	71.2			5.0	14.7	5.0			1.2	CaO 2.9
LC 523/58.6	6910	70.2			1.5	14.0	2.5			1.2	CaO 9.4; Cl 0.7; SO_2 0.5
CF 5295/51.6	1280	65.1	10.0	0.2		11.6	6.1	5.0	.2	1.8	
NBS Standard Sample 80[a]		74.1				16.85	0.04		.10		CaO 4.65; MgO 3.23
NBS Standard Sample 89[a]		65.35	17.5	1.40		5.70	8.4				

[a] Standard Sample values are from chemical analyses.

TABLE 2.—*Surface tension of some optical glasses*

Glass	Observer	$\frac{\Delta\sigma}{\Delta T}$	Surface tension (dynes/cm)						
			1,300°C	1,200°C	1,100°C	1,000°C	Reheating		
							1,100°C	1,200°C	1,300°C
82.2	2		230.5	228.7	226.7	225.0	227.1	229.2	231.1
	2	+	230.7	229.4	227.7	225.3	228.3	230.4	232.7
80.9	1	+	221.0	219.7	218.3	216.7			
	2		221.7	219.4	218.8	217.7			
7.9	2	+	218.6	216.4	214.3	213.7	215.1	217.6	219.2
1.6	1	+	222.8	220.6	218.9	216.5	218.7	220.9	223.3
	2		222.1	219.9	217.7		218.1	220.3	222.1
0.2	2	+	221.5	219.0	217.1	215.7			
	2		221.0	218.4	217.2	215.8			
3.8	1	+	216.0	214.1	212.0	212.6			
	2		216.3	214.4	212.3	212.2			
2.4	1	+	216.4	214.7	212.8	212.9	214.6		
	2		216.0	215.5	214.7	214.4	214.7		
32.2	2	+	217.2	215.8	214.0	214.2	217.1	217.1	
	2		216.0	214.3	214.2	214.5	215.5	216.0	
9.3	1		218.3	217.3	216.8	219.0			
	2		218.6	218.4	218.0	217.8			
7.7	2		219.0	219.0	218.9	218.7			
	2		218.4	218.6	219.6	219.3			
41/59.8	2		263.8	264.7	265.0	265.4			
725/57.4	1		269.6	268.9	273.3	275.5	274.7	270.4	271.0
	2		271.4	270.6	270.8	275.0	272.0		273.3
11/58.8	1	+	288.4	288.0	287.0	287.3	288.3	288.8	
	2		289.6	288.7	287.2	286.0	288.3	289.4	
17/55.0	2	+	310.6	309.7	309.3	309.3			
20/60.0	2	+	290.6	289.2	288.5	288.1			
54/46.0	2	+	251.5	249.9	247.7	243.9	247.1	249.9	252.2
88/53.4	1	+	235.6	235.1	234.3	233.8			
04/43.5	2		235.1	234.9	234.0	233.5			
11/63.5	2	+	246.4	244.4	242.1	239.4	242.1	245.0	246.9
17/64.5	2	−	231.4	232.5	238.1	243.5	239.6	233.4	231.6
	1	−	226.9	228.8	232.8	237.6			
38/64.5	2		227.7	229.3	232.3	237.2			
	2	+	245.2	244.5	244.9	244.6	245.6	245.2	246.1
25/60.5	2	−	251.6	254.4	262.1				
43/39.5	2	−	251.7	254.4	261.7				
38.6	1	−	277.2	277.2	278.1			254.8	252.3
	2		276.9	277.3	278.0			278.5	278.5
04/51.6	2		249.2	249.7	250.2		250.8	278.1	277.9
								250.0	249.6

1. Positive Temperature Coefficients

The large number of positive temperature coefficients of surface tension for these glasses may appear unusual and therefore worthy of special note. A search of the literature shows a number of examples of positive temperature coefficients of glasses, as well as of other systems. Thus, Badger [5] reported positive temperature coefficients for three glasses measured by the use of a maximum bubble pressure method. Bradley [6], using a sessile drop method, found a positive temperature coefficient for vitreous B_2O_3 in the range 300° to 500° C. Appen [2] measured the surface tensions of the PbO-SiO_2 and Na_2O-PbO-SiO_2 series by a modified drop-weight method, and found that all these glasses, containing more than about 3 percent of PbO, had positive coefficients. He also measured the effect of additions of various oxides to a base glass of mole composition $Na_2O.2SiO_2$ and found that all additions, which lowered the surface tension markedly, yielded glasses that had either positive or less negative coefficients than that of the base glass. Thus there is evidence furnished by four different methods on glasses of widely differing compositions as to the existence of positive temperature coefficients.

Freundlich [7] gives examples of positive temperature coefficients of surface tension for systems other than glasses. For instance, concentrated aniline or phenol solutions in water show positive coefficients in certain temperature ranges. Methylene cyanide and elementary sulphur also exhibit this behavior. According to Freundlich, the surface layer in these systems contains a component or molecular species that tends to lower the surface tension. As the temperature is raised this molecular species becomes more soluble in the main body of the liquid and is withdrawn from the surface, thereby raising the surface tension.

Tables 1 and 2 reveal that in general the optical glasses that are low in either silica or alkalies or both have positive temperature coefficients. The flint glasses, which have relatively high percentages of PbO, necessarily have low percentages of silica, alkalies, or both, but the mere presence of PbO to the extent of even 10 percent is not sufficient to cause a positive coefficient, as evidenced by the example of CF 5295. On the other hand, *BaC* 611, 617, and 620, as well as *BSC* 540, show positive coefficients, although these glasses contain little or no PbO.

2. Reproducibility

Inspection of table 2 shows that the average difference between two observers is less than 0.5 dyne/cm. In cases where duplicate determinations were made by the same observer, the average difference was also less than 0.8 dyne/cm.

3. Effect of Duration of Treatment at High Temperatures

In order to attain a high degree of reproducibility, observers must duplicate the time-temperature curve because the surface tension value obtained on a glass seems to be a function of the time the glass is maintained at elevated temperatures. For example, nearly all the values obtained in the second part of the schedule, designated "reheating," are higher than the earlier values. Bradley [6], reported that heating NBS Standard Sample 89 (lead-barium glass) at 1,500° C for 2 hours raised the surface tension, as measured by the bubble pressure method, 2 dynes/cm. This indicates that the effect of time at elevated temperatures in raising the surface tension of glass is not confined to the maximum pull-on-cylinder method.

A study was made of the effect of time at elevated temperatures on Standard Samples 80, 89, and 92. Figure 2 shows the results obtained. Standard Samples 80 and 92 exhibited a slow rise in surface tension followed by a leveling off after 22 and 44 hours, respectively. Sample 89 showed a continuous increase in surface tension up to 96 hours, when the test was discontinued.

4. Comparison With Other Observers

Both Badger [5], and Bradley [6], have reported surface tension measurements made by the use of a maximum-bubble pressure method, and these are compared in table 3 with the values obtained here. In general, the values obtained in this investigation are lower. However, considering differences in time-temperature schedule and the different methods used, the agreement may be considered satisfactory.

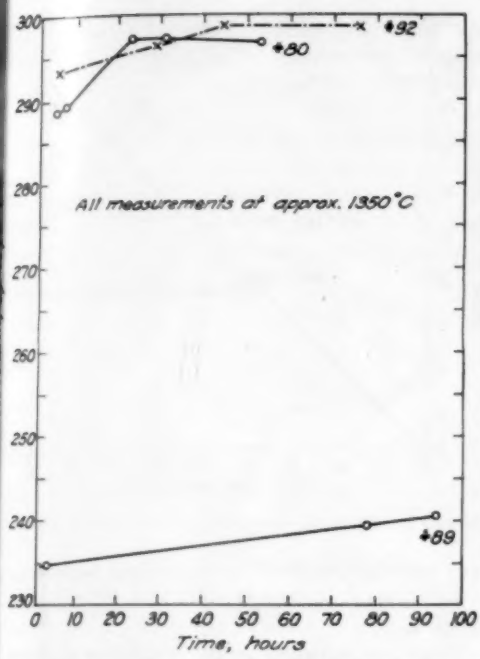

URE 2.—*Increase of surface tension with duration of treatment at elevated temperatures for Standard Samples 80, 89, and 92.*

TABLE 3.—*Comparison of surface tension values*

NBS Standard Sample	Temperature	Observers		
		Shartsis and Smock	Badger	Bradley
	°C	*Dynes/cm*	*Dynes/cm*	*Dynes/cm*
o. 80, bottle glass	1,350	[a] 297	302	304
o. 89, lead-barium glass	1,350	[b] 241+	245	243
o. 92, low-boron glass	1,400	[c] 290	290	305

[a] Heated 23 hours at 1,350° C.
[b] Value still rising after 94 hours at 1,350° C.
[c] Heated 40 hours at 1,400° C.

The surface tension of B_2O_3 in the range 700° to 1,400° C was measured and a plot of these data is shown in figure 3. A straight line was fitted to the data by means of least squares, and values of 58.2 at 300 ° C, and 65.3 at 500° C, were deduced from the extrapolation of this line. The corresponding values reported by Bradley [6], using a sessile drop method, were 57 and 67 dynes/cm. This agreement is well within the reproducibility of the sessile drop method.

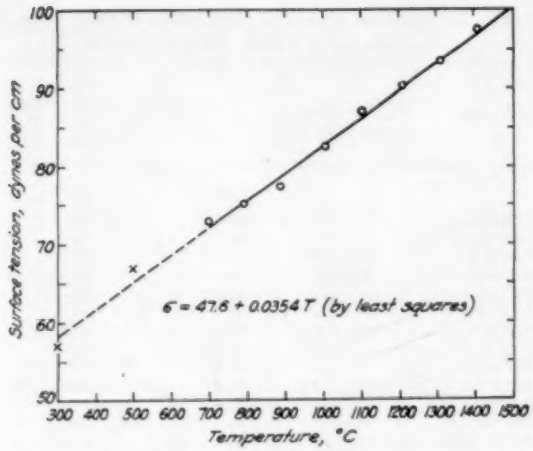

FIGURE 3.—*Surface tension versus temperature of* B_2O_3.

Points in circles by maximum pull-on cylinder method, crosses by Bradley, who used a sessile drop method.

5. Relation Between Seed Quality, Surface Tension, and Other Factors

To investigate the possible relation between surface tension and seed quality, which was one of the aims of this study, an analysis was made of the records of some 2,500 melts produced at the optical glass plant of the National Bureau of Standards. The system in use was for inspectors to rate the quality of the optical glass with respect to several properties, seed quality being one of the properties considered. Excellent melts were rated *A*, good ones *B*, fair ones *C*, poor ones *D*, and very poor ones *E*. The letters were converted to numbers by assigning the number 1 to *A* pots, 2 to *B* pots, etc. These numbers were then averaged for all the melts of a given glass and are to be found in the second column of table 4. Ratings for the corrosiveness of the various glasses toward the pots used in their manufacture were deduced from the data of Parsons [8]. The volume of gas liberated in the melting process was calculated from the batch components in cubic feet per pot of glass at 0° C and 760-mm pressure. The volatilization of batch materials, other than CO_2, NO_2, O_2, and H_2O vapor, was not considered.

727972—47——8

TABLE 4.—*Ranking of optical glass with respect to seeds, surface tension, pot attack and gas-in batch*

Glass	Number of pots	Seed rating	Rank in seed quality	σ	Rank in σ	Rank [a] in pot attack	Gas computed, per pot	Rank in gas
				1,300° C			*ft³*	
F 605/37.9	7	1.71	1	218.6	5	3	1549	8
F 606/32.4	4	2.00	2	216.2	1	4	908	2
F 649/33.8	60	2.02	3	216.2	2	7	1111	4
BaF 604/43.5	65	2.31	4	246.4	12	13	1763	10
BSC 511/63.5	110	2.34	5	231.4	10	8	3695	14
F 5795/40.9	166	2.59	6	221.3	7	2	1256	7
F 620/36.2	252	2.59	7	221.2	6	6	999	3
F 617/36.6	166	2.69	8	222.5	8	5	1135	5
BaF 584/46.0	9	2.89	9	251.5	13	12	1731	9
BSC 517/64.5	1,530	2.94	10	227.3	9	9	4005	15
F 6725/32.2	2	3.00	11	216.6	3	10	1154	6
BaC 541/59.8	28	3.28	12	263.8	14	15	2480	12
BaC 5725/57.4	893	3.39	13	270.5	15	16	4500	16
F 720/29.3	24	3.46	14	218.5	4	11	650	1
LC 523/58.6	8	3.50	15	277.1	16	1	2000	11
BaC 617/55.0	18	3.72	16	310.6	18	18	7733	17
BaF 588/53.4	4	4.00	17	235.3	11	14	3560	13
BaC 611/58.8	16	4.56	18	289.0	17	17	7771	18

[a] Ranks estimated by W. H. Parsons, based on his experience with petrographic examinations of pots.

Rank correlation coefficients of +0.62, +0.61, and +0.51, were obtained by computation for seed quality versus surface tension, pot attack and gas-in-batch, respectively. These values are large enough to be statistically indicative [9]. Figures 4, 5, and 6, show the departure of the individual points from the 45-degree line, which represents perfect rank correlation. A remarkably high rank correlation of +0.82 was found between gas-in-batch and surface tension, as illustrated by figure 7.

Attention is called to the weakness of some of the data upon which these correlations are based, and caution is advised in their full acceptance. The inspectors' ratings were affected by the factors that influence subjective ratings, personal temperament, demand for the glass, etc. The data of Parsons were based, for the most part, on pots that failed in service by leaking.

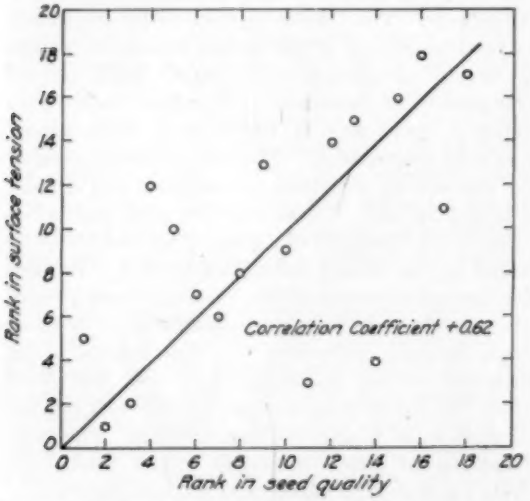

FIGURE 4.—*Rank in seed quality versus rank in surface tension.*

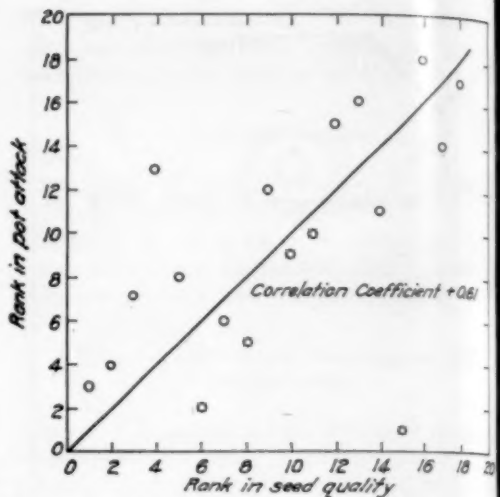

FIGURE 5.—*Rank in seed quality versus rank in pot attack.*

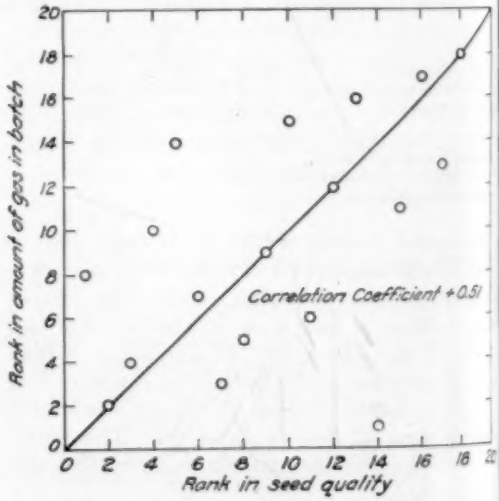

FIGURE 6.—*Rank in seed quality versus rank in amount of gas in batch.*

To substantiate these correlations, more and better data are necessary. Quantitative values for pot attack might be obtained by using tracers incorporated in the pot body. The effect of different amounts and kinds of gas might be investigated by varying the batch components used in making a glass of a certain composition. A quantitative system of seed ratings with cross checking by different inspectors should improve the objectivity of these estimates.

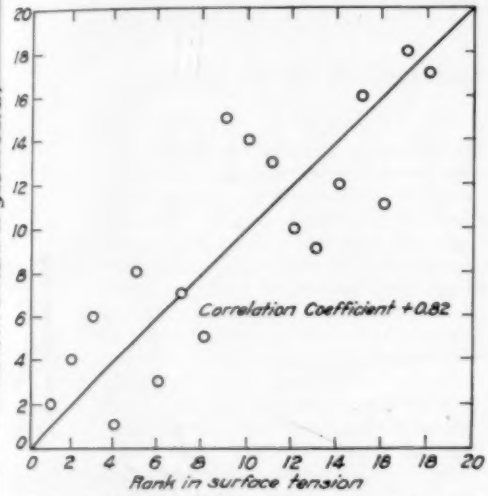

FIGURE 7.—*Rank in surface tension versus rank in gas in batch.*

Many of the favorable factors that have a bearing on seed quality occur together, and so do many of the unfavorable ones, thus making difficult the estimation of the exact contribution of each to the final result. Thus, in general, the barium crowns show high pot corrosion, have high surface tensions, and liberate large amounts of gas during the melting process. On the other hand, the flint glasses usually have low surface tensions, low corrosiveness, and liberate small amounts of gas when melting down. The simultaneous occurrence of like factors stems from the chemical composition. When exceptions to the rule that like factors occur together arise, the effect of the exceptional property can be noted. Thus, by reference to table 4, one can see that F 720 is poor for seeds, which may probably be explained by its ability to corrode the pot to a far greater extent than the other flints.

In addition to the factors already mentioned, it is known that a poor melting schedule or faulty furnace conditions may also cause seeds in glasses. It is possible that the good quality of *Ba*F 604, which seems unexpected because of its high corrosiveness and only moderate surface tension and gas content, is to be ascribed to an exceptionally good melting schedule. This theory could be tested by melting the other barium flints on a similar schedule with whatever changes are necessary because of differences in viscosity or fining time. The chief advantages of the data and correlations advanced here are in the indications as to the possible lines of attack in disentangling the factors operative in determining the seed quality of the optical glasses.

V. Summary

The surface tensions of a number of the optical glasses made at the National Bureau of Standards have been measured by a modification of the anchor-ring method. The values found seemed to be affected by the length of time the glasses were maintained at elevated temperatures immediately prior to measurement. Most of the glasses, especially those containing considerable amounts of PbO, were found to have positive temperature coefficients of surface tension. Positive rank correlations of statistical significance were found between seed quality and such factors as surface tension, pot attack, and amount of gas liberated during the melting process. In general, the flints rank low in surface tension, with values in the range 210 to 230 dynes/cm, the barium crowns high, with values around 260 to 310 dynes/cm, and the other glasses intermediate.

VI. References

[1] F. C. Champion and N. Davy, Properties of matter, p. 126 (Prentice-Hall, Inc., New York, N. Y. 1937).

[2] A. A. Appen, Optiko-Mechan. Prom. **6,** No. 3, F-12; No. 12, 17f (1936).

[3] W. N. Harrison and D. G. Moore, Surface tensions of vitreous enamel frits at and near firing temperatures, J. Research NBS **21,** 337 (1938) RP1133.

[4] C. L. Babcock, Surface tension by a modified cylinder method, J. Am. Ceram. Soc. **23,** 13 (1940).

[5] A. E. Badger, C. W. Parmelee, and A. E. Williams, Surface tension of various molten glasses, J. Am. Ceram. Soc. **20,** 325 (1937).

[6] C. A. Bradley, Jr., Measurement of surface tension of viscous liquids, J. Am. Ceram. Soc. **21,** 339 (1938).

[7] H. Freundlich, Colloid and capillary chemistry (E. P. Dutton & Co., Inc., New York, N. Y., 1922).

[8] W. H. Parsons and H. Insley, Attack on refractory clay pots by optical glass, J. Research NBS **36,** 31 (1946) RP1689.

[9] E. E. Day, Statistical analysis, p. 208 (The Macmillan Co., 60 Fifth Ave., New York, N. Y., 1937).

WASHINGTON, October 10, 1946.

U. S. Department of Commerce
National Bureau of Standards

Research Paper RP1722
Volume 38, February 1947

Part of the Journal of Research of the National Bureau of Standards

Laminar Boundary-Layer Oscillations and Transition on a Flat Plate[1]

By Galen B. Schubauer and Harold K. Skramstad

This is an account of an investigation conducted at the National Bureau of Standards, with the cooperation and financial assistance of the National Advisory Committee for Aeronautics, in which oscillations were discovered in the laminar boundary layer along a flat plate. These oscillations were found during the course of an experiment in which transition from laminar to turbulent flow was being studied on the plate as the turbulence in the wind stream was being reduced to unusually low values by means of damping screens. The first part of the paper deals with experimental methods and apparatus, measurements of turbulence and sound, and studies of transition. A description is then given of the manner in which oscillations were discovered and how they were found to be related to transition, and then how controlled oscillations were produced and studied in detail. The oscillations are shown to be the velocity variations accompanying a wave motion in the boundary layer, this wave motion having all of the characteristics predicted by a stability theory based on the exponential growth of small disturbances. A review of this theory is given. The work is thus experimental confirmation of a mathematical theory of stability which had been in the process of development for a period of approximately 40 years, mainly by German investigators.

I. Introduction

When any fluid flows past solid boundaries, the fluid near the surface is retarded by friction. This retarded layer is known as the boundary layer. While there are many kinds of boundary layers, the two main classes are laminar layers and turbulent layers. In the vast majority of cases of practical interest, a laminar layer will be present on the upstream portion of a body while a turbulent layer will be found on the after part of a body. Although a turbulent layer may cover the greater part of a body, the laminar layer may be regarded as the more natural one, because it must exist by virtue of the viscosity of the fluid. A turbulent layer is always formed from a laminar layer through a break-down of laminar flow resulting from an unstable condition. The nature of this instability and the fundamental causes of transition to turbulent flow have been the subject of many investigations, and theory and experiment have not been in agreement. The present experiment was undertaken to learn more about this controversial subject. One of the simplest cases was selected for the investigation, namely, the boundary layer on a thin flat plate with air flowing parallel to the surface. When the pressure is uniform, the laminar boundary layer on such a surface is known as the Blasius type.

1. Symbols and abbreviations

x = distance from leading edge of flat plate
y = distance from surface of flat plate
U_0 = mean velocity outside boundary layer
U = mean velocity at a point in boundary layer
u = instantaneous x-component of fluctuation velocity

[1] This paper was originally published by the National Advisory Committee for Aeronautics in April 1943 as an Advance Confidential Report. The material has recently been released for unrestricted publication. The introduction has been revised somewhat for the benefit of readers not familiar with boundary-layer flow.

v = instantaneous y-component of fluctuation velocity

w = instantaneous fluctuation velocity perpendicular to U_0 and parallel to surface of flat plate

$\left.\begin{matrix} u' \\ v' \\ w' \end{matrix}\right\}$ = root-mean-square values of u, v, and w

c_r = wave velocity

$\beta_r = 2\pi f$, where f = oscillation frequency

$\alpha = 2\pi/\lambda$, where λ = wavelength

β_i = amplification coefficient

ρ = density

μ = viscosity

$\nu = \mu/\rho$ = kinematic viscosity

q = dynamic pressure

δ = boundary-layer thickness

δ^* = boundary-layer displacement thickness

$\delta^* = 1.72\sqrt{\frac{\nu x}{U_0}}$ for Blasius velocity distribution

$\delta^* = 0.341\ \delta$ relation used by Tollmien and Schlichting [2, 4, and 5]

$R = U_0\delta^*/\nu$ = Reynolds number

$R_x = U_0 x/\nu = x$-Reynolds number

$R = 1.72\sqrt{R_x}$ for Blasius velocity distribution

$\Lambda = \frac{dU_0}{dx}\frac{\delta^2}{\nu}$ = Kármán-Pohlhausen parameter.

Past experiments have all indicated that disturbances in the form of velocity fluctuations, either in the oncoming stream or in the boundary layer itself, are the direct cause of transition. The accumulated evidence favored the view that transition depended on the extent to which a boundary layer was disturbed; that is, that a laminar boundary layer could withstand a certain amount of disturbance without becoming unstable, but that it became unstable when the disturbances were large enough. It was assumed by some that the velocity variations had to be large enough to cause intermittent separation of the layer from the surface to produce transition. Following this point of view, G. I. Taylor [1][2] advanced a theory of transition based on the varying pressure gradients accompanying turbulence in the surrounding flow outside the boundary layer.

In spite of this experimental evidence, a stability theory based on a quite different concept was favored by some mathematicians, mainly belonging to the German school. According to this theory, small disturbances in velocity of any wave length lying within a certain region would be amplified in the boundary layer, whereas disturbances of shorter or longer wave length would be damped. Thus stability would depend on the wave length rather than the magnitude of a disturbance.

Important contributions to this theory were made by Tollmien [2, 3], and Schlichting [4 to 7]. There was a little experimental evidence to support the theory found in flows known to be of the unstable type: namely, flow in a divergent channel [8], in a wake at low speeds [9], and in an acoustically sensitive jet [10]. However, this evidence was discounted on the basis of inherent instability, and stability theory was discredited by those who were inclined to trust experiment rather than theory.

Such was the state of the transition problem at the outset of the present investigation. The original purpose of the investigation was not to settle any controversy, but rather to find out where transition would occur on a flat surface and to learn as much as possible about transition when the turbulence of the surrounding stream was reduced to levels lower than had hitherto been obtained. It was a fortunate choice of experiment, for the discovery of laminar boundary-layer oscillations, made possible by the smoothness of the flow, was the first conclusive evidence of the validity of stability theory based on the growth of small disturbances. The subsequent study, described herein, of the waves producing the oscillations completely verified the theory.

The failure of previous investigations was due in large measure to disturbances that were initially large enough to cause transition, these disturbances coming in general from the relatively high turbulence in the surrounding stream. The first known observations of velocity fluctuations in a laminar boundary layer were made by Dryden [11]. These were regarded as disturbances impressed on the boundary layer by the turbulence in the outside stream. They were irregular and produced transition without showing any of the characteristics required by stability theory. Nikuradse [12] attempted to test the stability

[2] Figures in brackets indicate the literature references at the end of this paper.

theory by producing sinusoidal fluctuations in the boundary layer near the leading edge of a flat plate in water. His results were inconclusive, partly because the artificial fluctuations, as well as the general disturbances, were too large, and partly because he observed only the effect on the location of transition.

The investigation of transition on a flat plate at low turbulence was suggested by Hugh L. Dryden, and the authors acknowledge his assistance and many valuable suggestions in connection with the experimental program.

II. Apparatus and Methods

1. Wind Tunnel

The present investigation was conducted in the 4½-foot wind tunnel at the National Bureau of Standards. The general layout of the tunnel is shown in figure 1. The flat plate was located

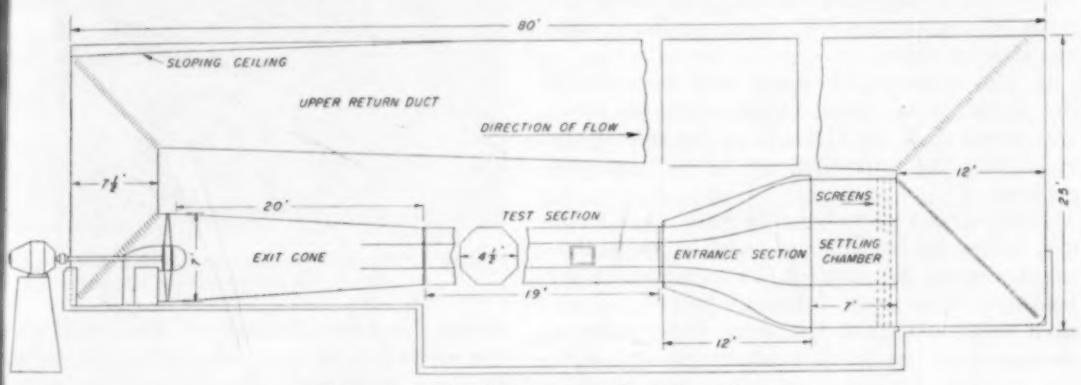

FIGURE 1.—*Elevation view of 4½-ft wind tunnel.*

vertically in the test section with the leading edge 6 feet from the upstream end. In order to reduce vibration, the test section of this tunnel is supported directly from the foundation and is joined to the rest of the circuit by only a sponge-rubber seal at each end. The area reduction from settling chamber to test section is 7.1:1. The guide vanes ahead of the settling chamber were made finer than the others in order to reduce the scale of the turbulence and to permit as much reduction in turbulence through decay as possible. Since directional fluctuations in the horizontal plane were found to be large, closely spaced straighteners were placed at right angles to and on top of the fine guide vanes. This combination was in effect a honeycomb and resulted in great improvement in the steadiness of the stream. Further reduction of turbulence was obtained by installing damping screens in the settling chamber. Without screens, the turbulence in the test section was 0.27 percent at 100 feet per second and, with seven screens, was 0.032 percent.

2. Flat Plate

The flat plate was a commercial sheet of aluminum ¼ inch thick, 4½ feet wide, and 12 feet long. The leading edge, which was symmetrical and pointed, was formed by the intersection of circular arcs tangent to the original surface 4 inches from the leading edge. The surface was left in its original condition and had a mirrorlike finish, marred slightly by small scratches barely perceptible to the finger tips. Waviness was quite perceptible when viewed near grazing incidence. A surface gage showed variations from approximately 0.01 to 0.02 inch over distances from 1 to 2 feet. These were bends in the plate evidently produced by the rolling process.

The plate was bolted along the top and the bottom edges to one side of 3-inch steel channels, which were in turn bolted to the floor and to ths ceiling of the tunnel. The flanges away from the plate served as rails at the floor and at the ceiling for a carriage on which all exploring apparatus was mounted. The carriage was simply a steel plate ⅜ inch thick and 6 inches wide, with runners and guides at the ends in contact with the rails. This plate was thus parallel to the wind and 3 inches from the flat plate. All explorations in the boundary layer were made 25 inches or more

ahead of the carriage to avoid the local pressure field. The carriage was propelled by hand from outside of the tunnel by a sprocket and chain.

3. Pressure Distribution

In order to control the pressure gradient along the flat plate, the cross section of the working chamber was varied by adjustable auxiliary walls on the vertical sides of the chamber. These walls were aluminum sheets 1/16 inch thick and 22 inches wide extending from opposite the trailing edge of the plate to a distance 4 feet ahead of the leading edge. The sheets, mounted on screws, spaced 9 inches, and threaded through the tunnel walls, were adjustable to and from the sides of the tunnel. In order to prevent discontinuity at the top and at the bottom edges, the sheets were backed by a stretched rubber diaphragm; the combination of aluminum sheet and rubber formed a continuous flexible wall that could be warped or displaced as desired. The maximum range of displacement of these auxiliary walls was about 4 inches.

By this means the pressure could be made to rise, to fall, or to remain constant along the plate. (See curves *A*, *B*, and *C*, fig. 30.) For most of the experiment the walls were set for zero pressure gradient.

The provision for warping the walls into a bulge or a hollow did not prove so useful as was anticipated because the effect of the warp usually extended over too great a distance to give the desired result. When it was desired to produce a sharp pressure rise or fall, other devices were used. For example, an airfoil extending from floor to ceiling near the plate produced a sharp pressure fall followed by an abrupt rise. A pressure fall without a rise was easily produced by proper blocking of the stream.

Although measurements were taken on only one side of the flat plate, the auxiliary walls on each side of the tunnel were given the same shape for symmetry. Some asymmetry nevertheless existed because of the presence of the carriage and the measuring equipment on only one side of the plate. Although this resulted in greater blocking of the stream on the working side, it was found that some excess blocking here was necessary to direct the flow at a slight angle to the leading edge of the plate so that the stagnation point was displaced slightly from the sharp edge to the working side of the plate. The transition point was unaffected by the position of the stagnation point so long as this point was not displaced to the opposite side of the plate. The slight excess blocking was therefore maintained at all times to prevent directional variations accompanying the turbulence in the stream from ever carrying the stagnation point to the opposite side.

4. Measurement of Pressure and Transition

A small pitot-static head was arranged as shown in figure 2 with the impact tube in contact with the surface and the static tube parallel to the

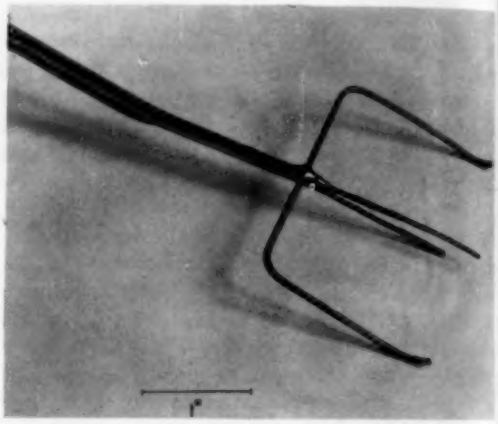

FIGURE 2.—*Pitot-static-surface tube used to measure pressure distribution and position of transition.*

stream 1/4 inch from the surface. This combination was carried on an arm attached to the carriage 28 inches to the rear and could slide fore and aft with fork-like guides and impact tube always in contact with the surface. Both tubes were made from thin-wall nickel tubing with 0.04-inch outside diameter. The impact tube was flattened on the end to form a slit 0.007 inch wide, the center of which was 0.006 inch from the surface when the tube was in contact. The static tube had four 0.008-inch holes drilled through the wall, 8 diameters from the closed end.

Only the static tube of this instrument was used when pressure distributions were measured and both tubes were used when transition points were determined. Traverses were always horizontal and usually made along the center line of the plate. The static pressure was thus measured 1/4 inch from the surface, which for most of the

rface corresponded to a position outside the undary layer. A large variation of pressure rmal to the surface was found near the leading ge where the pressure distribution was deter- ined by the shape of the leading edge. Also, ssure effects caused by waviness of the surface pended on the distance from the surface. Since e former variations were confined to the first inches from the leading edge and the latter were all, variations in pressure in the ¼-inch distance rmal to the surface were neglected.

The detection of transition by the surface-tube ethod depends on the variation with x of impact ssure near the surface, which corresponds osely to the variation of shearing stress at the rface. This impact pressure decreases with stance from the leading edge to the beginning transition, then rises through the transition gion, and again falls in the turbulent region. In e present work, the point of minimum pressure s taken as the beginning of transition, and e point of maximum pressure following the rise s taken as the point where turbulence was lly developed.

5. Boundary-Layer Thickness

Velocity distributions across the boundary layer ere determined by traversing normal to the rface with a flattened impact tube similar to e surface tube. This tube was carried on an arm milar to the one shown with the hot-wire emometer attached in figure 3. Both the

GURE 3.—*Apparatus for traversing normal to the surface.* Hot-wire head attached.

icrometer screw, A, and the fulcrum, E, were eld in contact with the surface of the plate by e rigid arm extending rearward to the carriage, d motion of the impact tube to and from the rface was obtained by rocking the arm about e fulcrum by means of the screw. The velocity distributions were used to determine δ^*. When the pressure gradient was zero, the measured values of δ^* were in agreement with those calculated by the Blasius formula

$$\delta^* = 1.72\sqrt{\frac{\nu x}{U_0}}.$$

Whenever the value of δ^* was needed for presenting results obtained at zero pressure gradient, the value calculated by this formula was used.

Tollmien and Schlichting, [2,4,5] used a constant in the above formula equal to 1.73 for computing δ^*. More recent values of the constant are 1.7207 given by Dryden [11] and 1.7208 given by Goldstein [13]. A value of 1.72 is therefore used in the present work.

6. Hot-Wire Turbulence Equipment

A variety of apparatus, such as amplifiers, bridges, potentiometers, oscillators, oscillographs, and numerous types of hot-wire anemometer, comes under the heading of hot-wire equipment for measuring turbulence. Amplifiers with attendant power supplies and hot-wire anemometers are usually special equipment, whereas the other equipment is of standard commercial design. Amplifiers used in turbulence work and circuits to compensate for the thermal lag of hot wires have, however, been standardized to a certain extent, and their essential features are described in the literature. Two amplifiers, which were designed and built by W. C. Mock, Jr., were used in the present investigation. One of the amplifiers is described in reference 14; the other was a newer and more portable type with about the same frequency response but using capacitance compensation instead of inductance compensation. Both types of compensation and the requirements to be met by each type are described in reference 15. The theory of compensation is given in reference 16. When properly compensated, the over-all response of wire and amplifiers was uniform from 3 to about 2,000 cycles per second.

In all cases hot-wire anemometers must be calibrated by measuring the voltage across the wire at known air speeds; or, if the anemometer is sensitive to direction changes, it must be calibrated by measuring the voltage at several angles to the wind. For this purpose a potentiometer is necessary. A Wheatstone bridge

must be used to obtain the resistance of the wire at air temperature. Throughout the present work, both in calibration and in use, the heating current was held constant and only the temperature and the voltage across the wire were allowed to vary. This condition was maintained during rapid velocity fluctuations by a sufficiently large choke coil in series with the wire. Amplifiers were calibrated by applying to them a known alternating voltage from an oscillator. By use of the calibration data, velocity fluctuations could be calculated from the amplified and properly compensated voltage fluctuations across the hot wire. A cathode-ray oscillograph was used for visual observation of fluctuations and also for making photographic records with a moving-film camera. When observations were simultaneously taken on two wires, an electronic switch was used in conjunction with the oscillograph.

7. Hot-Wire Anemometers

The hot-wire anemometers used here may be divided into two classes: (1) Those used in the free stream to measure turbulence, (2) those used in the boundary layer to study oscillations, transition phenomena, and turbulence. Anemometers of class 1 were designed for high sensitivity and for freedom from vibrational effects. Anemometers of class 2 were designed for working near a surface with a minimum of interference and with as little vibrational motion relative to the surface as possible. Both types used platinum wire 0.00025 inch in diameter, obtained by etching the silver coating from Wollaston wire. The etched wire was soft-soldered to prongs made either from fine sewing needles or from fine copper wire. Platinum wires of this size were adequately sensitive in lengths no greater than $\frac{3}{16}$ inch and, in the range of operating conditions, had time constants ranging from 0.0005 to 0.002 second.

Anemometers of class 1 were made with a single wire normal to the wind for measuring u' or with two wires set at an angle to the wind in the form of an X for measuring v' and w'. Heads of these two types are shown in figure 4. Both have platinum wires (not visible in the photograph) across the tips of the prongs; the four-prong head has the two wires forming an X. In the X-arrangement the wires lie as nearly as possible in a plane without touching and subtend an angle of 60 degrees, with each wire at an angle

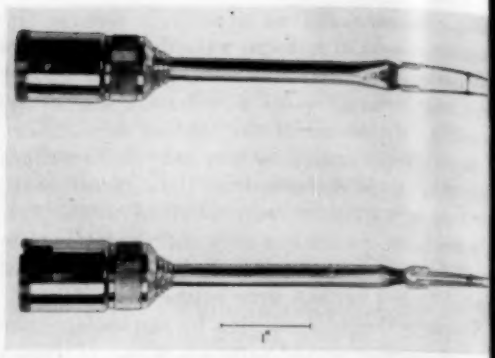

FIGURE 4.—*Hot-wire heads for the measurement of fr stream turbulence.*

of about 30 degrees to the wind. Braces of sil thread cemented across the prongs about ¼ inc from the tips were necessary to prevent wi breakage. All wires were about $\frac{3}{16}$ inch long These arrangements of wires take advantage the directional characteristics of a wire in ord to obtain sensitivity to the component desire The sensitivity of a wire to direction is known depend on the angle to the wind, being zero wh normal and again when parallel. Sensitivity u is a maximum when the wire is normal. Sinc v and w are small, their principal effect is to cau fluctuation in direction of the stream when adde vectorially to U and the effect on the magnitud of the instantaneous velocity is insignificant. wire normal to the wind responds thus to fluctuations rather than to v or w.

An X-arrangement of two identical wires, eac making the same angle to the wind, with voltag opposed produces a resultant voltage change onl when the wires are differentially cooled. Thi arrangement is then insensitive to u, but highl sensitive to direction changes in the plane of th wires and hence to v or to w depending on th orientation of the plane. When fluctuations ar large, isolation of single components in this wa is not complete and voltage changes are no exactly proportional to velocity changes. If th fluctuations do not exceed 5 percent of the mea speed, errors from these sources are believed t be less than 1 percent.

The mountings for the hot-wire heads are show in figure 5. The central member to which th head is attached is held within the cylindrical tub by a rubberband suspension and in this way i isolated from vibration from the tunnel walls

vibrational effects were not troublesome after a sufficiently "soft" suspension of this sort was used. The mounting for the X-wires contains an angle-changing device for calibrating the wires.

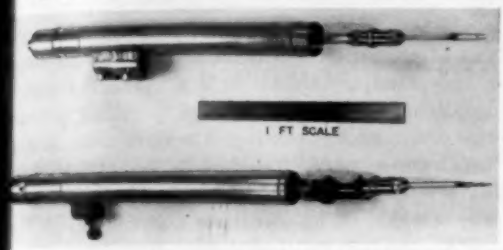

FIGURE 5.—*Rubber-suspension-type mountings with hot-wire heads attached.*

In the boundary layer only the u-component was measured, except when one attempt was made to discover whether the boundary-layer oscillations had a w-component. A study of v was considered desirable but no appropriate hot-wire head of sufficiently small dimensions was available for the purpose. For anemometers of class 2, therefore, most attention was given to hot-wire heads with the wire normal to the wind and parallel to the surface. The wire length was usually 0.04 inch. For traversing along the surface with the wire at a fixed distance, the wire was attached at the tips of prongs extending about 1/4 inch forward from a small celluloid sled, which was held against the surface by wire springs from a brass tube attached to the carriage. A sled assembly with two pairs of prongs for supporting two wires at different distances from the surface is shown in figure 6. Another sled was also used with two hot wires

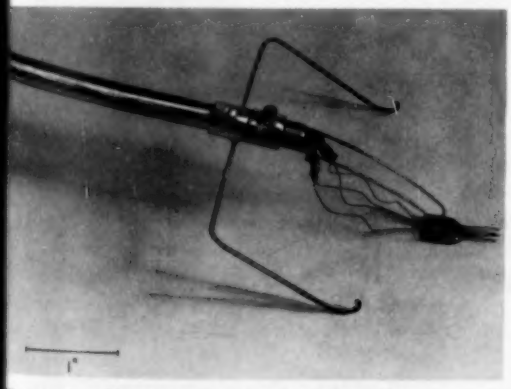

FIGURE 6.—*Sled-like hot-wire head arranged for two hot wires.*

making a V in a plane parallel to the surface. The latter arrangement was sensitive to w. The sled was believed to be the best possible type of hot-wire head to prevent relative motion between the wire and the surface. Interference effects were found negligible.

For traversing normal to the surface, the hot wire was supported on the tips of steel sewing needles extending into the boundary layer from the arm of the traversing apparatus shown in figure 3. This arrangement was made sufficiently rigid to be free from vibration troubles but was not appropriate for traversing parallel to the surface. A combination of this apparatus with a sled was used when it was desired to keep one wire at a fixed distance from the surface while moving the other in and out from the surface.

III. Reduction of Stream Turbulence and Effect on Transition, Zero Pressure Gradient

In the present investigation, effects of high stream turbulence were of little concern. Emphasis was placed rather on reducing the turbulence as far as practicable in order to study the boundary layer when it was as little disturbed from the stream as possible. The turbulence was successively reduced by placing various numbers and combinations of damping screens in the settling chamber. For each addition of a screen and for every recombination of screens, measurements were made of u'/U_o, v'/U_o, and w'/U_o in the working chamber and the values of R_x at the beginning and at the end of transition were determined.

No correction for wire length according to the method given in reference 17 was made, since the appropriate scale for v' and w' could not be determined. If the probable order of magnitude of the scale is considered, the correction is small and is believed to be unimportant in view of the accuracy attainable in the measurement of low turbulence.

Screens of fine mesh and small wire were used in order that the turbulence produced by the screen itself would decay rapidly. Each screen completely covered the cross section of the settling chamber and, when more than one screen was used, a spacing of 6 inches or more was allowed between them. Preliminary surveys with the hot-wire anemometer showed that the turbulence was uniform over the usable cross section of

the stream and that little or no decrease in turbulence occurred in the length of the working chamber. The turbulence could therefore be specified by hot-wire measurements made at one point in the working chamber. The measurements showed that v' and w' were nearly equal to each other but generally greater than u'. This nonisotropic condition is known to be caused by the contraction of the stream from the large area of the settling chamber to the smaller area of the working chamber. The more the turbulence was reduced by the addition of screens, the less this difference became and, finally, near the lowest turbulence u' was actually larger than v' and w'. In all cases the turbulence increased with the wind speed, an effect that could be partly accounted for by the decreasing resistance coefficient of the screens with increasing speed.

As the number of screens was increased, a reduction in turbulence was obtained with each additional screen but by successively decreasing amounts; and the reduction by this means appeared to have reached a practicable limit when six screens were installed. The measured values with six screens are given in table 1. It was believed at first that a level had been reached nearly equal to the turbulence produced by the screens themselves. A finer screen than any of the others was therefore added downstream from the six screens already present. As no screens with finer wires than those already used were commercially available, a screen made from silk bolting-cloth was installed. Some futher reduction was obtained but not so much as was expected. No attempt was made at further reduction. The measured values of the turbulence at this lowest level are given in table 2. The x-Reynolds numbers of transition found during the various stages of reduction are shown in figure 7. The highest turbulence shown in the figure (0.342 percent) was obtained by placing a square-mesh grid of ½-inch rope, spaced 6 inches, in the settling chamber a few inches downstream from the set of six wire screens. The transition point found by Hall and Hislop [*18*] for their lowest turbulence is indicated in figure 7. By definition, their transition point corresponds to the beginning of transition of the present paper.

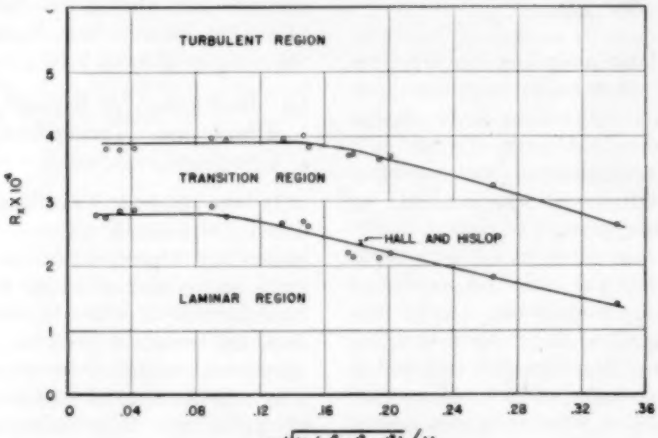

FIGURE 7.—*Effect of turbulence on x-Reynolds number of transition.*
Flat plate, zero pressure gradient.

TABLE 1.—*Turbulence with 6 damping screens in settling chamber*
Measurements at single station in working chamber

U_0	$\frac{u'}{U_0}$	$\frac{v'}{U_0}$	$\frac{w'}{U_0}$	$\frac{\sqrt{1/3(u'^2+v'^2+w'^2)}}{U_0}$
fps	*Percent*	*Percent*	*Percent*	*Percent*
30	0.019	0.011	0.012	0.0145
40	.021	.020	.019	.0200
50	.024	.023	.020	.0224
60	.027	.026	.021	.0248
70	.030	.030	.026	.0287
80	.033	.035	.032	.0334
90	.035	.039	.037	.0371
100	.037	.042	.041	.0401
110	.040	.044	.045	.0433
120	.045	.046	.047	.0459

Two questions are raised by the foregoing results: (1) Why was the addition of the bolting-cloth screen so ineffective in further reducing the turbulence? and (2) Why was transition on the flat plate unaffected by reduction of turbulence below about 0.08 percent? The first question is answered in the following section. The second question is more difficult, and an attempt will be made to answer it only after boundary-layer oscillations are considered. (See section VIII.)

IV. Residual Turbulence and Noise

While the measurements of the lowest turbulence were in progress, it was noted by the trace on the screen of a cathode-ray oscillograph that the velocity fluctuations did not have the random character usually ascribed to turbulence. Vibration of the hot-wire mounting was suspected but was ruled out since changes in the softness of the mounting failed to change the appearance of the trace. Consideration was next given to the effect of wind-tunnel noise and led to the startling conclusion that a reasonably loud sound could involve particle velocities sufficient to produce an apparent turbulence of the order of that actually found. For example, a calculation based on a plane wave with an intensity of 105 decibels above a base level of 10^{-9} erg per cm^2 per second showed a root-mean-square particle velocity of 0.028 foot per second. At a wind velocity of 100 feet per second, this is equivalent to an apparent turbulence of 0.028 percent, while the measured turbulence was 0.0315 percent. A few measurements of intensity with a sound meter connected to a crystal microphone showed that the noise level was probably between 105 and 110 decibels at 100 feet per second. As 110 decibels is equivalent to an apparent turbulence of 0.051 percent, the noise could account for the entire hot-wire reading at this speed. At the lower speeds, however, the noise intensity appeared insufficient to account for the measured turbulence. As the wave pattern in the tunnel was very complex, calculations based on plane waves can be at best only rough approximations. Furthermore, to avoid the direct effect of the wind on the microphone, it was necessary to measure the sound level at a distance from the hot wire.

An analysis was made by a wave analyzer of the spectrum of the noise from the tunnel picked up in the tunnel control room by the crystal microphone. A similar analysis was then made of the output from the hot wire in the wind tunnel. In both cases the wind velocity was 80 feet per second. A comparison of the two spectrums is shown in figure 8. As the distribution of intensity with frequency is compared here, uncertainties in absolute intensity are of minor importance. The similarity of the curves indicates that, at a wind velocity of 80 feet per second, a large part of the hot-wire output is derived from noise.

The values of turbulence in tables 1 and 2 probably contain a significant contribution from noise, especially at the higher velocities. A large part of the increase with velocity is probably due to noise. Also, a u' greater than v' and w' is evidence that not all the contributing fluctuations were carried with the stream through the entrance cone. As most of the noise comes from the propeller, it is obvious that damping screens can reduce only the true turbulence. On the other hand, the addition of screens must increase the noise because of the higher propeller speed needed to maintain a given wind velocity through the added resistance in the screen. These facts afford a satisfactory explanation of the effective limit of damping screens in the present tunnel.

TABLE 2.—*Turbulence with 6 damping screens followed by 1 bolting cloth in settling chamber*

Measurements at single station in working chamber

U_0	$\frac{u'}{U_0}$	$\frac{v'}{U_0}$	$\frac{w'}{U_0}$	$\frac{\sqrt{1/3(u'^2+v'^2+w'^2)}}{U_0}$
fps	*Percent*	*Percent*	*Percent*	*Percent*
30	0.018	0.012	0.009	0.0135
40	.019	.012	.010	.0142
50	.021	.014	.015	.0169
60	.026	.018	.016	.0204
70	.029	.020	.017	.0226
80	.033	.022	.018	.0251
90	.037	.026	.020	.0286
100	.040	.029	.023	.0315
110	.044	.034	.025	.0352

Figure 8 also suggests some information concerning the answer to the second question posed in section III regarding the effect of turbulence on transition. As the spectrum of this apparent turbulence is unlike that of isotropic turbulence [19], such turbulence will probably affect transition in a different manner from isotropic turbulence. Velocity fluctuations from sound involve pressure changes not related to those of turbu-

lence and involve motions correlated over great distances. As the proportion of noise to turbulence was increased with each reduction of turbulence, anomalous transition effects are to be expected.

V. Laminar Boundary-Layer Oscillations, Zero Pressure Gradient

1. First Evidence of Oscillations

When the stream turbulence had been reduced to nearly its lowest level with the six wire damping screens, it was decided to investigate the velocity fluctuations in the laminar boundary layer itself. For this purpose one of the sled-like heads with a wire sensitive to u was arranged to slide along the surface with the wire 0.023 inch from the surface. With greatly reduced stream turbulence, it was expected that the slow irregular fluctuations, reported for a much more turbulent stream in reference 11, would be correspondingly reduced. Such fluctuations were, in fact, almost nonexistent; but, as the wire was moved downstream through the boundary layer, a regular oscillation appeared, weak at first but with increasing amplitude as the distance downstream increased. Just ahead of the transition, bursts of very large amplitude occurred and, at the initial point of transition, these bursts were accompanied by a breaking into an irregular high-frequency fluctuation characteristic of turbulence.

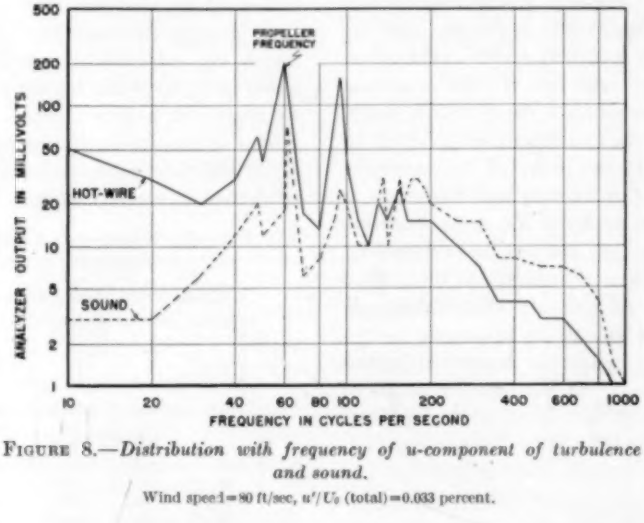

FIGURE 8.—*Distribution with frequency of u-component of turbulence and sound.*

Wind speed=80 ft/sec, u'/U_0 (total)=0.033 percent.

Records of the oscillations were made by photographing the screen of the cathode-ray oscillograph with a moving film camera. Two sets of such records are reproduced as figures 9 and 10. Figure 9 shows the progressive development of the oscillations. The traces at 6.25 and 6.5 feet already show the bursts of large-amplitude oscillations interspersed with highly disturbed turbulent motion. The final record at 8 feet indicates a completely turbulent boundary layer. The frequency of the oscillations may be judged by the $\frac{1}{50}$-second timing dots. The same phenomenon at a lower wind speed and at a greater distance from the leading edge of the plate is shown in figure 10. Here the amplifier gain (magnification) was adjusted to keep the recorded amplitude the same from position to position in order to bring out the weak as well as the strong oscillations. Attention is called to the lower oscilla-

tion frequency corresponding in this case to the lower speed and to the thicker boundary layer.

It was thought at first that these oscillations might possibly be due to vibration of the wire that gave rise to relative motion between the wire and the surface. This was soon ruled out since changes in the hot-wire head and support failed to cause any change in the oscillations. Furthermore, the oscillations appeared to be definitely connected with transition since the zone in which they occurred always preceded transition and moved with it fore and aft along the plate as the

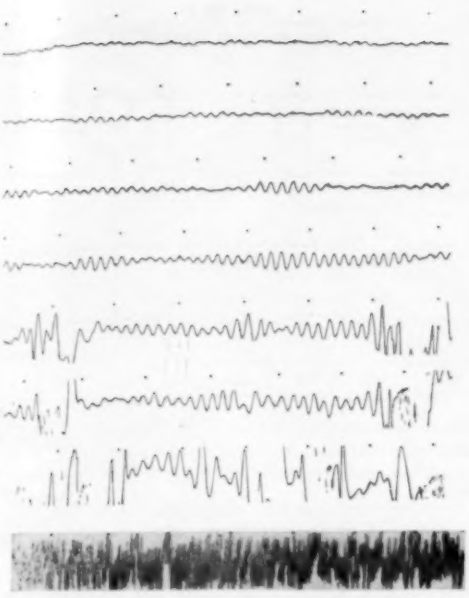

IGURE 9.—*Oscillograms of u-fluctuations showing laminar boundary-layer oscillations in boundary layer of flat plate.*

stance from surface=0.023 in. U_0=80 ft/sec. Time interval between dots=1/30 sec.

ind speed was varied. It could not be said ith certainty that the oscillations were the cause f transition, since there existed the possibility hat the boundary layer became shock-excited by ransition occurring a short distance downstream, iving rise to an oscillation that was possibly the esult of transition rather than the cause. The latter explanation was ruled out by removing transition ith an abrupt pressure drop and yet leaving the scillations totally unchanged at an upstream osition. The alternative conclusion, with no vidence to the contrary, was that transition esulted from the growing of the oscillations to the oint where the boundary layer was so highly isturbed that transition occurred.

It was soon found that the hot wire could be laced at any cross-section of the boundary layer o pick up the oscillations, although the amplitude uite evidently varied with position. The frequency remained the same throughout the section except very near the surface where there was a uggestion of frequency doubling on the low-velocity part of the cycle. This effect at the 4-foot osition is shown in figure 11. As the hot wire esponds to negative velocities as though they were positive, the doubling was believed to indicate that the amplitude of the oscillation was sufficiently high to reverse the direction of flow during half of each cycle.

A V-wire, sensitive to w, revealed a w-component in the oscillations. Little work was done with this wire, and the relative amplitudes of u and w were not compared. With the one exception cited here, all work was done with wires sensitive to u. Because of experimental difficulties no attempt was made to detect the v-component, although it is shown by theoretical considerations in section V, 2, that a v-component must exist. The presence of the w-component thus indicates that the oscillations were three-dimensional.

Because the effects of noise were so much in evidence, it might be supposed that the oscillations were a resonant acoustic phenomenon arising from some frequency in the sound spectrum. Among the evidence against this supposition is that presented in figure 12, which shows the effect of a tenfold increase in turbulence produced by the rope grid in the settling chamber downstream from the six damping screens. With the higher turbulence, it is seen that oscillations are present where they were absent before. It thus appears that dis-

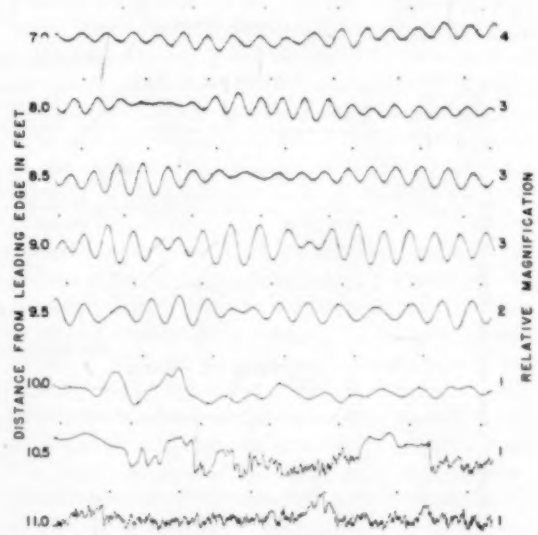

FIGURE 10.—*Oscillograms of u-fluctuations showing laminar boundary layer oscillations in boundary layer of flat plate.*

Distance from surface=0.023 in. U_0=53 ft/sec. Time interval between dots=1/30 sec.

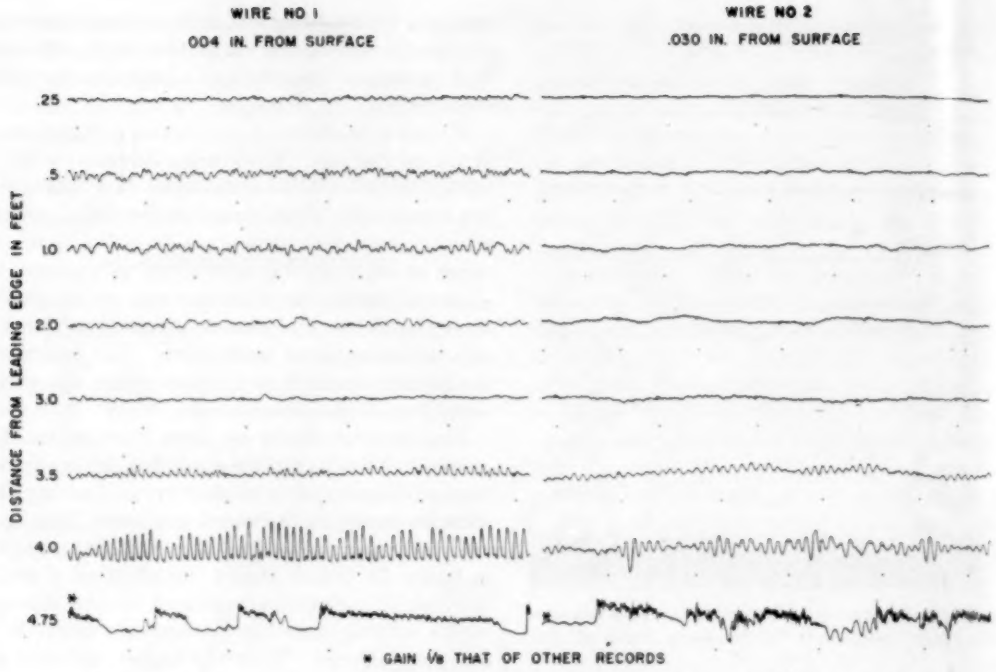

FIGURE 11.—*Oscillograms of u-fluctuations showing evidence of frequency doubling near surface.*
U_0=105 ft/sec. Time interval between dots=1/30 sec.

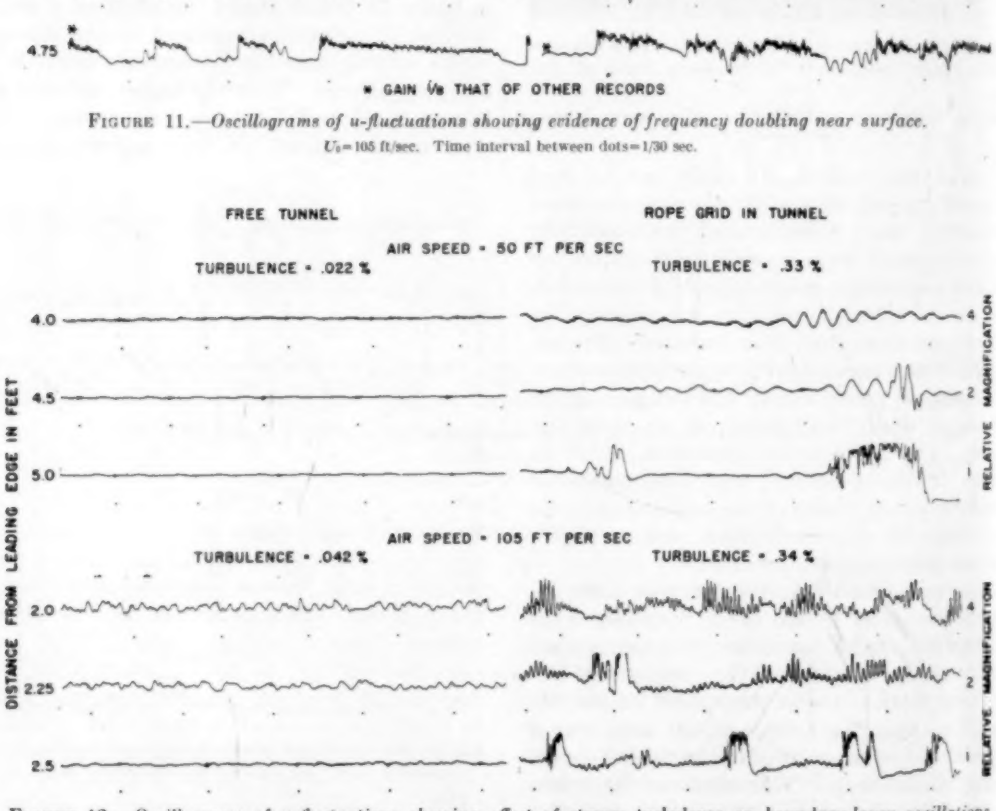

FIGURE 12.—*Oscillograms of u-fluctuations showing effect of stream turbulence on boundary-layer oscillations.*
Distance from surface =0.004 in. Time interval between dots=1/30 sec.

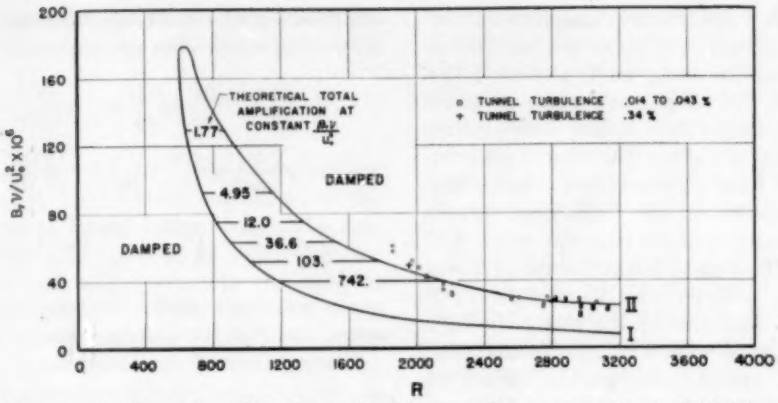

FIGURE 13.—*Zone of amplification enclosed by neutral curve, according to Schlichting.*
Theoretical total amplification from branch I to branch II as indicated. Experimental points from frequency of oscillations found on oscillograms. Branches I and II of neutral curve meet R-axis at $R=\infty$.

rbances in the stream, possibly acoustic as well turbulent, give rise to oscillations which are not hemselves sound waves.

It was believed almost from the start that the scillations were amplified disturbances, their urity resulting from selective amplification of a ngle frequency or, at most, a narrow band of equencies. Theories had been advanced to count for just such an amplification but were ten ignored in experiment because no conclusive vidence in their support had been found. In der to test whether these were in reality the mplified oscillations predicted by theory, frequencies were determined from numerous oscillograms, taken at as many positions and speeds as ossible and plotted in an appropriate manner on diagram derived from the theoretical results of chlichting. The diagram with the experimentally determined points is shown in figure 13. his figure will be made clear by the theoretical iscussion in section V, 2, and will be described in etail in section V, 3. For the present, it is sufficient to observe that the experimental points are istributed along branch II of the theoretical urve, which is the region in which the points hould fall if the initial disturbance, out of which scillations grow, have received approximately heir maximum amplification. The oscillations are herefore identified with those produced by instaility of the boundary layer.

2. Theory of Boundary-Layer Oscillations

Evidence has been found of oscillations of ther high purity resulting mostly from random disturbances. The oscillations observed at a fixed point suggest the presence of a traveling wave in the boundary layer. A theoretical answer is sought for the question: How can random disturbances produce a wave that looks closely sinusoidal and has a single predominant frequency?

The superposition of small disturbance velocities on a uniform velocity in one direction presents to a stationary observer the appearance of wave motion. The motion may be sinusoidal or irregular. For simplification, all the disturbance velocity components are assumed to be sinusoidal of the same frequency. In a uniform stream, this motion has the attributes of a traveling wave with a wave velocity equal to the mean velocity of the stream. The amplitude is the disturbance velocity with components u, v, and w, and the pressure involved is the dynamic pressure of the disturbance velocity. This kind of wave is involved in the application of stability theory to the boundary layer. Only two-dimensional motion has so far been successfully treated. In a nonuniform stream, such as a boundary layer, the wave velocity is not known at once but may reasonably be assumed (and can also be proved theoretically) to be less than the maximum velocity of the stream. The characteristics of the wave will depend on the characteristics of the stream, such as the velocity profile of a boundary layer, and on conditions imposed on the mean velocity and on the disturbance velocities at the boundaries. The theory treats the influence of all these conditions and how they determine the wavelength, the wave velocity, and the damping or the amplification of the wave.

72972—47——9

In general, the disturbances responsible for wave motion in a boundary layer are random in character and the resulting wave motion is irregular. One of the important characteristics of the wave is its ability to maintain itself against the damping action of viscosity or even to grow by absorbing energy from the basic flow. Since this characteristic depends on the frequency, certain component frequencies of an irregular wave will be damped and others amplified as the wave travels downstream. It will be seen in section V, 3 that this process accounts for the relatively high purity of the observed boundary-layer oscillations.

Energy considerations alone form the basis of an elementary treatment first used by Osborne Reynolds. According to the Reynolds concept, growth or decay of a disturbance depends on whether energy is transferred to the disturbance by absorption of energy from the basic flow or is extracted from the disturbance by the damping action of viscosity. The flow of energy then determines the stability of the boundary layer under the action of disturbances. As the kind of disturbance must be specified, this method does not have general applicability. The flow of energy is, however, a fundamental physical concept involved in all theories even though not explicity stated. As an introduction to the more advanced theories the energy relation will therefore be derived here. The development follows essentially that given by Prandtl [20].

(a) Basic Equations and Energy Relations

In general, only two-dimensional flow with two-dimensional disturbances has been treated successfully in stability theories. The basic flow is assumed to be steady and a function of y only. The basic flow in the boundary layer is then

$$U=f(y)$$
$$V=0.$$

The disturbances are a function of time as well as of x and y and are expressed by

$$u=f_1(x, y, t)$$
$$v=f_2(x, y, t).$$

The components of total velocity are therefore $U+u$ and v. As u and v are assumed to be small, the Navier-Stokes equations become, after squares and products of disturbance velocities and of their differential coefficients are neglected,

$$\frac{\partial u}{\partial t}+U\frac{\partial u}{\partial x}+v\frac{\partial U}{\partial y}= \tag{1}$$
$$\nu\left(\frac{\partial^2 U}{\partial y^2}+\frac{\partial^2 u}{\partial x^2}+\frac{\partial^2 u}{\partial y^2}\right)-\frac{1}{\rho}\left(\frac{\partial P}{\partial x}+\frac{\partial p}{\partial x}\right)$$

$$\frac{\partial v}{\partial t}+U\frac{\partial v}{\partial x}=\nu\left(\frac{\partial^2 v}{\partial x^2}+\frac{\partial^2 v}{\partial y^2}\right)-\frac{1}{\rho}\left(\frac{\partial P}{\partial y}+\frac{\partial p}{\partial y}\right), \tag{2}$$

where p is the pressure produced by the disturbances, and P is the pressure due to the basic flow.

The equation of continuity is

$$\frac{\partial u}{\partial x}+\frac{\partial v}{\partial y}=0. \tag{3}$$

By subtracting from eq 1 and 2, respectively, the corresponding Navier-Stokes equations for $u=v=p=0$, the following two equations are obtained in terms of only the disturbances:

$$\frac{\partial u}{\partial t}+U\frac{\partial u}{\partial x}+v\frac{\partial U}{\partial y}=\nu\left(\frac{\partial^2 u}{\partial x^2}+\frac{\partial^2 u}{\partial y^2}\right)-\frac{1}{\rho}\frac{\partial p}{\partial x} \tag{4}$$

$$\frac{\partial v}{\partial t}+U\frac{\partial v}{\partial x}=\nu\left(\frac{\partial^2 v}{\partial x^2}+\frac{\partial^2 v}{\partial y^2}\right)-\frac{1}{\rho}\frac{\partial p}{\partial y}. \tag{5}$$

Equations 4 and 5 are the fundamental hydrodynamic equations for small disturbances on which are based all stability theories herein discussed.

In order to derive an expression for energy balance, eq 4 is multiplied by u and eq 5 by v, and the resulting equations are added to give the single disturbance equation

$$\rho\left(\frac{\partial}{\partial t}+U\frac{\partial}{\partial x}\right)\left(\frac{u^2+v^2}{2}\right)=$$
$$\mu\left[u\left(\frac{\partial^2 u}{\partial x^2}+\frac{\partial^2 u}{\partial y^2}\right)+v\left(\frac{\partial^2 v}{\partial x^2}+\frac{\partial^2 v}{\partial y^2}\right)\right]-$$
$$\rho uv\frac{\partial U}{\partial y}-\left(u\frac{\partial p}{\partial x}+v\frac{\partial p}{\partial y}\right). \tag{6}$$

It will be noted that the left-hand member of this equation gives the time rate of change of kinetic energy, due to the disturbances, of a particle moving with the basic flow. Each term on the right-hand side of eq 6 is now integrated over the region containing the disturbance, as explained in

detail in reference [20]. The resulting expression is

$$\frac{dE}{dt} = -\rho \int\int uv \frac{dU}{dy} dxdy - \mu \int\int \left(\frac{\partial u}{\partial y} - \frac{\partial v}{\partial x}\right)^2 dxdy, \quad (7)$$

where dE/dt now represents the time rate of change of kinetic energy, due to the disturbance, of the fluid within the region of integration. The first term on the right-hand side of eq 7 involves the shearing stress ρuv and represents the rate at which energy is absorbed from the basic flow. This energy is added to that already present in the disturbance. The second term on the right-hand side, which is obviously always negative, is the rate of dissipation of the energy of the disturbance by viscosity. The predominance of one effect over the other will determine the net change in the energy of the disturbance.

The first term on the right-hand side of eq 7 has an interesting physical interpretation. First, if u and v differ in phase by 90 degrees, as in the usual wave motion, $\overline{uv}$ will vanish over one complete cycle, and no energy can be absorbed from the basic flow. Second, as dU/dy is positive, $\overline{uv}$ must be negative, if the disturbance is to receive energy from the basic flow. These and other conditions are treated in the more advanced theory to be considered next.

(b) Disturbance Equation and Solutions

Lord Rayleigh [21] appears to have been the first to outline a more general mathematical theory to which numerous investigators have contributed. The mathematical difficulties are so great that the basic velocity profile ($U=f(y)$) was usually approximated by a straight line or segments of straight lines. This imposed serious limitations on the generality of the results. Tietjens [22] was the first to apply Rayleigh's theory to profiles intended to reproduce flow along a wall, but his solution suffered from the serious limitations just mentioned. Important advances have been made by Tollmien [2, 3] and Schlichting [4 to 7], who successfully applied the theory to curved profiles intended to represent actual velocity distributions. Their most complete solutions apply to an approximation of the Blasius distribution. Schlichting's work [4, 5] is particularly complete and his results are used here for comparison with experimental results. The following outline of the theory is taken largely from references [4 and 5] with occasional help from reference [2]. The physical basis for the theory, the steps in the solution, and the more important results are given here. The mathematical aspects of the problem are discussed in the original references. Even in the original references details of the computations are lacking and checking of results is difficult.

From the basic eq 4 and 5, the pressure terms are eliminated by differentiating eq 4 and 5 with respect to y and x, respectively, and subtracting the second from the first. The result is a linear homogeneous equation in u and v:

$$\frac{\partial^2 u}{\partial y \partial t} + U\frac{\partial^2 u}{\partial x \partial y} + \frac{\partial U}{\partial y}\frac{\partial u}{\partial x} + v\frac{\partial^2 U}{\partial y^2} + \frac{\partial v}{\partial y}\frac{\partial U}{\partial y} - \frac{\partial^2 v}{\partial x \partial t} - \frac{U\partial^2 v}{\partial x^2} = \nu\left(\frac{\partial^3 u}{\partial x^2 \partial y} + \frac{\partial^3 u}{\partial y^3} - \frac{\partial^3 v}{\partial x^3} - \frac{\partial^3 v}{\partial y^2 \partial x}\right) \quad (8)$$

The disturbance velocities may be expressed in terms of a stream function ψ such that

$$u = \frac{\partial \psi}{\partial y}, \qquad v = -\frac{\partial \psi}{\partial x} \quad (9)$$

Any periodic disturbance may be represented by a Fourier series. As eq 8 is linear and homogeneous in u and v, its behavior may be investigated by using a single term of the series. This amounts to assuming a periodic disturbance whose stream function has the form

$$\psi = F(y)\ exp\ [i(\alpha x - \beta t)] = F(y)\ exp\ [i\alpha(x - ct)], \quad (10)$$

where $F(y)$ represents the initial amplitude of the stream function which depends only on y, $\alpha = 2\pi/\lambda$, where λ is the wavelength, and t is the time. Since β and hence c are generally complex quantities, eq 10 may be written

$$\psi = F(y)\ exp\ [i(\alpha x - (\beta_r + i\beta_i)t)] = F(y)\ exp\ [i\alpha(x - (c_r + ic_i)t)], \quad (11)$$

where β_r, the real part of β, is the angular velocity or $2\pi f$ (f=frequency); β_i, the imaginary part of β, is the coefficient of amplification or damping, depending on whether it is positive or negative; and $c_r = \beta_r/\alpha$ is the velocity with which the phase progresses and will be termed simply "wave velocity."

When eq 8 is written in terms of the stream function and substitution is made for ψ in accord-

ance with the second of eq 10, the result is

$$(U-c)(F''-\alpha^2F)-U''F=\frac{\nu}{i\alpha}(F''''-2\alpha^2F''+\alpha^4F), \tag{12}$$

where the primes represent differentiation with respect to y. Equation 12 is a homogeneous linear differential equation of the fourth order with a general solution of the form

$$F=C_1F_1+C_2F_2+C_3F_3+C_4F_4, \tag{13}$$

where F_1, F_2, F_3, and F_4 are the particular solutions and C_1, C_2, C_3, and C_4 are the constants of integration. The form of these particular solutions depends on the basic velocity assumed, that is, on the boundary-layer profile.

A solution of eq 12 was first obtained by Tollmien [2] for a velocity distribution intended to approximate closely a Blasius distribution. He considered the case in which amplification and damping were absent, that is, for real values of β and c, and obtained the so-called "neutral" oscillations. Schlichting [4] repeated Tollmien's calculation and in addition treated the case for small amplification. In a later paper [5] Schlichting determined the distribution of amplitude of neutral oscillations across the boundary layer and investigated the energy balance. Schlichting's work is therefore more complete and more suitable for comparison with experiment.

Both Tollmien and Schlichting approximated a Blasius distribution by a straight line and a parabola as follows:

For $0\leq\frac{y}{\delta}\leq 0.175$,

$$\frac{U}{U_0}=1.68\frac{y}{\delta}.$$

For $0.175\leq\frac{y}{\delta}\leq 1.015$,

$$\frac{U}{U_0}=1-\left(1.015-\frac{y}{\delta}\right)^2.$$

For $\frac{y}{\delta}>1.015$,

$$\frac{U}{U_0}=1.$$

This gave a sufficiently close approximation to the Blasius distribution of U but was not a sufficiently good approximation for U' and U''. The latter quantities were therefore taken directly from the Blasius solution; only the following terms of the series, which obviously apply to small values of y/δ, were used

$$\frac{U'}{U_0}=1.68\left[1-3.65\left(\frac{y}{\delta}\right)^3\right]$$

and

$$\frac{U''}{U_0}=-18.4\left(\frac{y}{\delta}\right)^2$$

The displacement thickness

$$\delta^*=\int_0^\delta\left(1-\frac{U}{U_0}\right)dy=0.347\delta.$$

Schlichting gives 0.341δ for the integral, and this value was used to compute the values of δ in figure 21.

It was assumed that $U=f(y)$ and that $V=0$. This is equivalent to assuming a nonthickening boundary layer, that is, constant δ, and is the basis for most of the adverse criticism of the theory. In a real boundary layer, δ depends on x, $U=f(x,y)$, and $V\neq 0$, but the dependence of U on x is small compared with the dependence on y, and V is small compared with U.

As the purpose in the present paper is merely to indicate the method of solving the equation, the solutions will be indicated in general form. The calculations have been carried through to numerical results for only a few velocity profiles.

Equation 12 is not readily solved in its entirety, and certain approximations must be made that involve the friction terms on the right-hand side of the equation. The simplest approximation is to neglect the friction terms entirely. In order to justify this, eq 12 is put in a dimensionless form that has the Reynolds number as one of the parameters. When the new independent variable y/δ^* is introduced and $F=U_0\delta^*\phi$, the result is

$$\frac{U-c}{U_0}(\phi''-\alpha^2\delta^{*2}\phi)-\frac{U''\phi}{U_0}=\frac{1}{i\alpha\delta^*R}(\phi''''-2\alpha^2\delta^{*2}\phi''+\alpha^4\delta^{*4}\phi), \tag{14}$$

where the primes now denote differentiation with respect to y/δ^* and R is the Reynolds number. When R is sufficiently large, the right-hand side of equation 14 may be small enough to neglect. The effect of the friction terms is actually neg-

ligible for all values of y/δ^* except those near the surface and near a plane,[3] which is also near the surface, where the wave velocity is equal to the local stream velocity. It has been shown by Tollmien [2] that c must always be less than U_o; a point will therefore always be found in the boundary layer where $U=c$. Exclusive of this point and the surface, two particular solutions, ϕ_1 and ϕ_2, may be obtained by solving the frictionless equation

$$\frac{U-c}{U_0'}(\phi''-\alpha^2\delta^{*2}\phi)-\frac{U''\phi}{U_0'}=0. \tag{15}$$

The solutions are expressed as power series developed about y_c, where y_c is the position of the critical point, $U=c$. These solutions are

$$\phi_1=\frac{(y-y_c)}{\delta^*}\left[1+a_2\frac{(y-y_c)}{\delta^*}+a_3\frac{(y-y_c)^2}{\delta^{*2}}+\ \ldots\right] \tag{16}$$

$$\phi_2=\frac{U_c''}{U_c'}\phi_1\log\frac{(y-y_c)}{\delta^*}+1+b_1\frac{(y-y_c)}{\delta^*}+b_2\frac{(y-y_c)^2}{\delta^{*2}}+\ \ldots\ , \tag{17}$$

where U_c'' and U_c' are the values of U'' and U' at the critical point. While ϕ_1 is regular throughout the whole layer, ϕ_2 possesses a singularity at the critical point and a correction to eq 17 must be found by another approximate solution that takes into account the friction at the critical point. This second approximation to eq 14, valid in the neighborhood of the critical point, results from neglecting all but the largest of the friction terms.

For this purpose a new independent variable η is introduced, defined by

$$\frac{y-y_c}{\delta^*}=\left(\alpha\delta^*R\frac{U_c''}{U_o}\right)^{-1/3}\eta=\epsilon\eta. \tag{18}$$

From this it is seen that η is a dimensionless variable that is equal to zero at the critical point $y=y_c$, positive for $y>y_c$, and negative for $y<y_c$. Equation 14 is now written with η as the independent variable for ϕ. As this equation will be used in the vicinity of $y=y_c$, $(U-c)/U_o$ can be approximated by $(U_c'/U_o)\epsilon\eta$ and U'' by U_c'', where the primes again denote differentiation with respect to y/δ^*. The equation becomes

$$i\phi''''+\phi''(\eta-2i\epsilon^2\alpha^2\delta^{*2})-\phi\left(\epsilon\frac{U_c'''}{U_c''}+\eta\epsilon^2\alpha^2\delta^{*2}-i\epsilon^4\alpha^4\delta^{*4}\right)=0, \tag{19}$$

where ϕ is differentiated with respect to η. As ϵ is small, the terms containing ϵ^2 and ϵ^4 are omitted, and eq 19 becomes

$$i\phi''''+\eta\phi''=\epsilon\frac{U_c'''}{U_c''}\phi. \tag{19a}$$

Equation 19a contains no singularity at $U=c$, and a solution of this equation at the critical point indicates the form of ϕ_2 to be used when $y-y_c<0$. This form is

$$\phi_2=\frac{U_c''}{U_c'}\phi_1\left(\log\left|\frac{y-y_c}{\delta^*}\right|+i\pi\right)+1-b_1\frac{(y-y_c)}{\delta^*}+b_2\frac{(y-y_c)^2}{\delta^{*2}}+\ \ldots \tag{17a}$$

By neglecting the term in eq 19a containing ϵ, the homogeneous equation

$$i\phi''''+\eta\phi''=0 \tag{20}$$

is obtained. The solution of eq 20 contains the two particular solutions ϕ_3 and ϕ_4 that are expressed in terms of Hankel functions as follows:

$$\phi_{3,4}=\int_\infty^\eta d\eta\int_\infty^\eta\eta^{1/2}H_{1/3}^{(1),(2)}\left[\frac{2}{3}(i\eta)^{3/2}\right]d\eta, \tag{21}$$

where $H^{(1),(2)}$ are Hankel functions of the first and second kinds. Equation 20 is valid all the way to the surface. It is found that ϕ_3 diminishes very rapidly from the surface outward and is therefore important only near the surface. On the other hand, ϕ_4 increases rapidly with y, and will not satisfy the requirement that $\phi=0$ at $y=\infty$; hence, C_4 in eq 13 is set equal to zero. The general solution of eq 14 may then be written

$$\phi=C_1\phi_1+C_2\phi_2+C_3\phi_3. \tag{22}$$

(c) Characteristic-Value Problem

The stability investigation is a characteristic-value problem—that is, one in which the boundary conditions afford sufficient equations between the solutions at the boundaries to determine the values of the parameters for which eq 14 is satisfied, those values being the characteristic values. At

[3] As the theory applies only to a boundary layer of constant thickness, the problem is essentially one-dimensional, and this plane is commonly referred to as the critical "point."

$y=\delta$ where $U=U_0=$constant, the solutions of eq 14 are of the simple form

$$exp\left(-\alpha\delta^*\frac{y}{\delta^*}\right)$$

$$exp\left(+\alpha\delta^*\frac{y}{\delta^*}\right)$$

The solution with the positive exponent must be ignored as it is infinite at $y=\infty$. As the outer boundary condition, then, $\phi'/\phi=-\alpha\delta^*$. Since ϕ_3 has already disappeared at the outer boundary, the result is

$$C_1(\phi'_{1\delta}+\alpha\delta^*\phi_{1\delta})+C_2(\phi'_{2\delta}+\alpha\delta^*\phi_{2\delta})=0$$

or

$$C_1\Phi_{1\delta}+C_2\Phi_{2\delta}=0 \tag{23}$$

where the subscript δ indicates the solution at the outer boundary and

$$\Phi_{1\delta}=\phi'_{1\delta}+\alpha\delta^*\phi_{1\delta}$$

$$\Phi_{2\delta}=\phi'_{2\delta}+\alpha\delta^*\phi_{2\delta}$$

At the surface, $y=0$ and $\phi=\phi'=0$. The surface boundary conditions are then simply

$$C_1\phi_{1_0}+C_2\phi_{2_0}+C_3\phi_{3_0}=0 \tag{24}$$

$$C_1\phi'_{1_0}+C_2\phi'_{2_0}+C_3\phi'_{3_0}=0, \tag{25}$$

where the subscript 0 denotes solution on the surface.

If ϕ in eq 22 does not vanish identically, the following determinant of the boundary solutions, formed from eq 23, 24, and 25, must equal zero:

$$\begin{vmatrix} \Phi_{1\delta} & \Phi_{2\delta} & 0 \\ \phi_{1_0} & \phi_{2_0} & \phi_{3_0} \\ \phi'_{1_0} & \phi'_{2_0} & \phi'_{3_0} \end{vmatrix}=0$$

Solving the determinant gives

$$\frac{\phi_{3_0}}{\phi'_{3_0}}=\frac{\phi_{2_0}\Phi_{1\delta}-\phi_{1_0}\Phi_{2\delta}}{\phi_{2_0}\Phi_{1\delta}-\phi_{1_0}\Phi_{2\delta}} \tag{26}$$

The left-hand side of eq 26 is a function of η_0, where η_0 is the value of η at the surface. Since, by eq 18, η is a function of the parameters $\alpha\delta^*$ and R, the left-hand side of eq 26 is also a function of these parameters. The right-hand side of eq 26 is a function of the parameters $\alpha\delta^*$ and c/U_0. Denoting the left-hand side by G and the right-hand side by E gives

$$G(\eta_0)=E\,(\alpha\delta^*,\ c/U_0). \tag{27}$$

Equation 27 is complex and may be separated into two real equations by separating real and imaginary parts. Between these two equations any one of the three unknown parameters, $\alpha\delta^*$, R, and c/U_0, may be eliminated and a relation between the other two found. This has been done by both Tollmien and Schlichting for c real, that is, for oscillations neither amplified nor damped. For this case, eq 27 may be written

$$G_n(\eta_{0n})=E_n(\alpha_n\delta^*,\ c_r/U_0) \tag{28}$$

where the subscript n denotes neutral oscillations. If c_r is eliminated, a relation between $\alpha\delta^*$ and R is found. This gives the theoretical neutral curve shown in figures 20, 25, and 27. By eliminating $\alpha\delta^*$, the relation between c_r/U_0 and R, shown in figures 26 and 33, is found. Recombination of these quantities results in $\beta_r\nu/U_0^2$, plotted in figures 13, 16, 17, 19, and 24.

The curves just mentioned extend only to the maximum values of R that are of practical interest. Tollmien [2] points out that both branches I and II of these curves approach the R-axis as R approaches infinity. Branches I and II, therefore, meet at infinity and form a closed curve. Amplification occurs within the region enclosed by the curve. Damping occurs in all other regions.

The values of the parameters are given in table 3. The computations were made by a combination of analytical and numerical methods. It may be pointed out that the values obtained by Tollmien and Schlichting show some differences. These are probably because of differences in the details of the computations. Values plotted in the foregoing figures and appearing in table 3 are Schlichting's results.

TABLE 3.—*Theoretical wave parameters for neutral oscillations, according to Schlichting* [4]

$\frac{c_r}{U_0}$	Branch I			Branch II		
	R	$\alpha\delta^*$	$\frac{\beta_{ir}\nu}{U_0^2}\times 10^5$	R	$\alpha\delta^*$	$\frac{\beta_{ir}\nu}{U_0^2}\times 10^5$
0.200	7200	0.077	2.14	37,600	0.149	0.79
.250	3010	.101	8.39	12,000	.188	3.92
.300	1530	.129	25.3	4,640	.223	14.4
.325	1150	.143	40.4	3,290	.238	23.5
.350	893	.159	62.3	2,070	.251	42.4
.375	736	.181	92.2	1,420	.264	69.7
.400	633	.205	129.5	1,020	.274	107.4
.420	606	.239	165.7	713	.273	161.0

Schlichting extended the calculations to include small amplification, applying only in the neighborhood of the neutral curve. The calculations were carried out, not by a direct solution of eq 27, but by a series development starting from the neutral eq 28. Thus $G(\eta_0)$ is found by

$$G(\eta_0)=G(\eta_{0n})+(\eta_0-\eta_{0n})G'(\eta_{0n})+\ \ldots \quad (29)$$

and $E(\alpha\delta^*, c/U_0)$ is found by

$$E(\alpha\delta^*, c/U_0)=E_n(\alpha_n\delta^*, c_r/U_0)+$$
$$(\alpha-\alpha_n)\left(\frac{\partial E_n}{\partial\alpha}\right)+(c-c_r)\left(\frac{\partial E_n}{\partial c}\right)+\ \ldots \quad (30)$$

With the values of G and E given by eq 29 and 30, amplifications were determined near and within the space enclosed by the neutral curve $\beta_i=0$. Values beyond the range permitted by this method were determined by interpolation, by assuming a cubic equation for β_i at constant R that meets both branches of the neutral curve with the known slope $\partial\beta_i/\partial\alpha$ at these points. Schlichting's diagram showing the theoretical amplification is given in figures 27 and 28. It will be noted that β_i has a maximum near the center of the zone and falls off toward both branches of the neutral curve. In accordance with eq 11, amplification of a disturbance is expressed by

$$\frac{A_2}{A_1}=exp\int_{t_1}^{t_2}\beta_i dt, \quad (31)$$

where A_1 is the amplitude at t_1, and A_2 is the amplitude at t_2. With t_1 taken on branch I of the neutral curve and t_2 on branch II, the total amplification at constant $\beta_{ir}\nu/U_0^2$ was calculated by Schlichting for several parts of the amplification zone. Schlichting's values are shown in figures 13, 19, and 20. The maximum total amplification up to a given value of x, when disturbances of all frequencies are present, is determined by the equation

$$\frac{A(x)}{A_1}=exp\left(max\int_{t_1}^{t(x)}\beta_i dt\right). \quad (32)$$

Schlichting found that the relation between this maximum total amplification and the x-Reynolds number up to an R_x of about 10^6 could be represented by the interpolation formula

$$\frac{A(R_x)}{A_1}=0.55\ exp\ (0.555\times 10^{-5}R_x). \quad (33)$$

The solution thus far has determined several characteristics of the wave. For any given value of R and the frequency, it is known whether the wave will be amplified, damped, or neutral. For a given frequency the wave velocity is related to U_0 in a known way and is constant over the cross section of the layer. In like manner the wave length is known in relation to δ^*.

(d) Amplitude, Correlation, and Energy Balance

The characteristic-value problem gives no information about the relative magnitudes of u and v nor how they are distributed through the boundary layer. How the boundary layer "vibrates," whether as a whole or in parts, remains unknown. This is because the boundary conditions were used to determine only the parameters of the problem and not the constants of integration.

In a second treatment of the theory applied to the flat plate [5], Schlichting completed the investigation by determining the constants in equation 22 for neutral oscillations, that is, for $\beta_i=0$. He was thus able to calculate relative values of u and v and their distribution across the boundary layer. The physically important questions of the correlation between u and v and the energy balance were also answered. The same approximation to the Blasius distribution as used earlier was used here.

As absolute values of u and v, which obviously depend on the intensity of the impressed disturbance, are of no interest in such a treatment, one of the constants was left undetermined and for convenience was made unity. Thus,

$$C_1=1,$$

and, from the boundary conditions expressed by eq 23 to 25, the following values for C_2 and C_3 are obtained:

$$\left.\begin{aligned} C_2&=-\frac{\Phi_{1\delta}}{\Phi_{2\delta}}\\ C_3&=\frac{1}{\phi_{3_0}}\left(\frac{\Phi_{1\delta}}{\Phi_{2\delta}}\phi_{2_0}-\phi_{1_0}\right)=\frac{1}{\phi'_{3_0}}\left(\frac{\Phi_{1\delta}}{\Phi_{2\delta}}\phi'_{2_0}-\phi'_{1_0}\right)\end{aligned}\right\} \quad (34)$$

When the values of the boundary solutions and their derivatives are known, C_2 and C_3 may be determined by eq 34. The general solution ϕ, is thereby determined except for an arbitrary intensity factor. From the nature of the particular solution, ϕ has real and imaginary parts, ϕ_r and ϕ_i, which must be known with their derivatives in order to determine u and v.

The stream function ψ in eq 9 and the first of eq 10 are used to obtain the real parts of u/U_0 and v/U_0, since $F=U_0\delta^*\phi$, as follows:

$$\left.\begin{aligned} \frac{u}{U_0}&=K[\phi'_r\cos(\alpha x-\beta_r t)-\phi'_i\sin(\alpha x-\beta_r t)]\\ \frac{v}{U_0}&=K\alpha[\phi_r\sin(\alpha x-\beta_r t)+\phi_i\cos(\alpha x-\beta_r t)]\end{aligned}\right\} \quad (35)$$

where K is an arbitrary intensity factor. The corresponding root-mean-square values of u and v are

$$\frac{u'}{U_0}=\frac{K}{\sqrt{2}}\sqrt{\phi'^2_r+\phi'^2_i} \quad (36)$$

$$\frac{v'}{U_0}=\frac{K\alpha}{\sqrt{2}}\sqrt{\phi_r^2+\phi_i^2} \quad (37)$$

An expression for the kinetic energy is readily obtained by squaring eq 36 and 37 and adding. The correlation coefficient defined by

$$K=\frac{\overline{uv}}{u'v'}$$

becomes

$$K=\frac{\phi'_r\phi_i-\phi_r\phi'_i}{\sqrt{(\phi'^2_r+\phi'^2_i)(\phi_r^2+\phi_i^2)}}. \quad (38)$$

Values of u'/U_0, v'/U_0, and K were calculated by Schlichting for neutral oscillations corresponding to the following two points, one of each branch of the neutral curve:

Branch	R	$\frac{\beta_r\nu}{U_0^2}$	$\alpha\delta^*$	$\frac{C_r}{U_0}$
I	894	62.3×10^6	0.159	0.35
II	2070	42.4	.251	.35

The value of K was chosen to give an average value of $u'/U_0=0.05$ from 0 to δ. Table 4 gives the values of u'/U_0, v'/U_0, and K calculated by Schlichting.

TABLE 4.—*Theoretical neutral oscillations taken from Schlichting* [5]

For average $u'/U_0=0.05$ from $y/\delta=0$ to $y/\delta=1$

$\frac{y}{\delta}$	$10\frac{u'}{U_0}$	$100\frac{v'}{U_0}$	K
Branch I; R, 894; $\alpha\delta^*$, [1] 0.159			
0.050	0.445	0.0546	−0.032
.090	.647	.158	−.061
.130	.804	.287	−.155
.170	.922	.434	−.169
.209	1.005	.608	−.140
.250	1.016	.795	−.109
.290	1.003	.973	−.064
.370	0.854	1.322	−.022
.451	.689	1.605	−.0075
.531	.524	1.820	0
.612	.371	1.984	0
.693	.244	2.098	0
.774	.121	2.170	0
.854	.007	2.193	0
.935	.103	2.180	0
1.015	.211	2.108	0
1.1	.203	2.027	0
1.2	.193	1.935	0
1.3	.185	1.849	0
1.4	.176	1.763	0
1.5	.168	1.681	0
Branch II; R, 2070; $\alpha\delta^*$, 0.251			
0.029	0.661	0.0655	------
.054	.937	.214	−0.121
.074	1.038	.359	−.170
.105	1.108	.595	−.191
.157	1.127	1.028	−.146
.209	1.086	1.445	−.076
.250	0.998	1.756	−.010
.290	.906	2.04	+.015
.370	.686	2.50	+.019
.451	.504	2.87	0
.531	.340	3.10	0
.612	.205	3.26	0
.693	.087	3.35	0
.774	.022	3.37	0
.854	.123	3.33	0
.935	.216	3.22	0
1.015	.305	3.11	0
1.1	.292	2.925	0
1.2	.272	2.72	0
1.3	.252	2.53	0
1.4	.234	2.35	0
1.5	.218	2.18	0

[1] $\delta^*=0.3418$.

It will be seen in table 4 that $u'/U_0=0$ at the surface and again at a point near $y/\delta=0.854$ for branch I and near $y/\delta=0.774$ for branch II, after which it again increases for greater y/δ. The values of u'/U_0 are plotted in figure 21, where the theory is compared with experiment. At the points within the boundary layer where u'/U_0 vanishes, a 180° phase shift occurs in u, meaning that the instantaneous u-component of the oscillation velocity is decreasing on one side of this point while it is increasing on the other. No such phase shift occurs in v. Table 4 also shows that correlation does exist between u and v and that $\overline{uv}$ is negative. This means that energy is drawn from the basic flow; and, in accordance with eq 7, this energy must be balanced by the dissipation if the oscillation is to be neither amplified nor damped. Schlichting evaluated both terms in eq 7 by integrating from $x=0$ to $x=\lambda$ and from $y=0$ to $y=\infty$. The net flow of energy was found to be very nearly zero, which indicated that the oscillations were nearly neutral. This result was interpreted as proof of the correctness of the solution to the characteristic-value problem.

A physical explanation of the correlation between u and v is attempted by Prandtl [20]. It appears that u and v would differ in phase by 90° and $\overline{uv}$ would vanish in consequence if there were no phase shift in v produced by the viscosity near the critical point. The viscosity is thus responsible for the flow of energy to as well as from the disturbance.

(e) Solutions for Other Conditions

Tollmien [3] has attempted to generalize the solution sufficiently to include boundary-layer profiles with an inflection point, such as occur with an adverse pressure gradient. For such profiles the sign of U'' changes from positive to negative in passing outward from the surface and, at the inflection point, $U''=0$. The velocity of the neutral wave is shown to be equal to the stream velocity at the inflection point, and an important consequence of this is the absence of a critical point at $U=c$, in the solution of the frictionless eq 15. The conclusion is that profiles with an inflection point are inherently unstable, although neutral oscillations can still exist. These considerations suggest that an adverse pressure gradient is favorable to amplification.

Görtler [23] has investigated the effect of wall curvature on the stability of the boundary layer and finds that velocity profiles are unstable if a change of sign occurs in $U''+U'/r$, where r is the radius of curvature of the wall. If an inflection point ($U''=0$) exists, the point where $U''+U'/r=0$ is farther from the surface than the point where $U''=0$ for a convex wall and nearer to the surface for a concave wall. If no inflection point exists, a point where $U''+U'/r=0$ can occur only on a convex wall. It is concluded that convex curvature has a destabilizing effect and that concave curvature has a stabilizing effect.

Solutions for profiles with inflection points are given in references 8 to 10. Rosenbrook [8] investigated the flow through a diverging channel as the channel was towed through still water. Streamlines were made visible by fine particles of aluminum in the water, and wavelike motions accompanied by the formation of eddies could be observed as well as the velocity distribution. A solution, following Tollmien [3], was obtained for S-shape velocity profiles approximating those observed. Fair agreement was obtained between the observed and the computed wavelengths. Hollingdale [9] obtained the solution appropriate to the laminar wake formed in one case behind a flat plate and in another behind an airfoil, both towed at low speeds through still water. Oscillating wakes were observed at certain Reynolds numbers and the wavelength and the wave velocity were measured. With the appropriate interpretation of theoretical results, fair agreement between calculated and observed wave length and wave velocity was obtained. Savic [10] obtained an exact solution of the frictionless eq 15 for the two-dimensional jet and obtained expressions for the neutral wave length and wave velocity in terms of characteristics of the jet. The theoretical results were compared with observations of wave length and wave velocity made on an acoustically sensitive jet and good agreement was obtained.

Schlichting [6] has determined the effect of centrifugal force by calculating the curves of neutral stability for a boundary layer developed on the inner wall of a rotating cylinder. Schlichting [7] has determined the effect of density gradient on the stability of the boundary layer, using the approximation to the Blasius distribution given in part b of this section. Neutral curves outlining the zone of amplification are

given. Stability is principally affected by a gravitational field in connection with the density gradient through the boundary layer.

The methods of Tollmien and Schlichting have been applied by Pretsch [24] to the boundary layer on bodies of revolution. The approximate forms of the general disturbance equations from which the four particular solutions are obtained are found to be the same as those for the two-dimensional case, the solutions are therefore the same. The solutions are applied to the known velocity profile at the stagnation point of a sphere and the curve of neutral stability is computed.

3. Naturally Excited Oscillations

Naturally excited oscillations are those originating from the amplification of small disturbances naturally present in the stream. These oscillations were treated in Section V, and their frequencies were experimentally obtained and plotted in figure 13. The concept of waves running downstream through the boundary layer has been introduced; the behavior of the oscillations in relation to figure 13 can now be discussed.

One important feature of figure 13 is that the values of amplification coefficient are positive within the zone enclosed by the neutral curve and have values reaching a maximum near the center and falling to zero on each boundary. Outside the zone β_i is negative. All disturbances, whether damped or amplified, travel downstream and therefore in the direction of increasing R, since δ^* increases with x. For example, a fixed speed U_0 and a disturbance of frequency such that $\beta_r\nu/U_0^2$ in figure 13 equals 40×10^{-6} are considered. Such a disturbance, if it began at the leading edge of the plate, would be damped as it passed along the boundary layer until it reached a point where R attained the value 1,180. From this point to R=2,160 the disturbance would be amplified and, as it passed beyond this point, would again be damped. If A_1 and A_2 are the amplitudes of the disturbance at the beginning and at the end of the amplification zone, the ratio A_2/A_1=742. In other words, the amplitude has increased 742 times while crossing the zone. This is the total amplification given by eq. 31. A disturbance of any given frequency will then be most highly amplified when it reaches branch II of the neutral curve.

Figure 8 shows that, in experiment, many fr
quencies are represented in the initial disturbanc
The fact that the observed boundary-layer osci
lations contain one predominant frequency mu
be explained. In order to determine whethe
theory and experiment are in agreement, the plac
on the theoretical diagram where the predominan
frequency should lie must be found. Instead o
traversing the diagram of figure 13 with a wav
of a single frequency as in the foregoing illustra
tion, waves of many frequencies, covering a wid
range of values of $\beta_r\nu/U_0^2$, are supposed to ente
the amplification zone through branch I and un
dergo amplification at a rate determined by thei
frequency as they proceed to the value of R a
which the observation is made. Initial disturb
ances are, of course, present in the boundary laye
at all values of R and disturbances enter th
diagram at all points. Those entering this dia
gram ahead of branch I are reduced by damping
below the prevailing level of the initial disturb
ances while those entering behind branch I cannot
receive full amplification. Disturbances occurring
at points corresponding to branch I have the
largest initial value and also receive the highes
amplification and are therefore assumed to be th
ones whose development should mainly determine
the final result at the point of observation. It
will be noted that amplification increases without
limit as the frequency decreases if no limit is
placed on the Reynolds number. The experi
mental observation, however, is made at a par
ticular value of R and hence of R_x; under this con
dition it is obvious that one particular value o
$\beta_r\nu/U_0^2$ will become more highly amplified than
any of the others, this one having the maximum
total amplification given by eq 33 in terms of R
and the initial amplitude A_1. This frequency
obviously is the predominant one that should be
found on the oscillograph records. The remaining
question now concerns the position of this most
prominent frequency on the diagram, that is
where the experimental points should lie. The
problem then becomes one of determining along
what line starting from branch I and running
parallel to the R-axis the total amplification is a
maximum up to a given value of R. By taking
into account the values of β_i given by Schlichting
it was found that for uniform energy distribution
with frequency, this line introduced into the dia-

ram along branch I intersects the prescribed value of R somewhere between the center of the zone and branch II. For more accurate results, both the initial energy distribution and the damping prior to reaching boundary I must be considered. The experimental points should lie inside the zone near branch II. The agreement with theory is not perfect, since many points lie on branch II and outside the zone, but is as good as can be expected from observations of this sort.

The process described here is believed to be one of considerable importance since it is the process by which laminar-boundary-layer oscillations develop from initially random disturbances. In order to develop a pure oscillation, initial disturbances must be so small that a large amount of amplification can occur before transition destroys the laminar layer.

It has been pointed out that the oscillations appear to be three-dimensional. This is to be expected because of the three-dimensional nature of the initial disturbances. The theory, however, concerns two-dimensional oscillations, and how this should affect the agreement with experiment is not known.

An apparent discrepancy between figures 7 and 13 must be pointed out. It will be observed in figure 13 that oscillations are indicated for R as high as 3,120. This corresponds to an R_x of 3.28×10^6 and, according to figure 7, is in the transition region. The oscillograph records actually showed intermittent turbulence, but it was still possible to read oscillation frequencies from nonturbulent parts of the records. The limits of the transition region are defined statistically by the surface-tube method. The discrepancy is therefore only apparent.

In connection with the surface-tube method, another effect was noted, namely, that a rise in the surface-tube reading was noted a little ahead of the point where turbulence was indicated by the hot wire. This is believed to be caused by a slightly modified velocity distribution arising from the shearing stress given by $\overline{uv}$ in the oscillations. The lower boundary of the transition region in figure 7 is therefore a little too low, but the displacement is small and has no significant effect on the shape of the curve.

VI. Artificial Excitation of Boundary-Layer Oscillations, Zero Pressure Gradient

It was soon realized that a study of boundary-layer oscillations could be carried out to better advantage if they were not caused by accidental disturbances occurring in the wind tunnel but were produced by a controlled disturbance of known amplitude and frequency at some chosen position. This was finally accomplished by the vibrating ribbon discussed in section VI, 3. While a search was being made for devices of various kinds that would accomplish the desired result, effects of sound were tried. Interference from naturally excited oscillations was minimized by making the artificial disturbances much greater than the natural disturbances. The bolting-cloth damping screen was also installed with the six wire screens, but the addition of this screen had no detectable effect on the natural oscillations.

1. Sound From Loudspeaker

The effect of sound intensity on the boundary layer is of interest because sound is an unavoidable source of disturbance both in wind tunnels and in free flight of power-driven aircraft. A 25-watt loudspeaker was accordingly installed in the top of the tunnel at the leading edge of the plate and fed by a variable-frequency oscillator through an amplifier. The intensity and the frequency were controllable.

Interesting effects were easily demonstrated. For example, boundary-layer oscillations could be induced at will merely by choosing the right frequency for a particular position and speed. Transition could be moved 1 or 2 feet ahead of its natural position by the right combination of intensity and frequency. In general, a random noise from the loudspeaker produced similar results, but the effect on the oscillations was not so marked. These were casual observations with no attempt at quantitative measurements.

When quantitative work was attempted, it became apparent that the complicated sound field in the tunnel was a decided draw-back. Figures 14 and 15 show the distribution of sound intensity along the center of the working chamber 3 inches from the plate. Figure 14 shows a standing wave

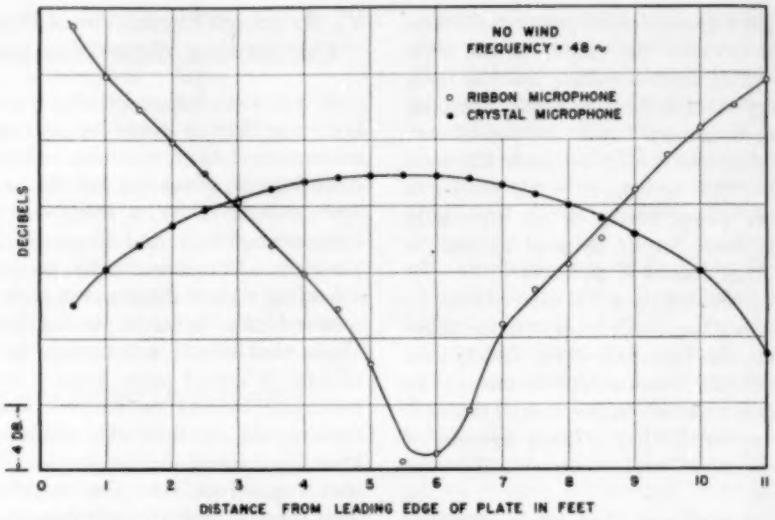
NO WIND
FREQUENCY • 48 ~
○ RIBBON MICROPHONE
• CRYSTAL MICROPHONE
DECIBELS
4 DB
0 1 2 3 4 5 6 7 8 9 10 11
DISTANCE FROM LEADING EDGE OF PLATE IN FEET

FIGURE 14.—*Relative sound intensity from loudspeaker in ceiling of working chamber at leading edge of plate, measured along center 3 in. from plate.*

U_0=0. Frequency=48 cps.

at 48 cycles per second with either a node or a loop at the center of the plate depending on the type of microphone—that is, whether crystal microphone, responding to sound pressure, or ribbon microphone, responding to particle velocity. This turned out to be the fundamental frequency of the 12-foot tube formed by the plate and the tunnel walls. The same standing wave could be set up without the loudspeaker when the exciting frequency came from the eight-blade wind-tunnel propeller running at a speed of 360 rpm. Figure 15 shows the distribution at 60 cycles per second. The ribbon microphone and the hot-wire anemometer show nearly the same distribution, as would be expected. These are only a few examples of the sound field and the change in distribution with frequency that serve to complicate any studies with controlled sound intensity.

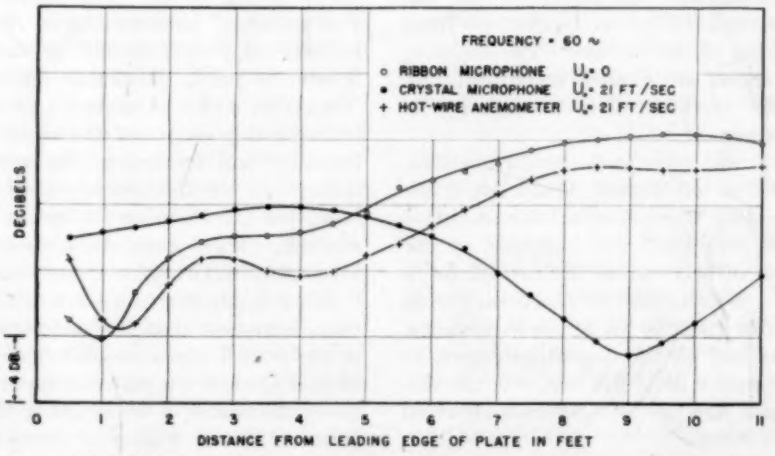
FREQUENCY • 60 ~
○ RIBBON MICROPHONE U_0 = 0
• CRYSTAL MICROPHONE U_0 = 21 FT/SEC
+ HOT-WIRE ANEMOMETER U_0 = 21 FT/SEC
DECIBELS
4 DB
0 1 2 3 4 5 6 7 8 9 10 11
DISTANCE FROM LEADING EDGE OF PLATE IN FEET

FIGURE 15.—*Relative sound intensity from loudspeaker in ceiling of working chamber at leading edge of plate, measured along center 3 in. from plate.*

Frequency=60 cps.

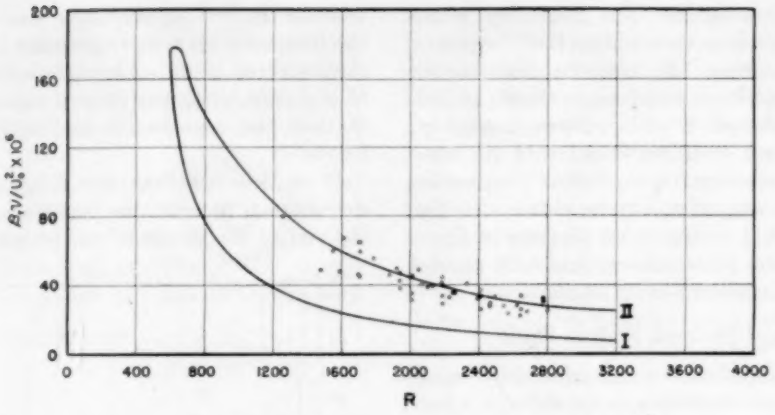

FIGURE 16.—*Boundary layer oscillations excited by loudspeaker.*

Points show sound frequency giving maximum amplification. Curve outlines theoretical amplification zone. (See fig. 13.)

When the loudspeaker was used to excite oscillations, two procedures were tried: (1) The sound frequencies that produced oscillations of maximum amplitude at chosen velocities and positions were determined and (2) a sound frequency and position were chosen and the velocity was then varied until the oscillations were a maximum. By use of the sound frequencies read on the oscillator together with the measured U_0 and x, $\beta_1\nu/U_0^2$ and R were calculated and plotted in figure 16. The solid line is again Schlichting's curve of neutral stability enclosing the zone of amplification. Since both procedures amounted to finding the condition for maximum total amplification, the points should lie within the zone near branch II to be in agreement with theory. In view of the difficulties encountered, the large scattering of the points is not surprising.

Another application of the loudspeaker consisted in directly connecting the amplified output of the hot wire to the loudspeaker so that regeneration could occur. Disturbances picked up by the hot wire were thereby fed back as sound, which in turn reinforced the initial disturbance when the proper phase relation existed, causing the system to oscillate. The resulting frequency was read from a variable-frequency oscillator connected to the oscillograph to form Lissajou figures

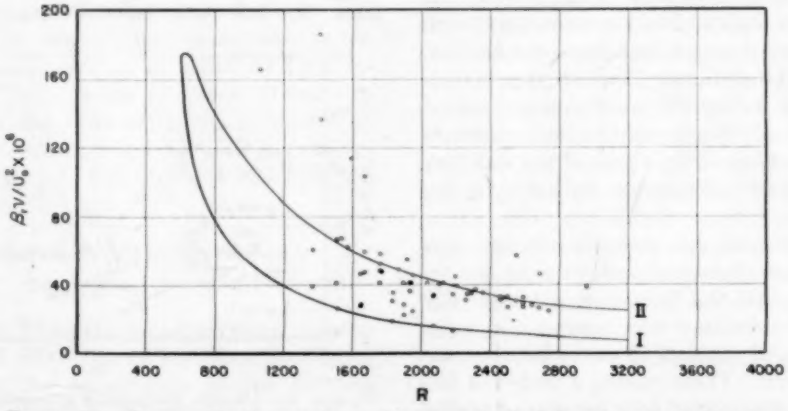

FIGURE 17.—*Regeneration frequencies resulting from feedback from hot wire in boundary layer to loudspeaker.*

Curve outlines theoretical amplification zone. (See fig. 13.)

with the hot-wire signal. The frequency of regeneration was determined by the frequency response of the wire, the electrical circuit, the loudspeaker, and the tunnel as a whole, as well as by the preferred boundary-layer frequency. Many frequencies could be found with no wind and only by rejecting these "false" frequencies could results of any reliability be obtained. The results are plotted on the usual diagram in figure 17. Many of the points shown evidently are not related to the boundary-layer oscillations.

2. Sound Through Hole in Plate

A localized disturbance was produced by bringing sound into the boundary layer through a hole in the plate. At a position 18 inches above the center line and 4 feet from the leading edge a ⅛-inch hole was drilled through the plate, and on the back was mounted a small headphone from a radio head set. This produced a three-dimensional disturbance emanating from a known location.

A hot wire, mounted on the small sledlike head, was arranged for traversing upstream and downstream at a fixed distance from the surface, usually along a line slightly displaced from the hole. A survey of possible types of measurement showed that the method could be used only for obtaining the type of result shown in figure 18. With the regeneration hook-up, that is, with the amplified output of the wire fed into the headphone, the frequencies of oscillation were determined with the wire at various distances downstream from the hole. The speed was constant during a run. Oscillation of the system occurred most easily for values of U_0 less than 40 feet per second and with the hot wire less than 0.1 inch from the surface. The solid curves of figure 18 show the discontinuous manner in which the frequency varied with the distance. Reversing the connections to the headphone changed the phase of the input by 180 degrees and gave the results indicated by the broken curves.

The explanation of this sort of performance is that proper phase relations had to exist for regeneration and that the frequency automatically decreased as the distance was increased in order to keep an integral number of waves between the hole and the wire. There existed a preferred frequency band, determined by the characteristics of the wire, electrical and acoustic circuits, and boundary layer. Jumps occurred when another wave between hole and wire was added to keep the frequency as near as possible to the center of the preferred band. The distance between curves of one type along any line of constant frequency is thus the wavelength corresponding to that frequency.

It is believed that the frequency band was determined more by the boundary layer than by the rest of the circuit when the wire was far from

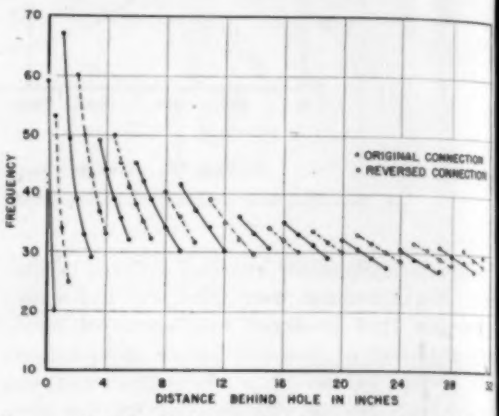

FIGURE 18.—*Oscillations excited by sound through hole in plate.*

Points show regeneration frequencies resulting from feedback from hot wire in boundary layer to head phone. Hot wire moved fore and aft along line 3/16 in. below hole. U_0=23 ft/sec.

the hole and that the preferred frequency was that for which amplification was a maximum over the path from hole to wire. The frequency midway between the extremes and as far as possible from the hole was therefore read from sets of

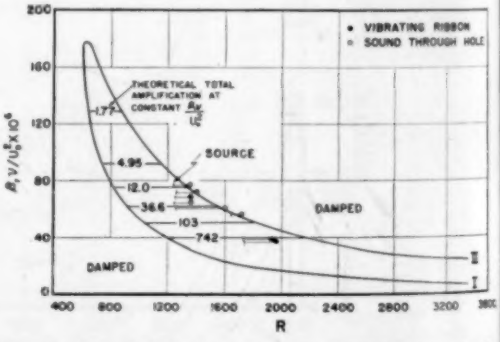

FIGURE 19.—*Middle frequencies of regeneration, wire far from hole, taken from curves of type shown in figure 18.*

Curve outlines theoretical amplification zone. Lines from points show length of amplification path.

rves for different wind velocities like that in ure 18 and placed on the usual Schlichting gram. The result is shown in figure 19. The th over which amplification could take place is licated by the horizontal line connected to each int.

As the wavelengths corresponding to these fre- encies were now known, it became possible for e first time to plot the results in terms of $\alpha\delta^*$ d R. The theoretical curve and the experi- ental results are shown in figure 20. The lines

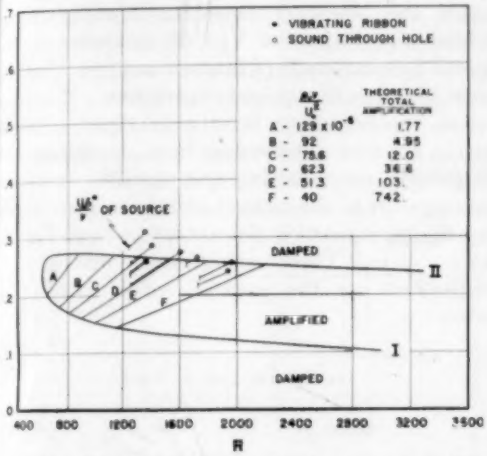

IGURE 20.—*Wavelength diagram showing zone of amplification according to Schlichting.*

ints show values of $\alpha\delta^*$ for frequencies of figure 19. Lines from points show path of amplification.

f total amplification for constant β_{rr}/U_0^2, corres- onding to those in figure 19, are known. The aths over which amplification could occur in the xperiment are represented as before by lines ex- ending from each point. Figures 19 and 20 enerally show the kind of results predicted by heory, if the frequency and wave length are de- ermined mainly by the characteristics of the oundary layer.

3. Excitation by Vibrating Ribbon

(a) The Ribbon

All attempts to excite boundary-layer oscilla- ions by wires vibrating in the boundary layer ailed because the disturbance of the eddying ake from the vibration of wires large enough to ffect the layer produced early transition. Flat trips outside the layer suffered from self-induced flutter and also had troublesome wakes that carried with them fluctuating pressure fields far downstream. A thin flat ribbon of phosphor bronze, placed edgewise to the flow in the boundary layer and only a few thousandths of an inch from the surface, was finally found capable of oscillating the boundary layer but produced no detectable effect when not vibrating. The ribbon was driven in and out from the surface by passing through it a small current of the desired frequency in the presence of a strong magnetic field from an electromagnet on the opposite side of the plate.

Several ribbons were tried to find the best width, distance from surface, and length of vibrating span. All ribbons were 0.002 inch thick. Widths ranged from $\frac{1}{16}$ to $\frac{1}{8}$ inch; distances from surface, from 0.006 to 0.015 inch; and vibrating segments, from 6 to 12 inches. None of these factors appeared to affect the performance to any noticeable extent. A certain amount of tension was necessary for stability. When it was desired to place the resonant frequency above the working range, high tension was necessary.

After this preliminary work, a ribbon 0.1 inch wide and 3 feet long was installed 4 feet from the leading edge of the plate. At a distance of 6 inches from each side of the center line of the plate, two strips of Scotch tape were laid on the surface for insulation and spacing. Another strip of tape was then laid on the ribbon to hold it firmly in contact with the tape on the plate, except for the segment 12 inches long at the center. Rubber bands at the ends supplied the tension. The 12-inch segment at the center was 0.006 inch from the surface and was free to vibrate under the action of the current and the magnetic field. Examinations with a microscope showed that the ribbon vibrated to and from the surface in a single loop. The same oscillator and amplifier that had been used for the loudspeaker were found to furnish ample power for driving the ribbon. Different positions for the ribbon were chosen to cover a large range of Reynolds number, but the method of attachment was always the same. Distance from the surface varied somewhat for different installations.

(b) Procedure

Two hot wires, one 0.010 inch and the other 0.110 inch from the surface, both sensitive only to u, were mounted on the small sled-like head and

arranged for sliding upstream and downstream along the center line of the plate with the distance of the wires from the surface fixed. The fluctuations introduced into the boundary layer could be picked up by either hot wire. The wave form showed some distortion for an inch or so behind the ribbon but in general became nearly sinusoidal at greater distances. Frequencies amplified by the boundary layer showed increasing amplitude with increasing distance from the ribbon, while those damped showed decreasing amplitude. For much of the working region the oscillations could probably be regarded as two-dimensional, but no attempt was made to verify this assumption.

Just as for the loudspeaker and the headphone behind the hole in the plate, the system could be made to oscillate by connecting the amplified output of the hot wire to the ribbon. Curves like those shown in figure 18 were obtained and, from them, three points plotted in each of figures 19 and 20 were obtained. Since the ribbon could be used for applications that were believed to be more important, very little work was done with the regeneration hook-up.

The wavelength was determined in the following simple manner: The input to the ribbon from the oscillator was connected to one pair of plates in the cathode-ray oscillograph and the output from the wire was connected to the other pair. A stationary Lissajou figure consisting of a single closed loop was obtained since the frequencies of both input and output were the same. As the spacing between ribbon and hot wire was changed this figure changed from a straight line to an ellipse, then to a circle, again to an ellipse, and finally to a straight line inclined 90 degrees to the first line. This indicated that the phase between input to the ribbon and output from the wire had changed by 180 degrees and that the change in spacing between wire and ribbon was one-half wavelength. With the oscillograph serving as the indicator, wavelength measurements were thus reduced to a measurement of the distance moved by the hot wire. The wave velocity was then obtained by multiplying the wavelength by the frequency of the oscillations.

Determinations of amplification and damping were carried out by setting the ribbon into vibration at an arbitrary fixed amplitude and reading the mean-square hot-wire output voltage as the wire was moved away from the ribbon. The results obtained are given in section VI, 3 (d). The distribution across the boundary layer was determined by traversing normal to the surface at some fixed distance behind the ribbon with a single hot wire sensitive to u, mounted on the traversing apparatus described in section II, 7.

During the course of the work frequencies ranging from 10 to 260 cycles per second were used.

(c) Distribution of Amplitude

Since a theoretical distribution of amplitude across the boundary layer has been given by Schlichting (see section V, 2 (d) and table 4), the actual distribution is of interest as a test of agreement between theory and experiment. Traverses across the boundary layer were therefore made with a hot wire downstream from the ribbon with frequency, air velocity, and distance from the leading edge of the plate chosen to conform to the conditions for which the theoretical calculations were made. These conditions correspond to oscillations on the neutral curve specified as follows:

Conditions required by theory

Branch	R	$\frac{\beta_{cr}\nu}{U_0^2}\times 10^6$
I	894	62.3
II	2,070	42.4

Experimental conditions

Branch	R	$\frac{\beta_{cr}\nu}{U_0^2}\times 10^6$	x		U_0	Frequency
			Ribbon[1]	Wire		
			ft.	ft.	fps	cps
I	902	61.4	0.75	1.09	41.8	103
II	2,080	40.6	5.00	5.33	46.0	82

[1] Ribbon about 0.009 in. from surface.

The distributions are given in figure 21 with amplitude expressed in terms of u'/U_0. The solid curves show the theoretical distribution and the broken curves through the points show the observed distribution. In both cases the traverses were made 4 inches behind the ribbon. The vibrational amplitude of the ribbon was set arbitrarily and about the same for branches I and

II. The smaller values of u'/U_0 in branch II result from the smaller effect of the ribbon on the thicker boundary layer. Since the theoretical values given by Schlichting were based on an arbitrary average amplitude of $u'/U_0=0.05$ from $y=0$ to $y=\delta$, Schlichting's values were reduced to give the average found by experiment; that is, areas under the theoretical curves were made equal to areas under the experimental curves from $y=0$ to $y=\delta$.

Although the general agreement between theory and experiment is good, perhaps the most striking confirmation of the theory is the 180 degree phase shift occurring at $y/\delta=0.7$. On moving outward from the surface all oscillations disappeared at this point and farther out they reappeared but with phase opposite to those that had disappeared. This phenomenon is shown in a more striking manner by the oscillograms in figure 22. The pairs of traces are simultaneous records of oscillations picked up by two wires, one of which was

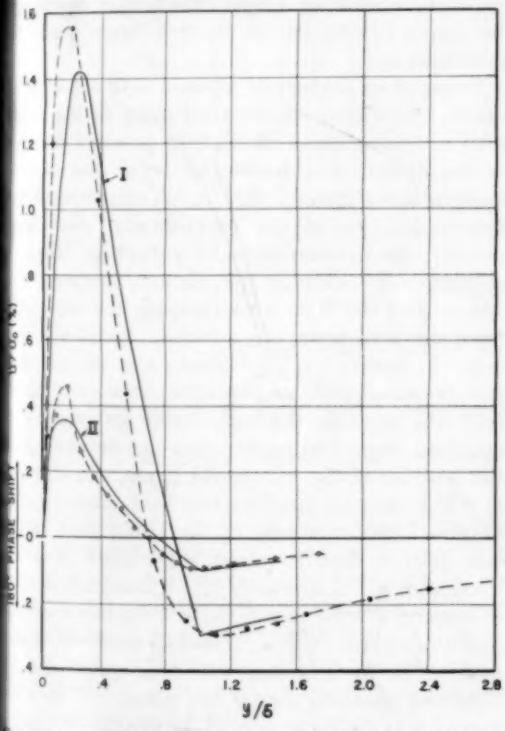

FIGURE 21.—*Distribution of amplitude of oscillations across boundary layer.*

Solid curves are theoretical according to Schlichting. Broken curves are experimental.

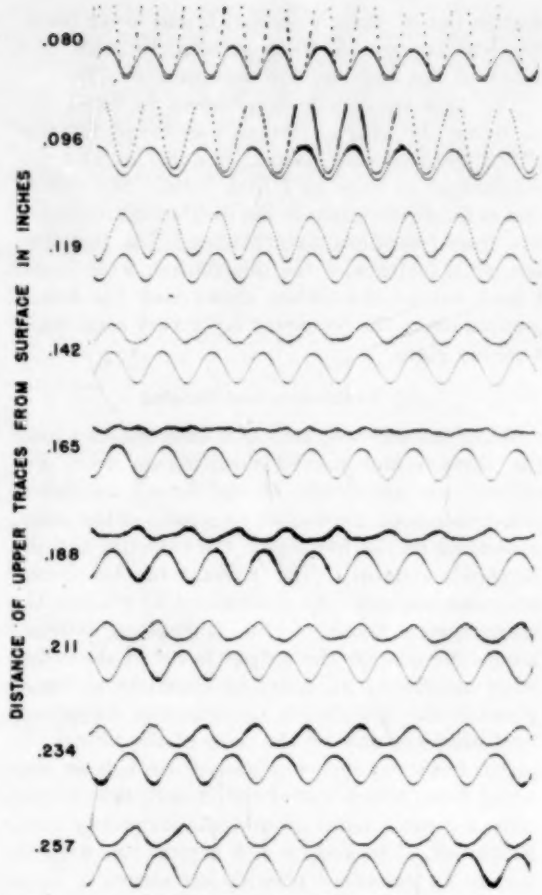

FIGURE 22.—*Oscillograms showing phase reversal in u-component of oscillations excited by vibrating ribbon.*

Simultaneous records from two hot wires located 1 ft downstream from ribbon. Lower trace—hot wire 0.055 in. from surface. Upper trace—hot wire at various distances from surface. Ribbon 3 ft from leading edge. Frequency=70 cps. U_0=42 ft/sec.

at a fixed distance of 0.055 inch from the surface (lower trace) and the other at varying distances, beginning at 0.080 inch (upper trace). The simultaneous records were made possible by an electronic switch that impressed the separately amplified voltages of the two wires on the oscillograph, alternately and in rapid succession. The switching from one to the other accounts for the dotted appearance of the trace. The waves are in phase for the first four records; the amplitude of the upper wave decreases with each succeeding record to zero in the fifth. Beginning with the sixth, an oscillation reappears in the upper trace but 180

727972—47——10

degrees out of phase with that in the lower trace. The oscillations in these records lie near the center of the amplification zone at $R=1{,}720$.

The type of distribution shown in figure 21, including the phase reversal, was found for amplified, damped, and neutral frequencies and for oscillations as close as 1 inch behind the ribbon and as far downstream as the oscillations remained free from transition disturbances. The fact that the main features of the distribution were found 1 inch behind the ribbon shows that the forced oscillations in the boundary layer very soon reach a steady state.

(d) Amplification and Damping

When the wire was kept at a fixed distance from the surface and moved downstream from the ribbon, the amplitude of the forced oscillation either increased, decreased, or remained the same, depending on the frequency, the velocity, and the Reynolds number. The amount of the change with distance could be determined by reading the mean-square value of the fluctuating voltage across the wire on the output meter of the turbulence amplifier. In order to eliminate as far as possible the extraneous disturbances introduced by turbulence and by the noise of the tunnel, the signal from the wire was passed through an electrical filter, which was tuned in each case to pass only a 5-cycle band around the frequency being measured. The results of a typical run with the ribbon at the 4-foot position are shown in figure 23. In this figure x_0 denotes a position 2 inches

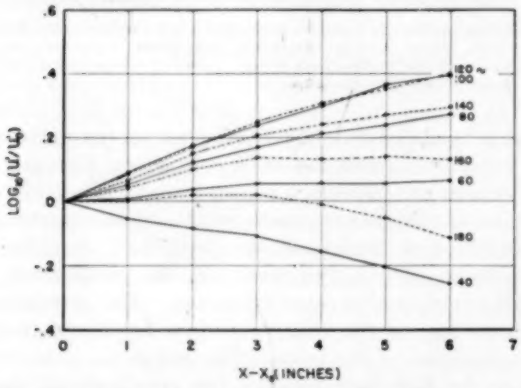

FIGURE 23.—*Growth and decay of u-component of oscillations produced by vibrating ribbon ¼ ft. from leading edge of plate.*

x_0 is 2 in. downstream from ribbon. U_0=64 ft/sec.

downstream from the ribbon. The ratio u'/u_0' is the square root of the meter reading at x divided by the square root of the meter reading at x_0.

According to eq 31

$$\frac{u'}{u_0'}=exp\int_{t(x_0)}^{t(x)}\beta_i dt$$

or

$$2.3\log_{10}\frac{u'}{u_0'}=\int_{t(x_0)}^{t(x)}\beta_i dt.$$

Differentiating with respect to t and using the relation $dx/dt=c_r$, where c_r is the wave velocity, gives

$$\beta_i=2.3c_r\frac{d\left(\log_{10}\frac{u'}{u_0'}\right)}{dx} \tag{39}$$

The wave velocity is obtained by multiplying the measured wavelength by the frequency. If the changes in u'/u_0' with distance shown in figure 2 are truly effects of amplification and damping, the slopes of the curves in this figure serve to determine β_i.

Before these slopes can be used with confidence, effects introduced by the thickening of the layer with increasing x and effects from possible changes in the distribution across the layer also with x must be investigated. Errors can arise from these sources because of the experimental procedure, namely, the determination of growth or decay of amplitude by varying the distance between the ribbon and the wire while keeping the wire at a fixed distance from the surface. From the evidence in section VI, 3 (c), changes in the distribution are small and can cause but little error; however, the increase of δ with x may give rise to an apparent amplification or damping, depending on the position of the wire in the layer. In all cases in which data on amplification and damping were obtained, the wire was in the rising part of the distribution, that is, values of y/δ below those for maximum u'/U_0 in figure 21. Consequently, the increasing δ with increasing x introduced an apparent damping, which caused all observed amplification to be less than the true value and all observed damping to be too great. If it is assumed that the inner part of the distribution curve is a straight line passing through the origin, the magnitude of the error in β_i calculated from eq 39 by use of observed slopes is $(½)c_r/x$. Any cur-

ature in the distribution curve like that shown tween zero and the peak value of u'/U_0 in figure lessens the error. Since $(\frac{1}{2})c_r/x$ therefore presents an upper limit, and since its value rned out to be about the order of the random viation in results, β_i was calculated by eq 39 th the use of the experimentally determined pes without correction.

and the corresponding values of R. This amounts to finding points of zero slope on curves like those shown in figure 23. Such points were obtained from a number of runs at various wind speeds with the ribbon at the 4-foot position and again with the ribbon 9 inches from the leading edge. Values of $\beta_r\nu/U_0^2$ and the corresponding values of R were computed and plotted in figure 24. The

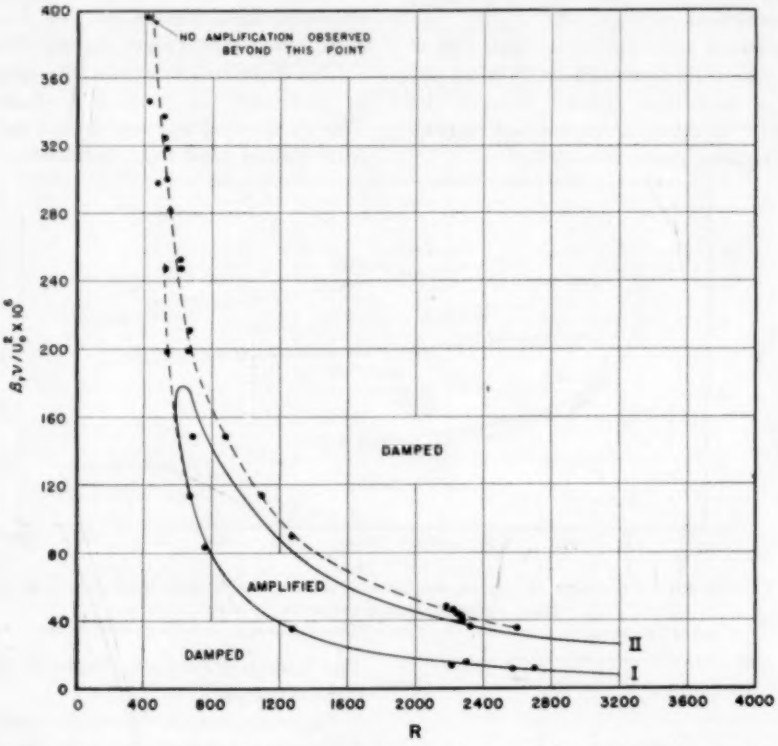

FIGURE 24.—*Frequency of neutral oscillations excited in boundary layer by vibrating ribbon.*

Solid curve is neutral curve according to Schlichting. Broken curves are neutral curves defined by experimental points.

In figure 23 the curve for 40 cycles per second hows damping throughout. As the frequency is creased amplification takes place, reaches a max- mum at 120 cycles per second, and then decreases ntil 180 cycles per second again shows damping. n the range of Reynolds number represented by his range in x, all frequencies below about 50 and bove 180 cycles per second are damped, while a and of amplified frequencies lies in between.

Of considerable interest are the frequencies for hich there is neither amplification nor damping

solid curve is again Schlichting's neutral curve and the broken curves are those defined by the experimentally determined points. The agreement is very satisfactory, except for points above $\beta_r\nu/U_0^2=200\times10^{-6}$.

By use of the measured wavelengths, $\alpha\delta^*$ was calculated for the neutral frequencies and the results were plotted on the wavelength diagram shown in figure 25. The open circles denote points on branch II, and the closed circles denote points on branch I. The broken lines drawn

through these points define the experimental neutral curves. Schlichting's theoretical curve is shown and also the theoretical neutral curve given by C. C. Lin.[4]

Still another type of representation involving both frequency and wavelength is the diagram of c_r/U_0 and R in figure 26. The points and the broken curves show the wave velocities found for the neutral oscillations. The solid curve is Schlichting's theoretical curve.

It is again pointed out that both branches of the theoretical curves in figures 24 to 26 meet the R-axis at $R=\infty$ and thus extend beyond the region indicated. Transition prevented experimental determinations above $R=2{,}800$.

The wavelength diagram is repeated in figure 2 and this time shows, in addition to the theoretic neutral curve, the curves of equal amplificati within the zone. These contours were copie directly from a figure given by Schlichting [4 The broken curves are defined by the neutr points, which are not shown in this figure. Th points with the values opposite (all to be mult plied by 10^{-4}) are the observed values of $\beta_i\delta^*/U$ obtained from values of the slopes other tha zero. Negative values signify damping.

The distribution across the amplification zon at particular values of R is shown in figure 2 The theoretical curves, drawn solid, are plotte from values read from Schlichting's figure in [4

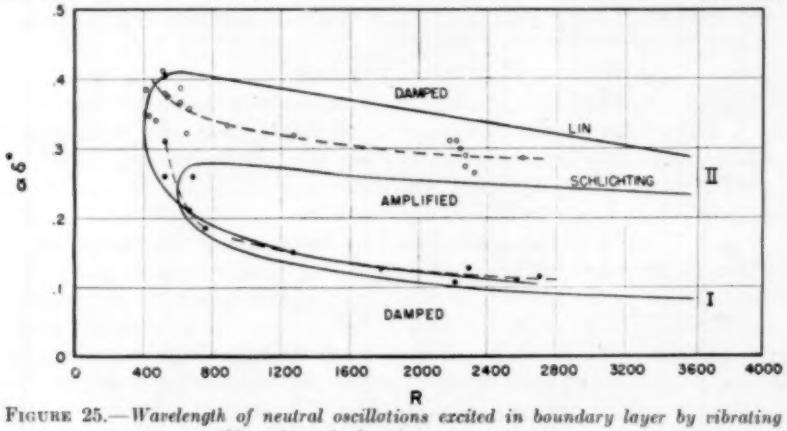

FIGURE 25.—*Wavelength of neutral oscillations excited in boundary layer by vibrating ribbon shown by broken curves and points.*

Closed circles—branch I. Open circles—branch II. Theoretical neutral curves shown by solid lines.

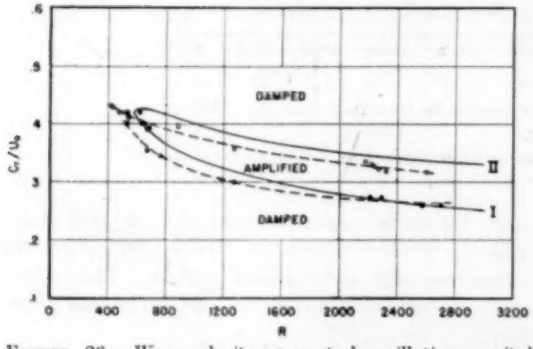

FIGURE 26.—*Wave velocity of neutral oscillations excited in boundary layer by vibrating ribbon.*

Solid curve is neutral curve according to Schlichting. Broken curves are neutral curves defined by experimental points. Closed circles—branch I. Open circles—branch II.

The broken curves are drawn through the experimental points.

The comparison between theory and experiment given in figures 24 to 28 shows, on the whole, better agreement than might be expected when it is considered that at the outset the very existence of such phenomena had not been proved. The observed amplification shown in figures 27 and 28 is less than the theoretical, but it will be recalled that the theoretical calculation yielded accurate values only near the neutral curve. In the neighborhood of the low Reynolds number limit the experimental inaccuracies are large because of the small amplification and damping. The maximum values of $\beta_i\nu/U_0^2$, $\alpha\delta^*$, and c_r/U_0 and the minimum value of R for which amplification can occur as determined approximately by experiment are compared with the theoretical limits in the following table:

[4] Lin's curve was not available when this work was originally published. The curve is a recent addition taken from C. C. Lin, On the stability of two dimensional parallel flows, Quarterly of Applied Mathematics, III, [2], 117 to 142 (July 1945); [3], 218 to 234 (Oct. 1945); [4], 277 to 301, (Jan. 1946).

	Experiment (approx.)	Theory	
		Schlichting	Tollmien
	450	575	420
	400×10^{-6}	178×10^{-6}	
	0. 4	0. 278	0. 367
	. 43	about 0. 42	. 425

Tollmien's limiting values, on the whole, agree better with experiment than Schlichting's values. A comparions of the experimental results in figure 25 with Tollmein's diagram of $\alpha\delta^*$ plotted against $\log_{10} R$ in [2] shows better agreement in general than with the corresponding diagram given by Schlichting in figure 25. In spite of this, Schlichting's results were used because they were more complete than Tollmien's.

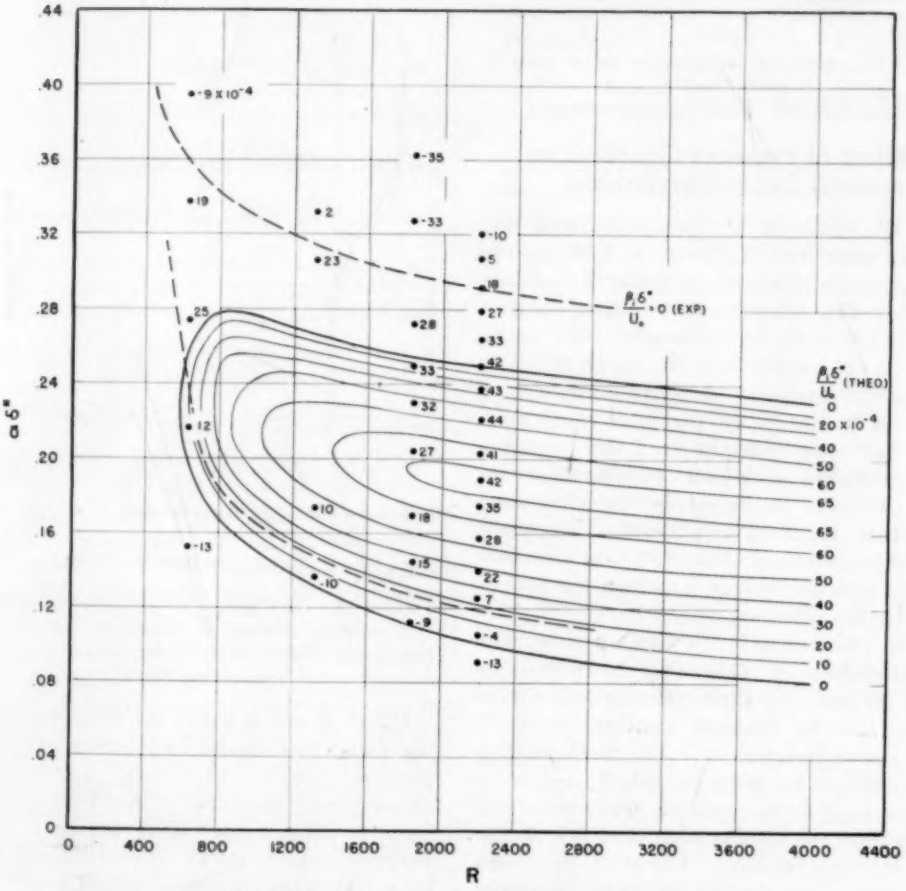

FIGURE 27.—*Contours of equal amplification according to Schlichting.*

Values of $\beta_0\delta^*/U_0$ (all values to be multiplied by 10^{-4}) opposite points are amplifications determined by experiment. Faired experimental contour of zero amplification shown by broken curves.

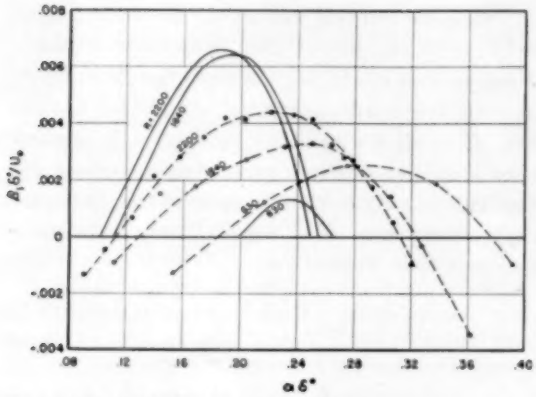

FIGURE 28.—*Distribution of amplification across zones of figure 27.*

Solid curves are theoretical. Broken curves are experimental.

VII. Effect of Pressure Gradient on Boundary-Layer Oscillations

Figure 29, obtained in connection with the earlier work presented in section V, 1, shows the effect of pressure gradient on naturally excited oscillations. The pressure distribution along a part of the plate is shown to the left in this figure. The reduction of amplitude in the region of falling pressure is very marked. Accelerated growth of amplitude is evident in the region of rising pressure. It was accordingly inferred that negative pressure gradients decreased amplification (or increased damping) of the oscillations while positive gradients increased amplification. A quantitative investigation of this effect was therefore undertaken with oscillations forced on the boundary layer by the vibrating ribbon.

When the ribbon was in the 3-foot position, the regular procedure of measuring amplifications and damping and of mapping the neutral curves was carried out for pressure distributions *B*, *C*, *D*, and E shown in figure 30. The corresponding pressure gradients are given in table 5.

In figure 30, q_x is the dynamic pressure at any distance x from the leading edge, and q_0 is a convenient reference pressure. Curve *A* shows one of the distributions for the condition generally termed "zero pressure gradient." This condition was obtained by giving sufficient divergence to the adjustable side walls of the working chamber to overcome the normal pressure drop. The shape of the curve in the first 6 inches was determined by the flow around the leading edge of the plate and hence could be changed but little by the setting of the walls. The walls also have little effect on the small local variations, since these were found to be produced by slight waviness of the surface. Curve *A* is thus a condition of zero gradient only when the length of the interval and the end points are properly chosen. With a pressure distribution given by curve *A*, the experimental values of velocity distribution and δ^* were in good agreement with the Blasius values; hence, the approximation to zero gradient is probably sufficiently good.

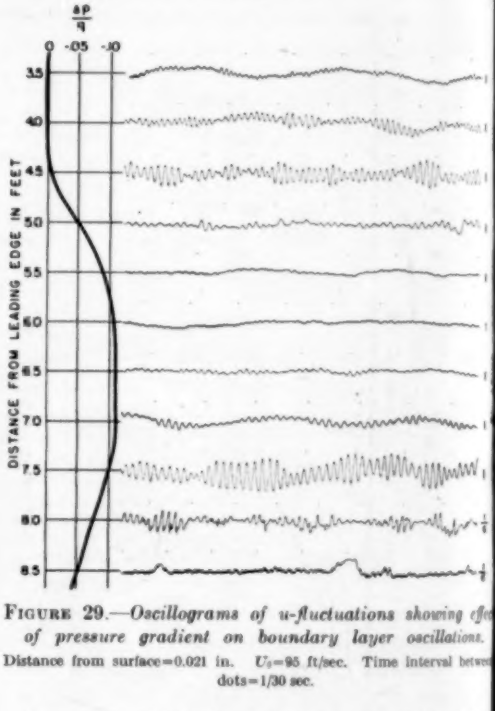

FIGURE 29.—*Oscillograms of u-fluctuations showing effect of pressure gradient on boundary layer oscillations.*

Distance from surface=0.021 in. U_0=95 ft/sec. Time interval between dots=1/30 sec.

Curve *B*, which shows the pressure rising along the plate, was obtained by giving the walls the greatest possible divergence. Curve *C*, which shows the pressure falling, was obtained with the walls forming a converging passage. The steep positive gradient shown by curve *D* was produced by a vertical airfoil placed 10 inches from the side of the plate running from the floor to the ceiling of the tunnel, and the steep negative gradient of curve *E* was produced by blocking the stream with a plywood panel ¾ inch thick and 28 inches wide extending from the floor to the ceiling placed parallel to and 10 inches from the plate.

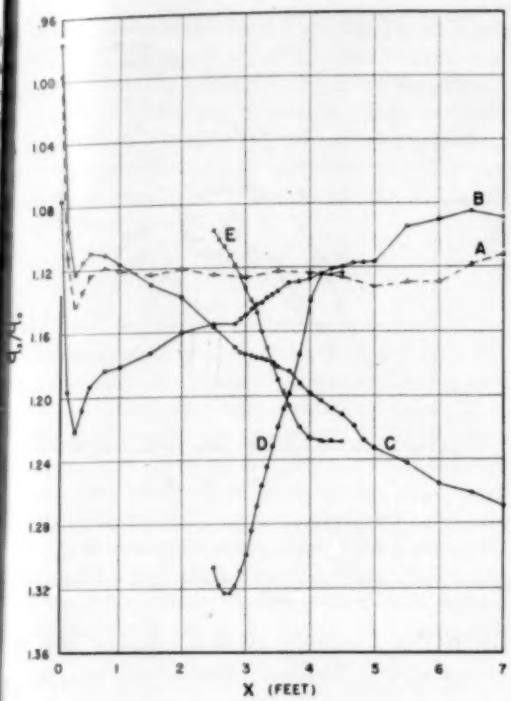

FIGURE 30.—*Dynamic pressure distribution along plate outside boundary layer.*

The results obtained on the effect of pressure gradient are given in figures 31 to 34 for distributions B and C and will be discussed in detail later in this section. Corresponding figures for distributions D and E could not be obtained because of the large effect of these gradients on the oscillations. With the large gradients, the general impression given by observing the oscillations was that amplification always occurred in gradient D regardless of the frequency and Reynolds number, while damping always occurred in gradient E; however, this statement must be somewhat qualified. For example, in E fluctuations of all frequencies were damped for values of R up to 2600, which was the highest value obtainable with the ribbon at the 3-foot position. It is quite possible that a zone of amplification lay beyond the range of the experiment. In the case of gradient D, the investigation had to be restricted to low Reynolds numbers because of the occurrence of transition. The few observations made here indicated a possible low limit of Reynolds number below which damping occurred, but the results are in doubt because of a possible scale effect on the airfoil used to produce the pressure gradient. The pressure rise may have been lessened by laminar separation on the airfoil at the low velocities and the positive gradient may have become less than that given by D. Accurate measurements of pressure distribution at the low velocities was difficult.

Before presenting the results for the two small gradients B and C, attention must be called to the effect of pressure gradient on δ^*. Since δ^* enters into certain dimensionless quantities used in plotting the results, its actual value must be known for each case. The value of δ^* was measured only for distribution B and the result was

$$\frac{\text{Observed } \delta^*}{\text{Blasius } \delta^*} = 1.09 \text{ at } x = 3.33 \text{ ft.}$$

For distribution C, δ^* was estimated by the aid of the Kármán-Pohlhausen method by assuming a linear pressure distribution. The validity of the method was tested by making a similar calculation

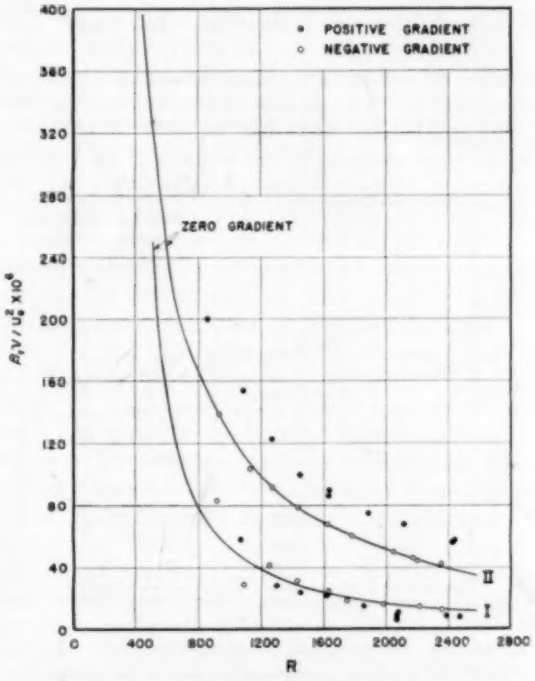

FIGURE 31.—*Frequency diagram of neutral oscillations.*

Experimental curve for zero pressure gradient shown without points. Positive gradient from distribution B and negative gradient from distribution C of table 5.

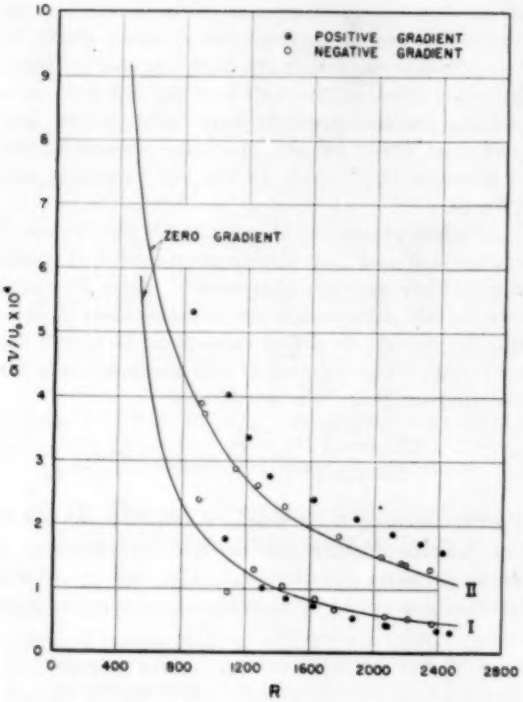

FIGURE 32.—*Wavelength diagram of neutral oscillations.*

Experimental curve for zero pressure gradient shown without points. Positive gradient from distribution *B* and negative gradient from distribution *C* of table 5.

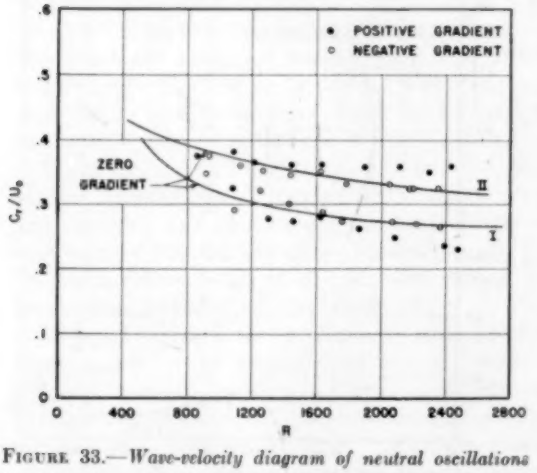

FIGURE 33.—*Wave-velocity diagram of neutral oscillations*

Experimental curve for zero pressure gradient shown without points. Positive gradient from distribution *B* and negative gradient from distribution *C* of table 5.

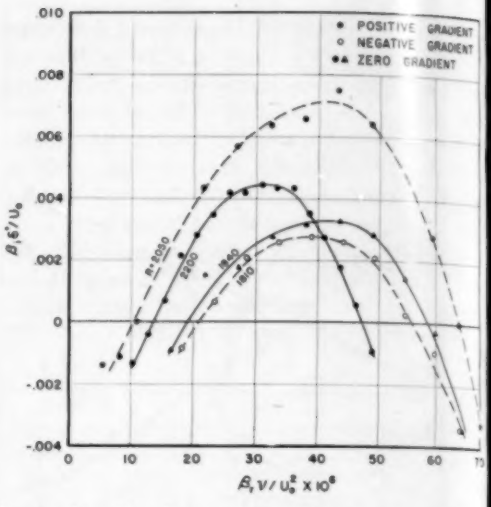

FIGURE 34.—*Distribution of amplification across zones of figure 31, showing effect of pressure gradient.*

Positive gradient from pressure distribution *B* and negative gradient from distribution *C* of table 5.

for B and obtaining good agreement with the measured δ^*. The estimated result for C was

$$\frac{\text{Calculated } \delta^*}{\text{Blasius } \delta^*} = 0.93 \text{ at } x = 3.33 \text{ ft.}$$

The values of δ^* for the Blasius distribution were multiplied by the above factors to give the values of δ^* pertaining to gradients B and C.

Figure 31 is the much-used frequency diagram showing the results for zero, positive, and negative gradients of distributions A, B, and C, respectively. The solid curve is the same as the broken curve of figure 24 for zero gradient, shown here without the experimental points. The points for negative gradient lie close to this curve; the points for positive gradient generally lie outside the zone of amplification for zero gradient. The positive gradient has therefore widened the amplification zone as expected. Contrary to expectation, the negative gradient failed to reduce the size of the zone. No observations were made below $R = 800$.

Since wavelengths of the oscillations were measured, the data for these same frequencies are given in a wavelength diagram (fig. 32) and a wave-velocity diagram (fig. 33). It will be noted that figure 32 is unlike the usual wavelength

agram (for example, fig. 25) in that the ordinate now $\alpha\nu/U_0$ instead of $\alpha\delta^*$. This change was ade in order to eliminate δ^* from one of the oordinates and thereby to restrict errors occurring the estimated value of δ^* with pressure gradient the Reynolds number coordinate. The new dinate is simply $\alpha\delta^*$ divided by the Reynolds umber, that is,

$$\frac{\alpha\delta^*}{\frac{U_0\delta^*}{\nu}}=\frac{\alpha\nu}{U_0}.$$

n both figures 32 and 33, the solid curves are the xperimentally determined neutral curves for zero radient with the experimental points omitted.

Figures 32 and 33, like figure 31, show an effect f the positive gradient but little or no effect of he negative gradient. These figures show only he neutral points and so merely define the bound- ries of the amplification zone. The effect of ressure gradient on the amplification within the one is demonstrated in figure 34. This figure, hich is similar to figure 28, except that zones are om the frequency diagram instead of the avelength diagram, shows the distribution of mplification coefficient, actually $\beta_i\delta^*/U_0$, across he zones of figure 31 at certain fixed values of the eynolds number. The positive and negative ressure gradients signify as before pressure dis- ibutions B and C, respectively. For compari- on, the experimental curves for zero gradient are iven as solid lines. The comparision is best made etween pairs of curves having Reynolds numbers ost nearly alike.

Since $\beta_i\delta^*/U_0$ increases with Reynolds number see fig. 27), the difference between $R=1{,}840$ for ero gradient and $R=1{,}810$ for negative gradient ay account for the reduced amplification with egative gradient. The failure to show conclusively n effect of the small negative gradient may be ue in part to the small local value of the gradient hown in table 5. The difference between $R=$,200 for zero gradient and $R=2{,}050$ for positive radient is significant, since $R=2{,}050$ for zero radient would lie below $R=2{,}200$.

VIII. Transition From Oscillations to Turbulence, Zero Pressure Gradient

The distinguishing feature of transition with low tream turbulence is the occurrence of boundary- ayer oscillations that grow until the layer becomes turbulent. Under such conditions, transition to turbulent flow is simply transition from a particular type of oscillatory motion to turbulent motion. The oscillations are now understood and the final step in an understanding of the origin of turbulence involves an investigation of this transition process.

TABLE 5.—*Pressure gradients* $(1/q_1)\ (\triangle P/\triangle x)$[1]

q_1=dynamic pressure outside boundary layer at 3.33 ft from leading edge of plate.
P=pressure near surface at distance x from leading edge.

Distribution	Average gradient from 1 to 6 ft	Local gradient
	Percent	*Percent*
A	−0.11	−0.78 from 4 to 5 ft
B	1.62	2.48 from 3 to 3.67 ft
C	−2.38	−1.36 from 3 to 3.67 ft
D		12.0 from 3 to 3.67 ft
E		−9.8 from 3 to 3.67 ft

[1] Note that pressure gradient and dynamic pressure gradient have opposite signs. (See fig. 30.)

Although transition in highly disturbed flow does not fall into this category, the two are similar in that both have to do with the effect of a disturbance large enough to bring about turbulent flow. The effect, however, depends on the type of the disturbance as well as its magnitude; and, as has been shown, an amplified disturbance does not have the random character of an initially large disturbance. Transition from an amplified disturbance promises to be of considerable importance in modern low-turbulence wind tunnels and in the atmosphere.

The vibrating ribbon to produce oscillations and the hot-wire apparatus to examine their development were suitable tools for the investigation of transition. The ribbon was placed at the 3-foot position and two hot wires at different distances from the surface were arranged for traversing parallel to the plate through the transition region. The Reynolds number was always chosen so that the undisturbed boundary layer (ribbon not vibrating) was laminar at the hot wires. Representative samples of the results obtained are shown in figures 35 to 37.

Figure 35 shows what happens at a fixed point 2.5 feet downstream from the ribbon as the vibrational amplitude of the ribbon is varied. The pairs of traces show simultaneously the response of the two wires. The values of gain control

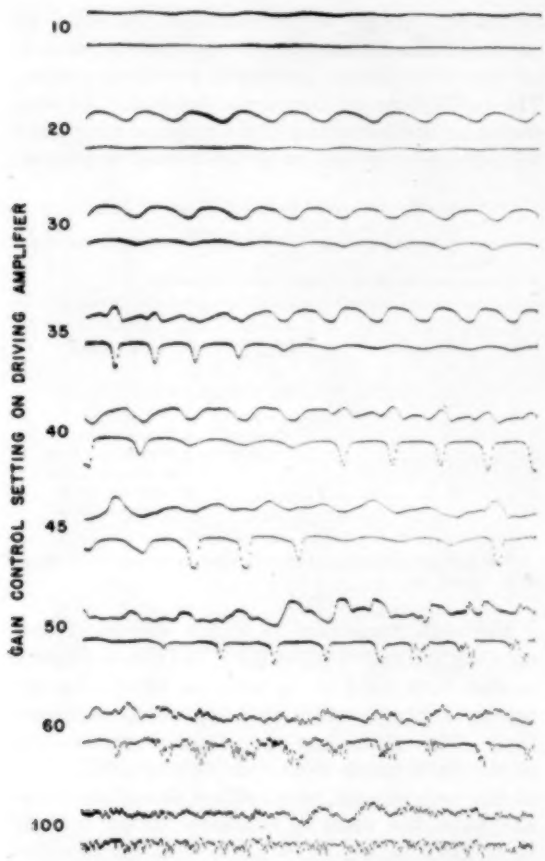

FIGURE 35.—*Oscillograms of u-fluctuations showing development of turbulence from oscillations produced by vibrating ribbon at position 2.5 ft down-stream from ribbon.*

Ribbon 3 ft from leading edge of plate. Simultaneous records at 0.014 in. from surface, upper trace; and 0.114 in. from surface, lower trace. Frequency 70 cps. U_0=50 ft/sec.

setting on driving amplifier are roughly proportional to ribbon amplitude. The amplitude of the waves on the traces cannot be quantitatively related to fluctuations of velocity because the sensitivity of the wires was unknown. The sensitivities of the two wires were different, and so comparison of amplitudes at inner and outer wires was impossible. It is known, however, that velocity increases produce upward displacement of the traces and that velocity decreases produce downward displacement. The direction of time in this figure is from left to right.

This figure shows that the boundary layer at a given point can be changed from laminar to turbulent by varying ribbon amplitude and shows qualitatively the progressive nature of the change. Examination of successive pairs of traces indicates that fairly regular waves first make their appearance, being first in phase at the two wires and later in the fifth and sixth records, in and out of phase in random fashion as the amplitude increases. The distances from the surface are such that an in-phase condition would be expected from the distribution of figure 21. A growing distortion of the waves then appears until, in the seventh record, bursts of high-frequency fluctuations occur. The latter, identified by the jagged appearance of the trace, are bursts of turbulence. The final record shows the completely turbulent state. The dotted character of the traces, due to the electronic switch, obliterates details of rapid fluctuations. A similar succession of changes is shown in figures 36 and 37.

In figure 36 simultaneous records are again shown, this time from two wires on the same

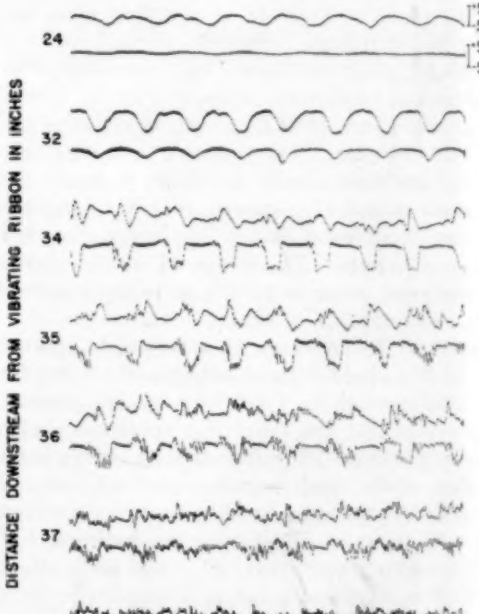

FIGURE 36.—*Oscillograms of u-fluctuations showing development of turbulence from oscillations produced by vibrating ribbon placed 3 ft from leading edge of plate.*

Simultaneous records at 0.011 in. from surface, upper trace; and 0.112 in. from surface, lower trace. Frequency 70 cps. U_0=50 ft/sec.

mounting moved downstream from the ribbon while the amplitude of the ribbon remained fixed. Figure 37 shows the same condition but for the two traces photographed separately in order to eliminate the dotting effect of the electronic switch. The difference in the appearance of the records in these two figures is due more to the different magnification than to the character of the traces. Since the frequency of 70 cycles per second is amplified by the boundary layer, the amplitude increases downstream and increasing distance is in one respect like increasing ribbon amplitude in figure 35. The two cases are not equivalent, however, because the boundary-layer thickness increases from record to record in figures 36 and 37.

From calibration data, obtained in connection with figures 36 and 37, it was possible to relate two particular displacements on the record to a percentage change in the mean velocity at the position of the wire. These two percentages are indicated at the right of each trace, an upward displacement indicating an increase and a downward displacement a decrease from the mean local velocity at the hot wire. The percentages are the same for all records in figure 36.

For fluctuations as large as most of those shown, it is not possible to indicate the zero- or mean-velocity position of the trace. This is because of the nonlinear characteristics of the hot wire which produces greater displacements of the trace for velocity decreases than for increases. A certain amount of distortion and some error in the records will result from this effect. It is certain, however, that crests are above the mean velocity while troughs are below the mean and the distance between the two is approximately the double amplitude. The scale at the right furnishes a measure of the double amplitude.

In the succession of changes occurring from point to point through the transition region, the oscillations first increase in amplitude and, once large, undergo increasing amounts of distortion. Turbulence appears at first in short intervals of the trace and finally for the full length of the trace. Randomness occurs gradually, and this suggests a continuous transition from wave to turbulent motion. It is not difficult to imagine a process

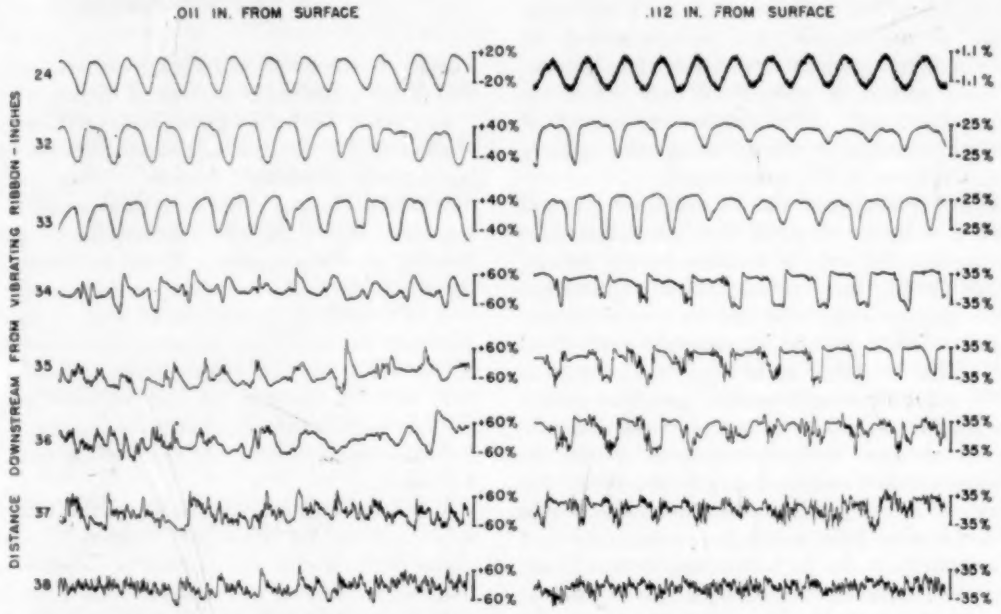

FIGURE 37.—*Oscillograms of u-fluctuations showing development of turbulence from oscillations produced by vibrating ribbon placed 3 ft from leading edge of plate.*

Frequency 70 cps. U_0=50 ft/sec.

here like that often assumed for the formation of eddies from a free vortex sheet. The sheet is imagined to take first a wavelike character, then as the wave grows, to curl up into discrete eddies. The disturbed laminar boundary layer may be regarded as a wavy vortex layer with the wave progressively increasing in amplitude and distorting until discrete eddies are formed. The eddies themselves are unstable and soon break up into a diffusive type of motion which characterizes turbulent flow. If the validity of this picture is granted, transition is understood when the wave motion is understood. An understanding of transition is therefore close, but only close because the wave motion is understood only when the amplitude is small. Furthermore, the important question, concerning where along the surface eddies first form, is still unanswered.

Another process may also be imagined. It will be noted in figures 35 to 37 that transition takes place in a more orderly manner at the greater distance from the surface. Here turbulence appears in certain parts of the wave cycle, generally in the sharp-pointed low-velocity part of the cycle. This behavior lends support to the view held by some investigators that transition occurs when the flow comes to rest or reverses direction near the surface (separation point). While the amplitudes shown do not reach the necessary 100 percent, it seems possible that this value would be found at some point nearer the surface. Against this argument is the fact that the records made nearer the surface do not show the turbulent bursts confined to the low-velocity side of the cycle. The argument is further weakened by the possibility of accounting for the observed effects at the greater y-values by the difference between the distribution of mean-velocity characteristic of a laminar layer and that characteristic of a turbulent layer. This is to say, that the observed effect is caused by the turbulence rather than a cause of the turbulence.

The idea of transition by separation has been formulated by Taylor [1] by assuming intermittent separation or near separation to be caused by the local pressure gradients accompanying disturbances. The assumption is that separation is imminent when the Kármán-Pohlhausen parameter Λ, derived from pressure gradients either steady or fluctuating, reaches a certain negative value. A steady adverse pressure gradient large enough to cause laminar separation is known to bring about transition rather than complete separation when the Reynolds number is sufficiently high. By analogy, intermittent separation is supposed to have the same effect. For isotropic turbulence in the surrounding flow the fluctuating pressure gradient is known in terms of measurable quantities, namely, u' and the scale. Taylor's relation is

$$\frac{u'}{U_0}\left(\frac{x}{L}\right)^{1/5}=F(R_x),$$

where L is the scale, and $F(R_x)$ expresses a function of the x-Reynolds number of transition.

In essence Taylor's relation rests on the concept of velocity fluctuations impressed on the boundary layer from pressures outside. When velocity fluctuations belong to the natural wave in the boundary layer, Taylor's relation can have little bearing on the problem. There is therefore no theory connecting oscillations to transition. The idea of transition by separation leads to the concept that transition results when the u-component of the wave gets sufficiently large to reverse the flow near the surface. A lack of knowledge regarding large-amplitude waves results in a lack of information concerning the point where transition will occur.

It has not been proved that separation is a necessary condition for transition. Figure 11, where a slight reversal near the surface is indicated by a frequency doubling in the lower part of the cycle in the trace at 4 feet, gives evidence that reversal alone is not a sufficient condition. Perhaps the former picture, based on the analogy to the vortex sheet is the more accurate one.

Since the Taylor relation is not applicable when transition results from amplified waves, the average scale of the initial disturbance is important only insofar as it is related to the spectrum of the disturbance. The frequency distribution of the initial disturbance is of great importance, since amplification finally selects only a very narrow band of frequencies from all those initially present to bring about transition. The presence or absence of frequencies near this amplified band is obviously more important than the total energy of the disturbance.

Only on the basis of certain prominent frequency bands in the stream turbulence can figure 7 be ex-

plained. The reasoning is as follows: If no disturbances were present, theoretically transition should not occur. The pairs of curves in figure 7 should then approach $R_x = \infty$ for zero turbulence. On the basis of amplification of initial distrubances in which all frequencies are present, equation 33 suggests that the curves defining the transition region should fall rapidly at first and then at a progressively diminishing rate as the turbulence is further increased. Actually, the opposite trend is shown in figure 7. Figure 8 shows that not all frequencies are represented alike and, furthermore, that noise is responsible for many of the peaks shown. As the present turbulence was decreased by the addition of damping screens, the ratio of noise to true turbulence was increased. While the total energy of the distrubance was decreased, the energy in certain frequency bands may actually have been increased. A reduction of noise might have greatly altered figure 7.

IX. Conclusion

Laminar boundary-layer oscillations are the velocity fluctuations that result from a wave traveling downstream through the boundary layer. The characteristics of this wave have been measured and good agreement with theory has been obtained. The wave may be set up either by a vibrating object in the boundary layer, such as a vibrating ribbon, or by disturbances from the outside, such as stream turbulence and sound. When the disturbance is random or nearly random and contains many frequencies, amplification and damping isolate a wave containing a narrow band of frequencies in the neighborhood of the frequency most highly amplified.

A wave in the boundary layer constitutes a disturbance that will cause transition on a flat plate with zero pressure gradient when the amplitude is sufficiently large. A sufficiently large random disturbance will also cause transition. When random initial distrubances are so small that transition is delayed until values of $R \leqslant 2{,}000$ have been reached, sufficient amplification can occur from the experimentally established lower limit $R = 450$, to $R \leqslant 2{,}000$ to give rise to a recognizable oscillation. Larger initial disturbances obscure the oscillations by irregular fluctuations of comparable magnitude.

Natural disturbances may be sound waves as well as turbulence. Turbulence generally has a more nearly random distribution of energy with frequency than sound. In view of the importance of frequency, sound disturbances with a concentration of energy in frequency bands that are highly amplified by the boundary layer may be more conducive to early transition than turbulence. This is important in free flight where turbulence is probably negligible but where engine and propeller noise is present in large amounts.

The effect of pressure gradient on the oscillations is a practicably important phase of the problem about which more should be known. Little more has been done here than to show the direction of the effect and to give some idea of its magnitude. The results are in accord with theory, which also is incomplete in this respect.

Other aspects of the problem remain to be investigated. One of these having practical importance is the effect of curvature. The importance of boundary-layer oscillations on airfoils cannot be determined until effects of curvature as well as pressure gradient are known. Other quantities associated with the wave but not investigated are v and uv. A study of these quantities would be interesting as a further check on the theory, although hardly necessary to identify the oscillations and their characteristics in view of the information derived from studies of u.

It is possible that boundary-layer oscillations may arise from internal disturbances as well as from external disturbances—that is, from surface irregularities and vibration of the surface. A randomly distributed small roughness may produce effects similar to small amounts of turbulence in the air stream. Small ridges or waves in the surface may start oscillations when the spacing is near some amplified wavelength. Vibration of the surface, like sound, may produce oscillations, especially when the frequency is near some amplified oscillation frequency. An investigation of these and other phases of the problem will throw additional light on the important problem of transition.

X. References

[1] G. I. Taylor, Statistical theory of turbulence. Part V. Effect of turbulence on boundary layer. Theoretical discussion of relationship between scale of turbulence and critical resistance of spheres, Proc. Roy. Soc. (London) [A] **156,** 307 (Aug. 1936).

[2] W. Tollmien, The production of turbulence, NACA Tech. Memo. 609 (1931).

[3] W. Tollmien, General instability criterion of laminar velocity distributions, NACA Tech. Memo. 792 (1936).

[4] H. Schlichting, Zur Entstehung der Turbulenz bei der Plattenströmung, Nach. Ges. Wiss. Gött. Math. physik. Klasse, 181 (1933).

[5] H. Schlichting, Amplitudenverteilung und Energiebilanz der keinen Störungen bei der Plattenströmung, Nach. Ges. Wiss. Gött., Math. physik. Klasse, **I**, 47 (1935).

[6] H. Schlichting, Über die Entstehung der Turbulenz in einem rotierenden Zylinder, Nach. Ges. Wiss. Gött., Math. physik. Klasse, 160 (1932).

[7] H. Schlichting, Turbulenz bei Wärmeschichtung, Z. a. Math. Mech. **15,** 313 (Dec. 1935).

[8] G. Rosenbrook, Instabilität der Gleitschicht im schwach divergenten Kanal, Z. a. Math. Mech. **17,** 8 (1937).

[9] S. H. Hollingdale, Stability and configuration of the wakes produced by solid bodies moving through fluids, Phil. Mag. [7] **29,** 211 (March 1940).

[10] P. Savic, On acoustically effective vortex motion in gaseous jets, Phil. Mag. [7] **32,** 245 (Sept. 1941).

[11] Hugh L. Dryden, Air flow in the boundary layer near a plate, NACA Tech. Rep. 562 (1936).

[12] J. Nikuradse, Experimentelle Untersuchungen zur Turbulenzentstehung, Z. a. Math. Mech. **13,** 174 (1933).

[13] S. Goldstein, Modern developments in fluid dynamics, **I,** 136 (Clarendon Press, Oxford, Eng., 1938).

[14] W. C. Mock, Jr., Alternating-current equipment for the measurement of fluctuations of air speed in turbulent flow, NACA Tech. Rep. 598 (1937).

[15] W. C. Mock, Jr. and H. L. Dryden, Improved apparatus for the measurement of fluctuations of air speed in turbulent flow, NACA Tech. Rep. 448 (1932).

[16] H. L. Dryden and A. M. Kuethe, The measurement of fluctuations of air speed by the hot-wire anemometer, NACA Tech. Rep. 320 (1929).

[17] Hugh L. Dryden, G. B. Schubauer, W. C. Mock, Jr., and H. K. Skramstad, Measurements of intensity and scale of wind-tunnel turbulence and their relation to the critical Reynolds number of spheres, NACA Tech. Rep. 581 (1937)

[18] A. A. Hall and G. S. Hislop, Experiments on the transition of the laminar boundary layer on a flat plate, British A. R. C. Rep. and Memo. 1843 (1938).

[19] Hugh L. Dryden, Turbulence investigations at the National Bureau of Standards, Proc. Fifth Inter. Congr. Appl. Mech., Cambridge, Mass., 362 (1938).

[20] L. Prandtl, The mechanics of viscous fluids, Aerodynamic Theory III, W. F. Durand, ed., 178 (Julius Springer, Berlin 1935).

[21] Lord Rayleigh, On the stability or instability of certain fluid motions, Proc. Lond. Math. Soc. **11,** 57 (1880); **19,** 67 (1887).

[22] O. Tietjens, Beiträge zur Entstehung der Turbulenz, Z. a. Math. Mech. **5,** 200 (June 1925).

[23] H. Görtler, Über den einfluss der Wandkrümmung auf die Entstehung der Turbulenz, Z. a. Math. Mech. **20,** 138 (1940)

[24] J. Pretsch, The stability of laminar flow past a sphere, NACA Tech. Memo. 1017 (1942).

WASHINGTON, October 2, 1946.

MATHEMATICAL TABLES

(Note that prices in parentheses are for countries not extending the franking privilege)

Attention is invited to a series of publications prepared by the Mathematical Tables Project of the National Bureau of Standards. The tables which have been made available through the Bureau are listed below. A list of other tables obtainable elsewhere will be sent on request.

Payment is required in advance. Make remittance payable to the "N ational Bureau of Standards" and send with order, using the blank form below. A mailing list is maintained for those who desire to receive announcements regarding new tables as they become available.

MT1. TABLE OF THE FIRST TEN POWERS OF THE INTEGERS FROM 1 TO 1000: (1938) VIII+80 pages; heavy paper cover. Out of print.

MT2. TABLES OF THE EXPONENTIAL FUNCTION e^x: The ranges and intervals of the argument and the number of decimal places in the entries are given below:

Range of x	Interval of x	Decimals given
−2.5000 to 1.0000	0.0001	18
1.0000 to 2.5000	.0001	15
2.500 to 5.000	.001	15
5.00 to 10.00	.01	12

(1939) XV+535 pages; bound in buckram. Out of print.

MT3. TABLES OF CIRCULAR AND HYPERBOLIC SINES AND COSINES FOR RADIAN ARGUMENTS: Contains 9 decimal place values of $\sin x$, $\cos x$, $\sinh x$, and $\cosh x$ for x (in radians) ranging from 0 to 2 at intervals of 0.0001. (1939) XVII+405 pages; bound in buckram, $2.00 ($2.50).

MT4. TABLES OF SINES AND COSINES FOR RADIAN ARGUMENTS: Contains 8 decimal place values of sines and cosines for radian arguments ranging from 0 to 25 at intervals of 0.001. (1940) XIX+275 pages; bound in buckram, $2.00 ($2.50).

MT5. TABLES OF SINE, COSINE, AND EXPONENTIAL INTEGRALS, VOLUME I: Values of these functions to 9 places of decimals from 0 to 2 at intervals of 0.0001. (1940) XXVI+444 pages; bound in buckram, $2.00 ($2.50).

MT6. TABLES OF SINE, COSINE, AND EXPONENTIAL INTEGRALS, VOLUME II: Values of these functions to 9, 10, or 11 significant figures from 0 to 10 at intervals of 0.001 with auxiliary tables. (1940) XXXVII+225 pages; bound in buckram, $2.00 ($2.50).

MT7. TABLE OF NATURAL LOGARITHMS, VOLUME I: Logarithms of the integers from 1 to 50,000 to 16 places of decimals. (1941) XVIII+501 pages; bound in buckram, $2.00 ($2.50).

MT8. TABLES OF PROBABILITY FUNCTIONS, VOLUME I: Values of these functions to 15 places of decimals from 0 to 1 at intervals of 0.0001, and from 1 to 5.6 at intervals of 0.001. (1941) XXVIII+302 pages; bound in buckram, $2.00 ($2.50).

MT9. TABLE OF NATURAL LOGARITHMS, VOLUME II: Logarithms of the integers from 50,000 to 100,000 to 16 places of decimals. (1941) XVIII+501 pages; bound in buckram, $2.00 ($2.50).

MT10. TABLE OF NATURAL LOGARITHMS, VOLUME III: Logarithms of the decimal numbers from 0.0001 to 5.0000, to 16 places of decimals. (1941) XVIII+501 pages; bound in buckram, $2.00 ($2.50).

MT11. TABLES OF THE MOMENTS OF INERTIA AND SECTION MODULI OF ORDINARY ANGLES, CHANNELS, AND BULB ANGLES WITH CERTAIN PLATE COMBINATIONS: (1941) XIII+197 pages; bound in green cloth. $2.00 ($2.50).

MT12. TABLE OF NATURAL LOGARITHMS, VOLUME IV: Logarithms of the decimal numbers from 5.0000 to 10.0000, to 16 places of decimals. (1941) XXII+506 pages; bound in buckram, $2.00 ($2.50).

MT13. TABLE OF SINE AND COSINE INTEGRALS FOR ARGUMENTS FROM 10 TO 100. (1942) XXXII+185 pages; bound in buckram, $2.00 ($2.50).

MT14. TABLES OF PROBABILITY FUNCTIONS, VOLUME II: Values of these functions to 15 places of decimals from 0 to 1 at intervals of 0.0001 and from 1 to 7.8 at intervals of 0.001. (1942) XXI+344 pages; bound in buckram, $2.00 ($2.50).

MT15. THE HYPERGEOMETRIC AND LEGENDRE FUNCTIONS WITH APPLICATION TO INTEGRAL EQUATIONS OF POTENTIAL THEORY. By Chester Snow, National Bureau of Standards. Reproduced from original handwritten manuscript. (1942) VII+319 pages; bound in heavy paper cover. Out of print.

MT16. TABLE OF ARC TAN x: Table of inverse tangents for positive values of the angle in radians. Second central differences are included for all entries. $x=[0(.001)7(.01)50(.1)300(1)2{,}000(10)10{,}000;\ 12D]$ (1942) XXV+169 pages; bound in buckram, $2.00 ($2.50).

(Continued on other side)

(Cut Here)

NATIONAL BUREAU OF STANDARDS
Washington 25, D. C.

_____
Date

Please send me the Mathematical Tables checked below. I enclose $_____ to cover the cost.

CHECK HERE (Note that prices in parentheses are for countries not extending the franking privilege)

☐ MT3—$2 ($2.50)	☐ MT10—$2 ($2.50)	☐ MT18—$0.25 ($0.30)	☐ MT26—$0.25 ($0.30)	☐ MT33—$0.25 ($0.30)
☐ MT4—$2 ($2.50)	☐ MT11—$2 ($2.50)	☐ MT19—$0.25 ($0.30)	☐ MT27—$0.25 ($0.30)	☐ MT34—$0.25 ($0.30)
☐ MT5—$2 ($2.50)	☐ MT12—$2 ($2.50)	☐ MT20—$0.25 ($0.30)	☐ MT28—$0.25 ($0.30)	☐ MT35—$0.25 ($0.30)
☐ MT6—$2 ($2.50)	☐ MT13—$2 ($2.50)	☐ MT21—$0.25 ($0.30)	☐ MT29—$0.25 ($0.30)	☐ MT36—$0.25 ($0.30)
☐ MT7—$2 ($2.50)	☐ MT14—$2 ($2.50)	☐ MT22—$0.25 ($0.30)	☐ MT30—$0.25 ($0.30)	
☐ MT8—$2 ($2.50)	☐ MT16—$2 ($2.50)	☐ MT24—$0.25 ($0.30)	☐ MT31—$0.25 ($0.30)	
☐ MT9—$2 ($2.50)	☐ MT17—$1.50 ($1.75)	☐ MT25—$0.25 ($0.30)	☐ MT32—$0.25 ($0.30)	

SEND ONLY MONEY ORDER OR CHECK PAYABLE TO THE "NATIONAL BUREAU OF STANDARDS" IN U. S. CURRENCY.

_____
(Name)

_____
(Address)

_____
(City, Zone, and State)